WHAT MAKES A STAR TURN VIOLENT?

EXPLORING HIGH-MASS STAR FORMATION AND STELLAR MAGNETIC HELICITY

Kristin Lund

A Thesis Submitted for the Degree of PhD
at the
University of St Andrews

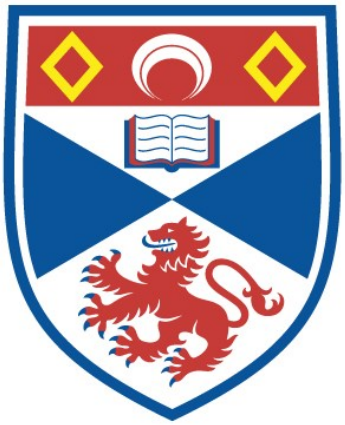

2020

Identifiers to use to cite or link to this thesis:

DOI: https://doi.org/10.17630/sta/136
http://hdl.handle.net/10023/23973

What makes a star turn violent?

Exploring high-mass star formation and stellar magnetic helicity

by

Kristin Lund

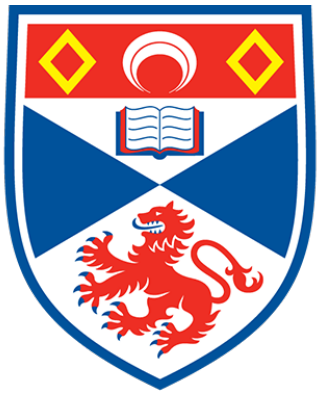

University of
St Andrews

This thesis is submitted in partial fulfilment for the degree of
Doctor of Philosophy (PhD)
at the University of St Andrews

April 2020

Declaration

Candidate's declaration

I, Kristin Lund, do hereby certify that this thesis, submitted for the degree of PhD, which is approximately 42,000 words in length, has been written by me, and that it is the record of work carried out by me, or principally by myself in collaboration with others as acknowledged, and that it has not been submitted in any previous application for any degree.

I was admitted as a research student at the University of St Andrews in September 2016.

I received funding from an organisation or institution and have acknowledged the funder(s) in the full text of my thesis.

07.08.20
Date Signature of candidate

Supervisor's declaration

I hereby certify that the candidate has fulfilled the conditions of the Resolution and Regulations appropriate for the degree of PhD in the University of St Andrews and that the candidate is qualified to submit this thesis in application for that degree.

14.08.20
Date Signature of supervisor

Permission for publication

In submitting this thesis to the University of St Andrews we understand that we are giving permission for it to be made available for use in accordance with the regulations of the University Library for the time being in force, subject to any copyright vested in the work not being affected thereby. We also understand, unless exempt by an award of an embargo as requested below, that the title and the abstract will be published, and that a copy of the work may be made and supplied to any bona fide library or research worker, that this thesis will be electronically accessible for personal or research use and that the library has the right to migrate this thesis into new electronic forms as required to ensure continued access to the thesis.

I, Kristin Lund, confirm that my thesis does not contain any third-party material that requires copyright clearance.

The following is an agreed request by candidate and supervisor regarding the publication of this thesis:

Printed copy

No embargo on print copy.

Electronic copy

No embargo on electronic copy.

07.08.20
Date Signature of candidate

14.08.20
Date Signature of supervisor

Underpinning research data or digital outputs

Candidate's declaration

I, Kristin Lund, understand that by declaring that I have original research data or digital outputs, I should make every effort in meeting the University's and research funders' requirements on the deposit and sharing of research data or research digital outputs.

07.08.20
Date Signature of candidate

Permission for publication of underpinning research data or digital outputs

We understand that for any original research data or digital outputs which are deposited, we are giving permission for them to be made available for use in accordance with the requirements of the University and research funders, for the time being in force.

We also understand that the title and the description will be published, and that the underpinning research data or digital outputs will be electronically accessible for use in accordance with the license specified at the point of deposit, unless exempt by award of an embargo as requested below.

The following is an agreed request by candidate and supervisor regarding the publication of underpinning research data or digital outputs:

No embargo on underpinning research data or digital outputs.

07.08.20
Date Signature of candidate

14.08.20
Date Signature of supervisor

Collaboration Statement

This thesis is the result of my own work carried out at the University of St Andrews between September 2016 and March 2020. Parts of the work presented in this thesis have been published in refereed scientific journals. In all cases the text in the chapters has been written entirely by me. All figures have been produced by me, except the illustration on the front pages of Chapters 1 and 6 which was made by Madeline Frederikke Lund Pedersen specifically for this thesis.

- Chapters 2 and 3 use a Radiation Hydrodynamical code provided by K. Wood and D. Falceta-Gonçalves. The code was tested and adapted by me with help from K. Wood and D. Falceta-Gonçalves.

- Chapter 3 is an extended version of "*Radiation hydrodynamic simulations of massive star formation via gravitationally trapped H*II *regions - spherically symmetric ionized accretion flows*", K. Lund, K. Wood, D. Falceta-Gonçalves, B. Vandenbroucke, N. S. Sartorio, I. A. Bonnell, K. G. Johnston and E. Keto, 2019 in Monthly notices of the Royal Astronomical Society. All authors provided comments on the final manuscript.

- Chapter 4 is an extended version of "*The formation of high-mass binary star systems*", K. Lund and I. A. Bonnell, 2018 in Monthly notices of the Royal Astronomical Society. I developed the code used for the calculations in this work. I. A. Bonnell provided comments on the final manuscript. This chapter is based on initial simulations conducted in my Master's thesis, but no results from that thesis is presented here.

- Chapter 5 is an extended version of "*Measuring stellar magnetic helicity density*", K. Lund, M. Jardine, L. T. Lehmann, D. H. Mackay, V. See, A. A. Vidotto, J.-F. Donati, R. Fares, C. P. Folsom, S. V. Jeffers, S. C. Marsden, J. Morin and P. Petit, 2020 in Monthly notices of the Royal Astronomical Society. Stellar magnetic field data, in the form of α, β and γ coefficients, were provided by M. Jardine, A. A. Vidotto, J. Morin, C. P. Folsom and S. V. Jeffers. Solar magnetic field data, in the form of α, β and γ coefficients, were provided by L. T. Lehmann (simulated) and A. A. Vidotto (observational). I developed the code used for the analysis in this work. All authors provided comments on the final manuscript.

Abstract

High-mass stars play an important role in both the dynamical and chemical evolution of the galaxy, hence how they form has long been a topic of interest. In this thesis I explore accretion as a possible means of forming high-mass stars. I use a radiation hydrodynamics code to simulate accretion onto a star which emits ionising radiation. Usually accretion is assumed to end once ionisation begins, however I find accretion continues through the ionisation front whilst the ionised region is gravitationally trapped. This extended period of accretion increases the amount of material added to the star. As most high-mass stars are observed in close binary systems, next I develop a semi-analytic model to investigate whether accretion onto wide low-mass binaries can increase the mass of the stars and simultaneously decrease their separation. The result suggests magnetic braking of the accretion flow is a feasible way of forming the most massive close binary systems.

The second part of this thesis focuses on the magnetic helicity density of low-mass stars. There has been growing interest in magnetic helicity as a potential tracer of stellar eruptions, but measurements based on observations have been limited to the Sun. I present an analytic expression for the magnetic helicity density across any stellar surface given only observable quantities. This expression is used to calculate the magnetic helicity density of 52 stars, which is then plotted against other stellar parameters. I find mostly different behaviours for the partially and largely convective stars, except when plotting helicity density against toroidal magnetic energy. In that case the entire stellar sample follows the same power law. Comparing the Sun to the other stars I find the variation in solar helicity densities across a solar cycle falls within the scatter of the stellar values.

Acknowledgements

The 3.5 years leading to this thesis have been simultaneously long and short, at times sad and frustrating, but ultimately joyous and rewarding. I am so grateful for this experience, and for all the people who supported me along the way.

First and foremost I want to give a huge thanks to my trio of supervisors. To Ian Bonnell, whose cheerful and relaxed nature was an appreciated counterbalance to my own anxious state of mind. To Kenny Wood, for his limitless enthusiasm from day one. And to Moira Jardine, for welcoming me into her world and introducing me to helicity when I wanted a change.

I was lucky to work in a department filled with people happy to share their time and experience. Thanks to Lisa for her help with all things magnetic, to Diego and Bert for patiently answering my coding questions, and to Will for never being too busy to provide tech support. I would also like to thank Anne-Marie and Vivienne for listening and always having my back.

I will miss St Andrews immensely, but I will miss my friends and colleagues in the physics and astronomy department more. For all the laughs, the rants, the coffee breaks, the pub trips and so much more, I thank you all. A shout-out to the Cupar crew, moving out of St Andrews would have felt like a tragedy if it wasn't for you guys. And a special thanks to Chris and Dom, the best part of my PhD was doing it alongside you.

Alistair, I treasure every day I get to spend with you. Writing a thesis is much easier with you around to give me a hug and to make me tea.

Finally, I would like to thank my family. I could not have gotten through the past 3.5 years without knowing that your doors are always open to me. A special mention must go to Madeline, without whom both my world and this thesis would have been a lot less colourful.

Funding

This work was supported by the Carnegie Trust for the Universities of Scotland through a Carnegie PhD Scholarship.

Research Data/Digital Outputs access statement

Research data underpinning this thesis are available at https://doi.org/10.17630/eeb14f5f-11a0-40d0-8ae0-f9075ec28363.

Contents

List of Figures

List of Tables

List of Physical Constants, Variables and Astronomical Data

This list describes the symbols I use throughout my thesis to represent physical constants, astronomical units and variables. In the cases where the variable has been defined by an equation the page number of said equation is given. Note that some variables will appear with subscripts which are not listed here. The most common examples are "i" and "n" for indicating an ionised or neutral case, and "$\star$", "bin", "cloud" and "clust" when referring to various properties of stars, binary systems, molecular clouds or stellar clusters respectively.

Physical Constants

μ_0	Permeability of free space	$4\pi \times 10^{-7}$ H m^{-1}
c	Speed of light	2.9979×10^{8} m s^{-1}
G	Gravitational constant	6.6743×10^{-11} m^3 kg^{-1} s^{-2}
h	The Planck constant	6.6261×10^{-34} J s
k	Boltzmann constant	1.3807×10^{-23} J K^{-1}
$m_{\rm H}$	Mass of a hydrogen atom	1.6737×10^{-27} kg
$m_{\rm p}$	Proton mass	1.6726×10^{-27} kg
R_g	Gas constant	8.3145 J K^{-1} mol^{-1}

Astronomical Units

au	Astronomical unit	1.496×10^{11} m
$\rm M_\odot$	Solar mass	1.989×10^{30} kg
pc	Parsec	3.086×10^{16} m
$\rm R_\odot$	Solar radius	6.957×10^{8} m

Other Symbols

α	Recombination coefficient	
α_{lm}	Coefficient characterising the poloidal magnetic field component	
β_{lm}	Coefficient characterising the poloidal magnetic field component	
$\boldsymbol{A}$	Vector potential field	page 145

$\boldsymbol{B}$	Magnetic field	page 145
$\boldsymbol{B}_{\text{pol}}$	Poloidal magnetic field component	page 25
$\boldsymbol{B}_{\text{tor}}$	Toroidal magnetic field component	page 25
Δt_{CFL}	Critical Courant-Friedrichs-Lewy timestep	page 38
Δx_{cell}	Grid cell width	
$\dot{M}$	Mass accretion rate	page 66
γ	Heat capacity ratio	
γ_d	Drag coefficient	
γ_{lm}	Coefficient characterising the toroidal magnetic field component	
Λ	Path length	
λ	Wavelength	
$\langle \mathrm{B}^2 \rangle$	Mean squared magnetic flux density	
μ	Mean molecular weight	
ν	Frequency	
Ω	Angular velocity	
ϕ_B	Magnetic flux	page 7
ρ	Mass density	
σ	Standard deviation	page 116
σ_ν	Cross section for ionisation by photons of frequency ν	page 51
σ_l	Spectral line width	
τ	Optical depth	page 51
τ_o	Torque	page 118
$\tilde{h}$	Helicity energy fraction	page 158
ξ	Random number	
A	Area	
c_{s}	Sound speed	page 20
c_{lm}	Normalisation constant	page 144
E	Energy	
e	Energy density	
E_A	Kinetic energy of magnetic Alfvén waves	page 6

E_B	Magnetic energy	page 126
E_G	Gravitational binding energy of molecular cloud	page 6
E_{bin}	The binding energy of a binary stellar system	page 107
E_{clust}	The binding energy of a stellar cluster	page 107
E_{rot}	Rotational energy	page 119
E_{turb}	Kinetic energy in turbulent motion	page 120
F	Force	
F_{G}	Gravitational force	page 67
F_{rot}	Force from rotational motion	page 114
g_L	Landé factor	
H	Magnetic helicity	page 140
h	Magnetic helicity density	page 143
I	Integral	
I_f	Ionisation fraction	page 16
I_m	Moment of inertia	page 120
J_ν	The mean intensity of photons at frequency ν	
L	Angular momentum	
l	Mode	
L_s	Length scale	
l_{mfp}	Mean free path	page 48
M	Mass	
m	Order	
M_A	Alfvén Mach number	page 126
M_J	Jeans mass	page 9
N	Number of particles	
n	Number density	
$N_\star$	Number of stars	
N_γ	Number of photon packets	
P	Probability	
p	Pressure	

$P_{\rm rot}$	Rotation period	
P_{lm}	Legendre Polynomial	
Q	Ionising luminosity	
q	Mass ratio	
R/r	Radius	
$R_{\rm st}$	Strömgren radius	page 16
R_J	Jeans length	page 9
$R_{\rm acc}$	Accretion radius	
$R_{\rm B}$	Bondi radius	page 66
$R_{\rm crit}$	Critical radius	page 114
$R_{\rm HI}$	HII region radius according to the Hosokawa Inutsuka solution	page 61
$R_{\rm o}$	Rossby number	page 30
$R_{\rm Sp}$	HII region radius according to the Spitzer solution	page 61
S	Source term	
s	Separation between two binary stars	page 109
$s_{\rm min}$	Minimum separation between two binary stars	page 105,107
T	Temperature	
t	Time	
t_c	Mean collision time between neutrals and ions	page 7
$t_{\rm AD}$	Ambipolar diffusion time	page 7
$t_{\rm conv}$	Convective turnover time	
$t_{\rm ff}$	Free fall time	page 9,91
$t_{\rm HD}$	Hydrodynamical timescale	page 40
$t_{\rm light}$	Light crossing time	page 40
$t_{\rm recomb}$	Recombination time	page 40
u	Conserved variable	
V	Volume	
v	Velocity	
v_A	Alfvén velocity	page 6
$v_{\rm D}$	Critical velocity for a D-type ionisation front	page 20
$v_{\rm R}$	Critical velocity for an R-type ionisation front	page 20
W	Lambert W function	

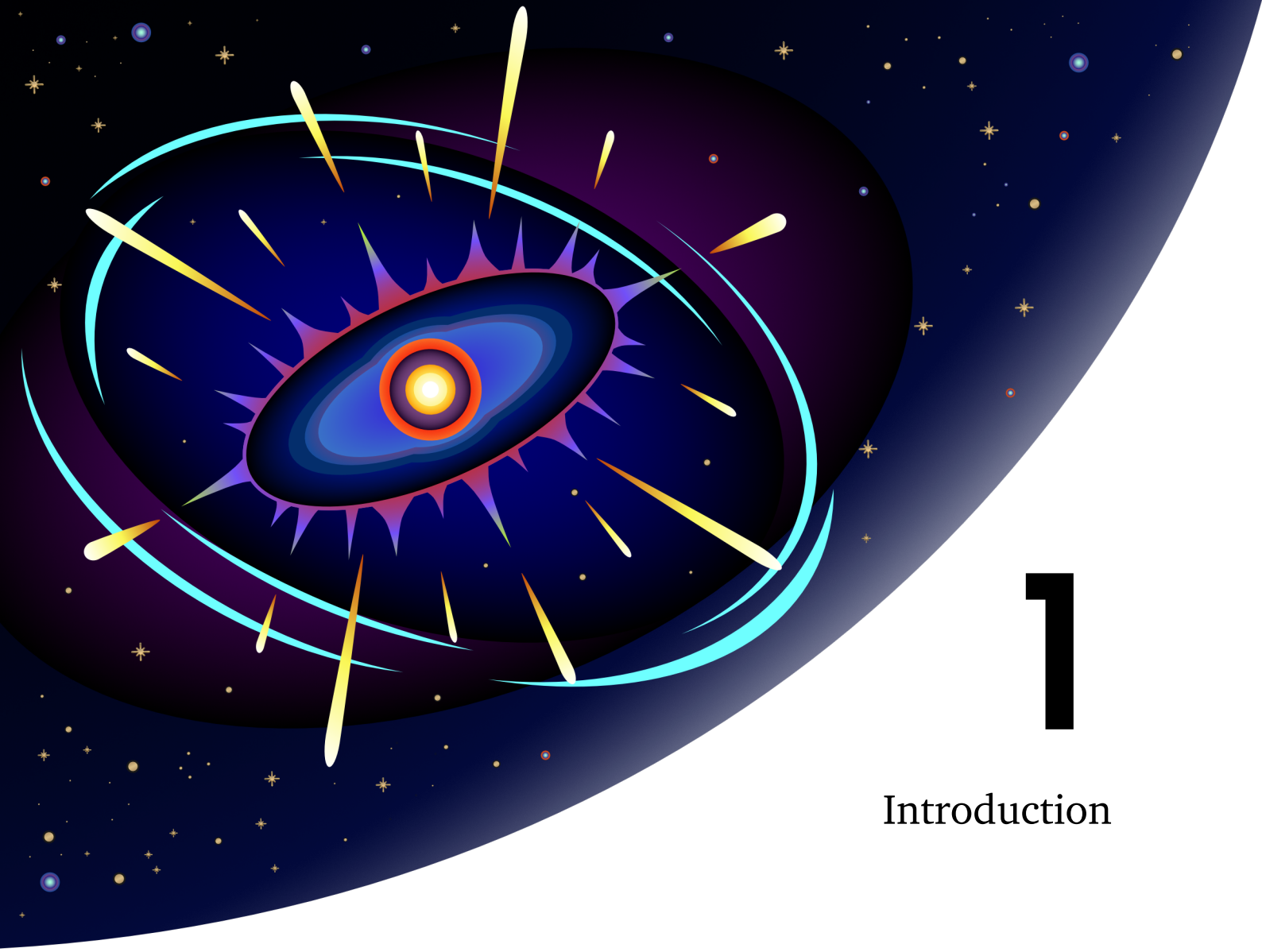

1

Introduction

Looking up at the night sky the stars appear calm and quiet. Up close however, stars can be extremely violent, blasting their surroundings with energy and material. High-mass stars are very energetic and have a big impact on galactic dynamics all the way throughout their lifetimes and at their deaths. Even lower-mass stars, which are significantly cooler and smaller, have ways of occasionally disrupting their environment. The following introduction will broadly cover where stars form, how they form, and two examples of how they impact their surroundings; the ionising radiation of high-mass stars and the magnetic activity of low-mass stars.

1.1 Star formation

Stars are key players in astrophysics on every scale; they are drivers of galactic evolution, birthplaces of planetary systems and sources of heavy elements. More fundamentally, as the main sources of visible light in the night sky, their formation has been a topic of interest for centuries. As early as 1692 Newton suggested stars form as a result of the gravitational collapse of material in space[1]. This is still the accepted theory.

Star formation takes place within dense clumps/cores of giant molecular clouds (GMCs) which are mainly found in spiral and irregular galaxies (e.g. Larson, 2003a). To reach this point gravity must have overcome all resisting opponents, including thermal pressure, turbulence and magnetic fields. Gas in the galaxy must have been allowed to gather into GMCs, regions of the GMCs must have contracted to form dense cores, and those cores must have collapsed to form stars. When these conditions are met, it usually results in more than just one individual star. Through the use of statistics, Michell (1767) realised some groups of stars on the sky were highly likely to be gravitationally bound and have a common origin. He further argued for the existence of stars orbiting a common centre of mass. In both cases he was right, and these systems are now known as "stellar clusters" and "multiples", or more specifically "binaries" in the case of two orbiting stars.

The distribution of stellar masses in a newly formed group of stars is described by the initial mass function (IMF), a power-law first introduced by Salpeter (1955). Based on observations of stars in the Milky Way there are different estimates of the exact form of the IMF (Miller & Scalo, 1979; Kroupa, 2001; Chabrier, 2003; Thies & Kroupa, 2007), but agreement that the vast majority of stars formed have lower masses than the Sun, with the number of more massive stars decreasing with increasing mass. Consequently, relatively low-mass stars are the ones dominating the overall galactic stellar mass. Over time the population of stars will evolve from the IMF, and with more massive stars being shorter lived than lower mass stars they become an increasingly rare sight with age. The fractions of stars of different masses in

[1] In a letter to Rev Richard Bentley, Newton wrote: *"It seems to me, that if the matter of our sun and planets, and all the matter of the universe, were evenly scattered throughout all the heavens, and every particle had an innate gravity towards all the rest, and the whole space throughout which this matter was scattered, was finite, the matter on the outside of this space would by its gravity tend towards all the matter on the inside, and by consequence fall down into the middle of the whole space, and there compose one great spherical mass. But if the matter were evenly disposed throughout an infinite space, it could never convene into one mass; but some of it would convene into one mass and some into another, so as to make an infinite number of great masses, scattered great distances from one to another throughout all that infinite space. And thus might the sun and fixed stars be formed, supposing the matter were of a lucid nature"* (Janiak & Newton, 2004).

the Milky Way can be broken down in terms of spectral classes (e.g. Morison, 2014): 0.003% O type ($\gtrsim$18 $M_\odot$ (Weidner & Vink, 2010)), 0.13% B type ($\sim$ 2.9–17 $M_\odot$ (Silaj et al., 2014)), 0.63% A type ($\sim$ 1.6–2.4 $M_\odot$ (Adelman, 2004)), 3.1% F type ($\sim$ 1.18–1.57 $M_\odot$ (Cram et al., 1989)), 8% G type ($\sim$ 0.84–1.15 $M_\odot$(Cram et al., 1989)), 13% K type ($\sim$ 0.67–0.81 $M_\odot$(Cram et al., 1989)) and 75% M type ($\sim$ 0.075–0.6 $M_\odot$ (Baraffe & Chabrier, 1996)).

Once stars are formed, they inject their surrounding medium with energy, momentum and material through various stellar feedback mechanisms (e.g. winds, jets, photoionisation, radiation pressure and supernovae). By recycling stellar material back into the interstellar medium (ISM), stars change the chemical content of their surroundings, which also impacts the ingredients of future generations of stars. In terms of dynamics, stars emitting energy and momentum can act both to disperse or compress surrounding material, potentially triggering or suppressing local star formation (see reviews by Mac Low & Klessen (2004); Ballesteros-Paredes et al. (2007); Krumholz (2014)).

Only stars with masses exceeding $\sim$ 8 $M_\odot$ (all O type and some B type stars) are hot enough to emit significant amounts of ionising radiation, and massive enough to end their lives in a supernova event. The feedback of these stars strongly dominates that of lower-mass stars, despite them being massively outnumbered. Throughout this thesis stars $>$ 8 $M_\odot$ will be referred to as "high-mass", making the rest "low-mass". Not only are these two categories of stars observed to lead different lives and deaths, they also require different formation theories.

I will go on to outline how low-mass stars are believed to form, and explain why a different explanation is needed for high-mass stars. However, first I describe the stellar birth sites (GMCs), which both groups of stars have in common. I will mainly focus on turbulence and magnetic fields, as these are two properties that impact star formation.

1.1.1 Giant molecular clouds

GMCs are cool and dense regions in the ISM that are dominated by molecular hydrogen (H_2). Their high densities ($\sim 10^2$ cm^{-3}) shield them from external UV radiation and results in a typical temperature of $\sim$ 10 K. However UV radiation from high-mass stars within the clouds can increase the temperature in surrounding areas up to $\sim$ 100 K (Larson, 2003a). The GMC masses are of the order of 10^4–10^6 $M_\odot$ and their sizes span tens of parsecs (Cernicharo, 1991). Generally the clouds are irregularly shaped and have considerable small-scale struc-

ture. Denser regions within the clouds are called clumps ($\sim 10^3$ $M_\odot$, ~ 1 pc) and cores (~ 1 $M_\odot$, $\lesssim 0.1$ pc), which may collapse under gravity to form stellar clusters and individual stars (Cernicharo, 1991; Williams et al., 2000). Based on the rate at which stars form in gravitationally bound clouds, it has become apparent that the clumps and cores must experience support against gravity, slowing down the formation of stars (Evans et al., 2009). Both turbulence and magnetic fields are thought to play crucial roles in moderating the stellar formation rate (e.g. McKee & Ostriker, 2007).

Turbulence

Random internal motions in the GMCs make up the "turbulence" of the clouds. The presence of turbulence is deduced from observations of supersonic spectral line widths (σ_l) that cannot be explained by thermal motions alone (e.g. Larson, 1981). Moving from small to large length scales (L_s) within the clouds, the velocity dispersion increases systematically ($\sigma_l \propto L_s^\alpha$, $\alpha \approx 0.5$) (Larson, 1981; Solomon et al., 1987). This turbulent structure appears to be a universal feature of GMCs (Heyer & Brunt, 2004).

Despite the presence of turbulence in clouds being well established, its source and lifetime is still unknown. Numerical simulations show that if it is not somehow replenished it decays on a dynamical timescale (Mac Low et al., 1998; Stone et al., 1998). This implies one of two things; either the turbulent molecular clouds exist only on timescales shorter than a few dynamical times, or the turbulence is somehow continuously driven. Possible sources of turbulence include various feedback effects from stars (e.g. supernovae or ionising radiation) (Joung & Mac Low, 2006; Gritschneder et al., 2009), effects of gravity (e.g. galactic flows or accretion) (Heitsch et al., 2008; Klessen & Hennebelle, 2010) and magnetic fields (e.g. by Alfvén waves) (e.g. Beresnyak, 2019). A study by Krumholz & Burkhart (2016), applying turbulence models driven by feedback and by gravity to a collection of data, suggests the latter is more successful at matching observations.

The supersonic turbulence has two main roles. On a large scale its energy can offer support against gravitational collapse (e.g. Klessen et al., 2000). On smaller scales however it generates shocks that create density enhancements, which develop into the clumps and cores that are needed for star formation (Mac Low & Klessen, 2004). Mac Low & Klessen (2004) suggests the overall effect is a decrease in star formation efficiency; it takes longer for a gravitational collapse to happen in a cloud with turbulence than in a cloud without.

Magnetic fields

Magnetic fields have been inferred in molecular clouds through two main observational techniques based on the Zeeman effect and dust polarisation, see Crutcher (2012) for a review of these. The Zeeman effect is the splitting of the energy levels of an atom in the presence of a magnetic field, causing the spectral lines to also split. This results in three spectral lines being observed, one at the original wavelength λ_0, and two components shifted by $\pm\Delta\lambda_z$. This shift is proportional to the magnetic field strength (B):

$$\Delta\lambda_z \propto g_L B \lambda_0^2, \tag{1.1}$$

where g_L is the Landé factor. Consequently the Zeeman effect allows the magnetic field strength to be directly measured via the spectral lines. Other sources of line broadening such as rotation and turbulence complicate this measurement. In the presence of these effects it is difficult to detect weak magnetic fields.

If the goal is simply detecting magnetic fields, not measuring strength, a different indicator of magnetic fields caused by the Zeeman effect can be used. Depending on the line-of-sight relative to the magnetic field direction the three spectral line components will have different polarisations. The polarisation should in theory provide information on the direction of the magnetic field. For example, if the line-of-sight aligns with the magnetic field direction the original spectral line component is polarised parallel to the magnetic field (not visible) and the two others are circularly polarised. If the line-of-sight is transverse to the magnetic field direction the three components are linearly polarised, at right angles to each other. An alternative source for tracing the direction of magnetic fields is linearly polarised emission from dust grains. In a magnetic field dust grains will preferentially align their short axes along the direction of the field, and most thermal emission will be emitted along the long axes. So the emission is polarised perpendicular to the magnetic field. Unfortunately polarisation data does not give any indication of the strength of the field, and it suffers from regions of opposite polarity cancelling each other. In conclusion, visualising magnetic fields is challenging, but they are best described through a combination of both spectral and polarisation information (spectropolarimetry), which allows insight into both their magnitudes and geometries.

Through Zeeman observations a range of magnetic field strengths have been detected in

molecular clouds. Generally they are estimated to be of the order of 10 μG, or slightly stronger in denser regions (Crutcher, 2012). The magnetic fields likely play a part in the molecular cloud dynamics, but to what extent depends highly on how well they are coupled to the cloud material. The magnetic field only directly acts on ions, therefore it follows that if the material of the cloud was perfectly conducting, the field and the matter would be bound together completely. This scenario is called "flux freezing", as it implies the magnetic flux ($\phi_B = B\pi R^2$) through the cloud must be conserved (Roberts, 2007). In reality however, the cloud will only be partially ionised (Ferrière, 2001), and neutral atoms are only partially coupled to the field through their interactions with ions.

Assuming sufficient coupling, the question becomes whether the magnetic field within a molecular cloud is strong enough to support against gravitational collapse. In a highly magnetised cloud the internal motions are dominated by Alfvén waves. These are magnetohydrodynamic waves consisting of ions oscillating transverse to the magnetic field lines. The corresponding Alfvén velocity is given by:

$$v_A = \frac{B}{\sqrt{\mu_0 \rho}}, \tag{1.2}$$

where ρ is density and μ_0 is the permeability of free space ($4\pi \times 10^{-7}$ H m^{-1}). According to the virial theorem, a given cloud clump/core is stable if the kinetic energy provided by the magnetic Alfvén waves (E_A) equals half the gravitational binding energy (E_G) of the system:

$$\begin{gathered} E_A = \frac{1}{2} E_G, \\ \Downarrow \\ \frac{1}{2} M v_A^2 = \frac{1}{2} \frac{3GM^2}{5R}, \\ \Downarrow \\ \frac{MB^2}{\mu_0 \rho} = \frac{3GM^2}{5R}. \end{gathered} \tag{1.3}$$

So for a collapse to occur the following condition must hold:

$$M > \frac{5B^2 R}{3\mu_0 \rho G}. \tag{1.4}$$

In the above equations M and R represent the mass and radius of the clump/core in ques-

tion, and G is the gravitational constant (6.6743×10^{-11} $m^3 kg^{-1}$ s^{-2}). Substituting for $\rho = 3M/4\pi R^3$ and $\phi_B = B\pi R^2$ the virial relationship can be rearranged into a critical mass-to-flux ratio:

$$\left(\frac{M}{\phi_B}\right)_{\text{crit}} = \frac{1}{3}\sqrt{\frac{20}{G\pi\mu_0}}. \tag{1.5}$$

Based on a series of numerical models Mouschovias & Spitzer (1976) introduced a correction factor ($c_1 \sim 0.53$), changing the critical value slightly:

$$\left(\frac{M}{\phi_B}\right)_{\text{crit}} = \frac{c_1}{3}\sqrt{\frac{20}{G\pi\mu_0}}. \tag{1.6}$$

Any mass-to-flux ratio below this value suggests the magnetic support is sufficient to prevent a gravitational collapse.

In a perfectly conducting cloud where flux freezing applies, the flux, and hence the critical mass-to-flux ratio of any given clump/core, stays constant. This means that in an isolated system whichever dominates, the gravitational force or the magnetic force, cannot change in time. A collapsing clump will experience an increase in magnetic field strength as the field lines are forced closer together as a consequence of flux freezing, but this will not halt the collapse. Conversely, a cloud that is magnetically supported will remain supported. In a partially ionised cloud where the field is not fully coupled to the mass however, the critical mass-to-flux ratio is subject to change.

Because neutral material is only collisionally coupled to the magnetic field, it can decouple when such collisions become rare, at which point the ions and neutrals can drift with respect to each other (Mestel & Spitzer, 1956). This process is called "ambipolar diffusion" and happens on a time scale given by (Shu et al., 1987):

$$t_{\text{AD}} \sim \frac{L_s^2}{v_A^2 t_c}, \tag{1.7}$$

where L_s is some length scale and t_c is the mean collision time between neutrals and ions:

$$t_c \equiv \frac{1}{\rho_i \gamma_d}. \tag{1.8}$$

γ_d is the drag coefficient associated with the momentum exchange in the collision, which can be approximated as 3.5×10^{13} cm^3 g^{-1} s^{-1} (Shu et al., 1987; Draine et al., 1983). ρ_i is the

density of the ionised material, which can be related to the overall gas density via its ionisation fraction (see Section 1.2.1):

$$\rho_i = I_f \rho. \tag{1.9}$$

Substituting the expressions for Alfvén velocity and mean collision time into Equation 1.7 the ambipolar diffusion time can be rewritten as:

$$t_{\mathrm{AD}} \sim \frac{L_s^2 I_f \rho^2 \mu_0 \gamma_d}{B^2}. \tag{1.10}$$

Taking the case of a uniformly dense spherical molecular cloud as an example, where $L_s = R$ and $\rho = 3M/4\pi R^3$, the ambipolar diffusion time can be expressed as:

$$t_{\mathrm{AD}} \sim \frac{9 I_f M^2 \mu_0 \gamma_d}{16\pi^2 B^2 R^4}. \tag{1.11}$$

How this timescale compares to the overall lifespan of the cloud gives an indication of whether or not the magnetic field could play a significant role in the dynamics of the cloud.

Several authors have argued that strong magnetic fields are the dominant source of support in molecular clouds against gravitational collapse, and that collapse only occurs as a result of ambipolar diffusion (e.g. Mestel & Spitzer, 1956; Nakano, 1973; Mouschovias, 1987). After about one ambipolar diffusion time they propose sufficient neutral material will have gathered in a clump or core for it to collapse into stars, leaving the magnetic flux behind in the surrounding envelope. Thus, this theory predicts a higher mass-to-flux ratio in cores/clumps than in envelopes. This has not been observed, in fact the opposite result has been reported (Crutcher et al., 2009), which is more in line with simulations of turbulence dominated weakly-magnetised clouds (Lunttila et al., 2008, 2009). Alternatively, it could be a result of magnetic field diffusion by "magnetic reconnection" being more efficient in envelopes than cores, see Lazarian et al. (2012) for a description of this mechanism.

Although the exact effects of turbulence and magnetic fields on star formation in molecular clouds are still not clear, observations and simulations suggest a mixture of both is needed to explain the observed star formation rate (e.g. Kudoh & Basu, 2008; Nakamura & Li, 2008; Price & Bate, 2008; Padoan & Nordlund, 2011; Federrath, 2016). For a further discussion on the joint effect of magnetic fields and turbulence on star formation see reviews by Larson (2003a); Mac Low & Klessen (2004); McKee & Ostriker (2007); Padoan et al. (2014).

1.1.2 Low-mass stars

Fundamentally, stars form when gravity dominates. In the case of a molecular cloud without turbulent or magnetic support, collapse will occur in regions where gravity exceeds thermal pressure. For a given density and temperature, Jeans (1902) showed there exists a critical length scale that would result in hydrostatic equilibrium; the point where the expansion by thermal energy is balanced by the collapse by gravity:

$$R_J = \left(\frac{5R_g T}{2G\mu}\right)^{1/2} \left(\frac{4\pi}{3}\rho\right)^{-1/2}, \tag{1.12}$$

where ρ is the gas density, T is the gas temperature, R_g is the gas constant (8.3145 J K^{-1} mol^{-1}) and μ is the mean molecular weight. The corresponding critical mass is given by the volume of a sphere with radius R_J times the gas density:

$$\begin{gathered} M_J = \frac{4\pi}{3} R_J^3 \rho, \\ \Downarrow \\ M_J = \left(\frac{5R_g T}{2G\mu}\right)^{3/2} \left(\frac{4\pi}{3}\rho\right)^{-1/2}. \end{gathered} \tag{1.13}$$

These quantities are known as the Jeans length and the Jeans mass. Typical values are $\sim 10^4$ au and ~ 1 $M_\odot$, corresponding to densities of 10^{-19} g cm^{-3} and temperatures of 10 K.

Once a collapse is triggered, the next steps of the process are well studied and documented, the brief discussion here broadly follows that of Larson (2003a). Thinking of the collapsing region as consecutive shells at different radii, each one will collapse at approximately the free-fall time, given by the density of the material enclosed by the shell:

$$t_{\rm ff} = \sqrt{\frac{\pi^2 R_{\rm shell}^3}{8GM_{\rm inner}}} \propto \frac{1}{\sqrt{G\rho}}. \tag{1.14}$$

Moving towards the centre the density increases, causing the shells to fall in with increasing speed, which further increases density, resulting in a runaway effect (Larson, 1973). In the case of uniform clouds, which initially have no density gradient, this process is triggered by edge effects. Depending on whether the collapse is isothermal or a polytropic process ($P \propto \rho^\gamma$, where γ represents the heat capacity ratio), models suggest the density profile eventually approaches $\rho \propto r^{-2}$ or $\rho \propto r^{-2/(2-\gamma)}$ (Ogino et al., 1999). Either way, only a small fraction of

the collapsing material becomes dense enough to form a pressure-supported central "protostar". The residual infalling material forms a surrounding envelope, from which the protostar accretes the majority of the final stellar mass. For example, if the result is a 1 $M_\odot$ star, the initial protostellar mass would have been < 0.01 $M_\odot$, with the remaining $\sim 99\%$ being accreted material (Larson, 2003a). Once the envelope is depleted of gas and accretion stops, the protostar enters a period of contraction. As it contracts its temperature increases, until eventually it reaches the point where the core becomes hot enough to initiate hydrogen burning; this is when the star is born (Palla & Stahler, 1993; Baraffe et al., 2002).

1.1.3 High-mass stars

The formation of high-mass stars is a challenging problem, not made easier by the limited observational information available: high-mass stars are far away, so it is difficult to get a good angular resolution; they form in dense molecular clouds, so optical extinction is an issue; they are short-lived, so not many are observed, and even fewer in the process of forming. Multiple theoretical models have been proposed, but no consensus has been reached (Zinnecker & Yorke, 2007).

To complicate matters, the majority of high-mass stars are observed in close binary or multiple systems (Mason et al., 1998; García & Mermilliod, 2001; Zinnecker & Mathieu, 2001; Chini et al., 2012; Sana et al., 2014). Recently, Gravity Collaboration et al. (2018) studied O and B type stars in the Orion Trapezium Cluster and found 50% of the stars with masses $\leq$ 1–2 $M_\odot$ had companion stars, a percentage that increased to 100 % for stars above 16 $M_\odot$. They also found the average number of companions increased for higher mass stars, from ~ 0.6 for $\leq$ 1–2 $M_\odot$ stars to 2.3 ± 0.3 for $>$ 16 $M_\odot$ stars. It has been suggested that massive stars favour massive companions (Kobulnicky & Fryer, 2007), however Gravity Collaboration et al. (2018) did not find evidence of this. Any formation theory must be able to account for the fact that most high-mass stars are observed in close multiple systems, this will not be discussed further here, but is explored in Chapter 4.

Focusing on individual high-mass stars, the main question is how to account for masses $10-100$ times that of a typical star. Stars exceeding 100 $M_\odot$ have been observed (Crowther et al., 2010; Crowther et al., 2016; Tehrani et al., 2019), the most massive to date being R136a1 at 315^{+60}_{-50} $M_\odot$ (Crowther et al., 2016). Is this huge amount of mass gathered during the formation process or afterwards? For a Jeans mass ($M_J \sim \rho^{-1/2} T^{3/2}$) to reach masses of

this scale it would require an extremely high temperature (which is not observed) or a very low density (implying a very long free-fall time). Furthermore, these high-mass stars tend to be found in the crowded centres of stellar clusters (e.g. Drissen et al., 1995; Hillenbrand, 1997). Is that where they formed? If not, how did they get there? It is evident that the situation is a lot more complex for high-mass stars than low-mass stars, and the same formation mechanism can not be applied. I will outline three theories: the mass accumulating before a monolithic collapse, the mass accreting throughout the star formation process and mergers of smaller stars. Following this I will also briefly discuss the radiation pressure problem in the formation of high-mass stars.

The turbulent core model

The idea of the turbulent core model is essentially to form high-mass stars in a process similar to low-mass star formation, only scaling it up in mass by invoking a "turbulent Jeans mass" instead of the traditional Jeans mass (McKee & Tan, 2003). Whereas the Jeans mass balances gravity with thermal energy, this method uses turbulence, in a way exchanging the kinetic energy associated with a given sound speed by that of a turbulent velocity. The proposition is that turbulence would be able to support a more massive cloud core than thermal energy, a core that would then collapse to form more massive stars. A variation on this concept with a magnetically supported core instead has also been discussed (Commerçon et al., 2011). However, it might not be as straightforward as simply substituting one energy source for another.

Whether massive turbulent cloud cores would actually undergo monolithic collapse and form high-mass stars directly, or fragment into multiple ~ 1 Jeans mass stars has been debated (Dobbs et al., 2005; Krumholz et al., 2007). Dobbs et al. (2005) point out that turbulent support is not isotropic and cannot be treated like a thermal pressure term. Through numerical simulations they find turbulence causes a density structure in the core that serves as the foundation for subsequent fragmentation. In response, Krumholz et al. (2007) argue that including radiation feedback limits fragmentation, however their initial conditions do not include a turbulent density structure that could shield against radiation (Krumholz & Bonnell, 2009).

Another challenge the turbulent core model faces is proving massive cloud cores form in the first place. A major question being: how are they supported during the time it takes them to assemble? If they are out there it should be possible to detect them, however as of now there only exists a handful of potential high-mass pre-stellar core candidates (Duarte-Cabral et al.,

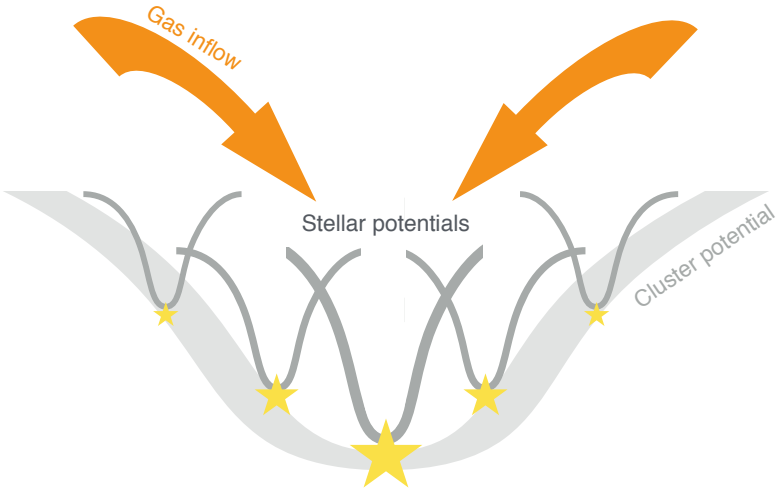

Figure 1.1: A diagram of competitive accretion in a stellar cluster, based on Figure 7 in Bonnell et al. (2007). The cluster potential is made up of the combined stellar potentials and acts to funnel gas to the massive stars at the centre of the cluster.

2014; Cyganowski et al., 2014; Wang et al., 2014; Kong et al., 2017; Nony et al., 2018). The statistical study by Tigé et al. (2017) suggests these objects either have a lifetime of 1–7 $\times$ 10^4 yrs, or alternatively they may not exist.

Competitive accretion

When employing "competitive accretion" (Zinnecker, 1982; Bonnell et al., 2001b) to explain high-mass stars the story begins with the familiar low-mass star formation; cloud fragmentation leads to the birth of a group of stars with masses of the order of the Jeans mass. What happens next is the crucial part. The combined gravitational potential of the stars forms a gravitational potential for the entire cluster that funnels gas preferentially to the centre of the cluster, see Figure 1.1. Consequently, the closer a star is to the core of the cluster, the more gas it will be able to accrete, resulting in a higher stellar mass (Bonnell et al., 1997, 2001a,b, 2004; Bonnell & Bate, 2006). In their review paper Zinnecker & Yorke (2007) aptly describe competitive accretion as a combination of the real estate concept: "location, location, location" and the capitalistic concept: "the rich get richer". This results in the central stars growing massive, whereas most other stars do not accrete a significant amount of gas, leading to a large range of final stellar masses. In fact, the process appears to give a power-law IMF, similar to what is observed (Bonnell & Bate, 2006; Bonnell et al., 2007).

This theory is dependent on there being gas available in the stellar cluster, i.e. some gas

must be left behind after the initial cloud collapse has turned cores into stars. Observations show this is the case, with gas being the biggest contributor to the total mass in young stellar clusters (Lada & Kylafis, 1991). Even if this gas is not in the immediate vicinity of the stars at the centre of the cluster, it is expected to be channelled there from a region similar in size to the initial cloud (Smith et al., 2009). A result of this type of accretion is that the mass of the highest mass star should relate to the overall mass of the cluster. This seems to be supported by observations (Weidner & Kroupa, 2006). Additionally, the final stellar masses should have little to no relation to the initial masses, or to the immediate surroundings of the stars at the time of formation. This idea has been challenged by observations indicating a mapping between the final IMF and the mass distribution of pre-stellar cloud cores (Motte et al., 1998; Alves et al., 2007; Chabrier & Hennebelle, 2010). However, a more recent higher resolution study by Motte et al. (2018) reveals a cloud core mass function that is decidedly different from the IMF.

Stellar collisions and mergers

A final option is high-mass stars forming through the collisions and mergers of lower-mass stars (Bonnell et al., 1998). Based on expected stellar densities these events would be rare, and are unlikely to be the main mechanism responsible for high-mass stars (Bonnell & Bate, 2005). Clarke & Bonnell (2008) showed that stellar collisions are only feasible in stellar clusters that are richly populated and tightly bound, such as globular clusters. The clusters must have a dense core that smoothly joins the rest of the cluster in order to ensure the core does not dissolve before collisions can take place.

The radiation pressure problem

Both the turbulent core model and competitive accretion rely on gathering a lot of material into a single object, either from the collapsing cloud core or more distant gas. Historically speaking, concerns have been raised that radiation pressure would introduce an upper limit on how much mass could be added to a star (Kahn, 1974; Yorke & Kruegel, 1977). Beyond some critical luminosity, the radiation pressure of the star will overpower the pull from gravity and force surrounding material to move away from the star. Assuming steady state spherically symmetric infall, the material will reverse once the star reaches $\sim 10\ M_{\odot}$ (Wolfire & Cassinelli, 1987; Edgar & Clarke, 2004). Though, in general, accretion is not expected to be spherical,

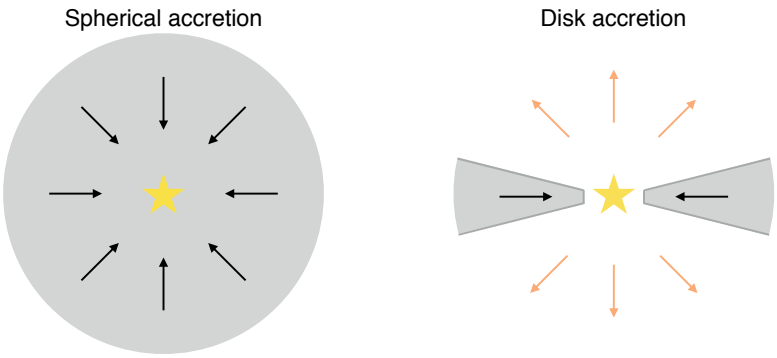

Figure 1.2: Spherical accretion (*left*) versus accretion through a disk (*right*). The grey regions show the distribution of material, and the black and orange arrows represent inflow and outflow respectively.

and this allows for much higher masses to be reached.

Any rotation in the cloud results in the formation of a flat disk of material, as the angular momentum of the gas will prevent it from falling directly onto the central protostar (Norman et al., 1980). Additionally, magnetic fields can also aid the flattening of material perpendicular to the field lines (Mouschovias, 1991). In the presence of a disk the radiation is no longer isotropic, as in the case of spherical accretion, it is instead focused preferentially along the axis perpendicular to the disk (Yorke & Bodenheimer, 1999). This is because the radiation can more easily penetrate the low-density material above and below the disk. Innermost parts of the dense disk could be largely shielded from radiation, hence allowing material to accrete through the disk relatively unhindered by radiation pressure. See Figure 1.2 for an illustration of this process, which is known as the "flashlight effect". This effect can be amplified in the case of rapidly rotating stars, as they have been found to be cooler at the equator and warmer at the poles, resulting in stronger radiation in the polar directions (Yorke & Sonnhalter, 2002).

Simulations by Kuiper et al. (2010, 2015); Kuiper & Hosokawa (2018) have convincingly shown that accretion disks can survive the radiation pressure of a growing central star. By allowing material to flow through a radiation shielded disk simulations have been able to form increasingly massive stars (Nakano, 1989; Yorke & Sonnhalter, 2002; McKee & Tan, 2003; Kuiper et al., 2010). Kuiper et al. (2010) for instance, reaches stellar masses up to $\sim 140\ M_{\odot}$.

In conclusion both theory and simulations suggest the radiation pressure problem can be avoided by assuming a circumstellar disk. In terms of high-mass stars circumstellar disks have only been detected around B type stars, not O type Cesaroni et al. (2007). Bipolar outflows on

the other hand are widely observed in regions of massive star formation (Shepherd & Churchwell, 1996; Garay & Lizano, 1999; Shepherd et al., 2001), which could suggest the presence of disks.

Although radiation pressure is no longer considered a hindrance for high-mass star formation other effects of radiation could still be problematic. It is unclear whether or not photoionisation can limit the stellar mass by choking off accretion or photoevaporating the disk (Krumholz, 2015). The possibility of continued accretion through an ionisation front will be discussed in Chapter 3.

1.2 HII regions

HII regions are made up of ionised hydrogen. They are a result of high-mass stars emitting high-energy, ionising photons. For this reason they are generally observed in locations of ongoing star formation such as spiral and irregular galaxies, and they are commonly used to trace hot, young, high-mass stars. In this section I will briefly describe the formation and evolution of HII regions, as well as the puzzling case of the ultra-compact HII regions.

1.2.1 Formation

An ionising star emits energetic "stellar" photons (> 13.6 eV) which, when travelling in a neutral medium, do not get far into the ISM before being absorbed by neutral hydrogen, splitting them into ions and electrons. As this process turns the gas surrounding the star from neutral to ionised, inevitably there will be ions and electrons in close proximity that will recombine to atoms. The recombination will in turn emit a new photon, which may or may not be ionising, these photons will be referred to as "diffuse". This process is illustrated in Figure 1.3.

The ionisation fraction of a medium is given by the balance of photoionisations and recombinations. The photoionisation rate per unit volume is proportional to the density of the neutral material ($n_{\rm n}$) and the recombination rate per unit volume is proportional to the product of the ion and electron density ($n_{\rm i} n_e$). Assuming the gas mainly consists of hydrogen, the number of electrons and ions will balance ($n_{\rm i} n_e \sim n_{\rm i}^2$), and equating the two rates gives: $n_{\rm i}^2 \propto n_{\rm n}$. In a weakly magnetised medium, such as a molecular cloud, the density of the neutral material is close to the overall density ($n_{\rm n} \sim n$). In which case the ionisation fraction is approximately proportional to one over the square root of the density: $I_f = n_{\rm i}/n \propto 1/\sqrt{n}$.

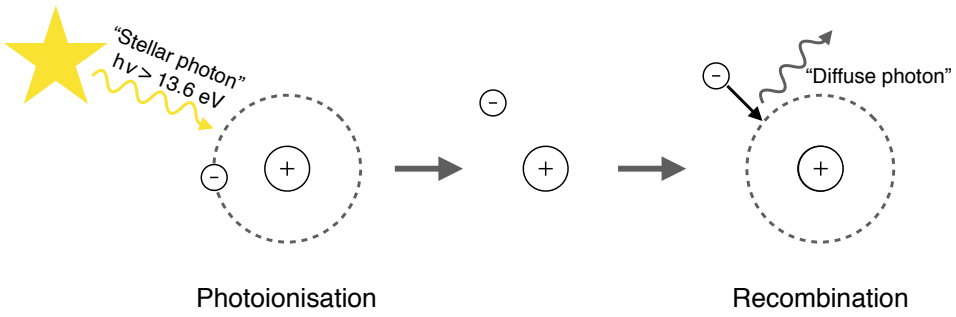

Figure 1.3: Photoionisation occurs when an energetic photon, for instance a "stellar" photon emitted by an ionising star, is absorbed by an atom and ejects an electron in the process. The result is a free electron and an ion. Recombination occurs when the ion reconnects with an electron, this process emits a "diffuse" photon.

For molecular cloud cores of $\sim 10^4$ cm^{-3} the typical ionisation fraction is $\sim 10^{-7}$ (Williams et al., 1998), hence the ionisation fraction of similarly weakly ionised regions can be estimated as the following:

$$I_f = \frac{n_i}{n} \approx 10^{-7}\sqrt{\frac{10^4 \text{ cm}^{-3}}{n}}. \tag{1.15}$$

This is an intuitive result as it would be harder for photons to penetrate and ionise denser regions. A more detailed and general calculation of the ionisation fraction, applicable to both strongly and weakly ionised material, is presented in Section 2.3.5.

A HII region is fully ionised, and to maintain it requires there to be at least one ionisation happening for every recombination, otherwise the region will shrink. If there are additional photons emitted after all recombinations have been compensated for, they act to expand the HII region. These photons travel more or less freely through the ionised region until they reach the boundary where they encounter atoms to ionise. This way, the HII region expands until ionisations are balanced by recombinations.

By assuming a star radiates ionising photons isotropically into a homogeneous medium, creating a spherical fully ionised region, Strömgren calculated its size by balancing ionisations and recombinations (Strömgren, 1939):

$$R_{\text{st}} = \left(\frac{3Qm_{\text{p}}^2}{4\pi\alpha_{\text{B}}\rho^2}\right)^{\frac{1}{3}}. \tag{1.16}$$

R_{st} is the radius of the spherical HII region, which is now known as the Strömgren sphere. Q represents the number of ionising photons emitted per second. Throughout the thesis I

will refer to this as the ionising luminosity. α_B is the recombination coefficient to all excited energy levels (n $\geq$ 2), m_p is the mass of a proton (1.6726×10^{-27} kg) and ρ is the mass density. This size estimate is for an idealised symmetric case, however in reality we observe HII regions not as perfect spheres, but with a wide variety of often irregular shapes (Wood & Churchwell, 1989b; Peters et al., 2010). In an inhomogeneous medium the distance travelled by photons depends on gas density. Equation 1.16 shows that the size of the HII region is inversely proportional to density. In other words, HII regions will extend further in lower density areas and dense gas will shield regions from ionisation. As a result, the shape of any HII region depends on the density structure of the surrounding material (see Figure 1.4 for an example).

Similarly to how the structure of a HII region is governed by the balance between ionisations and recombinations, its temperature depends on the balance between heating and cooling processes, which add and remove thermal energy. The heating is dominated by photoionisation and the cooling is made up of a mix of recombinations and various other radiative losses. A brief description of the main processes affecting temperature follows (Osterbrock & Ferland, 2006).

Heating

- Photoionisation: When a photon ionises an atom it gives the ejected electron kinetic energy equal to the photon energy minus the ionisation energy.

Cooling

- Recombination: When a free electron is captured by an ion, the kinetic energy of the electron is radiated away. Note that slower electrons are more easily captured.
- Free-free (Bremsstrahlung) radiation: The acceleration of a free electron by an encounter with an ion emits a continuous spectrum.
- Collisionally excited line radiation: When the impact of a free electron excites a bound electron to a higher energy level, it will subsequently decay and emit radiation.

The net result of these processes depends on the density of the gas and the abundances of different ions. The exact temperature of a given region of gas can not be determined without going into the detailed calculations of heating and cooling rates, however HII regions typically

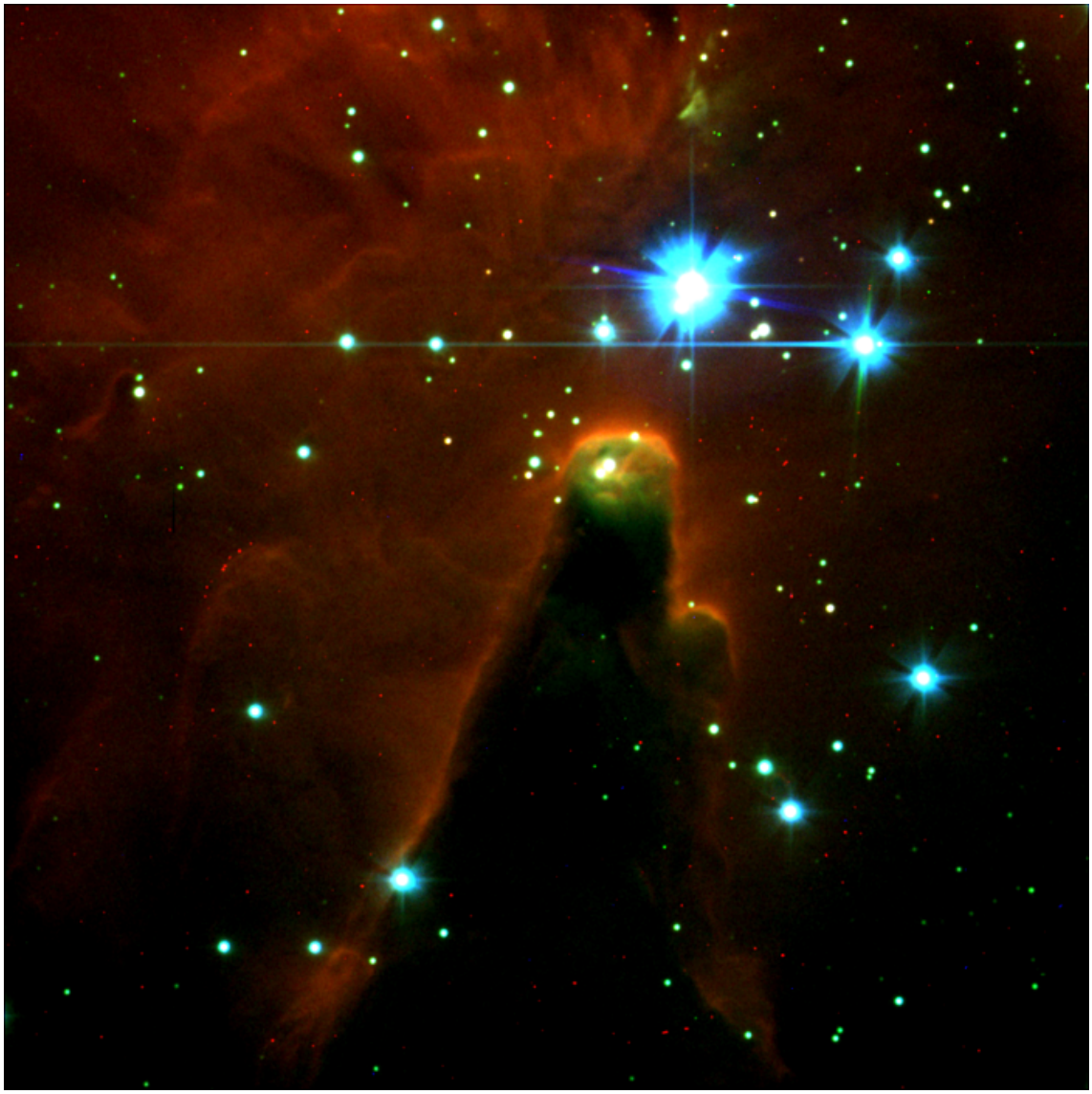

Figure 1.4: Colour composite image of the Cone Nebula, named after the dark cone-shaped region of dust and dense molecular gas at the centre of the image. Image taken by me using the Hα, r' and g' filters on the IAC-80 telescope at the Observatory del Teide. Exposure times: Hα = 300 s, r' = 30 s and g' = 30 s. Hα is shown in red, which means the red glow traces ionised gas.

have temperatures of $\sim 10^4$ K (Osterbrock & Ferland, 2006). This is significantly higher than the neutral surrounding material, hence an overpressure is created which leads HII regions to expand.

1.2.2 Evolution: R-type and D-type ionisation fronts

Expanding HII regions are separated from their surrounding neutral material by an ionisation front. By considering mass and momentum conservation across this boundary, we can solve for the ionised to neutral gas density ratio and classify the type of ionisation front. The ionisation front is either a dense (D)-type or rarefied (R)-type based on its propagation velocity. The derivation follows below. More details can be found in textbooks dealing with radiation transport and gas dynamics, such as Osterbrock & Ferland (2006).

At the ionisation front dividing the neutral and ionised material there is a discontinuous change in parameters such as density (ρ), temperature (T), pressure (p) and velocity (v). Throughout this thesis I will use subscripts "i" and "n" to indicate ionised and neutral respectively. We apply the Rankine-Hugoniot jump conditions at the boundary; mass conservation:

$$\rho_{\rm i} v_{\rm i} = \rho_{\rm n} v_{\rm n}, \tag{1.17}$$

and momentum conservation:

$$p_{\rm i} + \rho_{\rm i} v_{\rm i}^2 = p_{\rm n} + \rho_{\rm n} v_{\rm n}^2. \tag{1.18}$$

By applying the ideal gas law the pressures in the ionised and neutral gas are given by:

$$p_{\rm i} = \frac{\rho_{\rm i} k T_{\rm i}}{\mu_{\rm i} m_{\rm H}}, \tag{1.19}$$

$$p_{\rm n} = \frac{\rho_{\rm n} k T_{\rm n}}{\mu_{\rm n} m_{\rm H}}, \tag{1.20}$$

where k is the Boltzmann constant (1.3807×10^{-23} J K^{-1}), $m_{\rm H}$ is the mass of a hydrogen atom (1.6737×10^{-27} kg), and μ is the mean molecular weight. The mean molecular weight is the average mass per particle in units of $m_{\rm H}$, so assuming a hydrogen dominated medium means $\mu_{\rm i} \approx 1$. When hydrogen is ionised the number of particles double and so $\mu_{\rm n} \approx 0.5$. We

introduce the following expression for sound speed:

$$c_{\rm s} = \sqrt{\frac{\gamma kT}{\mu m_{\rm H}}}, \tag{1.21}$$

where γ represents the heat capacity ratio, and rewrite the pressure expressions (Equations 1.19 and 1.20) in terms of the sound speeds of the neutral and ionised material:

$$p_{\rm i} = \rho_{\rm i}\gamma c_{\rm si}^2, \tag{1.22}$$

$$p_{\rm n} = \rho_{\rm n}\gamma c_{\rm sn}^2. \tag{1.23}$$

Assuming isothermal sound speeds ($\gamma = 1$) and substituting these pressures (Equations 1.22 and 1.23) into the expression for momentum conservation (Equation 1.18) gives:

$$\rho_{\rm i}\left(v_{\rm i}^2 + c_{\rm si}^2\right) = \rho_{\rm n}\left(v_{\rm n}^2 + c_{\rm sn}^2\right). \tag{1.24}$$

Finally we substitute for $v_{\rm i}$ using mass conservation (Equation 1.17) and rearrange to get a quadratic equation for the ionised to neutral gas density ratio:

$$\left(\frac{\rho_{\rm i}}{\rho_{\rm n}}\right)^2 c_{\rm si}^2 - \left(\frac{\rho_{\rm i}}{\rho_{\rm n}}\right)\left(c_{\rm sn}^2 + v_{\rm n}^2\right) + v_{\rm n}^2 = 0. \tag{1.25}$$

Solving this quadratic equation results in the following expression for the density ratio across the ionisation front:

$$\frac{\rho_{\rm i}}{\rho_{\rm n}} = \frac{c_{\rm sn}^2 + v_{\rm n}^2 \pm \sqrt{(c_{\rm sn}^2 + v_{\rm n}^2)^2 - 4c_{\rm i}^2 v_{\rm n}^2}}{2c_{\rm si}^2}. \tag{1.26}$$

Considering that the ratio of these two densities must be a real number, and the sound speed of the ionised gas always exceeds that of the neutral gas (see Equation 1.21), $v_{\rm n}$ is limited to two allowed regimes. The nature of $v_{\rm n}$, the relative velocity between the ionisation front and the surrounding neutral gas, determines whether the ionisation front is R-type or D-type:

$$v_{\rm n} \leq c_{\rm si} - \sqrt{c_{\rm si}^2 - c_{\rm sn}^2} = v_{\rm D} \approx \frac{c_{\rm sn}^2}{2c_{\rm si}}, \tag{1.27}$$

$$v_{\rm n} \geq c_{\rm si} + \sqrt{c_{\rm si}^2 - c_{\rm sn}^2} = v_{\rm R} \approx 2c_{\rm si}. \tag{1.28}$$

Two critical velocities are defined above; $v_{\rm D}$ and $v_{\rm R}$. When $v_{\rm n}$ is lower than $v_{\rm D}$ the ionisation front is a subsonic D-type front, and when $v_{\rm n}$ exceeds $v_{\rm R}$ the ionisation front is a supersonic

R-type front. For instance, in the case of a neutral gas at 500 K that increases in temperature to 8000 K when ionised, $v_D \approx 0.2$ km s^{-1} and $v_R \approx 23.0$ km s^{-1}. Any velocity between v_D and v_R is not a stable solution and does not result in a single shock front. Instead a shock wave moves ahead of the ionisation front which compresses the gas before ionisation happens.

The expansion and evolution of HII regions is currently being explored numerically through simulations using various radiation hydrodynamics codes (e.g. Klassen et al., 2014; Roth & Kasen, 2015; Harries, 2015; Salz et al., 2015; Williams et al., 2018; Vandenbroucke et al., 2019). In Bisbas et al. (2015) the STARBENCH project presents results from 12 different numerical 1D and 3D codes modelling the D-type expansion of a spherical HII region into a neutral uniform medium. Their setup assumes the absence of gravity and magnetic fields, essentially having photoionisation be the only factor influencing the HII region. They find good agreement between the codes, but with a slight deviation from analytical expressions. In the wake of this study, Williams et al. (2018) has presented a new equation describing this expansion that follows the numerical solution more closely than previous works. A more realistic treatment of HII regions is challenging, as there are a large range of factors that affect its shape and evolution. Recently, Geen et al. (2020) explored analytically the effect of factors such as radiation pressure, gravity and stellar winds on HII regions. They conclude photoionisation is dominant on molecular cloud scales, but suggest that winds and radiation pressure drive the HII regions on size scales less than 0.1 pc.

Mackey et al. (2013) performed the first 3D simulations of a flow of material moving past an O star. The results show both R-type and D-type ionisation fronts propagating from the star as the relative velocities change depending on the orientation to the flow, this is consistent with Equations 1.27 and 1.28. Furthermore, they highlight the impact O stars have on the dynamics of their surroundings as a source of ionisation. For this particular simulated O star, during its main sequence lifetime, the expanding HII region generates momentum and kinetic energy comparable to that of the stellar wind and the eventual supernova. The momentum is over 100 and 4 times larger than that associated with the stellar wind and supernova respectively. Whereas the kinetic energy is over 100 times smaller than that of the supernova, but larger than the kinetic energy of the stellar wind.

In Chapter 2 I test the radiation hydrodynamics code I use against the results presented by Mackey et al. (2013) and Bisbas et al. (2015).

1.2.3 Ultra-compact HII regions

HII regions come in a range of sizes and densities, the densest ($\geq 10^4$ cm^{-3}) and smallest (radius 0.1 pc) are called ultra-compact (UC) HII regions. These densities and sizes indicate they are young ionised regions, still embedded in molecular clouds, which have not yet expanded enough to turn into diffuse HII regions.

Observing UCHII regions is inherently difficult as the surrounding molecular clouds obscure them in the UV and optical. Using the Very Large Array (VLA) Wood & Churchwell (1989b) performed the first radio-survey of UCHII regions. They detected 75 cases and classified them according to five distinct morphological types: cometary, with a clear ionisation front at one end and a long trailing tail of emission (20%); core-halo, cores of bright emission with surrounding faint halos (16%); shell, a ring of emission (4%); spherical/unresolved (43%) and irregular, structures with multiple emission peaks (17%). Subsequent surveys have observed similar morphologies, but not a consistent distribution (e.g. Kurtz et al., 1994; Kim & Koo, 2001; De Pree et al., 2005; de la Fuente et al., 2020). Forming a unified theory explaining the existence of all the morphologies is challenging as the shape of the UCHII region will depend on a range of factors such as its age, gas dynamics, the density structure of the surrounding medium and its motion relative to those surroundings (Churchwell, 2002). Simulations have been able to reproduce the different structures, and suggest the spherical, cometary and shell-like structures could be one and the same, only viewed from different orientations, (Mac Low et al., 1991; Peters et al., 2010). This simplifies the problem, however, as a further complication, any theory explaining the UCHII region morphology must also be able to explain their long lives.

The lifetime problem

By counting O stars inside and outside of molecular clouds Wood & Churchwell (1989a) estimate that 10-20% of all O stars are surrounded by UCHII regions. This implies HII regions must remain in the UC state for approximately 10-20% of the lifetime of an O star. According to the evolutionary stellar models by Maeder & Meynet (1987) the average lifetime of an O star is 2.4×10^6 yrs, which in turn suggests the average lifetime of UCHII regions must be of the order of $\sim 10^5$ yrs in order to explain the observed numbers.

Unfortunately the lifetime deduced from the observations ($\sim 10^5$ yrs) is inconsistent with

what is expected. The time it would take an UCHII region to expand to a size where it is no longer classified as UC, being opposed only by the pressure of the surrounding dense molecular cloud, is estimated to be $\sim 4 \times 10^4$ yrs ($\sim 1.7\%$ of the average lifetime of an O star) (Wood & Churchwell, 1989b). This is approximately a factor of 10 shorter than what the observations imply, consequently there must be some physical process slowing or halting the expansion and thereby extending their lives. Current theories include high-density material or gravity causing a temporary confinement of the ionised region (e.g. Keto, 2002b; Mac Low et al., 2007).

Bow shock models aim to explain both the observed cometary shape of some UCHII regions as well as their long lives as a result of ram pressure (van Buren et al., 1990; Mac Low et al., 1991). If a high-mass star is moving supersonically through a molecular cloud a bow shock will be created in the forward direction. Material is swept up exterior to the shock and becomes a shell of dense neutral material which traps the ionisation front. This mechanism only works for as long as the star remains within a molecular cloud, so confining the HII region for the supposed lifetime requires a significant amount of surrounding material (Mac Low et al., 2007).

An alternative trapping mechanism was suggested by Keto (2002b), who believes it is a consequence of the gravitational attraction of the high-mass star. This model suggests material accretes onto the star through a trapped ionisation front, until the radius of ionisation equilibrium exceeds some critical value, at which point both the accretion and the trapping ceases. In this case the UCHII region would essentially be the ionised part of the accretion flow (Keto, 2007). In Chapter 3 I present numerical simulations of the gravitational trapping of HII regions and discuss this concept further as a potential solution to the lifetime problem.

1.3 Stellar magnetic activity

Early in the 20th century Hale (1908) observed the Zeeman effect in solar spectra and became the first to realise the Sun hosted a magnetic field. It was not until $\sim$ 40 years later that magnetic fields were discovered on other stars (Babcock, 1947), and even longer before it was detected on another solar like star (Robinson et al., 1980).

Throughout this section when I mention the Sun it is as a reference point; the focus will be on stellar, not solar, magnetism. I will first discuss how stellar magnetic fields are detected and modelled. Next I consider how the fields differ in geometries and strength for different types

of stars. Finally I describe a range of energetic phenomena associated with magnetically active stars, indicators of such stellar activity and the possibility of cyclic variation in the activity.

1.3.1 Observing and modelling stellar magnetic fields

Recent advances in observational techniques has allowed surveys such as MagIcS[2], Bcool[3], MaTYSSE[4] and Toupies[5] to explore the magnetic field behaviour in a range of different types of stars.

Zeeman-Doppler imaging

Spectroscopy is used to determine the strength of stellar magnetic fields through measurements of the Zeeman splitting of spectral lines. As previously mentioned, there is a lower limit to the strength of magnetic fields that can be detected due to other mechanisms broadening the spectral lines. This limitation would lessen by moving from optical data to nIR, e.g. using SPIRou[6], as the Zeeman effect for these wavelengths is greater. What will not change however, is that spectroscopy alone can only provide a single field strength value averaged over the visible stellar surface.

Through polarisation, the magnetic field orientation can be explored. The different polarisation states are usually described in terms of the Stokes parameters: I, Q, U and V. Stokes I measures the intensity of unpolarised radiation, Stokes Q and U measures linearly polarised radiation, and Stokes V measures circularly polarised radiation. Maximum information is obtained when measuring all four parameters, however it is common for only Stokes V to be used, as it typically has considerably higher signal-to-noise than Stokes Q and U. Another important limitation to remember when dealing with polarised light is that opposite polarities cancel within a resolution element.

The Zeeman-Doppler imaging (ZDI) technique, uses the combined power of spectroscopy and polarisation, i.e. spectropolarimetry, along with stellar rotation to map magnetic fields across stellar surfaces (Semel, 1989; Brown et al., 1991). The fact that magnetic features at different positions of the star move at different velocities means they will experience different Doppler shifts. Rotation also results in a changing angle between the line-of-sight to the star

[2]http://www.ast.obs-mip.fr/users/donati/magics/v1/
[3]http://bcool.ast.obs-mip.fr/Bcool/Bcool___cool_magnetic_stars.html
[4]https://matysse.irap.omp.eu/doku.php
[5]http://ipag.osug.fr/Anr_Toupies/
[6]http://spirou.irap.omp.eu

and the vector components of the magnetic field. All this put together allows for a reconstruction of the magnetic field at the stellar surface, assuming the magnetic field stays constant during the time across which it is measured.

Key limitations are carried through from the spectroscopy and polarisation measurements. Detecting fields with a relatively small Zeeman effect is still a problem. The faster a star rotates, the stronger the magnetic field needs to be in order to be detected, so this could bias observational samples. The technique is still insensitive to small-scale magnetic flux elements whose polarities cancel out (Reiners & Basri, 2009; Morin et al., 2010; Kochukhov & Shulyak, 2019; See et al., 2019). Consequently measurements will only pick up on large scale magnetic fields. Finally, the dependence on Doppler shift creates a potential degeneracy between hemispheres; if viewing a star equator-on it is impossible to tell which hemisphere a magnetic feature is located on.

Toroidal and poloidal decomposition

The resulting magnetic field is commonly described as the sum of a toroidal and poloidal field: $\boldsymbol{B} = \boldsymbol{B}_{\rm pol} + \boldsymbol{B}_{\rm tor}$ (Donati, 2001). The poloidal and toroidal field components are defined in terms of the scalars Φ and Ψ as (e.g. Appendix III of Chandrasekhar, 1961):

$$\boldsymbol{B}_{\rm pol} = \boldsymbol{\nabla} \times [\boldsymbol{\nabla} \times [\Phi \hat{\boldsymbol{r}}]], \tag{1.29}$$

$$\boldsymbol{B}_{\rm tor} = \boldsymbol{\nabla} \times [\Psi \hat{\boldsymbol{r}}]]. \tag{1.30}$$

In a spherical coordinate system, the toroidal field lies purely on spherical surfaces while the poloidal field passes through these surfaces. Lehmann et al. (2019) finds the ZDI technique is particularly good at determining the ratio of toroidal to poloidal magnetic energies.

1.3.2 Magnetic fields of different stellar types

According to the BOB[7] and MiMeS[8] surveys, approximately 7% of high-mass stars show signs of hosting magnetic fields at their surfaces (Grunhut et al., 2017; Schöller et al., 2017). These fields usually have a simple structure and are believed to be "fossil fields", which essentially means they were created at some earlier stage of the stellar evolution and are not being re-

[7]https://www.astro.uni-bonn.de/BOB/
[8]http://www.cfht.hawaii.edu/Science/MiMeS/

newed (e.g. review by Briquet, 2015). Magnetic fields in low-mass stars below 1.5 $M_\odot$ on the other hand are ubiquitous, being continuously generated and maintained by an internal dynamo transforming a meridional field into an azimuthal field, and vice versa (e.g. Donati et al., 2011). I will focus my discussion of stellar magnetic activity on these magnetically active low-mass stars.

Stars within the mass range of 0.35 $M_\odot < M_\star <$ 1.5 $M_\odot$ have a radiative core and an outer convection zone separated by an interface layer called the "tachocline" (Spiegel & Zahn, 1992). This is the internal structure found in the Sun, hence the magnetic fields of this group of stars are expected to be created via a solar-like dynamo. Despite not being fully understood, the general mechanism of the solar dynamo is believed to consist of the following components (Parker, 1955):

- The Ω-effect: an initial meridional field is stretched into an azimuthal field by differential rotation.
- The α-effect: fluid elements are made to rotate by the Coriolis force as they move through the azimuthal field. This causes the field lines to twist, creating small loops that eventually coalesce and regenerate a meridional field.

It has been suggested the solar dynamo is an interface dynamo operating at the tachocline, as this is the location of the largest rotation gradients (Charbonneau & MacGregor, 1997).

Stars below $\sim$ 0.35 $M_\odot$ are fully convective (Chabrier & Baraffe, 1997), which means they do not possess a tachocline and consequently cannot support an interface dynamo. These fully convective stars are nonetheless observed with strong magnetic fields (e.g. Donati et al., 2008a), indicating either some other form of dynamo must be acting or the solar-like dynamo does not require a tachocline (Wright & Drake, 2016). If there are in fact two different types of dynamos generating magnetic fields in stars with partially or fully convective interior structures, the type of field geometries produced are expected to differ.

Field strength and geometry

Observations indicate a transition from weaker, complex magnetic fields to stronger, simpler fields in stars below $\sim$ 0.5 $M_\odot$ (Morin et al., 2008b; Donati et al., 2008b; Morin et al., 2010). This could be related to a transition in stellar internal structure towards fully convec-

tive stars, and the expected corresponding change in the nature of the dynamo. It appears fully-convective stars have strong and mostly axisymmetric fields, whereas partially convective stars have weaker, more complex fields (Donati & Landstreet, 2009; Donati et al., 2011). Furthermore, the ratio of toroidal to poloidal magnetic energies seems to change for partially and fully convective stars (Donati et al., 2008a; Gregory et al., 2012; See et al., 2015). With fully convective stars being dominantly poloidal, and the toroidal component increasing in strength if the stars develop radiative cores (Donati et al., 2011).

For solar like stars there is an apparent correlation between the rate of stellar rotation and the magnetic field geometry. Slow rotators have predominantly poloidal fields, and as the rotation rate increases the field becomes increasingly toroidal (Petit et al., 2008). Folsom et al. (2016) proposes the nature of the stellar magnetic fields of solar like stars changes in time, initially driven by the development of a radiative core, and after that point mainly being affected by changes in the rotation rate.

Bi-stability

Through their study of 11 fully convective M dwarfs Morin et al. (2010) found stars below 0.15 $M_\odot$ show two distinct magnetic topologies; strong, axisymmetric, simple fields (like those observed for $\sim$ 0.15–0.5 $M_\odot$ stars) and weaker ones with a significant non-axisymmetric component. Further investigation suggests simultaneous support of these two field types does not occur below a stellar mass limit, but instead below a critical Rossby number (defined in Section 1.3.3) of $\sim$ 0.1 (Schrinner et al., 2012; Gastine et al., 2013).

There is no obvious difference in masses or rotation rates of stars belonging to the two categories. One possible explanation is the existence of bi-stability within the dynamo, where stars with similar stellar parameters may either exhibit strong, simple fields or weaker, more complex ones (Morin et al., 2011b,a; Schrinner et al., 2012; Gastine et al., 2013). A cyclic variation between these two states has also been proposed, where the weak field appears during an inversion of the strong field (Kitchatinov et al., 2014). Further observations are required to confirm whether this is the case.

1.3.3 Stellar activity

Magnetically active regions of the Sun, i.e. sites of especially strong magnetic fields, are sources of features such as sunspots, filaments/prominences, solar wind, flares and coronal mass ejec-

tions (CMEs). Such processes are expected to also occur on other magnetically active stars. Some of the features are anchored to the star, whilst others eject material and energy into the ISM, essentially creating space weather. I will focus on activity falling within the latter category.

Stellar wind

The solar wind is made up of a stream of hot ionised gas escaping the Sun. Its properties have been explored for decades by numerous spacecraft, such as *Mariner 2* (Neugebauer & Snyder, 1962), *Voyager 1*, *Voyager 2* (Richardson & Stone, 2009) and *Ulysses* (McComas et al., 2000). In the case of solar-like winds around other stars direct measurements are a lot more challenging. Instead, an alternative indirect approach based on observations of UV spectra of stars can be used: when the stellar wind interacts with the ISM it results in a region of hot neutral hydrogen (HI) that produces detectable Lyα absorption. For a detailed description of this Lyα technique as well as, less successful, direct stellar wind detection techniques see the review by Wood (2004).

The impact of the stellar wind is experienced both by the host star and the surrounding environment. The nature of the stellar wind automatically implies stellar mass loss, with rates being derived based on the amount of Lyα absorption (Wood et al., 2002). Furthermore, the stellar wind is thought to play an important role in slowing stellar rotation by carrying away angular momentum (Weber & Davis, 1967; Kawaler, 1988). As for external impact, under certain conditions (e.g. weak planetary magnetic fields) stellar winds could be a means of stripping planets of their atmospheres, which would lead to habitability issues (Zendejas et al., 2010; Vidotto et al., 2011, 2013; See et al., 2014; Rodríguez-Mozos & Moya, 2019). Within our own solar system it has been suggested that solar wind has eroded the atmospheres of Titan (Lammer et al., 2000), Venus (Futaana et al., 2017) and Mars (Jakosky et al., 2018). Closer to home, the impact of the solar wind is visible to the naked eye in the form of aurorae. When charged particles from the solar wind collide with atoms and molecules in the Earth's atmosphere they create coloured lights. A strong aurora, however beautiful, also indicates a strong solar wind that could wreak havoc. Strong solar winds can disturb and compress the Earth's magnetosphere, a phenomenon called a geomagnetic storm (Parker, 1962). Such a storm can impact the Earth's technologies, both in space and on the ground (Lakhina & Tsurutani, 2016).

Stellar flares and coronal mass ejections

As stellar magnetic fields twist and rearrange they can trigger eruptions of energy and material. Stellar flares and CMEs are examples of such explosive events. They can be coincident or occur separately (Shaltout et al., 2019). A stellar flare is a sudden release of energy which very rapidly heats stellar material and results in a burst of radiation, which can be detected at all wavelengths from radio waves to gamma rays (Benz, 2008). A CME is a release of stellar matter with an embedded magnetic field into space. Solar CMEs are detected using a coronagraph, an instrument that blocks direct light from the sun, hence allowing observations to be made of the corona (Webb & Howard, 2012). Stellar CMEs however cannot be directly observed, instead observers rely on Doppler shifts of spectral lines to reveal the ejected material (Houdebine et al., 1990; Vida et al., 2019; Argiroffi et al., 2019; Leitzinger et al., 2020).

As in the case of stellar winds, these eruptive phenomena also pose a threat to habitability on nearby planets. Despite being localised in the stellar atmosphere, flares can do widespread damage through radiation. Certain wavelengths associated with flares are known to be harmful to life, but fortunately much of this radiation can be absorbed in the atmosphere before reaching the planetary surface (Segura et al., 2010). A potentially bigger problem is radiation altering the chemical composition of planetary atmospheres (Venot et al., 2016). If the flares are frequent and energetic enough nearby planetary atmospheres may never settle to a steady state, creating a hostile environment (Vida et al., 2017). Unlike flares, CMEs carry material which can collide with planets, when doing so they are believed to be capable of eroding planetary atmospheres unless there is sufficient shielding by a magnetic field (Lammer et al., 2007; Kay et al., 2016).

A solar flare will reach the Earth in approximately 8 minutes, whereas a CME emitted in the direction of the Earth can take days to arrive (Cliver et al., 1990). On the occasions when they do reach the Earth, they interact with the magnetosphere in a similar way to the stellar wind and cause geomagnetic storms, but they are generally stronger than those caused by the stellar wind. In 1859 the English astronomers Richard C. Carrington and Richard Hodgson both independently reported an uncommonly bright solar flare on September 1st (Carrington, 1859; Hodgson, 1859), which was followed $\sim$ 18 hours later by the most powerful geomagnetic storm recorded, later referred to as the "Carrington Event" (Muller, 2014; Viljanen et al., 2014). If an event such as that one was to hit the Earth today, it is predicted to have serious

consequences on the current infrastructure, for instance leading to large scale power outages and damage to communication and navigation systems (Feynman & Gabriel, 2000; Cid et al., 2014; Muller, 2014; Lakhina & Tsurutani, 2016). As a result of the potentially destructive effects of solar flares and CMEs, a lot of research is currently being done on models predicting these solar eruptions (e.g. Ahmed et al., 2013; Bobra & Ilonidis, 2016; Liu et al., 2020) and forecasting extreme geomagnetic storms (e.g. Riley & Love, 2017; Moriña et al., 2019).

Activity tracers

Observing magnetic activity in stars directly can be challenging or even impossible, hence the overall magnetic activity level is estimated using a range of indirect diagnostics. Studies of the Sun can be used to identify indicators of stellar activity.

Solar magnetograms reveal strong magnetic fields coincide with regions of strong X-ray emission and strong Ca II H and K emission (Leighton, 1959; Krieger et al., 1971). Both have been used to estimate stellar magnetic activity (e.g. Schrijver et al., 1989; Baliunas et al., 1995; Drake et al., 2000). Measurements of Ca II H and K emission from 111 stars suggest both magnetic activity and rotation rate decrease with age (Baliunas et al., 1995).

As both X-ray emission and Ca II H and K emission from low-mass stars generally increase with increasing rotational velocity, the stellar rotation rate can also be used as a proxy for magnetic activity (Pallavicini et al., 1981; Walter & Bowyer, 1981; Baliunas et al., 1995). Both partially and fully convective stars show this relationship between rotation rate and magnetic activity (Wright et al., 2011, 2018). Note however that this trend is limited to only a fraction of stars. The fastest rotators are part of a "saturated regime" where the X-ray emission stays constant (Pizzolato et al., 2003). The exact rotation period at which saturation occurs is mass dependent, and increases with decreasing mass (Pizzolato et al., 2003).

The rotation-activity relation can also be represented in terms of the Rossby number (Noyes et al., 1984). This is a parameter which describes how strongly the stellar Coriolis force affects convection. Mathematically it is defined as the ratio of the stellar rotation period to the convective turnover time:

$$R_o = \frac{P_{rot}}{t_{conv}}. \tag{1.31}$$

Magnetic activity increases with decreasing Rossby number, until a saturation is reached at $R_o \sim 0.13$ (Wright et al., 2011). Whether activity correlates better with Rossby number or

rotation rate is a debated topic (e.g. Noyes et al., 1984; Montesinos et al., 2001; Kiraga & Stepien, 2007; Reiners et al., 2014).

Recently magnetic helicity has been suggested as a potential tracer for activity. This possibility will be discussed in Chapter 5.

Stellar cycles

It was through observations of sunspots, i.e. dark areas on the Sun with stronger magnetic fields and lower temperatures than their surroundings, that the solar cycle was discovered. The periodic nature of the number and sizes of sunspots had been noted already in 1775 by the Danish astronomer Christian Pedersen Horrebow (Jørgensen et al., 2019), long before it was realised the Sun was magnetic. The cycle begins at what is called a "solar minimum" (when the number of sunspots is lowest), reaches the "solar maximum" in the middle of the cycle (when the number of sunspots is highest), and finally returns to a minimum before starting a new cycle. The amount of solar activity follows the solar cycle, with relatively more flares and CMEs etc at the solar maximum. The overall magnetic activity level however can vary between cycles. Each cycle will vary in length, but on average the process takes $\sim$ 11 years. Hale et al. (1919) showed that during a cycle, sunspots appear in pairs with polarities which are constant, but opposite across the equator. At the beginning of a new cycle the sunspot polarity reverses, meaning it takes the Sun $\sim$ 22 years to return to the same state.

It is currently not clear how common it is for other magnetic stars to undergo cycles similar to the Sun versus random or non-existent variability. Perhaps there is a difference between stars with different types of magnetic dynamos. Long term monitoring of Ca II H and K emission of magnetically active stars found evidence for long term cyclical variation, but also cases of no variation and some with short term variation seemingly without a cycle (Wilson, 1978; Baliunas et al., 1995). More recently, ZDI observations of stellar magnetic topologies over long time periods have been studied to reveal cyclic behaviour (e.g. Morgenthaler et al., 2011). τ Boo was the first star for which a full magnetic cycle was detected using this method, with an estimated period of $\sim$ 2 years (Fares et al., 2009). This is contrary to the $\sim$ 12 year period previously derived based on Ca II H and K emissions from the same star (Baliunas et al., 1995). This suggests factors such as the method, the frequency and the period of observations could affect which conclusions are made regarding stellar cycles.

1.4 Thesis outline

The discussion in these introductory pages establishes that high-mass stars are always affecting their surroundings in one way or another, and that even low-mass stars can pack the occasional punch in the form of flares and CMEs. The remaining question motivating this thesis is: what makes those stars turn violent? In response I investigate two very different mechanisms; accretion and magnetic helicity. I consider the possibility of accretion being the means by which stars reach high masses in Chapters 3-4. More specifically, I address whether accretion can continue even after the star has grown to the point where it emits ionising radiation, and whether it can explain the formation of high-mass stars found in close binaries. I use a radiation hydrodynamics code and write a semi-analytic accretion model to explore this. Chapter 5 explores magnetic helicity; a diagnostic of stellar eruptions and a potential trigger of the events themselves. Despite the interest in helicity in connection to stellar activity, measurements have been limited to the Sun. I take the first step towards extending the study of this property to stars. A brief description of the content of each of the chapters follows.

In Chapter 2 I describe how the radiative transfer code and the hydrodynamics code works, and how they function together. I also perform tests and modifications of the combined code to make sure it is capable of investigating the physics of high-mass stars.

In Chapter 3 I use the radiation hydrodynamics code to model ionised accretion onto high-mass stars and the accompanying HII region development.

In Chapter 4 I continue the investigation of accretion as a means of forming high-mass stars, this time specifically considering high-mass binaries. Using a semi-analytic accretion model I estimate under what conditions close high-mass binaries are likely to form, with a focus on how the presence of a magnetic field impacts the accretion and aids the formation process.

In Chapter 5 I present an expression estimating the magnetic helicity density of stars, given the poloidal and toroidal magnetic field components at the stellar surface. Subsequently I apply it to a sample of stars and determine how it relates to other stellar parameters as well as to the solar helicity density.

In Chapter 6 I summarise my results and present my concluding remarks.

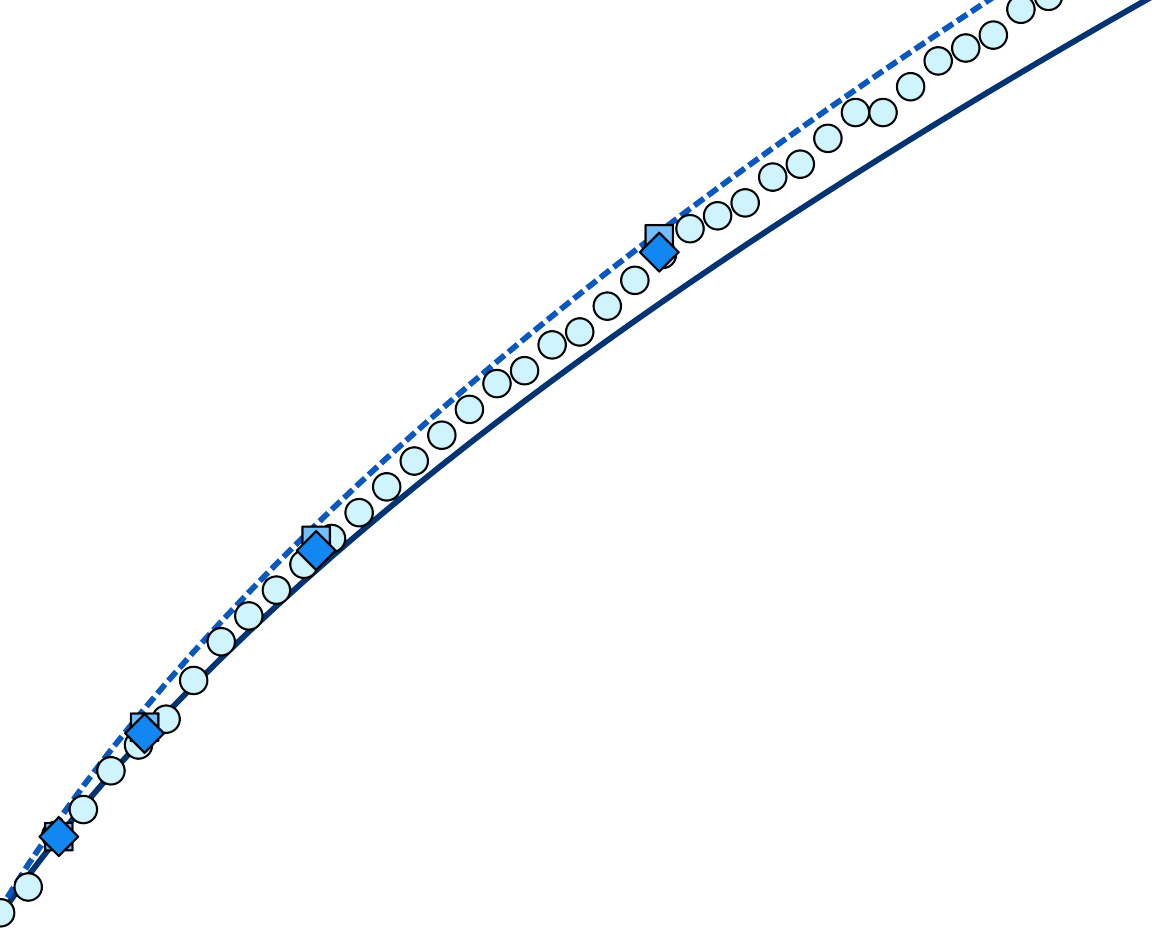

2

The radiation hydrodynamics code

In this chapter I review a code which couples time-independent radiative transfer with hydrodynamics, allowing for a cohesive look at both fluid dynamics and photoionisation. I describe the main principles of how both parts of the code work individually, as well as how they are coupled to work together. Some aspects of the code are developed further by me, these changes will be highlighted. In the last part of this chapter I perform tests on the radiation hydrodynamics (rad-hydro) code. The aim of which is to ensure the code is capable of investigating the evolution of HII regions surrounding high-mass stars. Chapter 3 details how the code is applied to this scenario and the results it produces.

2.1 Introduction

Coding to automate tasks is an old idea, predating the computers it is now so closely associated with. For instance, in 1804 Joseph Marie Jacquard invented the automated "Jacquard Loom", capable of weaving intricate images in silk, programmed using punch cards (Essinger, 2004; Hobsbawm, 2010). The same idea of punch cards would later be used in the first computers. The loom is an example of coding to automate a task it is also possible to do by hand, however as technology and computers evolved coding has reached a point where it allows us to solve problems that are not feasible to tackle with simply a pen and paper. In some cases an analytic approach might be impossible, or simply too time consuming, whereas codes implementing numerical methods can provide good and relatively quick approximate solutions. The numerical simulations of today are powerful tools we can apply to study complex physical systems.

In Chapter 3 I investigate the early evolution of HII regions surrounding high-mass stars and how they impact the mass accretion onto the central source stars. This requires a code capable of both modelling the flow of material in the system as well as ionisation by a central source. The dynamics of fluids are described by hydrodynamics (hydro) codes which use numerical methods to solve the Euler equations; conservation laws of mass, momentum and energy written as partial differential equations. The ionisation structure of a system is determined by radiative transfer codes describing the propagation of photons through a given medium.

The code I am working with couples a magnetohydrodynamics (MHD) code, modified from the publicly available GODUNOV code[1] (Kowal et al., 2011; Falceta-Gonçalves et al., 2015; Falceta-Gonçalves & Kowal, 2015; Kowal et al., 2017; Santos-Lima et al., 2017), with a time-independent Monte Carlo radiation transfer (MCRT) code (Wood & Reynolds, 1999; Wood & Loeb, 2000; Wood et al., 2004). The workings of the combined rad-hydro code are described in detail by Falceta-Gonçalves et al (in prep), in this chapter I will outline its main features and highlight any changes I make. Note that I will describe the code as though it was purely hydrodynamical, since magnetic fields are not included in any of the simulations I run.

[1] https://bitbucket.org/amunteam/godunov-code

2.2 The hydrodynamics code

The hydro code I am using is written to describe fluid dynamics in a 3D Cartesian grid, i.e. a simulation box composed of identical cubed cells in a Cartesian coordinate system. For each cell the code is solving the Euler equations describing mass conservation,

$$\frac{\partial \rho}{\partial t} + \boldsymbol{\nabla} \cdot (\rho \vec{v}) = 0; \tag{2.1}$$

momentum conservation,

$$\frac{\partial (\rho \vec{v})}{\partial t} + \boldsymbol{\nabla} \cdot (\rho \vec{v} \vec{v} + p) = F; \tag{2.2}$$

and energy conservation,

$$\frac{\partial e}{\partial t} + \boldsymbol{\nabla} \cdot (e \vec{v} + p \vec{v}) = S_H - S_C. \tag{2.3}$$

All three equations have a time derivative of the conserved quantity; density (ρ), momentum density (ρv) or energy density (e), plus the spatial derivative of the flux of that conserved quantity. p appears in the momentum and energy conservation equations and represents pressure, the gradient of which introduces a force. The right sides of the equations contain source terms such as external forces F, heating terms S_H and cooling terms S_C. Equations 2.1-2.3 can be rewritten as a single differential equation:

$$\frac{\partial u}{\partial t} = -\boldsymbol{\nabla} \cdot (u \vec{v}) + S, \tag{2.4}$$

where the u represents the conserved variable, $\vec{v}$ is the bulk velocity of the fluid and S represents source and sink terms. The hydro code solves Equation 2.4 by following the three steps of the Godunov scheme (Godunov, 1959; Sweby, 2001)[2]: 1. Discretise, 2. Solve the Riemann problem, 3. Evolve in time.

2.2.1 Discretisation

The first step in the Godunov scheme is rewriting equation 2.4 in terms of discrete values:

$$\Delta u = -\boldsymbol{\nabla} \cdot (u \vec{v}) \Delta t + S \Delta t. \tag{2.5}$$

[2]A reference to the original Russian paper (Godunov, 1959) where the Godunov scheme was first proposed is included for completeness, however as I do not speak Russian I have not read the paper myself and refer to Sweby (2001) for a description of the method in English.

Δt represents a variable time step, and Δu is the change in the conserved variable across that time step. For ease, when solving this equation, the source term is temporarily ignored, and will be reintroduced later.

2.2.2 Riemann problem

Physical parameters are defined and subsequently calculated at the centre of each cell, however to solve Equation 2.5 the fluxes $u\vec{v}$ at every cell boundary are needed, i.e. at the surfaces where the cubed cells are touching, this will be referred to as the cell walls. Some form of interpolation from the known values at the centres of the cells is required to obtain values at the walls. The Riemann problem says the flux estimate at a cell wall depends on which side of the wall you are approaching it from, which would result in an inconsistency. For instance, using a linear interpolation where the value of a variable at the centre of the cell stays the same throughout the entire cell would result in a discontinuity at the cell walls. The cells on either side of the wall would want to assign two different values to their interface, this scenario is illustrated in Figure 2.1. To choose an intermediate flux value at the cell wall a so called Riemann solver is applied. This code specifically uses the HLL flux solver (Harten et al., 1983), named after its inventors Harten, Lax and van Leer. Broadly speaking, the HLL solver uses the velocities in the two adjacent cells to calculate a weighted average of the fluxes at the interface. Note that the Riemann solver checks for shocks in order to prevent smoothing out physical discontinuities that should be present.

2.2.3 Time evolution

The final step is to solve Equation 2.5 and obtain new values for the conserved variables after some time step. The size of the time step is picked based on a stability condition called the Courant-Friedrichs-Lewy (CFL) condition[3] (Courant et al., 1967):

$$\Delta t_{\mathrm{CFL}} \leq \frac{\Delta x_{\mathrm{cell}}}{v_{\mathrm{max}}}, \tag{2.6}$$

where Δx_{cell} is the width of a grid cell and v_{max} is the maximum local speed throughout all the cells in the simulation box. This ensures mass cannot move further than one grid cell width in a single time step.

[3]The time step I use is a fraction of the critical CFL value: $\Delta t = 0.2\Delta t_{\mathrm{CFL}}$. This value was suggested as a safe choice in personal correspondence with one of the authors of the code, D. Falceta-Gonçalves.

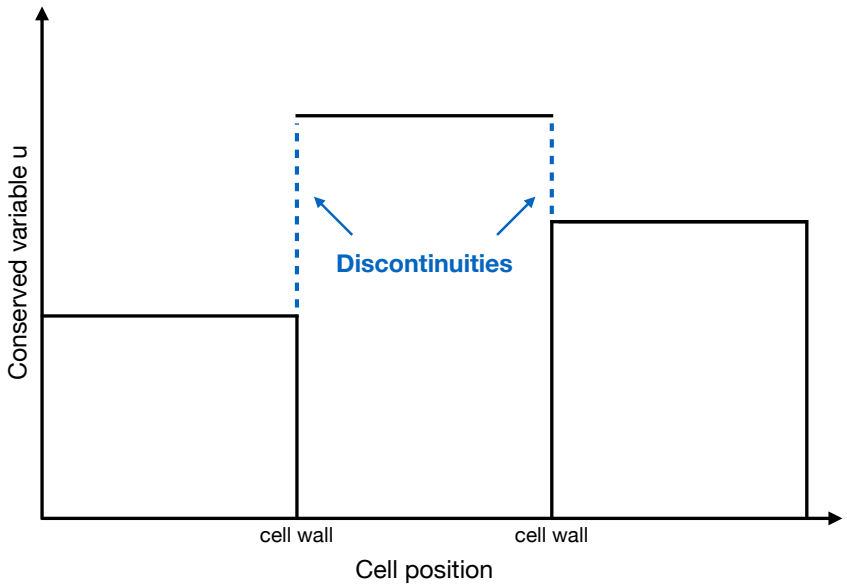

Figure 2.1: Example of the Riemann problem for a linear interpolation of conserved variables u across cells. At the cell boundaries the variable values from either side do not match.

Because the code uses discrete time steps the solution will always be an estimate of the true values. To improve the results a second order Runge-Kutta time integration scheme is applied. When describing the Runge-Kutta scheme I will rewrite Equation 2.5 for clarity as

$$\Delta u = f(u,t)\Delta t, \tag{2.7}$$

and let the current time and variable be given by t_0 and $u(t_0) = u_0$. The Runge-Kutta integration estimates the conserved variable after half a time step:

$$u_{1/2} = u\left(t_0 + \frac{\Delta t}{2}\right) = u_0 + \frac{\Delta t}{2} f(u_0, t_0), \tag{2.8}$$

and then uses this result when determining the variable after the full time step:

$$u(t_0 + \Delta t) = u_0 + \Delta t f\left(u_{1/2}, t_0 + \frac{\Delta t}{2}\right). \tag{2.9}$$

At this point any relevant source terms are added to Equation 2.5 to update the final variables. This is the stage where the photoionisation from the MCRT code enters the hydrodynamical scheme, for more detail see Section 2.4. If gravity is included in the simulation, as in my case of accretion onto a central star, source terms representing the effect of gravity are added to

both the energy density and momentum density calculations, see Section 2.5.3. Starting from the new variables the entire process repeats.

2.3 The Monte Carlo radiation transfer code

The MCRT code runs after every timestep of the hydro code and is assumed to be instantaneous. How the two codes are coupled will be covered in Section 2.4. Note the use of a time-independent photoionisation code in this context is only a good approximation as long as the hydrodynamical timescale, $t_{\rm HD} \sim L_s v_{\rm max}^{-1}$, is substantially greater than the radiative timescales; the light crossing time $t_{\rm light} \sim L_s c^{-1}$ and the recombination time $t_{\rm recomb} \sim (n_e \alpha_{\rm A})^{-1}$ of ionised hydrogen in the system. n_e is the electron density, $\alpha_{\rm A}$ is the recombination coefficient to all levels, c is the speed of light (2.9979×10^8 m s^{-1}) and L_s represents the length scale of the system, i.e. in this case the length of the simulation box. This condition holds for all simulations presented in this thesis, but could be an issue if dealing with rapidly moving fluids (high $v_{\rm max}$ values) or low recombination rates (small $n_e \alpha_{\rm A}$ values).

In this section I will first describe the basics of the MC method, then the specifics of how the MCRT code I am using works.

2.3.1 The Monte Carlo method

As suggested by the name "Monte Carlo", which brings to mind gambling and casinos, MC codes model problems using a probabilistic approach. Stan Ulam first came up with the concept in 1946 when attempting to work out the probability of a successful game of Solitaire (Roger, 1987): *"After spending a lot of time trying to estimate them by pure combinatorial calculations, I wondered whether a more practical method than "abstract thinking" might not be to lay it out say one hundred times and simply observe and count the number of successful plays."* According to the law of large numbers, the more games are played the closer the average number of wins gets to the real probability.

A simple example of the MC method is estimating the value of π by "throwing darts". Random points are generated in a square with sides of length R and the number of points falling inside a circle of radius R is counted. Assuming the points are uniformly distributed, the ratio of the number of points inside the circle ($N_{\rm inside}$) to the total number of points (N)

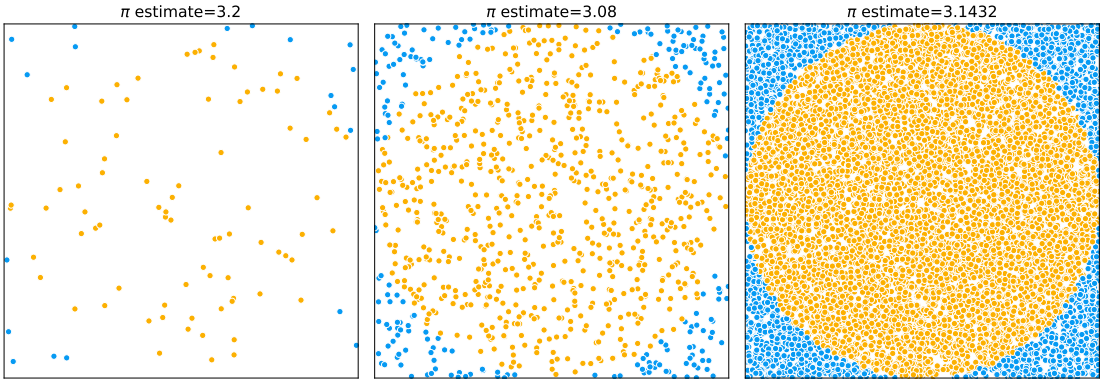

Figure 2.2: π is estimated using the ratio of orange points to the total number of points (Equation 2.10). From left to right the number of random points are 10^2, 10^3 and 10^4. The accuracy of the estimate increases as the number of points is increased.

should approach the ratio of the area of the circle (πR^2) to the area of the square ($4R^2$):

$$\begin{aligned} \frac{N_{\text{inside}}}{N} &\approx \frac{\pi R^2}{4R^2}, \\ &\Downarrow \\ \pi \text{ estimate} &\approx 4\frac{\mathrm{N_{acc}}}{\mathrm{N}}. \end{aligned} \tag{2.10}$$

This provides an estimate of π. As illustrated by Figure 2.2, the accuracy of the estimate increases as the number of random points increases.

Both examples presented so far have considered estimates of probabilities expressed by a single number: the chance of winning a game of solitaire and the probability of hitting the circle with a dart. The major strength of the MC method however is that through statistical sampling it can reproduce full probability distributions, not just single values.

The relative probability that a parameter has a value that lies within a particular range can be computed using the probability density function (PDF). The principle behind MC techniques is randomly sampling values of the parameter such that its PDF is recovered. This can be done in different ways depending on the form of the PDF.

The fundamental principle

Consider a PDF given by $P(x)$ where the parameter has limits $\{a, b\}$. The cumulative distribution function (CDF) of the parameter describes the probability of its value x falling between

the lower limit a and some $x_0 \in \{a, b\}$:

$$C_P(x_0) = \int_a^{x_0} P(x)\,\mathrm{d}x\,. \tag{2.11}$$

This function equals the area under the PDF. If the CDF can be easily inverted the "fundamental principle" of the MC method can be applied to sample the corresponding PDF:

1. Generate a random number $\xi \in \{0, 1\}$ from a uniform distribution.
2. Equate the random number $\xi = \xi(x_0)$ to the value of the normalised CDF when $x = x_0$:

$$\xi = \frac{\int_a^{x_0} P(x)\,\mathrm{d}x}{\int_a^{b} P(x)\,\mathrm{d}x}. \tag{2.12}$$

3. Invert the normalised CDF to get an expression for x_0 - a random value of the parameter x sampled from the PDF.

As an example consider the simple function $P(\theta) = \cos\theta$ with limits $\{0, \pi/2\}$. Following the method outlined above a random number $\xi \in \{0, 1\}$ is equated to the corresponding CDF:

$$\xi = \frac{\int_0^{\theta_0} \cos\theta\,\mathrm{d}\theta}{\int_0^{\frac{\pi}{2}} \cos\theta\,\mathrm{d}\theta}, \tag{2.13}$$

with solution:

$$\xi = \sin\theta_0. \tag{2.14}$$

This equation is then inverted to solve for θ_0:

$$\theta_0 = \arcsin\xi. \tag{2.15}$$

Figure 2.3 shows how repeated sampling using this expression results in a distribution of values approaching the original PDF.

The rejection method

For PDFs where the associated CDF cannot be inverted, an analytic formula for sampling random parameter values cannot be obtained. In these cases sampling can be done through the "rejection method". The earlier estimate of π was based on the rejection method. More gener-

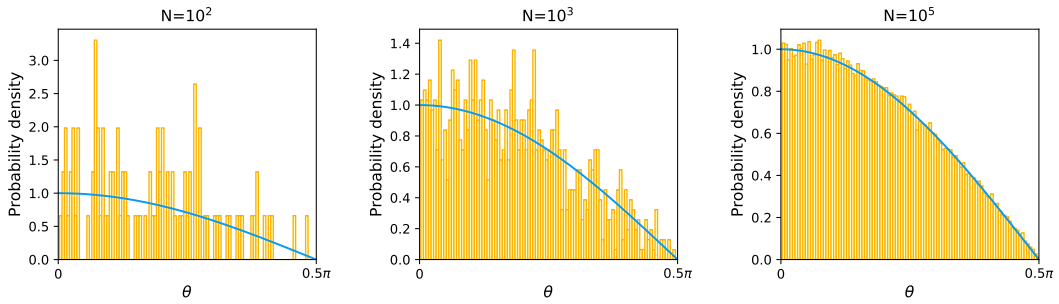

Figure 2.3: The blue lines show the probability density function (PDF) $P(\theta) = \cos\theta$. The yellow bars show the probability density obtained through a random sampling of the PDF by inverting the corresponding cumulative distribution function (CDF). From left to right the number of θ values sampled are 10^2, 10^3 and 10^5. The greater the sample size, the closer the randomly sampled distribution gets to the original PDF.

ally, given a PDF $P(x)$ with limits $\{a, b\}$ and a maximum value of $P_{\max}$, the steps for sampling are:

1. Generate a random value $x_0 \in \{a, b\}$ from a uniform distribution.

2. Generate a second random value $y_0 \in \{0, P_{\max}\}$ from a uniform distribution.

3. If $y_0 \leq P(x_0)$ accept x_0, otherwise repeat process.

The ratio of the number of accepted values to the total number of values generated equals the ratio of the area under the PDF (A_{PDF}) to the total area of the parameter space sampled ($A_{\text{total}} = (b-a) \times P_{\max}$).

As an example I will use the rejection method to sample the function $P(\theta) = (\cos^3\theta + 2)/4\pi$ with limits $\{0, 2\pi\}$. Within this range the maximum value of $P(\theta)$ is $3/4\pi$, at the points $\theta = 0$ and 2π. A random θ value falling somewhere between 0 and 2π is picked according to:

$$\theta_0 = \xi 2\pi, \tag{2.16}$$

where ξ is a uniformly sampled random number $\in \{0, 1\}$. Another random value, this time between 0 and $P_{\max} = 3/4\pi$ is then generated:

$$y_0 = \xi \frac{3}{4\pi}. \tag{2.17}$$

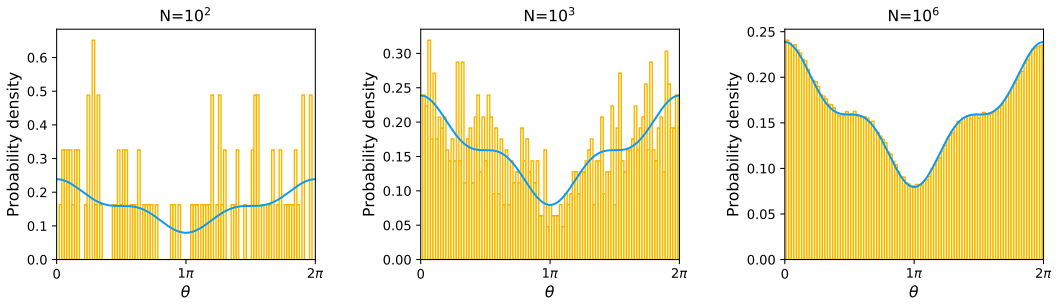

Figure 2.4: The blue lines show the probability density function (PDF) $P(\theta) = (\cos^3\theta + 2)/4\pi$. The yellow bars show the probability density obtained through a random sampling of the PDF using the rejection method. From left to right the total number of θ values sampled are 10^2, 10^3 and 10^6 (this includes the values that were rejected by the method). The greater the sample size, the closer the randomly sampled distribution gets to the original PDF.

Again ξ is a uniformly sampled random number $\in \{0, 1\}$. This is repeated until the y_0 value is equal to or less than $P(\theta_0) = (\cos^3\theta_0 + 2)/4\pi$, in which case the θ_0 value is accepted. Figure 2.4 shows how repeated sampling using this method reproduces the shape of the original PDF.

The rejection method should also provide the area under the PDF, i.e. the area under the curve plotted in Figure 2.4. When generating 10000 θ_0 values, 6655 of them were accepted. Comparing this success ratio to the ratio of areas gives:

$$\begin{gathered} \frac{6655}{10000} \approx \frac{A_{\text{PDF}}}{2\pi \times \frac{3}{4\pi}}, \\ \Downarrow \\ A_{\text{PDF}} \approx 0.99825. \end{gathered} \tag{2.18}$$

This approximately matches the true value of the area under the PDF as given by the associated CDF:

$$\int_0^{2\pi} \frac{\cos^3\theta_0 + 2}{4\pi} = 1. \tag{2.19}$$

The benefit of this method is that it can be used to sample any PDF. The downside is its efficiency depends highly on the form of the PDF. If the area under the PDF is relatively small compared to the parameter space being sampled it will require a large number of samples to get a good representation of the PDF.

2.3.2 Code description

MCRT codes use the statistical sampling techniques described in the previous section to model ionisation structures. Through the MC method it is possible to estimate overall ionisation without studying the behaviour of every single emitted photon individually. Probabilities are used to determine the propagation of photons (directions and distances travelled), including potential interactions occurring along the way (scattering or absorption events). The general workings of the MCRT code I use can be outlined in these four steps:

1. Set up a density grid and place ionising sources in the grid.

2. Track photon packets emitted from every source.

3. Calculate the ionisation fraction in every cell and update the grid to the new ionisation/opacity structure.

4. Repeat steps 2-3 until the ionisation structure of the grid has converged.

What follows is a more specific description of how each step is carried out or modified in the context of modelling the ionisation surrounding a growing high-mass star.

2.3.3 Setup

A 3D grid of density values is imported from the hydrodynamics code. For simplicity, the material is assumed to be 100% hydrogen, with no heavier elements or dust. Pure hydrogen is sufficient for estimating the ionisation structure of the system as heavier elements have much lower abundances and do not significantly impact the radiation transport (Wood et al., 2004). The effect dust would have had depends highly on the type of grains. Mathis & Wood (2005) argue that silicate dust is fairly untouched by ionising photons, whereas carbon dust is capable of absorbing about 90% of them. They show that HII regions likely contain carbon-depleted dust, hence the omission of dust is reasonable for the simulations presented in this thesis.

For the purposes of my work I place an ionising point source at the centre of the grid, this represents the star.

2.3.4 Tracking photon packets

The code is written so that the central ionising source emits packets of multiple photons. The number of photons released per second per packet is determined by the magnitude of the ionising luminosity of the source and the number of packets specified. The number of packets emitted is 100000 unless otherwise specified. These packets are tracked through a random walk of photoionisations and recombinations until the packet either escapes the grid or is re-emitted as non-ionising photons, see the flow chart in Figure 2.5.

Instead of considering a full spectrum of photon frequencies for the emitted photon packets, the code uses a two-frequency approximation; the ionising photon packets have one of two frequencies, depending on whether they originate from the central star or a re-emission. Any photons emitted from the central source are called "stellar photons" and are released with an energy of 17.9 eV, corresponding to the average frequency of photons emitted by a 40000 K star (Wood & Loeb, 2000). Re-emitted photons are called "diffuse photons", these can either be ionising or non-ionising. The ionising diffuse photons are assigned an energy of 13.6 eV, which corresponds to the peak of their frequency spectrum. If non-ionising diffuse photons are emitted they are not assigned an energy as these types of photons are not tracked by the code. This simplification of limiting the code to consider only two frequencies is documented and tested in Wood & Loeb (2000). They found, in the case of hydrogen photoionisation, that both the resulting ionisation fractions and the ionisation structure were in excellent agreement with those obtained when sampling photon frequencies from full spectra.

Initial emission of photon packet

The process begins by the source emitting a photon packet of stellar photons isotropically, that means there is no preferred direction of emission. The photon packet is assigned an initial direction of $\boldsymbol{n} = (n_x, n_y, n_z)$ where

$$\begin{aligned} n_x &= \sin\theta\cos\phi, \\ n_y &\sin\theta\sin\phi, \\ n_z &= \cos\theta. \end{aligned} \tag{2.20}$$

The ϕ and θ values are randomly sampled from PDFs that ensure isotropy. $P(\phi) = 1$ with limits $\{0, 2\pi\}$ and $P(\theta) = \sin\theta$ with limits $\{0, \pi\}$. Using the fundamental principle of the MC

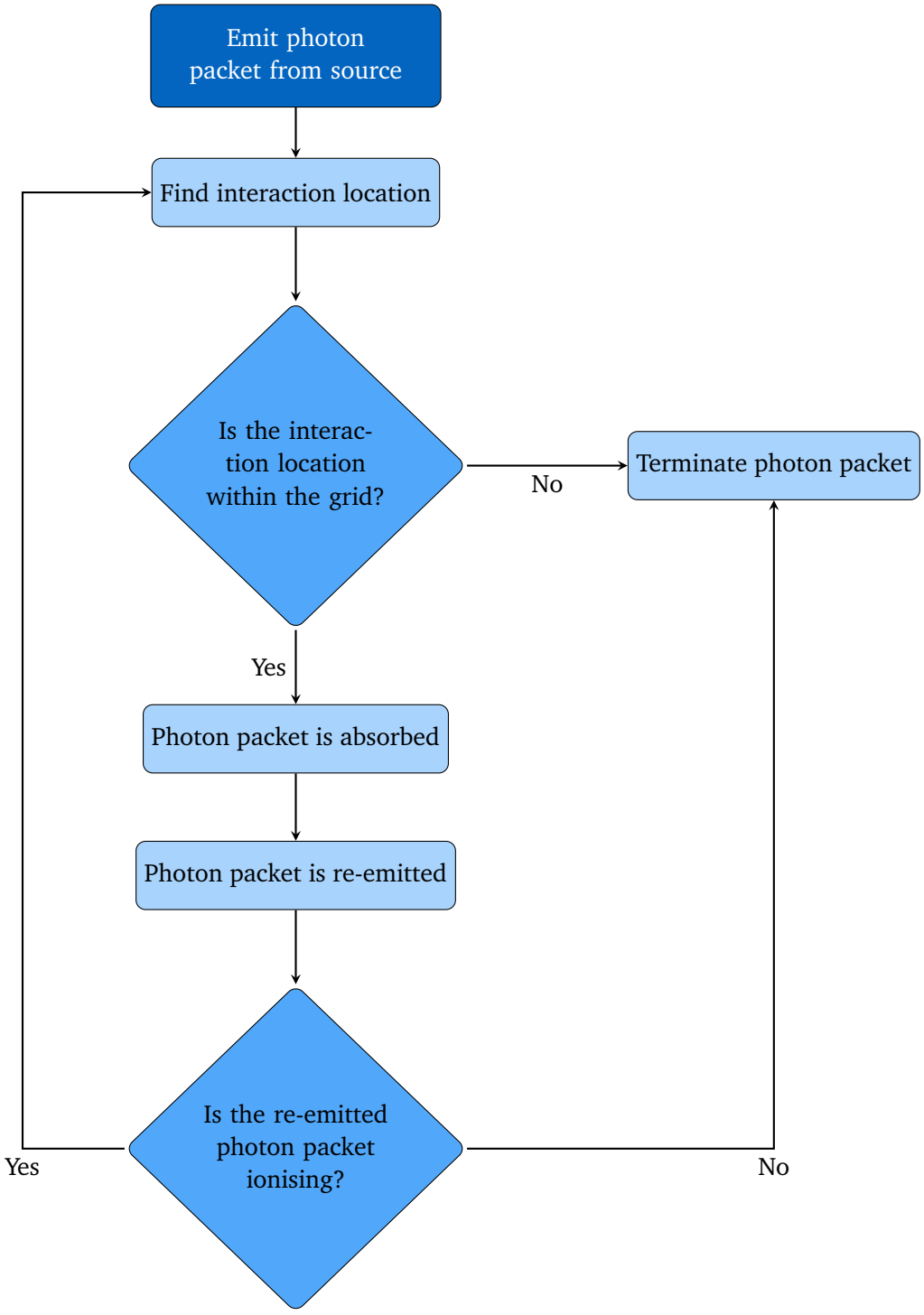

Figure 2.5: A flowchart describing how photon packets are tracked from their emission to termination.

method, the ϕ value is assigned in the following way:

$$\begin{aligned} \xi &= \frac{\int_0^{\phi_0} \mathrm{d}\phi}{\int_0^{2\pi} \mathrm{d}\phi}, \\ &\Downarrow \\ \xi &= \frac{\phi_0}{2\pi}, \\ &\Downarrow \\ \phi_0 &= 2\pi\xi. \end{aligned} \tag{2.21}$$

Similarly the random θ value is chosen according to:

$$\begin{aligned} \xi &= \frac{\int_0^{\theta_0} \sin\theta \, \mathrm{d}\phi}{\int_0^{\theta} \sin\theta \, \mathrm{d}\theta}, \\ &\Downarrow \\ \xi &= \frac{1}{2}(1-\cos\theta), \\ &\Downarrow \\ \theta_0 &= \cos^{-1}(2\xi - 1). \end{aligned} \tag{2.22}$$

Figure 2.6 shows that once the total number of photon packets have been emitted the overall distribution of angles is close to the original PDFs and an isotropic distribution.

Finding the interaction location

Once a photon packet has been emitted in some direction the next step is determining its interaction location, i.e. how far it travels before it is absorbed. The distance travelled depends both on the energy of the photon packet and the properties of the medium it passes through.

The average distance travelled by the photon packet between interactions is called the mean free path (l_{mfp}). For a medium with number density n and a cross section for ionisation of σ the mean free path is defined as:

$$l_{\mathrm{mfp}} = \frac{1}{n\sigma}. \tag{2.23}$$

Intuitively it makes sense that the distance the photon packet travels before being absorbed by a particle will depend on the density of the particles as well as the effective cross section

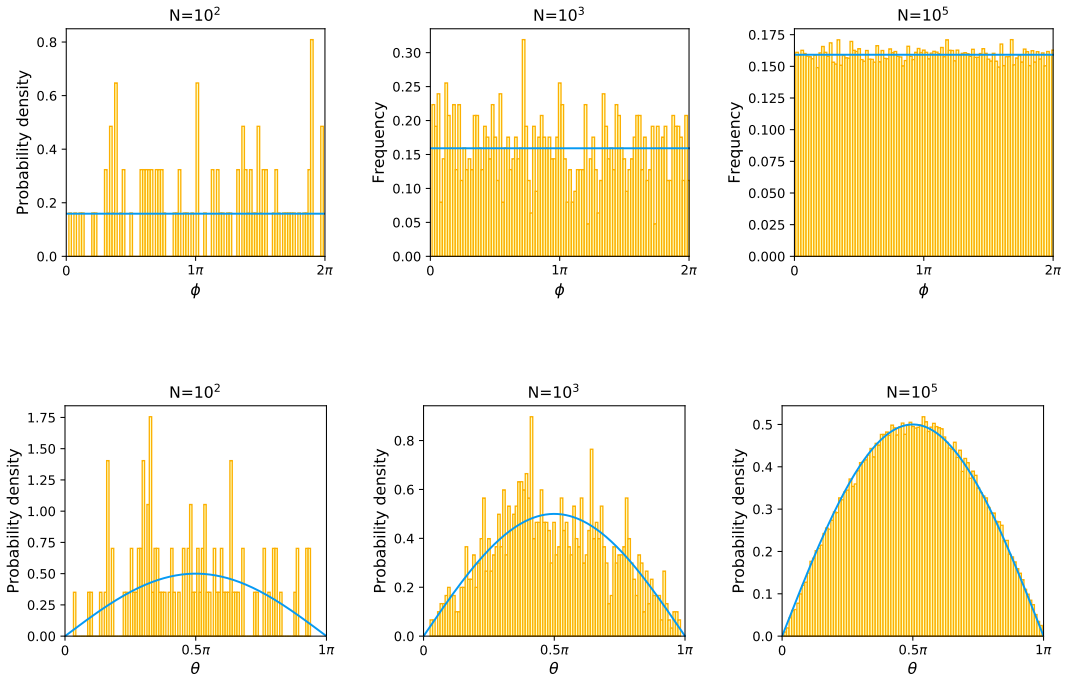

Figure 2.6: The blue lines show the normalised probability density functions (PDFs) $P(\phi) = 1/2\pi$ (*top*) and $P(\theta) = \frac{1}{2}\sin\theta$ (*bottom*) for isotropically choosing a direction (ϕ, θ). The yellow bars show the probability densities obtained through a random sampling of the PDFs. From left to right the number of ϕ and θ values sampled are 10^2, 10^3 and 10^5. The greater the sample sizes, the closer the randomly sampled distributions get to the original PDFs.

for a collision of a photon with a particle, the combination $n\sigma$ is defined as the "opacity" of the material. The higher the opacity of a medium, the harder it is for photons to pass through it without being absorbed. Hence, the probability of an interaction happening along an infinitesimal length $\mathrm{d}\Lambda$ is

$$\frac{\mathrm{d}\Lambda}{l_{\mathrm{mfp}}} = n\sigma\,\mathrm{d}\Lambda\,. \tag{2.24}$$

Conversely, the probability of the photon packet travelling $\mathrm{d}\Lambda$ without an interaction is

$$1 - \frac{\mathrm{d}\Lambda}{l_{\mathrm{mfp}}} = 1 - n\sigma\,\mathrm{d}\Lambda\,. \tag{2.25}$$

If a distance Λ_{total} is divided into N equal segments of length $\mathrm{d}\Lambda = \Lambda_{\mathrm{total}}/N$, the probability of travelling Λ_{total} without an interaction is given by

$$P(\Lambda_{\mathrm{total}}) = P(\Lambda_{\mathrm{total}}/N)^N = \left(1 - n\sigma\frac{\Lambda_{\mathrm{total}}}{N}\right)^N. \tag{2.26}$$

As $\mathrm{N} \to \infty$, the Taylor expansion for the exponential function can be used to rewrite the above as

$$P(\Lambda_{\mathrm{total}}) = \mathrm{e}^{-n\sigma\Lambda_{\mathrm{total}}} = \mathrm{e}^{-\tau}. \tag{2.27}$$

A substitution has been made for the optical depth $\tau = n\sigma\Lambda_{\mathrm{total}}$, which represents the number of mean free paths over the distance Λ_{total}. Hence, $P(\tau) = \mathrm{e}^{-\tau}$ can be described as the probability the photon packet reaches an optical depth τ before interacting. Based on this PDF the photon packet will be assigned a random optical depth (τ_{r}) according to the fundamental principle of the MC method:

$$\begin{gathered} \xi = \frac{\int_0^{\tau_{\mathrm{r}}} P(\tau)\,\mathrm{d}\tau}{\int_0^{\infty} P(\tau)\,\mathrm{d}\tau}, \\ \Downarrow \\ \xi = 1 - \mathrm{e}^{-\tau_{\mathrm{r}}}, \\ \Downarrow \\ \tau_{\mathrm{r}} = -\ln(1-\xi) = -\ln(\xi). \end{gathered} \tag{2.28}$$

Figure 2.7 shows that this sampling method results in a distribution of optical depths approaching the original PDF as the sample size increases.

Given the randomly chosen optical depth reached by the photon packet, the corresponding distance travelled can be determined, as long as the physical properties of the medium

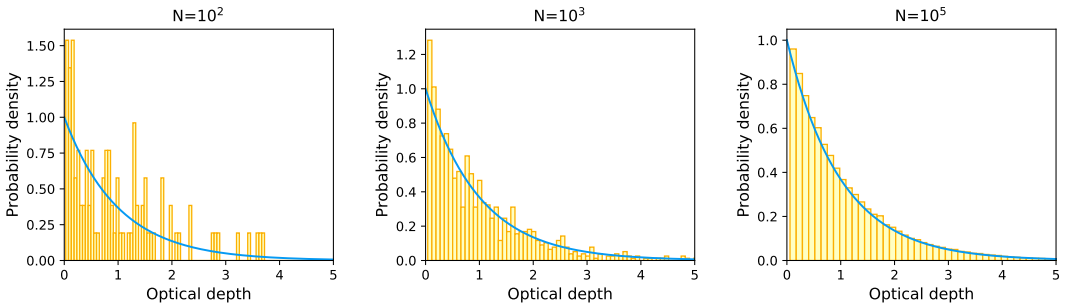

Figure 2.7: The blue lines show the probability density function (PDF) $P(\tau) = e^{-\tau}$ for photons to reach some optical depth τ before interacting. The yellow bars show the probability density of optical depths obtained through a random sampling of the PDF. From left to right the number of random optical depths sampled are 10^2, 10^3 and 10^5. The greater the sample size, the closer the randomly sampled distribution gets to the original PDF.

traversed is known. The optical depth was introduced as $\tau = n\sigma\Lambda_{\rm total}$, however since the opacity can change along the path of travel and is also frequency dependent the optical depth is more accurately expressed as:

$$\tau_{\rm r} = \int_0^{\Lambda_{\rm total}} n_{\rm H^0}(\Lambda)\sigma_\nu(\Lambda)\mathrm{d}\Lambda. \tag{2.29}$$

In the above equation $n_{\rm H^0}$ is the number density of neutral hydrogen, σ_ν is the cross section for ionisation by photons of frequency ν, Λ is distance, and the limit $\Lambda_{\rm total}$ is the total distance travelled to reach the random optical depth $\tau_{\rm r}$. The dependence of the photoionisation cross section of hydrogen on photon frequency can be approximated as:

$$\sigma_\nu = \sigma_{\nu_0}\left(\frac{\nu}{\nu_0}\right)^{-3}, \tag{2.30}$$

where ν_0 is the minimum frequency required to ionise hydrogen, i.e. $h\nu_0 = 13.6$ eV, and σ_{ν_0} is the corresponding cross section of $6.3{\times}10^{-18}\mathrm{cm}^2$ (Hummer & Seaton, 1963). There are two frequency options in this code, depending on whether the photon packet consists of stellar photons ($h\nu = 17.9$ eV) or ionising diffuse photons ($h\nu = 13.6$ eV). For a given photon frequency, the opacity is a constant property within each grid cell. That means Equation 2.29 can be discretised to calculate the cumulative optical depth of the photon packet as it moves through grid cells:

$$\tau_{\rm sum} = \sum \tau_{\rm cell} = \sum n_{\rm H^0}\sigma_\nu\Lambda_{\rm cell}, \tag{2.31}$$

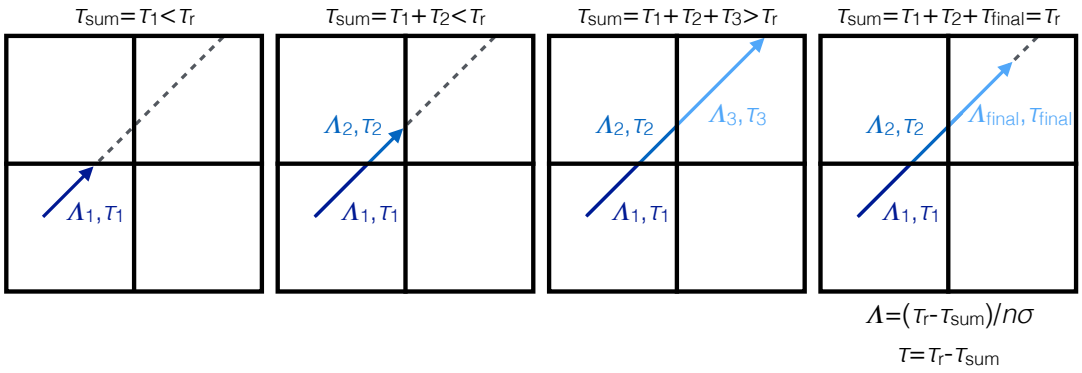

Figure 2.8: A 2D representation of the propagation of a photon packet from emission to its interaction location. The dotted line shows the direction the photon packet is travelling and the arrow represents the progression of the photon packet along that direction. The photon packet travels a random optical depth τ_r, crossing cells along the direction of travel until the cumulative optical depth across the cells, τ_{sum}, exceeds τ_r. In this example that happens when the photon packet has moved through three cells. After initially overshooting, the photon packet reaches the interaction location by changing the final step size to Λ_{final} given by Equation 2.32 such that $\tau_{sum} = \tau_r$.

with Λ_{cell} being the distance travelled within each cell. The interaction location is reached at the point when $\tau_{sum} = \tau_r$.

Starting from the point of emission and given the direction the photon packet is moving in, the distance and optical depth to the nearest cell wall to be encountered is calculated. As long as the cumulative optical depth given by Equation 2.31 is less than the random optical depth chosen ($\tau_{sum} < \tau_r$) the photon packet travels through its current cell to the next. When crossing the current cell would lead to τ_{sum} exceeding τ_r the photon packet has reached the cell where it interacts. Instead of moving through this cell a shorter final step is calculated such that $\tau_{sum} = \tau_r$:

$$\Lambda_{final} = \frac{\tau_r - \tau_{sum}}{n_{H^0}\sigma_\nu}. \tag{2.32}$$

To visualise this process of moving through cells until the interaction location is reached see Figure 2.8. Note that as the photon packet is being tracked through the grid cells in this way the distance it travels within each cell is recorded along with the photon type (stellar or diffuse). This information is used later on to calculate the ionisation structure of the simulation box.

Re-emission

As only photon packets that are capable of ionisation are tracked it follows that at the interaction location a photoionisation/recombination event occurs. Hydrogen is ionised, and since the code is time-independent these hydrogen ions immediately recombine with electrons resulting in the re-emission of a new photon packet. Whether or not the diffuse photons in the new photon packet are ionising depends on whether the electrons recombine to the ground level or not. Only recombinations to the ground level produce photons energetic enough to ionise hydrogen (e.g. Osterbrock & Ferland, 2006).

The probability of a recombination to the ground level is given by:

$$P_1 = \frac{\alpha_1}{\alpha_A} = 1 - \frac{\alpha_B}{\alpha_A}, \tag{2.33}$$

where α_A, α_B and α_1 are the recombination coefficients to all levels, all excited levels and the ground level of hydrogen respectively. For instance, in the case of Hydrogen at a temperature of 8000 K, $\alpha_A = 5.25 \times 10^{-13}$ cm^3 s^{-1} and $\alpha_B = 3.26 \times 10^{-13}$ cm^3 s^{-1}, which gives a probability of $P_1 = 0.379$ (see Table 2.1 in Osterbrock & Ferland, 2006). If a randomly generated number satisfies $\xi \leq P_1$ the re-emitted photon packet contains ionising diffuse photons with an energy of $h\nu = 13.6$ eV. Conversely, if $\xi > P_1$, the re-emitted photon packet is not ionising.

Re-emitted ionising photon packets are assigned an iosotropic direction upon emission and are tracked to a new interaction location, where a new photoionisation/recombination event occurs. Re-emitted non-ionising photon packets on the other hand are not tracked by the code.

Termination

The photon packets are tracked through potentially multiple photoionisation/recombination events until either the photon packet leaves the grid or a non-ionising photon packet is emitted. These two fates are illustrated in the diagram in Figure 2.9. In both cases the tracking stops and the next photon packet is emitted from the source. This is repeated until 100000 stellar photon packets have been emitted.

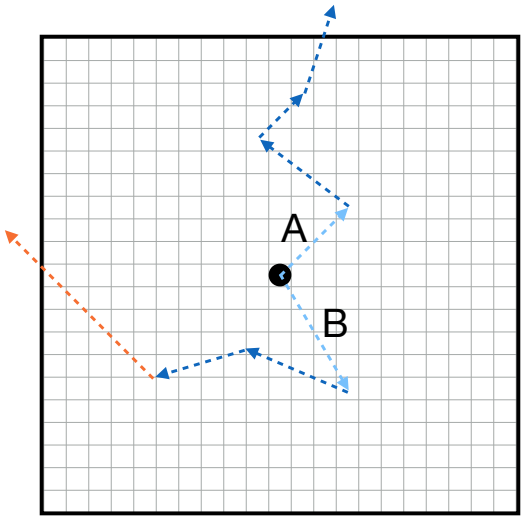

Figure 2.9: The two possible fates of a photon packet: A escapes the simulation box and B is re-emitted as a non-ionising photon packet. The light blue arrows show the path of stellar photons leaving the source, the dark blue arrows show diffuse ionising photons and the orange arrow shows non-ionising photons leaving the system (note that the non-ionising photons are not tracked by the code).

2.3.5 Calculating the ionisation fraction

The code assumes instantaneous photoionisation equilibrium, meaning the number of photoionisations per second is balanced by the number of recombinations per second. Hence for each grid cell the photoionisation rate per unit volume (left hand side) is equated with the recombination rate per unit volume (right hand side):

$$n_{\mathrm{H}^0} \int_{\nu_0}^{\infty} \frac{4\pi J_\nu}{h\nu} \sigma_\nu d\nu = \alpha_{\mathrm{A}} n_{\mathrm{e}} n_{\mathrm{p}}. \tag{2.34}$$

h is the Planck constant (6.6261×10^{-34} J s), J_ν is the mean intensity of the photons at frequency ν, n_{e} is the number density of electrons and n_{p} is the number density of protons. Given the box contains pure hydrogen only, the number densities of electrons and protons are expected to be equal, and their product can be rewritten as the number density of ionised hydrogen squared: $n_{\mathrm{e}} n_{\mathrm{p}} = n_{\mathrm{H}^+}^2$. Furthermore, since the total hydrogen density (n_{H}) can be split into a neutral and an ionised component, the neutral hydrogen density can be expressed as $n_{\mathrm{H}^0} = n_{\mathrm{H}} - n_{\mathrm{H}^+}$.

Using path length estimators (Lucy, 1999) the integral in Equation 2.34 can be expressed

in terms of tracked photon paths:

$$I = \int_{\nu_o}^{\infty} \frac{4\pi J_\nu}{h\nu} \sigma_\nu d\nu = \frac{Q}{N_\gamma V_{\text{cell}}} \sum \Lambda_{\text{cell}} \sigma_\nu. \tag{2.35}$$

Q is the ionising luminosity of the source, meaning the number of ionising photons emitted per second, N_γ is the number of photon packets emitted and V_{cell} is the volume of each cell, all of which is defined in the setup. From tracking the photon packets in the previous step the distances they travelled through each cell (Λ_{cell}) are known, and also the cross section corresponding to the type of photon packet (σ_ν).

Adapting Equation 2.34 as described, i.e. by discretising the integral and rewriting the hydrogen number densities in terms of the ionised and total component results in the following quadratic equation:

$$\alpha_{\text{A}} n_{H^+}^2 + I n_{H^+} - I n_H = 0. \tag{2.36}$$

This quadratic can be solved to obtain the ionisation fraction of each grid cell; $I_f = n_{H^+}/n_H$. The ionisation fraction, and hence opacity, throughout the simulation grid is updated according to these new values.

The simulation grid is initially set to be fully ionised. The entire process of emitting and tracking photon packets, then calculating ionisation fractions, has to be repeated multiple times to eventually reach a converged ionisation structure. Convergence generally occurs within 7 iterations, but the default setting of the code is to run 10 iterations. During the last 3, the number of photon packets emitted are increased by a factor of 10 to increase the signal-to-noise ratio of the final ionisation structure.

2.3.6 Increasing signal to noise

The reliability of the calculated ionisation fraction in each grid cell is dependent on the density of photon packets. A bigger simulation box size or a higher number of grid cells will reduce the likely number of photon packets propagating through any given grid cell. This is in particular a problem for the grid cells furthest from the photon emitting source. In order to ensure good statistics using the Monte Carlo technique more photon packets can be added. The problem with increasing the number of photon packets, however, is computing time. To increase the signal to noise without increasing the number of photon packets, and hence computing time,

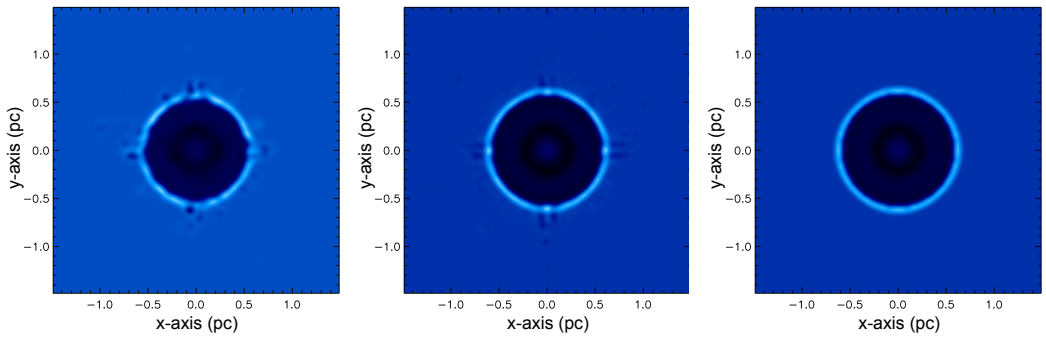

Figure 2.10: Illustrating the effect of radial averaging of photon path lengths on a spherically symmetric system consisting of a central radiative source in a uniform density medium. The above are density plots at the same time step showing a slice through the centre of the simulation box, with the lighter colour representing a higher density. *Left*: 10000 photon packets emitted. *Middle*: 1000000 photon packets emitted. *Right*: 10000 photon packets emitted with radial averaging.

I introduce two averaging schemes to the code which can be used for spherical and eight-fold symmetry respectively.

Spherical symmetry

For spherically symmetric systems the mean photon intensity is a function of radius only, hence I develop a radial averaging scheme. In Chapter 3 the rad-hydro code is applied to model the ionisation surrounding a growing high-mass star, which will for simplicity be treated as spherically symmetric and hence employs this radial averaging scheme. Due to the isotropic nature of the source and the spherical symmetry of the system every cell at a certain radius should contain the same overall photon path length, in reality however, with a finite number of photon packets emitted in random directions, this will not be the case. I average the photon path lengths across every cell that has the same distance from the origin by looping through every grid cell, sorting the photon path lengths according to cell radius, and then calculating the mean total path length at each radius. Then I loop back through the cells and repopulate them with the new average total path length values, giving better statistics for the Monte Carlo ionisation estimator. Figure 2.10 shows an example of the effect of implementing the radial averaging versus increasing the number of photons. This radial averaging is used whenever the code is applied to a spherically symmetric problem, which includes all simulations presented in Chapter 3. The averaging results in these simulations being idealised spherically symmetric 3D simulations, effectively making them 1D.

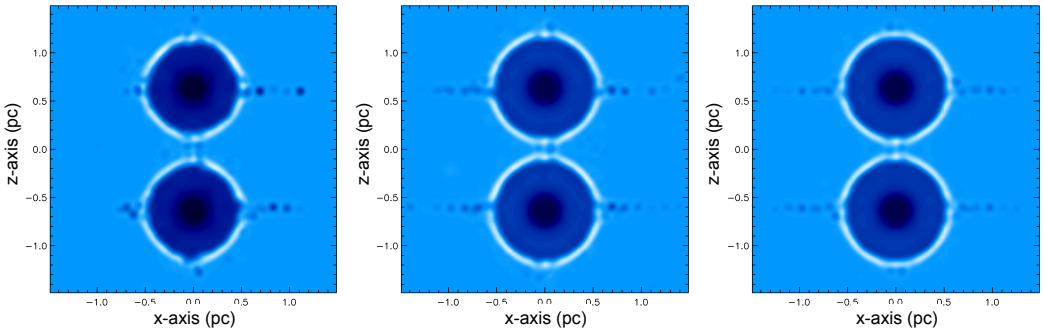

Figure 2.11: Illustrating the effect of axi-symmetric averaging of photon path lengths on a system symmetric about the z-axis consisting of two radiative sources in a uniform density medium. The above are density plots at the same time step showing a slice through the centre of the simulation box, with the lighter colour representing a higher density. *Left*: 10000 photon packets emitted. *Middle*: 80000 photon packets emitted. *Right*: 10000 photon packets emitted with axi-symmetric averaging.

Eight-fold symmetry

For systems symmetric about an axis I develop a similar scheme, where instead of sorting the grid cells according to radii I use the eight-fold symmetry to split the simulation box into octants which should be identical. For every cell there are seven equivalent cells in the other octants, I calculate the average photon path length for each set of eight equivalent cells and repopulate the grid with path length values accordingly. Figure 2.11 shows an example of the effect of implementing this axi-symmetric averaging versus increasing the number of photons. It effectively gives the same result as increasing the number of photons by a factor of eight.

2.4 Coupling the codes

In the full rad-hydro scheme the hydrodynamics code calculating the fluid dynamics, described in Section 2.2, and the time-independent MCRT code calculating the ionisation structure, described in Section 2.3, have to communicate in order to model both processes consistently. The overall structure of how the codes are coupled is summarised in these steps:

1. Setup a grid of conserved variables (ρ, ρv,e).

2. Solve the hydrodynamical equations of motions using the Godunov scheme.

3. Add source terms.

(a) Import the density grid from the hydro code into the MCRT code and place ionising sources.

(b) Track photon packets and calculate the resulting ionisation fraction

(c) Calculate the resulting temperatures and pressures.

(d) Export the new pressure from the MCRT code to the hydro code and calculate the corresponding source term.

4. Update the conserved variables.

5. Repeat steps 2–4.

At the end of each timestep of the hydrodynamics code the MCRT code imports the current density grid and calculates the corresponding ionisation structure from which temperatures and hence pressures are estimated. The pressures are then exported to the hydrodynamics code to provide a source term in the hydrodynamics equations representing the amount of energy provided by photoionisation. This source term will then be taken into account when updating the variables of the system. The specifics of how temperatures, pressures and the resulting source terms are calculated is outlined in more detail in the following sections.

2.4.1 Calculating temperatures and pressures

The temperature of interstellar gas is determined by the balance between heating from photoionisation and cooling from recombination and various forms of radiation. The MCRT code presented in this chapter does not calculate heating and cooling rates, this would require a higher level of complexity, furthermore it would require a more accurate picture of the composition of the gas being considered than pure hydrogen. Whilst the assumption of 100% hydrogen is sufficient to determine the ionisation structure, it is a poor approximation when considering heating and cooling where heavier elements become significant. Wood et al. (2004) present a more extensive version of the MCRT code I am using, their version includes heating and cooling mechanisms, as well as all important species (H, He, C, N, O, Ne and S). They find the resulting temperature in an ionised region surrounding a 40000 K star is approximately 8000 K. As my code is unable to similarly calculate temperatures based on heating/cooling rates, I assign fixed temperatures for fully neutral and fully ionised gas, $T_{\rm n}$ and $T_{\rm i}$. I let the value of the ionised temperature be 8000 K, according to the findings of Wood et al. (2004),

to approximate the existence of heavier elements. The neutral gas temperature is set to 500 K, this specific value is chosen to ensure a reasonable runtime[4].

To estimate the temperature in each grid cell corresponding to any given ionisation fraction the commonly used practice of mapping the fraction to a linear scale ranging from the neutral to the ionised temperature is adopted(Haworth & Harries, 2012):

$$T = T_{\mathrm{n}} + (T_{\mathrm{i}} - T_{\mathrm{n}})I_f\,. \tag{2.37}$$

Corresponding pressures are estimated using the ideal gas law:

$$pV = NkT, \tag{2.38}$$

where capital N in this case represents the number of particles and k is the Boltzmann constant. Assuming a constant volume (V), the pressure of the gas (p) depends only on the number of particles and temperature. When the hydrogen gas is photoionised the number of particles in the region will double since there is an ion and an electron for every original atom. Given the ionisation fraction, the pressure of fully neutral gas, the neutral temperature, and the current temperature provided by Equation 2.37, the pressure is calculated as follows:

$$p = \left(1 + I_f\right) p_{\mathrm{n}} \frac{T}{T_{\mathrm{n}}}. \tag{2.39}$$

This approach will assign the correct pressures to the fully ionised and neutral regions, and thus captures the correct pressure jump, however it is only a first order approximation of the pressures in the ionised-to-neutral transition region.

2.4.2 Calculating photoionisation source terms

As described in Section 2.2, when solving the hydrodynamics equations, source terms are added after performing the Godunov scheme, but before updating the values of conserved variables. Photoionisation is accounted for through such a source term. To calculate the photoionisation source term the code starts by exporting the pressures calculated based on the ionisation structure of the system from the MCRT code to the hydrodynamics code. They will be used to estimate the amount of energy provided by photoionisation. These predicted pres-

[4]The runtime of the simulations increases along with the difference in temperature between the neutral and ionised gas.

sures (p_p) given by the MCRT code are compared to the current pressure values (p_c) of each grid cell in the hydro code. If the pressure in the cell is already at the value predicted by the ionisation no additional energy is added. If the cell has either been ionised or turned neutral since the previous timestep the current pressure in the cell will be lower or higher than the predicted value, and the pressure is increased or decreased according to the difference $\Delta p = p_p - p_c$.

The change in energy density, e, can be estimated based on this pressure difference using the equation of state for an ideal gas, $p = (\gamma - 1)e$, where γ is the heat capacity ratio. This leads to the following energy source term:

$$S = \frac{\Delta p}{(\gamma - 1)\Delta t}, \tag{2.40}$$

which is used in Equation 2.5 when calculating the new total energy density. This effect of photoionisation is added at the end of every time step of the simulation.

2.5 Code tests

This section presents tests of the code against work done by others and against analytic solutions. They provide useful sanity checks. Furthermore the specific tests chosen are all meant to illustrate the code is capable of handling different physical processes required when simulating the early evolution of HII regions surrounding young high-mass stars, which is the scenario investigated in Chapter 3. The ability of the code to model the expansion of HII regions is addressed in Sections 2.5.1 and 2.5.2, where I do a benchmark test on the rate of expansion of D-type ionisation fronts, and demonstrate the formation of both D and R-type fronts. The purely dynamical problem of material being gravitationally attracted by the central star is considered in Section 2.5.3, where spherically symmetric accretion is tested against the analytic prediction.

2.5.1 Expanding D-type ionisation front

The D-type expansion (see Section 1.2.2) of a spherically symmetric HII region has been explored both analytically and numerically (Bisbas et al., 2015; Williams et al., 2018). Here I compare the D-type expansion of the rad-hydro code in the absence of gravity with the theoretical Spitzer (1978) and Hosokawa & Inutsuka (2006) solutions, as well as results from various

1D and 3D codes presented in a benchmarking paper by the STARBENCH project (Bisbas et al., 2015).

The Spitzer solution (Spitzer, 1978) describing the radius of the D-type ionisation front as a function of time is given by:

$$R_{\rm Sp}(t) = R_{\rm St}\left(1 + \frac{7c_{\rm s\,i}t}{4R_{\rm St}}\right)^{\frac{4}{7}}, \tag{2.41}$$

where $c_{\rm s\,i}$ is the sound speed of the ionised material, t is time, and $R_{\rm St}$ is the Strömgren radius[5] (Equation 1.16). A characteristic of the D-type front is a dense shell of neutral material that builds up between the ionised region and the undisturbed neutral region and is pushed outward as the HII region expands. The Spitzer approach assumes this shell is thin and does not consider the effect of the inertia of material inside the shell. This is however taken into account by Hosokawa & Inutsuka (2006) in their derivation, and consequently they predict a slightly more rapid expansion,

$$R_{\rm HI}(t) = R_{\rm St}\left(1 + \frac{7}{4}\sqrt{\frac{4}{3}}\frac{c_{\rm s\,i}t}{R_{\rm St}}\right)^{\frac{4}{7}}. \tag{2.42}$$

When simulating the D-type expansion using the rad-hydro code the initial conditions used are adopted from the STARBENCH test. The main parameters are given below, however for a more detailed description see Bisbas et al. (2015). The simulation box size is $x,\ y,\ z \in [-1.5, 1.5]$ au, with the box being divided into 128^3 grid cells. An isotropic ionising source emitting 10^{49} photons per second is placed at the centre of the grid surrounded by a uniform medium of density $\rho = 5.21 \times 10^{-21}$ g cm^{-3}. Any gravitational force due to the source is neglected. Neutral gas is given a temperature of $T_{\rm n} = 10^2$ K, and once it is ionised the temperature increases to $T_{\rm i} = 10^4$ K. Emitted photons are assumed to all have an initial energy of $h\nu = 13.6$ eV, which is large enough to ionise hydrogen. The photoionisation cross section is given by $\sigma = 6.3 \times 10^{-18}$ cm^2 and the recombination coefficient to excited levels (n $\geq$ 2) is $\alpha_{\rm B} = 2.7 \times 10^{-13}$ cm^3 s^{-1}. For this benchmarking test diffuse photons are not tracked. Instead the "on-the-spot" approximation is used, where all re-emitted diffuse photons are assumed to be re-absorbed "on-the-spot". This is a reasonable simplification to make for this particular

[5]The radius of an HII region where ionisations are balanced by recombinations (Strömgren, 1939).

spherically symmetric problem, but it could lead to unrealistic results in cases where dense obstacles shield regions from non-diffuse radiation (Ercolano & Gritschneder, 2011).

The result of this simulation is a spherical HII region, created by the central ionising source, which grows in time. This is shown in Figure 2.12 where the radius of the HII region as a function of time is plotted alongside analytic predictions as well as the mean values of the numerical codes participating in the STARBENCH test Bisbas et al. (2015). The radius of the ionised region at each time step is chosen by radially averaging the neutral gas fraction of the grid cells. Bins of approximately half a cell width are looped through in radial order until the neutral fraction is ≥ 0.5. The midpoint of the corresponding bin is used as the ionisation radius.

Figure 2.12 shows the D-type expansion rate from my simulation is consistent with the results by the other numerical codes. The expansion initially looks similar to the Spitzer solution, but follows the analytic Hosokawa-Inutsuka solution more closely at later times. This is perhaps not so surprising considering the assumption of a thin shell at the ionisation front, which the Spitzer solution makes, will be worse at later times when more material has been able to build up. This result will be presented in Falceta-Gonçalves et al (in prep.).

2.5.2 Flow past an ionising source: D-type and R-type ionisation fronts

Whether an HII region expands as a D-type or R-type front depends on the relative velocity between the ionisation front and the neutral gas it is expanding into (see Equations 1.27 and 1.28). To test whether the code is capable of reproducing both fronts, I set up a simulation with a flow of material moving past a stationary source of ionising radiation. For this simulation I am not including the radial averaging routine of the photoionisation, meaning the simulation is fully 3D.

I use a similar initial setup to Mackey et al. (2013), who simulated a flow moving past an O-star with the rad-MHD code PION, the key difference being I am not including a magnetic field. The simulation box has dimensions $x \in [-32, 19]$ pc and $y,\ z \in [-25.5, 25.5]$ pc, each direction is split into 128 cells. A radiative source emitting 3.63×10^{47} ionising photons per second is placed at the origin $x,\ y,\ z = (0, 0, 0)$. Any gravitational force due to the source is neglected. Neutral material is given a temperature of 1000 K, when ionised the temperature increases to 7000 K, which corresponds to a sound speed of $c_{\rm s\,i} \approx 10.8$ km s^{-1}. Material is

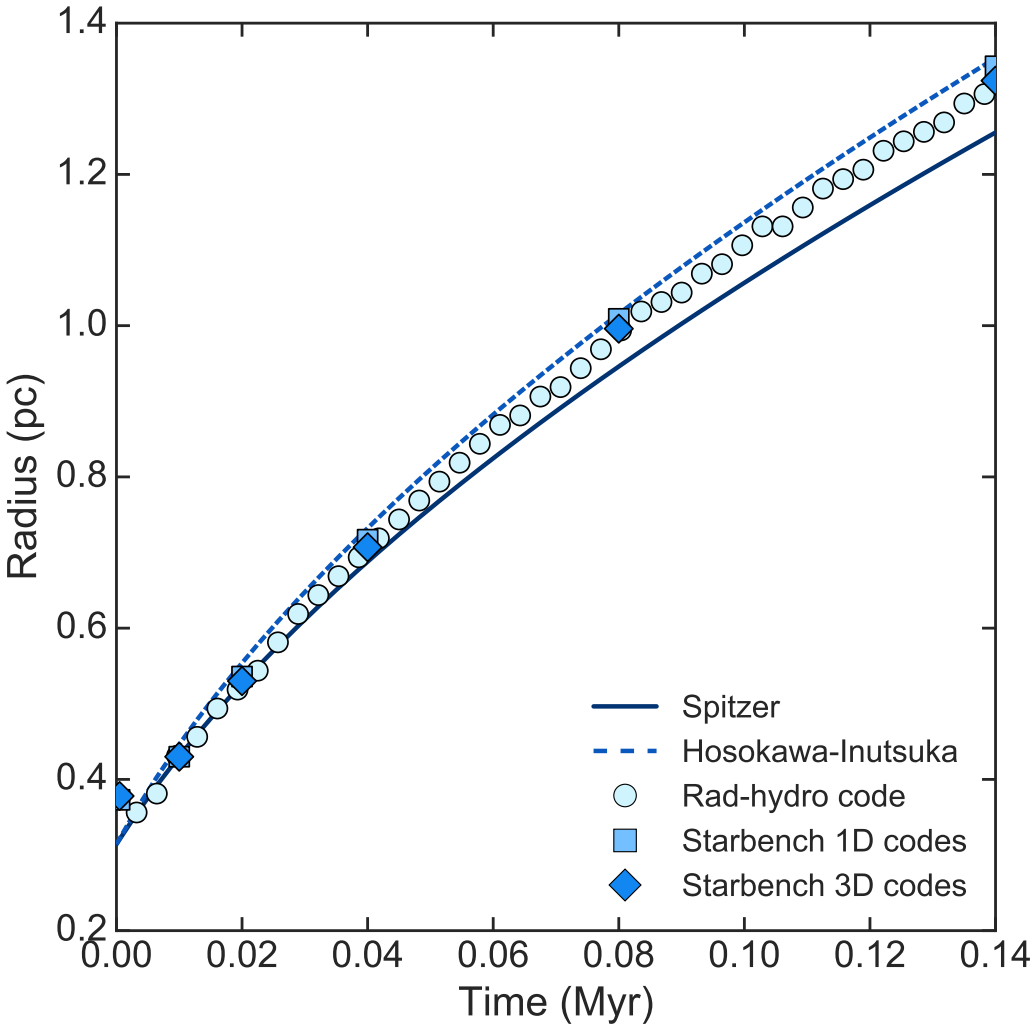

Figure 2.12: The ionisation front radius as a function of time in the absence of gravity. The plot compares results from the rad-hydro code described in this chapter with the analytical Spitzer (Equation 2.41) and Hosokawa-Inutsuka (Equation 2.42) expressions, as well as mean results from the 1D and 3D codes participating in the STARBENCH paper (Bisbas et al., 2015).

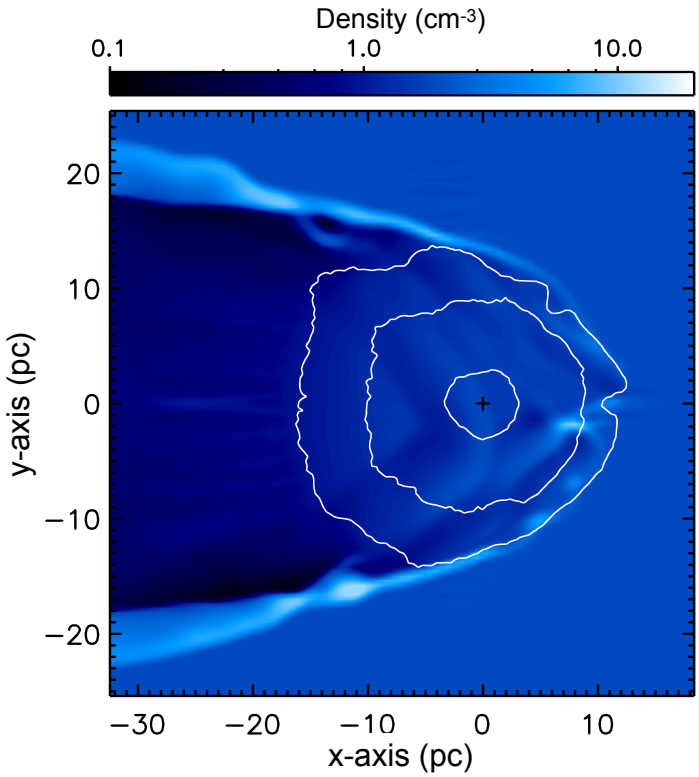

Figure 2.13: A slice through the centre of the 3D simulation box showing density on a logarithmic colour scale. Material flows from right to left with a velocity of 26.5 km s^{-1}. The black cross marks the position of the ionising source. The white contours correspond to fractions of ionisation; 0.999, 0.99, and 0.9.

continuously injected into the simulation box from the boundary at $x = 19$ pc, flowing parallel to the x-axis in the negative x direction. The material has a number density of $n = 2.5$ cm^{-3} and an initial velocity of $v = 26.5$ km $s^{-1} \approx 2.5$ $c_{s\,i}$.

Figure 2.13 shows the density (colour scale) and ionisation level (contour lines) of a slice through the centre of the simulation after 1.7 Myr, at which point the system is no longer changing. The flow past the ionising source results in an over-dense conical shell of material and an under-dense area behind the source. The HII region is nearly spherical, but expands further in the direction of lower density material, as is expected (see Section 1.2.1). Both the density and ionisation profile qualitatively match those of Mackey et al. (2013), a perfect agreement in values is not expected since their simulation includes magnetic fields.

The ionisation front perpendicular to the direction of flow has a relative velocity equal to the flow of material: $v_r = 26.5$ km $s^{-1} \approx 2.5$ $c_{s\,i} > 2$ $c_{s\,i}$, which satisfies the criteria for an R-type front. There is a transition from R-type to D-type where the ionisation front is parallel

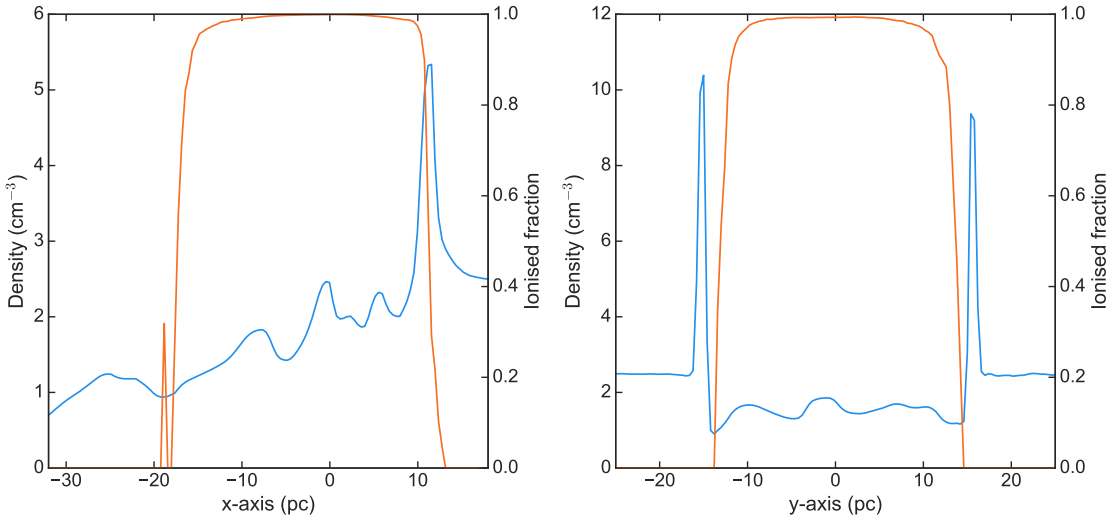

Figure 2.14: The density (blue) and ionisation fraction (orange) through the centre of the 3D simulation box along the x-axis (*left*) and y-axis (*right*) after 1.7 Myr. The ionising source is placed at the origin and material flows along the x-axis from the positive to negative end at 26.5 km s^{-1}.

to the flow since the relative velocity at this point is zero. For a closer look at the differences between the densities along the y-axis and x-axis, see Figure 2.14. Along the x-axis (*left*) there is an increase in density directly within the ionisation front before the density drops in the wake of the source. In contrast, along the y-axis (*right*) there are significant peaks in density outside the ionisation fronts, which is a characteristic of D-type fronts.

In conclusion, the rad-hydro code I am using gives similar ionisation and density profiles to the rad-MHD code PION used by Mackey et al. (2013). It is capable of producing both R-type and D-type ionisation fronts, as well as a smooth transition between the two.

2.5.3 Steady state Bondi accretion

In this section I test the rad-hydro code against the Bondi problem; the steady and spherically symmetric infall of material onto a central object (Bondi & Hoyle, 1944; Bondi, 1952). The analytic solution which was presented originally by Bondi (1952) is summarised and extended in Vandenbroucke et al. (2019). Below I am highlighting the equations relevant to my work, however I refer to Vandenbroucke et al. (2019) for more detail on the origin of these equations.

Bondi accretion assumes a constant accretion rate ($\dot{M}$), given as a function of density (ρ),

velocity (v) and radius (r) as:

$$\dot{M} = 4\pi r^2 \rho(r) v(r). \tag{2.43}$$

Assuming the sound speed (c_s) also stays constant, a so-called Bondi radius is defined:

$$R_B = \frac{GM}{2c_s^2}, \tag{2.44}$$

with M being the mass of the central gravitationally attracting object and G being the gravitational constant. The Bondi radius is the radius where the infall velocity equals the sound speed. A neutral and an ionised Bondi radius can be defined depending on whether the sound speed of ionised or neutral gas is being used. During steady state Bondi accretion the density and velocity of the accreting material as a function of radius is given by:

$$\rho(r) = \frac{\rho_B R_B^2 c_s}{r^2 v(r)}, \tag{2.45}$$

$$v(r) = \begin{cases} c_s \sqrt{-W_{-1}\left(-\left(\frac{R_B}{r}\right)^4 \exp\left(3-4\frac{R_B}{r}\right)\right)} & r \leq R_B, \\ c_s \sqrt{-W_0\left(-\left(\frac{R_B}{r}\right)^4 \exp\left(3-4\frac{R_B}{r}\right)\right)} & r > R_B, \end{cases} \tag{2.46}$$

where ρ_B is the density at the Bondi radius, and W_{-1} and W_0 represent different branches of the Lambert W function[6]. Note a positive velocity represents material moving towards the central star.

Figure 2.15 shows examples of these Bondi density and velocity profiles resulting from placing stars of different masses in an environment of pure hydrogen with a number density (n) of 30000 cm^{-3} at the neutral Bondi radius and a neutral sound speed of $\sim$ 2 km s^{-1}.

The next step is determining whether the rad-hydro code is capable of reproducing these predicted density and velocity profiles. No radiation is included in this scenario, so technically it is a test of the hydrodynamical aspects of the code only. In order to model this scenario, material falling onto a central source, with the rad-hydro code, the effect of gravity needs to be added. This is done through source terms in the hydrodynamics equations described earlier, see Section 2.2. The equations governing the momentum and energy of each cell are both modified through an added source term to account for the presence of a gravitational force, F_G. The gravitational force can be written as a relationship between the central star of

[6]The Lambert W function is a set of functions/branches of the inverse relation of $f(W) = W\exp\{W\}$. $W_{-1}(x)$ and $W_0(x)$ are real-valued for $x \in [-1/e, 0]$, with $W_{-1}(-1/e)$ = -1 to $W_{-1}(0)$ = -∞ and $W_0(-1/e)$ = -1 to $W_0(0) = 0$.

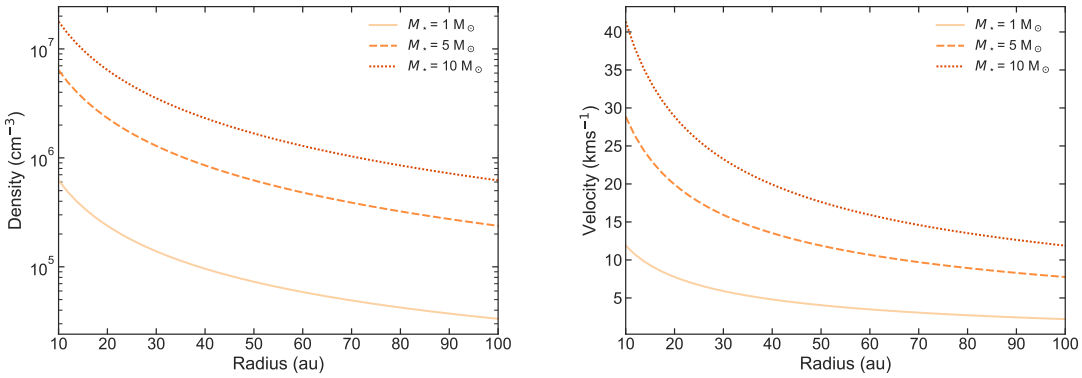

Figure 2.15: The analytic density (*left*) and velocity (*right*) profiles of Bondi accretion onto three different stellar masses, assuming $n = 30000$ cm^{-3} at the neutral Bondi radius and a neutral sound speed of ~ 2 km s^{-1}. In this scenario each mass, $M_\star = 1$, 5 and 10 M$_\odot$, corresponds to a different Bondi radius; ~ 111, 555 and 1109 au respectively.

mass $M_\star$ and the cell of mass $M_{\rm cell}$, separated by a distance r:

$$F_{\rm G} = -\frac{GM_\star M_{\rm cell}}{r^2}\hat{r}, \tag{2.47}$$

where G is the gravitational constant, or as the rate of change of momentum:

$$F_{\rm G} = \frac{{\rm d}M_{\rm cell}v}{{\rm d}t}. \tag{2.48}$$

Using both representations I can express the source term used in the conservation of momentum equation, i.e. the change in momentum density over time due to gravity, as:

$$S_{\rho v} = \frac{\Delta(\rho\vec{v})}{\Delta t} = -\frac{GM_\star\rho}{r^2}\hat{r}. \tag{2.49}$$

Integrating the gravitational force gives a change in energy due to gravity:

$$\Delta E_{\rm G} = \int \vec{F_G}\cdot d\vec{r}. \tag{2.50}$$

Transforming this into a change in energy density over time gives the source term used in the conservation of energy equation:

$$S_e = \frac{\Delta e}{\Delta t} = \frac{GM_\star\rho}{r^2}\hat{r}\cdot\frac{{\rm d}\vec{r}}{{\rm d}t} = \frac{GM_\star}{r^3}\vec{r}\cdot\rho\vec{v}. \tag{2.51}$$

$M_\star$ ($M_\odot$)	n_B (cm^{-3})	T_n (K)	$c_{s\,n}$ (km s^{-1})	Inner mask (au)	Outer mask (au)	Grid cells -
17.87	30000	500	2.0	10.4	38.0	128^3

Table 2.1: Steady state Bondi accretion setup. Columns show stellar mass, number density at the neutral Bondi radius, neutral temperature, neutral sound speed, radii of inner and outer mask and number of grid cells.

This treatment of the gravitational force exerted by the central star on each cell is included in all subsequent rad-hydro simulations presented in this thesis. Any gravitational effect of the surrounding gas on the star is neglected, which results in the star remaining stationary throughout the simulation. This is fine in the case of spherically symmetric simulations.

As a consequence of this inclusion of gravity, the density and velocity of surrounding material increases and their radial profiles become progressively steeper as you approach the central gravitational source. To avoid the problem of a central singularity the source is placed inside a spherical mask. I assume any material passing through the mask finds its way onto the central gravitational source, but I do not consider how this happens. A second mask is introduced around the edges of the simulation box to transform it from a cube to a sphere, this is done to avoid asymmetrical effects. All variables inside both masks are kept fixed throughout the simulation. What is left is a spherical shell between the two masks where the hydrodynamics are allowed to evolve.

The simulation box size is $x,\ y,\ z \in [-40, 40]$ au, with the box being divided into 128^3 grid cells. The inner spherical mask has a radius of 10.4 au and the outer mask is the region outside a radius of 38.0 au. The magnitude of the density and velocity inside the inner mask is set to equal those at the mask boundary ($r = 10.4$ au) predicted analytically by Bondi accretion. The density and velocity of the outer mask however changes with radius, following the analytic Bondi profiles. To calculate the density and velocity of Bondi accretion as a function of radius (Equations 2.45 and 2.46) it is necessary to know the mass of the central attracting object, a star in this case $M_\star$, the neutral sound speed, and the number density n_B at the neutral Bondi radius. The variables used in the setup for this simulation are listed in Table 2.1. The mass of the central star is 17.87 $M_\odot$, the number density at the neutral Bondi radius is 30000 cm^{-3}, and the neutral gas has a temperature of 500 K, which corresponds to a sound speed of $\sim$ 2.0 km s^{-1}.

The region between the two masks starts with zero velocity and a density matching the density at the boundary of the outer mask. It is then allowed to evolve in time with the gravitational pull of the central star being the only force present. The simulation reaches a steady state with inflowing material which perfectly matches the analytic Bondi accretion solution. Figure 2.16 shows the radially averaged densities and velocities from the simulation plotted over the analytic solution. As I am able to reproduce the Bondi profile perfectly, this will be the starting point for all simulations presented in Chapter 3.

2.6 Conclusions

The tests show the combined rad-hydro code is capable of producing both D-type and R-type ionisation fronts in cases with negligible gravity. Furthermore gravity is successfully integrated to the code and produces the expected inflows of material towards a central non-ionising source. The next step is putting both aspects together, simulating simultaneously the gravitational pull and ionisation of a high-mass star, see Chapter 3.

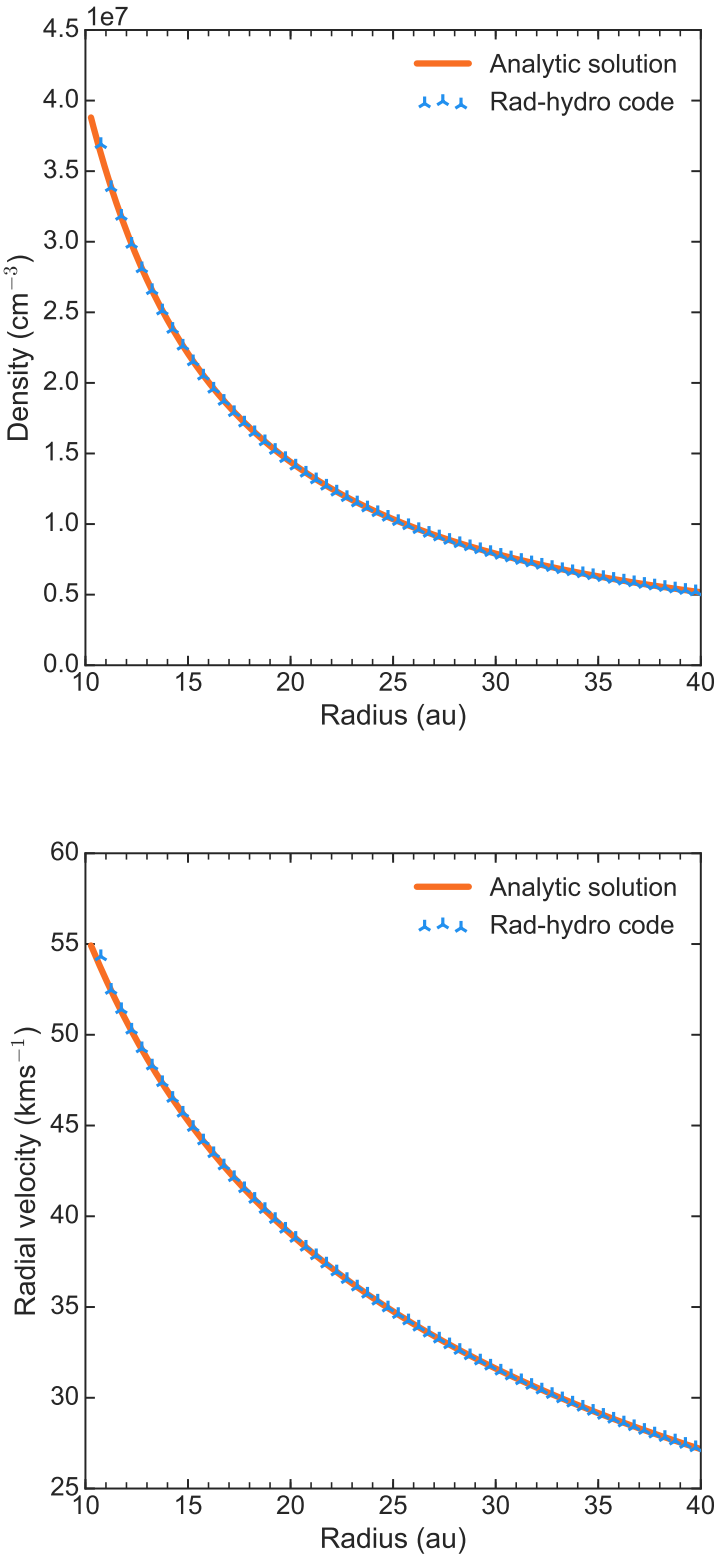

Figure 2.16: Radially averaged steady-state density (*top*) and inflow velocity (*bottom*) from the rad-hydro simulation of material accreting onto a central source compared to the analytic Bondi accretion solution (Equations 2.45 and 2.46).

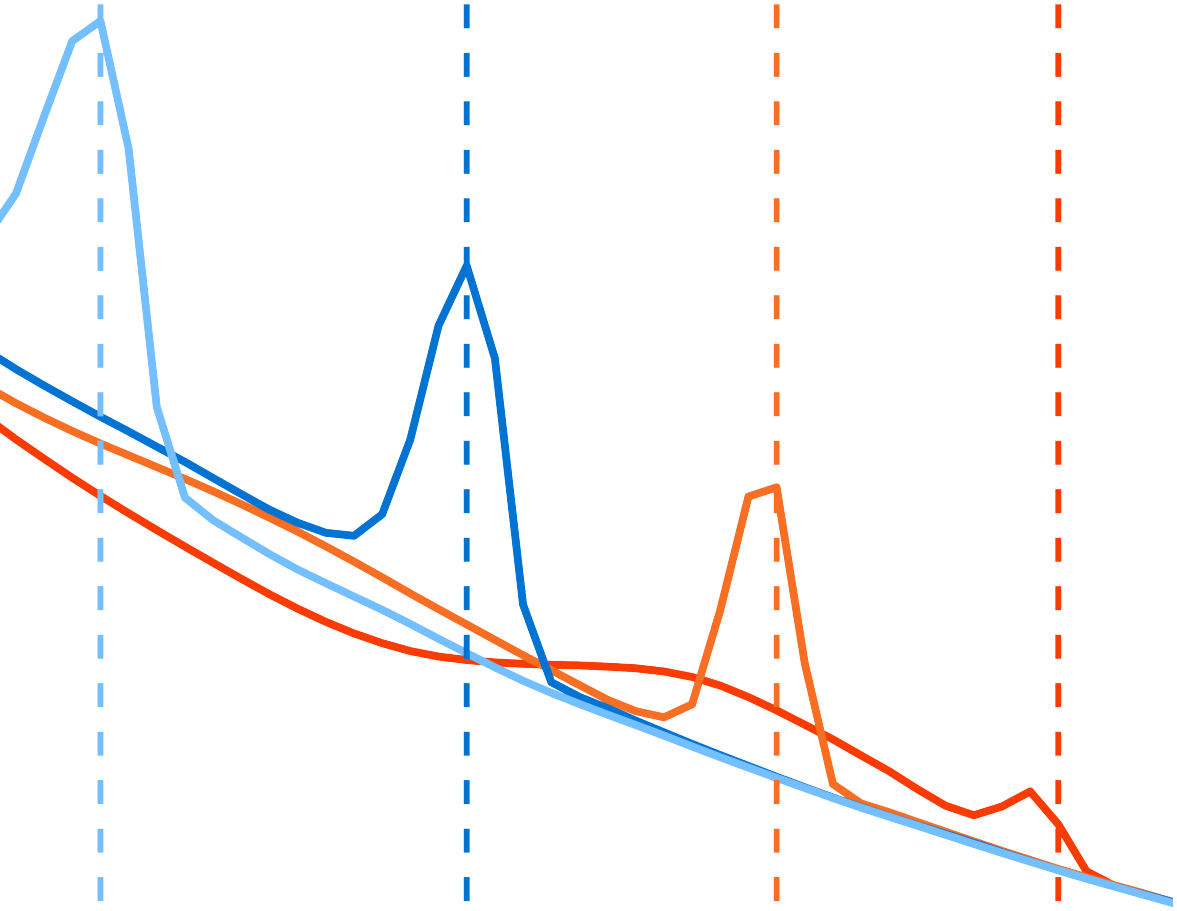

3

The formation of high-mass stars via gravitationally trapped HII regions

This chapter is based on Lund et al. (2019). The concept of gravitational trapping of newly formed HII regions is first described, this is a stage of the HII region evolution predicted by steady-state analysis. Next I present the first ever numerical simulations of this scenario, using the rad-hydro code described in Chapter 2. The stability of the gravitationally trapped HII region is explored, as well as the end of the trapping stage. Furthermore the chapter extends the work in Lund et al. (2019) by discussing the resulting implications for UCHII region lifetime estimates.

3.1 Introduction

As high-mass stars grow through accretion their luminosity increases accordingly, and eventually they reach the point where their stellar radiation is energetic enough to ionise the surrounding medium, for details on the ionisation process see Section 1.2. Broadly speaking the classical treatment of the development of a HII region is to assume a pressure-driven expansion, where the gravity of the source is completely neglected, see for instance Spitzer (1978). At late times when the ionisation front is at a large distance from the stellar source the assumption that gravity plays no part is good, since gravitational attraction at these size scales is small compared to the pressure driving expansion. Hence it is possible to successfully model the dynamics and structures of older systems where the HII regions are large. However a potentially problematic consequence of neglecting gravity throughout the life of a HII region is that it implies accretion stops as soon as the HII region appears. Meaning in this scenario ionising stars must have reached their final mass before they initiate nuclear burning and enter the main sequence. However, observations of infalling material coincident with UCHII regions (He et al., 2015) suggests accretion onto a massive star continues after the star begins nuclear burning. Radio recombination lines and kinematic arguments are used to determine the direction of movement of ionised material. Several observations support the presence of ionised accretion flows (Keto, 2002a; van der Tak & Menten, 2005; Sollins & Ho, 2005), and show simultaneous inflow and outflow of material (Sollins et al., 2005; Klaassen & Wilson, 2007; Klaassen et al., 2018). Ionised material moving towards the central source can only be explained by the gravity of the source dominating the gas dynamics, this suggests we cannot neglect gravity when describing the early evolution of HII regions.

In this chapter I present numerical simulations of a star with gravitational pull and ionising radiation. Based on such simulations I explore the possibility of high-mass stars growing via ionised accretion flows moving through gravitationally trapped HII regions.

3.2 Gravitationally trapped HII regions

Mestel (1954) and later Keto (2002a,b) examined the early evolution of spherically symmetric HII regions, taking the effect of gravity into account. The result was three proposed evolutionary stages: quenching, trapping and expansion. These three stages are illustrated in Figure 3.1, and a brief description of each stage follows.

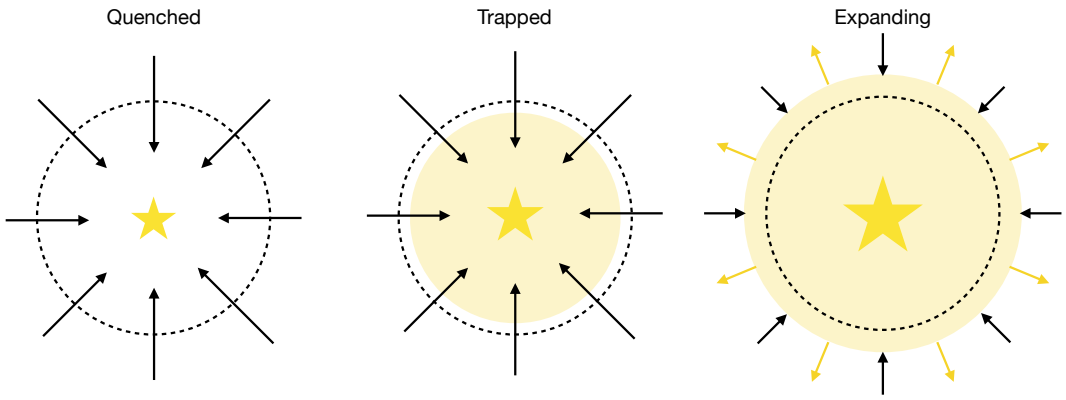

Figure 3.1: The three stages of evolution of HII regions: quenched, trapped and expanding. The black dotted line shows the ionised sonic point, at which the infall velocity equals the ionised sound speed. This is the critical radius for gravitational trapping. The HII region is shown in yellow, the black arrows show movement of accreting material and the yellow arrows show pressure-driven movement of the ionisation front. When the HII region is non-existent or within the critical radius material accretes onto the star. When the HII region is outside the critical radius it experiences a pressure-driven expansion and material cannot flow across the ionisation front. Note the HII region can still grow whilst it is in the trapped stage, but this is not a pressure-driven expansion, it is due to an increase in luminosity.

Quenching: When the ionising luminosity of the star is low, the rate of inflow of accreting material can overwhelm the flux of ionising photons (Walmsley, 1995). In which case no HII region is present, and it is called "quenched".

Trapping: When the HII region first forms, its ionisation equilibrium radius is directly outside the ionising star. At this size scale the gravitational attraction dominates over the outward pressure of the ionised region. The HII region is trapped by gravity, and material is allowed to accrete through the HII region and onto the star, forming an ionised accretion flow. As accretion continues the star grows in mass and ionising luminosity, and the radius of the ionisation equilibrium will increase accordingly, see Equation 1.16. It is important to note this growth of the HII region is not a pressure-driven expansion, but purely a result of the increased luminosity, and the HII region is still classified as trapped.

Expansion: As the ionisation front moves further from the star the velocity of the accretion flow passing through it decreases, since the gravitational force is weaker further from the star. Once the ionisation front reaches the ionised sonic point gravity no longer dominates over the thermal pressure. At this critical point the HII region transitions from being gravitationally trapped to the expansion stage of its evolution. The ionisation front now experiences a pressure-driven expansion, and accretion through the HII region ceases. Already ionised ma-

terial within the HII region can still accrete onto the star, but once the region is drained all accretion stops.

Some amendments to this are required when considering HII region evolution in more realistic axisymmetric rotationally flattened structures (Keto, 2007). When the star is surrounded by a high density disk the resulting HII region will not be spherical, but instead it will expand faster into the lower density regions (as was the case for the flow past a radiative source in section 2.5.2), creating a bipolar outflow. Material can still flow onto the star through the plane of the disk. If the disk is dense enough to be shielded completely from radiation molecular gas is accreted (Nakano, 1989; Yorke & Sonnhalter, 2002; Krumholz et al., 2009; Kuiper et al., 2010; Harries et al., 2017; Kuiper & Hosokawa, 2018), if the disk becomes partially ionised accretion can continue as long as the ionisation front is within the critical radius. Similar to the spherical case accretion stops once the ionisation front in the midplane passes beyond the critical radius. This scenario is in agreement with the observations showing simultaneous inflow and outflow from high-mass stars (Sollins et al., 2005; Klaassen & Wilson, 2007; Klaassen et al., 2018).

Despite real stars being embedded in rotating systems this chapter will only consider spherically symmetric systems. This simplified geometry is sufficient for investigating the feasibility of gravitationally trapped HII regions and it allows for a simple analytic description.

3.2.1 Analytics

The dynamics during the trapped phase can be described analytically for a spherically symmetric system by modifying the solution for Bondi accretion, described in Section 2.5.3. A transition from neutral to ionised material during the infall is required, with a matching temperature change. The work done by Mestel (1954) and Keto (2002a,b) on this so called two-temperature steady state accretion was recently extended by Vandenbroucke et al. (2019), who gives full analytic expressions for the resulting density and velocity profiles. A general outline of these expressions follows, note they assume an R-type ionisation front, for a detailed derivation see Vandenbroucke et al. (2019).

The neutral material outside the ionisation front follows the classic Bondi accretion profile as it has no knowledge of the HII region it is approaching. At the ionisation front, represented by the radius $R_{\rm IF}$, a sharp transition from neutral to ionised gas is assumed. The density and

velocity profiles in both regions are given by:

$$\rho_{\rm n}(r) = \frac{\rho_{\rm B\,n} R_{\rm B\,n}^2 c_{\rm s\,n}}{r^2 v_{\rm n}(r)} \quad r > R_{\rm IF}, \tag{3.1}$$

$$\rho_{\rm i}(r) = \frac{\rho_{\rm i}(R_{\rm IF}) R_{\rm IF}^2 v_{\rm i}(R_{\rm IF})}{r^2 v_{\rm i}(r)} \quad r < R_{\rm IF}, \tag{3.2}$$

$$v_{\rm n}(r) = \begin{cases} c_{\rm s\,n}\sqrt{-W_{-1}\left(w_{\rm n}(r)\right)} & r \leq R_{\rm B} \text{ and } r > R_{\rm IF}, \\ c_{\rm s\,n}\sqrt{-W_{0}\left(w_{\rm n}(r)\right)} & r > R_{\rm B} \text{ and } r > R_{\rm IF}, \end{cases} \tag{3.3}$$

$$v_{\rm i}(r) = c_{\rm s\,i}\sqrt{-W_{-1}\left(w_{\rm i}(r)\right)} \quad r < R_{\rm IF}, \tag{3.4}$$

with

$$w_{\rm n}(r) = -\left(\frac{R_{\rm B\,n}}{r}\right)^4 \exp\left(3 - 4\frac{R_{\rm B\,n}}{r}\right), \tag{3.5}$$

$$w_{\rm i}(r) = -\left(\frac{R_{\rm IF}}{r}\right)^4 \left(\frac{v_{\rm i}(R_{\rm IF})}{c_{\rm s\,i}}\right)^2 \exp\left(4\frac{R_{\rm B\,i}}{R_{\rm IF}} - 4\frac{R_{\rm B\,i}}{r} - \frac{v_i^2(R_{\rm IF})}{c_{\rm s\,i}^2}\right). \tag{3.6}$$

All the same symbols have the same meaning as in Section 2.5.3, where the Bondi profile is described, except for subscripts "i" and "n" referring to ionised and neutral respectively. $\rho_{\rm i}(R_{\rm IF})$ and $v_{\rm i}(R_{\rm IF})$ relate to the neutral Bondi accretion profile at the ionisation front through the jump conditions:

$$\rho_{\rm i}(R_{\rm IF}) = \Gamma \rho_{\rm n}(R_{\rm IF}), \tag{3.7}$$

$$v_{\rm i}(R_{\rm IF}) = \frac{v_{\rm n}(R_{\rm IF})}{\Gamma}, \tag{3.8}$$

where

$$\Gamma = \frac{1}{2}\left(\frac{v_{\rm n}^2(R_{\rm IF})}{c_{\rm s\,i}^2} + \frac{c_{\rm s\,n}^2}{c_{\rm s\,i}^2} - \sqrt{\left(\frac{v_{\rm n}^2(R_{\rm IF})}{c_{\rm s\,i}^2} + \frac{c_{\rm s\,n}^2}{c_{\rm s\,i}^2}\right)^2 - 4\frac{v_{\rm n}^2(R_{\rm IF})}{c_{\rm s\,i}^2}}\right). \tag{3.9}$$

By assuming an R-type ionisation front with $v_{\rm n}(R_{\rm IF}) \geq v_{\rm R}$, $\Gamma > 1$ is guaranteed, meaning the velocity drops and the density jumps at the ionisation front when going from neutral to ionised.

The full two-temperature accretion profile described in Equations 3.1-3.4 is fully defined in terms of the mass of the central star $M_\star$ (via the Bondi radius, see Equation 2.44), the position of the ionisation front $R_{\rm IF}$, the density at the neutral Bondi radius $\rho_{\rm B\,n}$ and the neutral and ionised sound speeds $c_{\rm s\,n}$ and $c_{\rm s\,i}$. An example of a two-temperature accretion profile going from neutral to ionised at 24.74 au is plotted in Figure 3.2, calculated using the parameters

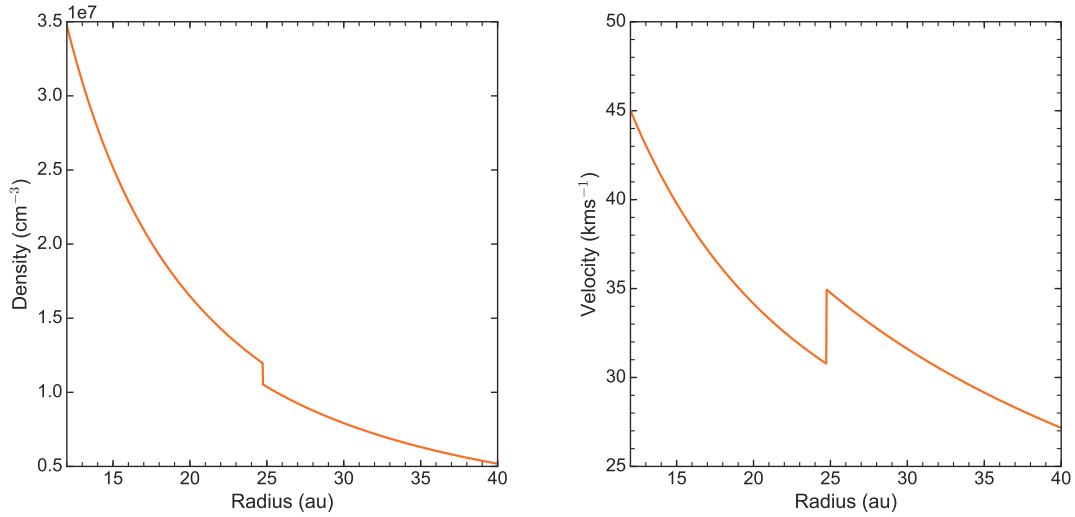

Figure 3.2: Analytic two-temperature accretion density (*left*) profile and velocity (*right*) profile. The central star attracting material is 17.87 $M_\odot$ and the surrounding gas transitions from ionised to neutral at 24.74 au.

listed in Table 3.1.

3.3 Results

The work on gravitationally trapped HII regions have until now been purely analytic. Using the rad-hydro code presented in Chapter 2, I explore the topic using numerical simulations. By simulating spherically symmetric accretion onto an ionising star, the result can be compared to the analytic prediction of a two-temperature accretion profile. This is the first numerical test of the analytic model and an important first step towards more complex fully 3D simulations of ionised accretion.

3.3.1 Setup

Every scenario simulated in this chapter is spherically symmetric, essentially making the 3D simulations 1D, with properties varying along the radial direction. As in Section 2.5.3 an inner mask is applied around a central star and an outer mask is applied to make the simulation region spherical. The size scale of the simulated region will be specified separately for each simulation.

The central star has a mass of 17.87 $M_\star$, the gas number density at the neutral Bondi

$M_\star$ ($M_\odot$)	n_B (cm^{-3})	T_n (K)	c_{sn} (km s^{-1})	T_i (K)	c_{si} (km s^{-1})	Grid cells -
17.87	30000	500	2.0	8000	11.5	128^3

Table 3.1: Basic simulation properties. Columns show, respectively, stellar mass, number density at the neutral Bondi radius, neutral temperature and sound speed, ionised temperature and sound speed and number of grid cells.

radius is 30000 cm^{-3}, the temperature of the neutral gas is 500 K with a sound speed of $\sim$ 2.0 km s^{-1} and the material in the simulated region between the two spherical masks is initially specified as fully neutral and following the corresponding Bondi accretion profile. Infalling material is defined as having a positive radial velocity. At the start of each simulation the ionising luminosity of the central star is switched on. The ionising luminosity differs for each simulation, but in all cases the temperature of fully ionised gas increases from the neutral 500 K to 8000 K, corresponding to a sound speed of $\sim$ 11.5 km s^{-1} and an R-critical velocity of $v_R \approx$ 23.0 km s^{-1}. These parameter values are summarised in Table 3.1, and are used for all simulations in this chapter.

The stellar mass and luminosity are not updated during the simulations as a result of accretion because any change would be minuscule. The rate of spherical inflow of material, given by Equation 2.43 can be calculated at any point along the Bondi profile as $\sim 4 \times 10^{-7}$ $M_\odot$ yr^{-1}, which implies a timescale of megayears to accrete 1 $M_\odot$ of material onto the star. Considering the simulations run over tens to hundreds of years any significant change in mass and luminosity will occur over timescales much greater than those investigated here. Consequently exploring the evolution of the system from the early stage of a HII region to the point where the ionising luminosity is strong enough for the HII region to pass the critical radius for gravitational trapping in a single simulation is not feasible. Instead I take a piece-wise approach, simulating the early and the late stage of the evolution separately over relatively short periods of time.

3.3.2 Early stage: accretion onto a source with constant ionising luminosity

As I am interested in an early stage of the HII region evolution, where it falls well within the critical radius for gravitational trapping, the size scale of this simulation is chosen such

as to capture infall velocities exceeding the R-critical value of $\approx$ 23.0 km s^{-1}. Specifically $x,\ y,\ z \in [-40, 40]$ au, with each direction being divided into 128 cells. The inner and outer masks have radii of 10.4 and 38.0 au respectively.

Starting from a stable Bondi accretion structure I turn on radiation of a fixed luminosity from the central star. An ionising luminosity of $Q = 2.5 \times 10^{46}$ s^{-1} is chosen, such that the star initially ionises material out to a radius of $\sim$ 32 au. Notice that, because of the use of an internal mask, the value of Q in the simulations corresponds to the ionizing photon luminosity escaping the mask, and not the total stellar luminosity. By considering the complete ionization of the gas within the inner mask, I find Q corresponds to $\sim$ 3% of the central source ionizing luminosity. The total central source ionizing luminosity implied by the Q value is in agreement with what is expected from a $\sim 18 M_\odot$ star (Vacca et al., 1996).

Figure 3.3 shows the resulting radius of the ionised region as a function of time. When the stellar radiation is first turned on it ionises a region out to $\sim$ 32 au, but then the ionisation front proceeds to shrink until it disappears within the inner mask and then moves back out. This process recurs on a 7 year timescale.

To get a better picture of what is happening during this 7 year cycle four snapshots of the density and velocity profile of the system at different times during the first collapse of the HII region is plotted in Figure 3.4. The different colours correspond to different times and the vertical lines mark the ionisation radius. There is a growing density peak around the ionisation radius which moves inward as the HII region shrinks. The appearance of an initial density perturbation can be explained by considering the jump conditions across the ionisation front. Given $v_n \geq v_R \gg c_n$ the ionised to neutral density ratio, Equation 1.26, is always positive.

The increase in density leads to an increased recombination rate, meaning the fixed ionising luminosity cannot ionise to the same radius at the next time step of the radiation hydrodynamics simulation. Material keeps piling up at the front and the density increases because the inflow velocity of material is greater outside the ionised region than inside. As the density peak grows the ionisation radius must shrink further, resulting in the runaway behaviour shown in Figure 3.4.

When the ionisation front and the density enhancement reaches the inner mask we assume it accretes onto the central star. As the density peak disappears inside the mask the amount of

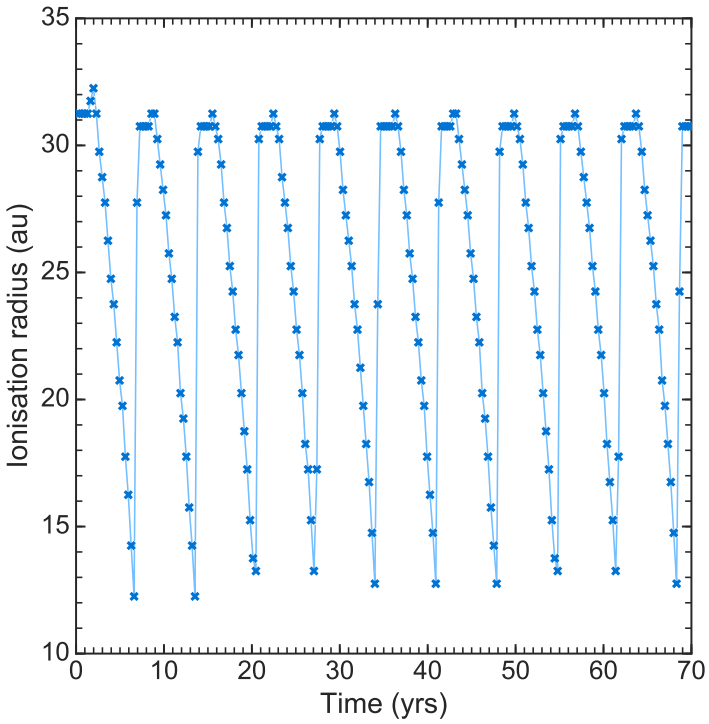

Figure 3.3: Ionisation front radius as a function of time during the simulation of a 17.87 $M_\odot$ central star with constant ionising luminosity of $Q = 2.5 \times 10^{46}$ s^{-1}. Zero years marks the moment radiation is switched on.

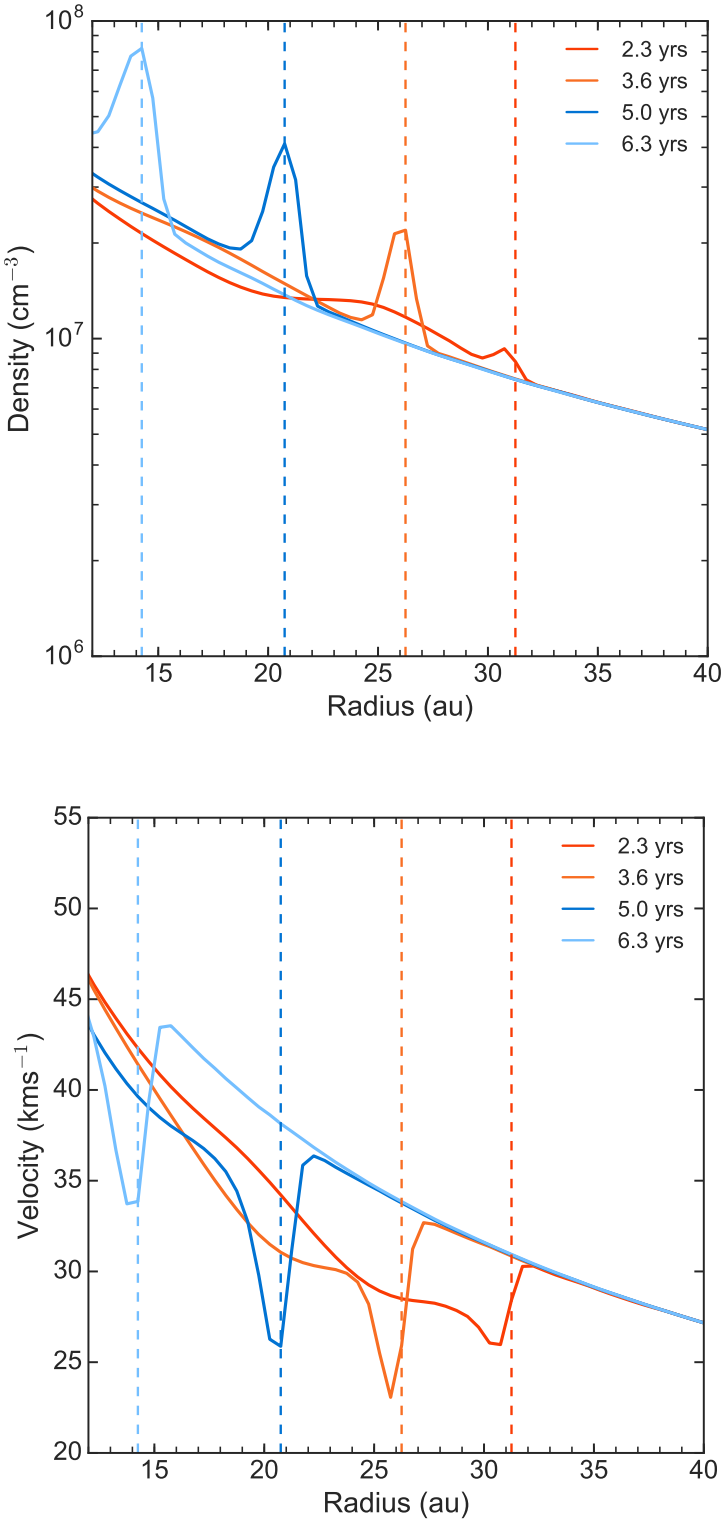

Figure 3.4: Density (*top*) and inflow velocity (*bottom*) at four different times during the simulation of an 17.87 $M_\odot$ central star with constant ionising luminosity of $Q = 2.5 \times 10^{46}$ s^{-1}. The vertical lines represent the position of the ionisation front. Zero years marks the moment radiation is switched on.

material inside the ionised region decreases drastically and in response the ionisation front expands. The region outside the ionisation front has returned to a neutral Bondi profile, meaning the problem is essentially reset and the process repeats. For the parameters of this simulation, the HII region oscillates from just outside the inner mask to a maximum radius $R_{\rm max} \approx 31$ au over a regular period of ~ 7 yrs.

According to the three stages of HII region evolution proposed by Mestel (1954) and Keto (2002b, 2003), if the initial HII region starts out close enough to the star for the ionisation front to be of the R-type, such as in this simulation, it would be gravitationally trapped. There would be no expansion of the HII region, and accretion would continue with material moving through the ionised region. The numerical simulation shows continuous accretion of material onto the star as predicted, and successfully traps the HII region within a radius $R_{\rm max}$, but the recurring expansion and contraction indicates it is not a steady state solution. Further investigation into this instability was performed by Vandenbroucke et al. (2019) and is described in Section 3.4.1.

3.3.3 Early stage: accretion onto a source with a constant ionisation radius

In the previous section the code produced a gravitationally trapped, but oscillating, HII region. In an attempt to produce a steady state two-temperature accretion flow, the next simulation forces the ionisation radius to remain constant.

The simulation is again started from the stable neutral Bondi accretion flow, and all parameters match those in Section 3.3.2 except for the luminosity. Instead of switching on a constant ionising luminosity at the start of the simulation, the ionising luminosity is calculated before each call to the radiation transfer scheme to be whichever value that will fully ionise gas out to a radius $R_{\rm IF} = 24.75$ au. The luminosity value is determined by balancing photoionisation with radiative recombination inside the radius $R_{\rm IF}$:

$$Q_{R_{\rm IF}} = \Sigma n^2 \alpha_B V_{\rm cell}. \tag{3.10}$$

The sum is over all cells with a radius $r \leq R_{\rm IF}$, n is the number density of the cell, $\alpha_B = 3.26 \times 10^{-13}$ cm^3 s^{-1} is the Case B recombination coefficient for hydrogen at 8000 K, and $V_{\rm cell}$ is the volume of each cell.

At the beginning of the simulation, there is an initial density peak directly within the ioni-

sation radius, as was the case in the previous simulation. However this time around, because the size of the ionised region is kept constant, the peak does not grow and move inwards, instead the entire ionised region increases in density over time. In the case of this particular simulation it took $\sim$ 3 yrs for the system to settle into a stable profile. In Figure 3.5 the final result from the numerical simulation is overplotted on the analytic solution from Section 3.2.1 for a steady state two-temperature Bondi accretion, with the vertical line indicating the position of the ionisation front. The plot shows the rad-hydro code is able to produce an accretion profile which closely follows the analytics.

Figure 3.6 shows how the calculated ionising luminosity changes as a function time, with year 0 marking the point when the radiation is switched on. Whilst the higher density region builds up from the neutral Bondi profile, the luminosity required to ionise the region increases. Once the steady state is reached after $\sim$ 3 yrs the luminosity stays at an almost constant value. If I were to stop calculating the luminosity, and keep it constant once the steady-state solution is reached, in time the simulation would return to the oscillatory behaviour seen in the previous section. This is due to numerical noise in the rad-hydro code, whereas previously the oscillations were triggered by a density perturbation resulting from a sudden ionisation.

In conclusion the only way of reaching a steady-state two-temperature accretion profile is through careful fine-tuning of the ionising luminosity. The ionising luminosity needs to be adjusted, not just during the build up of the two-temperature profile, but also after the solution is reached. This suggests the steady-state two-temperature accretion profile is not in fact a stable state. Any small fluctuation, including any caused by numerical noise, is enough to return the system to the cyclic behaviour of an expanding and contracting HII region.

3.3.4 Late stage: the end of accretion onto an ionising source

As material accretes onto stars and they grow in mass, their luminosity is expected to grow correspondingly, meaning they can ionise increasingly larger volumes. As previously mentioned this increase in mass and luminosity happens over greater timescales than those I am able to simulate, hence the evolution of the ionised region is treated piece wise. The first two simulations both considered HII regions close enough to the star for the infall velocity to exceed v_R, where the ionisation front exhibits an R-type behaviour. Once the relative velocity of the ionisation front decreases below v_D it will transition to D-type. At this point gravity is no longer dominant and the ionisation front experiences a pressure-driven expansion. For

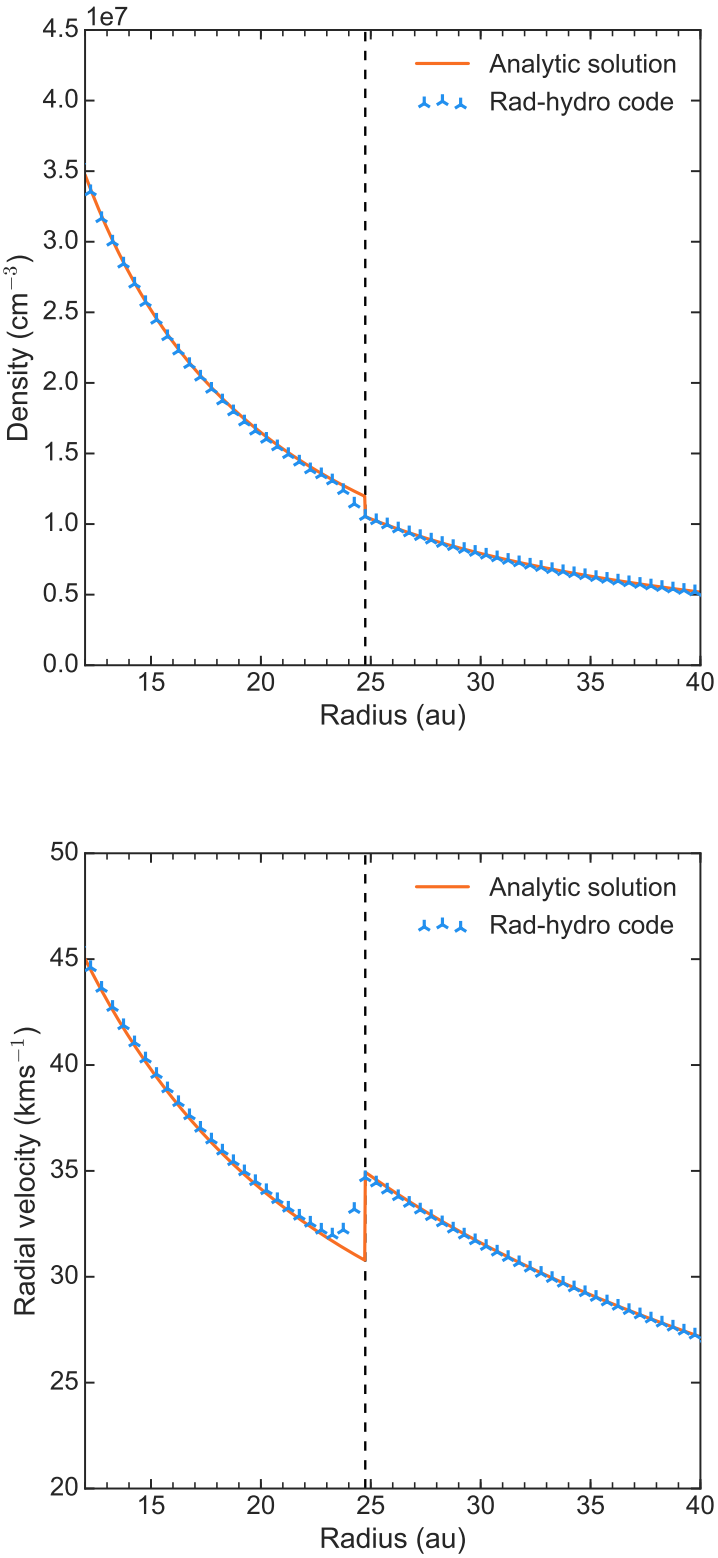

Figure 3.5: Steady state two-temperature density (*top*) and inflow velocity (*bottom*) from the rad-hydro simulation compared to the analytic solution outlined in Section 3.2.1. The simulation forces a HII region out to the fixed radius $R_{\rm IF} = 24.75$ au, and the vertical line represents the position of this ionisation radius.

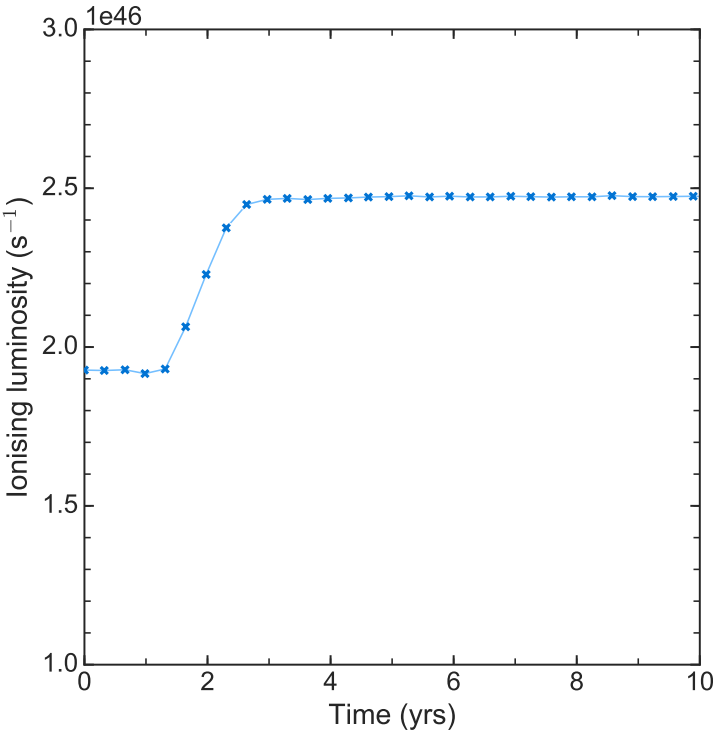

Figure 3.6: Ionising luminosity, Q_{R_i}, required to maintain a HII region out to the fixed radius $R_{\rm IF} = 24.75$ au as a function of time. Zero years marks the moment radiation is switched on.

velocities between v_R and v_D there is no single front solution to the jump across the ionisation boundary, as described in Section 1.2.2.

In order to investigate the evolution of the HII region past the R-critical radius a number of different luminosity values are tested which would all ionise beyond this radius. The size of the simulation box is increased to $x,\ y,\ z \in [-480, 480]$ au, which in turn increases the inner and outer mask radii to 124.8 au and 456.0 au. Simulations show the HII region remains trapped and oscillating past the R-critical radius, until it extends beyond the ionised sonic point, at which point rapid expansion begins and accretion of material through the ionisation front stops.

The sonic point, where the infall velocity equals $c_i = 11.5$ km s^{-1}, is at a radius of ~ 200 au. Setting a luminosity of $Q = 2 \times 10^{46}$ s^{-1} results in an initial ionisation radius of ~ 260 au, exceeding the sonic point. The fact that the luminosity is smaller than that previously needed to ionise out to ~ 30 au is because only material outside the inner mask is being ionised, and as the simulation box is now larger the inner mask is further away from the star and thus the material outside the mask is at a much lower density than before. The actual total luminosity emitted by the star would have had to increase for the corresponding ionisation radius to grow from ~ 30 au to the sonic point. Figure 3.7 shows how, now that the ionisation radius is beyond the sonic point and the HII region is no longer gravitationally trapped, it is expanding with no indication of collapse or halt. The discrete jumps the ionisation front makes every 3-4 time steps is a result of the grid resolution.

Figures 3.8 and 3.9 show the directions of motion of the material in the simulation region at four different time steps, with orange and blue indicating inflow and outflow respectively. Oblivious to the pressure expansion of the HII region, the neutral material moves towards the central star due to gravity just as it would if there was no radiation, until it reaches the expanding dense shell. The shell, along with most of the ionised material it accumulates, moves radially outwards, but close to the star ionised material still accretes. The material inside the HII region is not replenished, since no material crosses the ionisation front now that it is no longer gravitationally trapped, meaning the region is eventually drained and accretion stops.

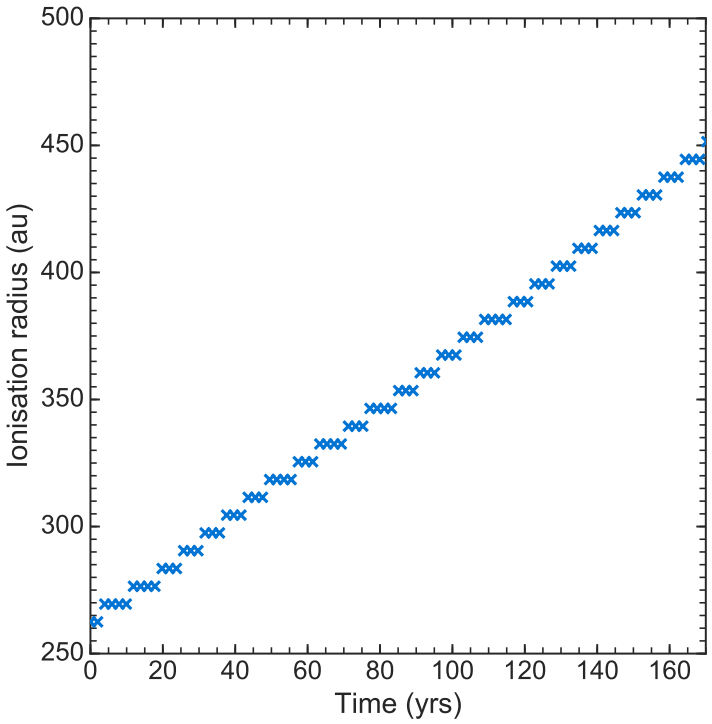

Figure 3.7: Ionisation front radius as a function of time during the late time simulation of a 17.87 $M_\odot$ central star with constant ionising luminosity of $Q = 2 \times 10^{46}$ s^{-1}. Time zero years marks the moment radiation is switched on.

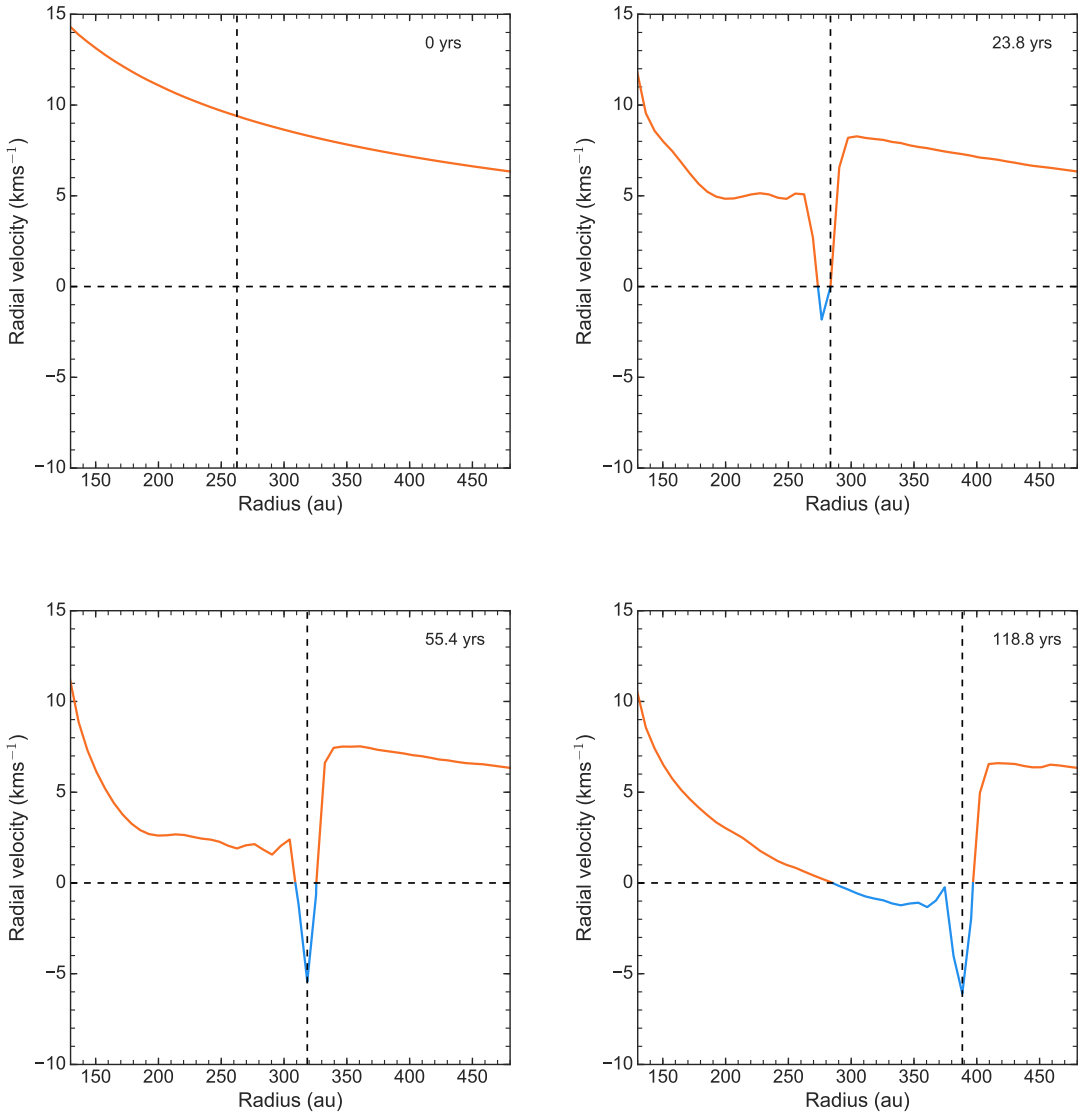

Figure 3.8: The velocity profile at four different times during the late time HII region expansion, a positive radial velocity corresponds to inward motion. Zero years marks the moment radiation is switched on. The simulation models an 17.87 $M_\odot$ central star with a constant ionising luminosity of $Q = 2 \times 10^{46}$ s^{-1}, large enough for the ionisation radius to exceed the ionised sonic point ($\sim$ 200 au). The vertical line represents the position of the ionisation front. The horizontal line marks zero velocity, the point across which the velocity changes direction. The profile is orange where the velocity points towards the central star, and blue where the velocity points away from the star.

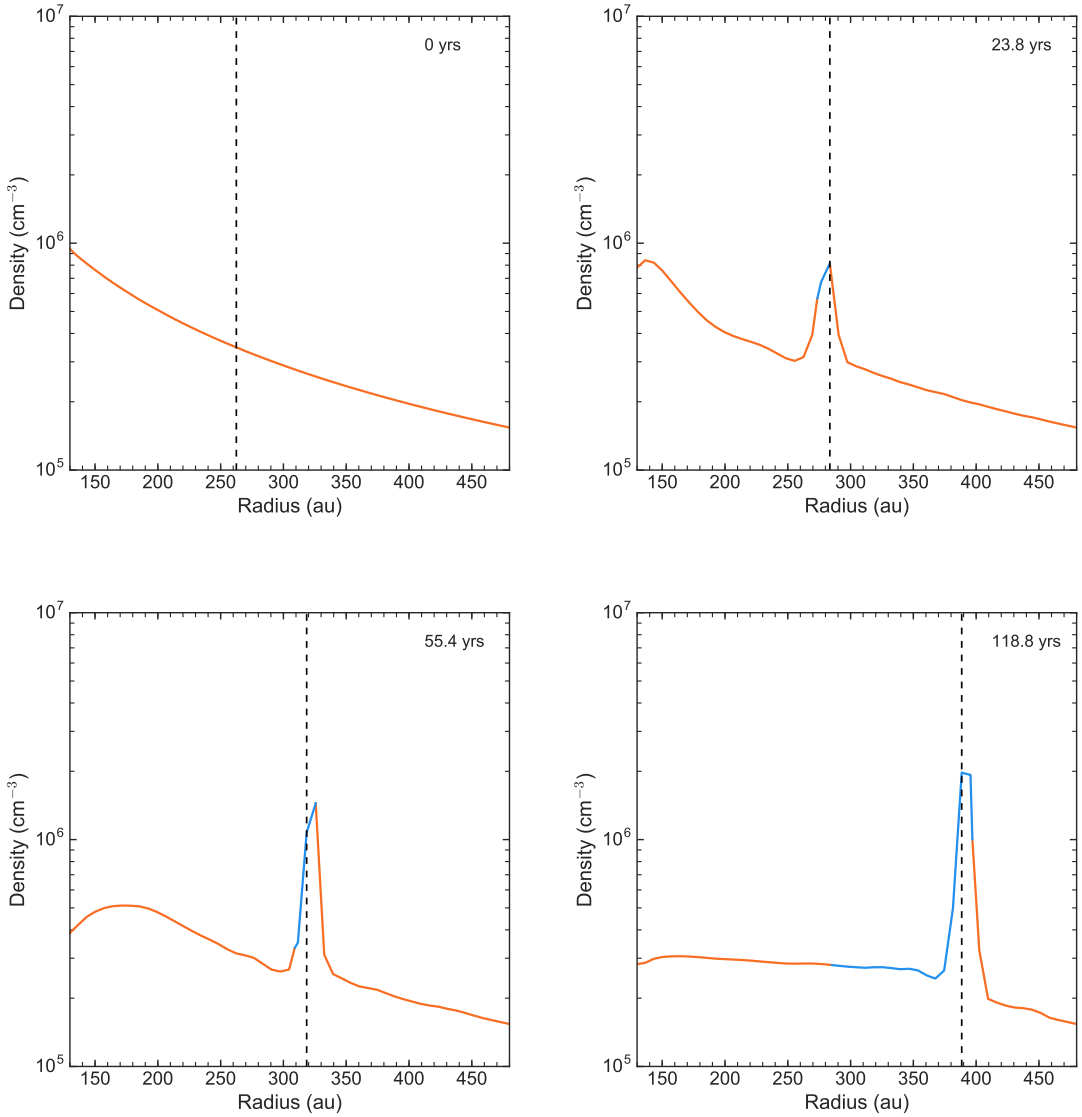

Figure 3.9: The density profile at four different times during the late time HII region expansion. Zero years marks the moment radiation is switched on. The simulation models an 17.87 $M_\odot$ central star with a constant ionising luminosity of of $Q = 2 \times 10^{46}$ s^{-1}, large enough for the ionisation radius to exceed the ionised sonic point ($\sim$ 200 au). The vertical line represents the position of the ionisation front. The profile is orange where the velocity points towards the central source, and blue where the velocity points away from the source.

3.4 Discussion

3.4.1 Stability analysis of spherically symmetric ionised accretion flows

Simulations presented in this chapter reveal an oscillating behaviour of the HII region during the gravitationally trapped phase; first in the case of a fully neutral medium being ionised by

a constant luminosity, and later when a steady state two-temperature profile is exposed to a constant luminosity. Following up on this discovery Vandenbroucke et al. (2019) performed tests of the stability of spherically symmetric ionised accretion flows, and found that the two-temperature steady state Bondi profile described by Keto (2002b) is only a marginally stable solution.

Starting from the analytic expression for the two-temperature steady state solution, with some lower cut off radius similar to the central mask used in my simulations, the stability of the solution was tested by perturbing the density outside the ionisation radius and predicting the resulting evolution of the system. The density perturbation would move towards the central source and eventually enter the ionised region, consequently the position of the ionisation front will change. A positive perturbation, meaning a density enhancement, would cause the ionisation front to move closer to the source whereas a negative perturbation, i.e. a dip in density, would cause it to move further away from the source. There is no restoring force present to balance the effect of the perturbation and cause the ionisation front to return to its starting point. Once the perturbation disappears past the inner cut off radius the density profile left behind will essentially have created a new density perturbation of the opposite sign. For instance, when introducing an initial negative density perturbation the ionisation front will move outwards, ionising material at larger radii which in turn results in an increase in the density at this radii. Once the negative perturbation passes the inner cut off radius this density increase represents a new positive perturbation when comparing to the initial two-temperature steady state Bondi profile. In fact, any small perturbation would lead to another, resulting in an oscillating ionisation radius.

Vandenbroucke et al. (2019) point out that the timescale of the oscillation, i.e. the time it would take a perturbation to accrete onto the central mask from the initial ionisation radius, is of the order of the local free-fall time at the initial ionisation radius:

$$t_{\mathrm{ff}} = \sqrt{\frac{2R_{\mathrm{IF}}^3}{GM}}. \tag{3.11}$$

The simulation presented in Section 3.3.3 showed a HII region which was oscillating between an outer radius of ~ 32 au and the inner mask on a timescale of approximately 7 yrs. Using the simulation parameters the local free fall time at $R_{\mathrm{IF}} \sim 32$ au can be calculated as approximately 9 yrs, which is not far off the observed oscillation timescale.

The paper proceeds to simulate 1D spherically symmetric ionised accretion flows using various rad-hydro codes, including a time-dependent code and TORUS (Harries, 2000, 2014; Haworth et al., 2015). For all codes periodic HII region shrinkage and reappearance matching the predictions is observed. This verifies my result and shows this oscillating feature is not specific to my rad-hydro code. Furthermore it is worth mentioning that the oscillation is stated as appearing regardless of whether a perturbation is seeded manually or not, which is also what my simulation in Section 3.3.3 showed. After building up a steady state two-temperature profile, as I stop forcing an ionisation radius and keep the luminosity constant the HII region collapses and begins oscillating. The perturbation in this case is a result of numerical noise, e.g. accumulated round off error in the code. Hence the steady state two-temperature profile is only marginally stable, with the tiniest of numerical noise triggering its collapse.

Interestingly, Vandenbroucke et al. (2019) reports the recurring expansion and contraction of the HII region seems to be a result of the idealised spherically symmetric geometry, and in fully 3D simulations the same behaviour is not observed. When modelling the same scenario in full 3D using the rad-hydro code CMACIONIZE (Vandenbroucke & Wood, 2018b,a) they find the 1D instability inevitably leads to the ionisation front breaking away from the initial spherical symmetry into an asymmetric shape. Consequently the regular expansion and contraction of the HII region is not a behaviour I would expect to see in any 3D simulation, or in real life observations.

3.4.2 Ultra-compact HII regions: the lifetime problem

The simulations presented in this chapter show both trapped and expanding HII regions. The transition point from trapped to expanding can be used to estimate the time scale of the UCHII region phase. As mentioned during the discussion of UCHII regions in Section 1.2.3 observations suggest the lifetime of UCHII regions must exceed 10^5 yrs, which is longer than the time it would take an UCHII region to evolve into a diffuse HII region through pressure-driven expansion alone (Wood & Churchwell, 1989b). Including a gravitationally trapped stage before the pressure-driven expansion phase begins will increase the total lifetime estimate of UCHII regions. In fact since the trapped period is when the HII region is expanding most slowly this is the phase which will dominate the total lifetime.

Starting from the same central star and neutral Bondi profile as presented in Section 3.3.2 (parameters listed in Table 3.1) I apply an iterative method to determine how much the mass

and luminosity of the star will need to grow before the ionisation front reaches the ionised sonic point. It has to be done iteratively because as soon as the mass of the star increases the Bondi accretion profile changes, along with the position of the ionised sonic point. Broadly speaking the steps of the process are as follows:

1. Assign an initial stellar mass and an initial luminosity.
2. Calculate the neutral Bondi profile corresponding to the current stellar mass.
3. Calculate the luminosity required to ionise along the Bondi profile from the inner mask to the ionised sonic point.
4. Based on how much the luminosity has increased from the initial value estimate the corresponding increase in mass.
5. Update the stellar mass.
6. Repeat steps 2–5 until the stellar mass has converged.

The initial stellar mass is 17.87 $M_\odot$, the same value used in the simulations. If a luminosity of 2.5×10^{46} s^{-1} leaves an inner mask of radius 10 au the simulation in Section 3.3.2 shows the star will ionise out to $\sim$ 32 au. For the upcoming calculations the inner mask is set to 15 au, a slightly larger radius than that used in the simulation referred to. This change is made to account for the future increase in stellar mass, which will result in a steeper Bondi profile, and hence a larger part of the profile will be too close to the central singularity to calculate, due to numerical precision issues. Using the slightly bigger mask, but keeping the ionised radius the same, decreases the escaping luminosity. The exact value can be calculated using a similar approach to Equation 3.10, balancing photoionisations with radiative recombinations between the inner mask radii, $R_{\rm mask}$, and the desired position of the ionisation front, $R_{\rm IF}$. Because I am using analytic expressions, which do not confine me to a simulation grid, I can perform the calculation radially this time:

$$Q = 4\pi\alpha_B \sum_{R=R_{\rm mask}}^{R_{\rm IF}} \frac{\rho(R)^2}{m_H^2} R^2 \, \mathrm{d}R \,. \tag{3.12}$$

The sum is performed over radii increasing from $R_{\rm mask}$ to $R_{\rm IF}$ in steps of dR which has been chosen as 1 au. $\rho(R)$ represents the neutral Bondi accretion density at the given radius R,

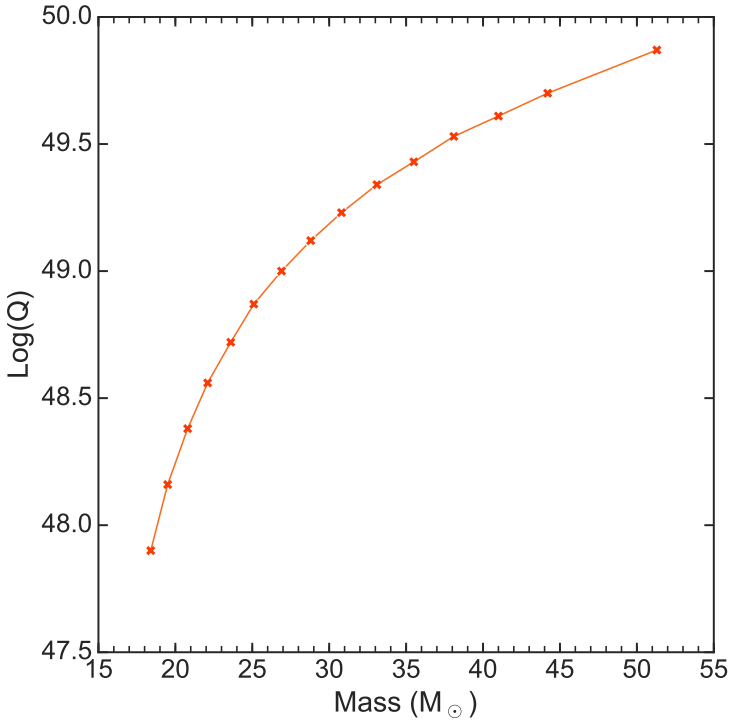

Figure 3.10: Stellar masses and luminosities from Vacca et al. (1996) plotted with a linear fit between consecutive points.

calculated using Equation 3.1. Using $R_{\rm mask} = 15$ au and $R_{\rm IF} = 32$ au the result is an initial luminosity of $Q_{\rm i}$ =1.78×10^{46} s^{-1}. The same equation is used to determine the luminosity, $Q_{c_{\rm si}}$, required for the HII region to reach the ionised sonic point, by defining $R_{\rm IF}$ as the radius where $v = c_{\rm si}$.

The difference between $\log(Q_{c_{\rm si}})$ and $\log(Q_{\rm i})$ is translated to a change in mass using the empirical mass to luminosity relation shown in Figure 3.10. Since my luminosities are a measure of how many photons escape some mask per second, and not the total luminosity emitted by the star, I am only interested in the slope between the data points on the plot, not the actual luminosity values. I use a linear interpolation (in $\log(Q)$) between the data points, and I extrapolate to lower masses by assuming the rate of change of mass per $\log(Q)$ between the 18.4 and 19.5 $M_\odot$ stars stays the same down to my initial stellar mass of 17.87 M$_\odot$. Applying different rates for different mass ranges I can estimate a mass increase based on $\Delta\log(Q) = \log(Q_{c_{\rm si}})$–$\log(Q_{\rm i})$, and update the stellar mass accordingly.

A greater stellar mass implies the star has a bigger gravitational pull, consequently the

Bondi profile of the surrounding material is no longer the same and must be updated accordingly, the same goes for the position of the ionised sonic radius. Having calculated a new Bondi profile and ionised sonic radius, Equation 3.12 is used to make a new estimate of the luminosity required, which leads to a new mass estimate. This process is repeated until the values for the stellar luminosity and mass converge. The final result is a luminosity of $Q_{c_{si}} = 1.56 \times 10^{47}$ s^{-1} required to ionise to the ionised sonic point at $\sim$ 248 au. This is a luminosity increase of $\Delta\log(Q) = 0.94$ which corresponds to a mass increase of $\Delta M = 5.70$ $M_\odot$, giving a new stellar mass of 23.57 $M_\odot$.

Using the rate of flow of material along the Bondi profile it is possible to estimate how long it would take the star to accrete $\Delta M = 5.70$ $M_\odot$, thereby reaching the point where the HII region breaks free from the gravitational trapping. The rate of spherical inflow of material is evaluated at some radius using Equation 2.43, for simplicity I will consider the neutral Bondi radius, since both the number density ($\rho_B = 30000$ cm^{-3}) and velocity ($v_B = c_{sn}$) is well known at that point. The Bondi radius depends on the stellar mass according to Equation 2.44, it follows that as the star grows the Bondi radius changes, and so does the rate of inflow of material. Hence I track the evolution of the star in discrete time steps; $M_\star = M_\star + \dot{M}\,dt$, updating the value of $\dot{M}$ according to the new stellar mass after every time step, the smaller the time steps chosen the more accurate the result would be. When using $dt = 1$ yr, this method predicts it would take $\sim 2.58\times10^6$ yrs for the central star in question to accrete 5.70 $M_\odot$.

A couple of key assumptions are required to make this time estimate of how long it takes to go from a gravitationally trapped 32 au HII region to an expanding one. Such as the extrapolation of the mass-to-luminosity relationship to lower masses, and the shape of the density profile of the material to be ionised. Based on the general trend of the points in Figure 3.10 it would be reasonable to assume the slope would steepen further when moving onto lower mass stars than those plotted, as opposed to the linear extrapolation I assume. A potentially steeper slope means the star would not need to accrete as much material to get the required luminosity increase, this would suggest the current accretion time is an overestimate. On the other hand, assuming a neutral Bondi profile results in a conservative time estimate. Introducing a two-temperature profile, such as the one seen in Section 3.3.3, or denser clumps of material, would increase the luminosity required for ionisation out to the ionised sonic point, which in turn would increase the time estimate. The approximated time period is only considering a fraction of the full time the HII region remains trapped, as it does not account for

the time it took to reach the initial size of 32 au. Still it gives some indication of how long I would expect the HII region to remain gravitationally trapped, and as such it acts as a first estimate of whether it is feasible that gravitational trapping can increase the lifetime of the UCHII regions past the minimum 10^5 yrs which are required by observations. Considering my rough estimate of the gravitationally trapped stage of the life of a HII region being at least 2.58×10^6 yrs, it seems an evolution which includes gravitational trapping could help explain the lifespan of UCHII regions.

3.5 Conclusions

In this chapter I have presented the first numerical radiation hydrodynamic simulations of the steady-state models of HII region evolution within spherically symmetric Bondi accretion flows by Keto (2002b, 2003) and Mestel (1954). My simulations reproduce the main features of the analytic steady-state analyses, namely gravitationally trapped HII regions at early times and pressure-driven expansion when the ionising luminosity increases to produce a HII region extending beyond the critical radius at approximately the ionised sonic point.

The main difference between the analytic work and my simulations is the stability of the gravitationally trapped spherically symmetric HII region. Any density perturbation within the ionised region, whether due to jump conditions across the ionisation front or noise in the simulation, initiates a runaway instability of the HII region, where it collapses and reappears periodically. Figure 3.11 illustrates how the HII region behaviour in the simulations differ from that predicted. According to work by Vandenbroucke et al. (2019) this instability is expected to occur only in a 1D idealised spherically symmetric geometry, and would prevent the formation of spherically symmetric HII regions in fully 3D simulations by introducing asymmetry to the system.

Regardless of the oscillating nature of the HII region, my results still show gravitational trapping, with accretion through the ionisation front. The implication of this on massive star formation is that accretion of material onto forming stars can continue even after the stars begin emitting ionising radiation, which is longer than previously expected, see also Kuiper & Hosokawa (2018). All velocities in the system are inflowing until the HII region escapes the gravitational trapping and pressure-driven expansion begins. At this stage the accretion rate onto the star decreases to zero and the star reaches its maximum accreted mass. Having

accretion last for longer could potentially decrease estimates of the required accretion rate during the formation of high-mass stars.

Gravitational trapping can also help explain the surprisingly long lifetimes of UCHII regions (Churchwell, 2002). By taking gravitational trapping into consideration the timescale for the growth of the HII region will initially depend on the accretion timescale and is not solely due to the rate of the pressure-driven expansion. An initial rough estimate suggests this is indeed a feasible solution to the lifetime problem.

The simulations presented in this chapter produce idealised spherically symmetric ionised accretion flows in an isolated system, where both rotation and magnetic fields are neglected. This simplified approach is necessary for a direct comparison to the analytic model presented by Mestel (1954); Keto (2002b, 2003). Future work on ionised accretion flows could benefit from introducing rotation, this would lead to a more realistic system where there is accretion of material through a gravitationally flattened disk, and the majority of the radiation would be directed along the poles. For a model at this stage it might be possible to produce synthetic continuum and line intensity maps to compare with real observations.

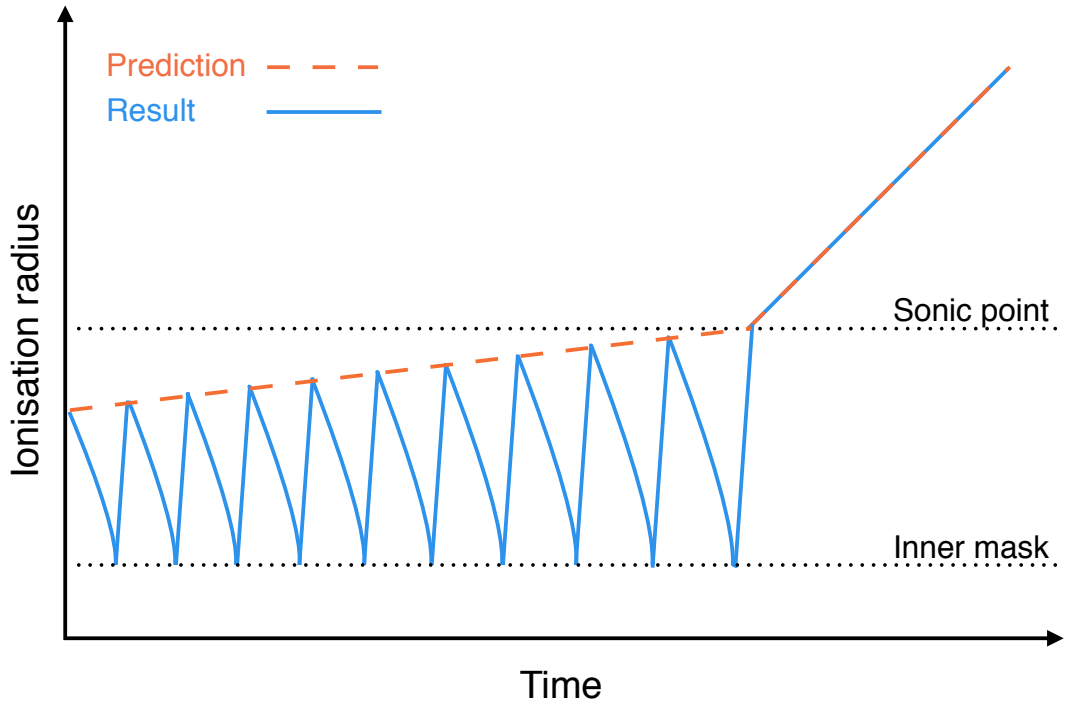

Figure 3.11: An illustration comparing the predicted and simulated evolution of HII regions. HII regions are predicted to be gravitationally trapped while within a critical radius. Growing only due to accretion which increases stellar mass and luminosity over time, causing further ionisation. Once the ionised region exceeds the critical radius it is expected to experience a much more rapid pressure-driven expansion. Simulations show the HII regions generally behave as predicted, but while they are gravitationally trapped they experience periodic collapses followed by rapid expansions.

4

The formation of high-mass binary stars

This chapter is based on Lund & Bonnell (2018). I begin with a brief review of the literature on different formation mechanisms of binary stellar systems, highlighting the challenges associated with each one. The rest of the chapter focuses solely on binary formation through accretion. I develop a semi-analytic model to investigate under which conditions accretion onto wide low-mass binary stars can result in a close high-mass binary system. I specifically explore the role of magnetic fields during the accretion process.

4.1 Introduction

Up to this point my discussion of star formation has been limited to single stars. The story of how single low-mass stars form has been well established, for an overview see the introductory Section 1.1.2. Creating high-mass stars is more problematic, as discussed in Section 1.1.3 and the previous chapter. To complicate matters further, any theory on high-mass star formation must be able to account for the high frequency of close (stellar separation $\lessapprox$ 1 au) binaries (Mason et al., 1998; Zinnecker & Mathieu, 2001; Sana et al., 2014). The observed close high-mass binary stars must either be formed *in situ*, or two stars evolve into this state. Examples of the latter are two individual high-mass stars becoming gravitationally bound, or a binary system decreasing its separation, increasing its mass, or both, after formation. In Section 4.2 I discuss the main formation theories of stellar binaries, all of which it turns out have difficulties in one way or another explaining systems with both small separations and high-mass stars. In the case of accretion however I propose this problem can be solved by taking into account the magnetic fields in the interstellar medium, making it a viable binary formation theory.

4.2 Binary formation theories

What follows is a brief review of different binary formation theories, I evaluate each one on the following two criteria: 1. It must be capable of producing the observed close high-mass systems, and 2. Due to the high frequency of such binaries, the formation mechanism can not be a rare occurrence.

4.2.1 Fission

The "Fission theory" was first proposed by Darwin (1879), who argued a rapidly rotating single mass could divide into two masses. Darwin originally developed the theory to explain the origin of the Moon, but the principle was later applied to the formation of binary stars (e.g. Jeans, 1919; Roxburgh, 1966; Bodenheimer & Ostriker, 1970). The theory goes as follows; as a protostar contracts it spins up due to the conservation of angular momentum, once the ratio of rotational to gravitational energy reaches a critical value the protostar becomes unstable, deforms to a bar-like object which eventually breaks up into two separate fragments.

Such a mechanism would likely form close relatively low-mass binaries. The separation between the two resulting stars would be of the order of the size of the initial protostar, and the

total binary mass would be limited by the mass of the initial protostar. So already theoretically speaking fission would not be able to produce the observed close high-mass binaries, the real death blow however came in the form of numerical simulations. Various three-dimensional hydrodynamics codes have shown that the spinning protostar, turned bar-like object, does not split into binaries (Durisen et al., 1986; Williams & Tohline, 1988; Bonnell, 1994; Bate, 1998). Instead, the consensus is that the bar develops spiral arms which allow the majority of the angular momentum of the initial protostar to be ejected, along with a small fraction of the initial mass. The result is a more slowly rotating central protostar surrounded by either a ring or a disk made up by the ejected material.

4.2.2 Capture

Splitting a single star into two does not work, but how about bringing two individual stars together into a single system? Forming a bound system from unbound stars requires the two unbound stars to lose kinetic energy. There are three ways this has been imagined to occur; 1. Energy is lost through a dissipating medium surrounding the two stars, such as a circumstellar disk (Larson, 1990), 2. Three stars come together, with the third star being ejected along with the excess energy (Szebehely, 1967), or 3. Orbital energy is transferred into tides during a close encounter (Fabian et al., 1975; Press & Teukolsky, 1977).

If a star passes close enough to interact with a disk surrounding a second star it likely leads to the destruction of the disk, but in the process there is also a chance the two stars become bound (Larson, 1990; Clarke & Pringle, 1991; Hall et al., 1996). The star-disk capture rate depends on the stellar mass of the star at the centre of the disk, being an order of magnitude higher for ~ 22 $M_\odot$ stars than for solar mass stars, but it is still not high enough to account for the observed multiplicity of high-mass stars (Moeckel & Bally, 2007b,a). Furthermore, the binary separation in a system forming this way would have to be of the order of the disk size, typically tens to hundreds of au, with no way of producing either wider systems ($\gtrsim 1000$ au) or the close systems (< 1 au) (Larson, 1990; Clarke & Pringle, 1991).

Without a circumstellar disk the cross section for stellar capture shrinks significantly, making capture less likely, but still possible. It has been found that the close encounter of three stars is likely to be followed by the fast escape of one of the stars, leaving the remaining two stars in a binary system (Szebehely, 1967). The probability of such an encounter occurring depends highly on stellar density. When considering the solar neighbourhood, or even

denser globular clusters, this process is also too inefficient in light of the number of binaries observed (Mansbach, 1970). Tidal capture faces a similar problem, as it only happens during very close encounters it too requires a high stellar density (Press & Teukolsky, 1977). Bonnell et al. (1998) suggests a scenario where the three-body and tidal capture mechanisms could be responsible specifically for the high-mass binaries. The theory supposes high-mass stars are formed through accretion-induced collisions. As gas falls onto stars in the core of a stellar cluster the core contracts, potentially to the point where stellar collisions occur frequently and the stars experience a significant build-up of mass. As capture relies on close encounters, which are more likely to happen than collisions, it is reasonable to assume most of these high-mass stars are found in binary systems. This analytical prediction was later put to the test in a numerical simulation of gas accretion in a stellar cluster (Bonnell & Bate, 2002). Note that the simulation did not include tides, and so any binaries were formed exclusively through three-body capture. The result was a high-density core, 10^5 times the mean stellar density in the cluster, with a significant number of relatively wide high-mass binary stars (separations $\sim$ 10–10^3 au). Close (a few stellar radii) high-mass binaries would be expected if tidal capture had been included (Bonnell et al., 1998).

4.2.3 Fragmentation

As described in the introductory Section 1.1.2, when the self-gravity of a molecular cloud exceeds any opposing forces it collapses, eventually creating a star. During the collapse, if the cloud mass exceeds two Jeans masses ($M_{cloud} \gtrsim 2M_J$), the cloud might break into multiple fragments (Hoyle, 1953; Hunter, 1962) which in turn leads to multiple stars, such as binaries. Alternatively, fragmentation could happen after the cloud collapse, in a protostellar disk (Bonnell, 1994). These two options fall under the categories thermally driven fragmentation and rotationally driven fragmentation. Broadly speaking these are two different ways of achieving the same goal; multiple regions where the timescale for gravity to pull material together is shorter than the timescale for any opposing forces to pull it apart.

Thermally driven fragmentation happens during the collapse of a molecular cloud when the gravitational energy of the cloud increases at a greater rate than the thermal energy. This results in a decrease in the Jeans mass and consequently the cloud may reach a stage where it can accommodate multiple Jeans masses. Fragmentation may or may not follow depending on the properties of the cloud. If the cloud density always increases towards its centre, the free

fall time for global collapse ($t_{\rm ff} \propto \rho^{-1/2}$) demonstrates that material at any given radius can never catch up with interior material and similarly can never be caught by exterior material. Consequently no fragmentation can occur and the cloud collapses as a whole. However, clouds can fragment if they contain sub-regions with shorter local free-fall times than the mean free-fall time of the entire cloud at that radius. This favours non-spherical geometries and excludes spherically symmetric clouds where these two timescales will always be the same.

The presence of a binary system formed by this mechanism implies it started as two cloud fragments separated by at least the distance of both their Jeans lengths, otherwise there would be an overlap and the result would be a single star. This argument leads to restrictions on the possible binary properties; the resulting stellar masses are proportional to their separation (Bate & Bonnell, 1997; Bonnell, 1999). In other words a binary system where the two stars are both high-mass and are orbiting close together can not form this way.

As an example take two identical fragments, the resulting total binary mass can be estimated as $M_{\rm bin} = 2M_J$, and the minimum separation as $s_{\rm min} = 2R_J$. This gives a direct relationship between the minimum separation and the binary mass (using Equations 1.12 and 1.13 for the Jeans length and Jeans mass):

$$s_{\rm min} = \propto \frac{M_{\rm bin}}{T}, \tag{4.1}$$

where T is gas temperature. By assuming the initial cloud fragments consist of pure hydrogen gas with a density of 10^{-19} g cm^{-3} the resulting binary mass can be written as:

$$M_{\rm bin} \approx 20\ M_\odot \left(\frac{T}{10\ \rm K}\right)\left(\frac{s_{\rm min}}{50000\ \rm au}\right). \tag{4.2}$$

Given a reasonable temperature of 10 K, the relationship between total binary mass and minimum binary separation is shown in Figure 4.1. For a binary system to have a mass of 20 M$_\odot$ or more the stars must be at a separation of at least 5×10^4 au.

In the case of rotationally driven fragmentation rotational support halts the cloud collapse, which allows more time for fragmentation to occur. If the molecular cloud is rotating, the spinning core deforms into a bar-like object, which develops spiral arms, as was previously discussed in the context of fission. The spiral arms gather surrounding material, and in the process remove its rotational support by transporting angular momentum outward. If

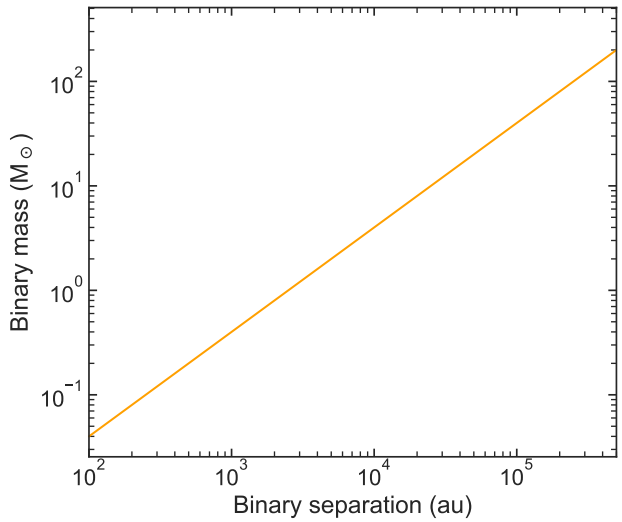

Figure 4.1: Masses and corresponding minimum separations for binary systems formed through cloud collapse and thermally driven fragmentation, assuming a hydrogen cloud with a density of 10^{-19} g cm^{-3} and a temperature of 10 K.

enough material is accumulated the outcome is a gravitationally unstable condensation which collapses, thereby creating a companion to the central object (Bonnell, 1994). So in contrast to thermally driven fragmentation, it is not a question of decreasing the Jeans mass, but rather of building up sufficient material to reach it.

Using a smoothed particle hydrodynamics (SPH) code Bonnell (1994) ran simulations of rotationally driven fragmentation where he tracked the individual particles which eventually formed the secondary. All the particles originated in either a disc surrounding the central core or an accretion flow, the presence of an accretion flow adding material to the system proved crucial to the process. Hence, despite starting off with a spinning core and ending up with a binary system, this is not an example of fission, as the material which ends up forming the secondary star does not come from the core.

The range of possible binary separations resulting from this type of fragmentation depends on the reach of the spiral arms and can vary. Fragmentation towards the core can even form close binaries with separations of the order of a few $R_\odot$, but the corresponding mass of the binary system would be as small as 1% of the solar mass (Bonnell & Bate, 1994).

Despite not being able to form close high-mass binaries directly, there is still evidence to support that fragmentation might be the first step on the path towards these systems. Sadavoy

& Stahler (2017) tested evolutionary models for stellar populations embedded within cores in molecular clouds and concluded that the observations were best matched when all stars initially formed as wide binaries (separations > 500 au). Subsequently most of them break apart, which is how single stars are formed. Considering fission is ruled out as a binary formation mechanism, by default the only option for creating binaries *in situ* is fragmentation. After fragmentation there must then be some other mechanism which shrinks the binary separation to form the observed close high-mass binaries.

4.2.4 Binary hardening

Assuming a wide binary system within a stellar cluster is already formed the two stars can be brought closer together through so called binary hardening. Hard binaries in a cluster tend to become harder, another term for closer, through stellar interactions (Heggie, 1975). Assuming no direct collisions or tidal effects take place this process conserves energy. This essentially means the total binding energy of the cluster sets a limit to how close a pair of binaries can get through this process.

In theory, minimum separation is reached by the binary absorbing all the binding energy of the surrounding cluster, and in doing so forcing the rest of the cluster to dissolve. Equating the binding energy of a binary consisting of two stars of masses $M_{\rm bin1}$ and $M_{\rm bin2}$ at a separation s,

$$E_{\rm bin} = \frac{GM_{\rm bin1}M_{\rm bin2}}{s}, \tag{4.3}$$

with the binding energy of a cluster of mass $M_{\rm clust}$ and radius $R_{\rm clust}$,

$$E_{\rm clust} = \frac{GM_{\rm clust}^2}{R_{\rm clust}}, \tag{4.4}$$

I can rearrange to get an expression for the minimum separation possible:

$$s_{\rm min} = \frac{M_{\rm bin1}M_{\rm bin2}}{M_{\rm clust}^2}R_{\rm clust}. \tag{4.5}$$

The two binary masses can be estimated by relating the mass of the cluster to the expected highest mass star ($M_{\rm max}$) that cluster would contain (Larson, 1982, 2003b; Elmegreen, 2000; Weidner et al., 2010). To do this I am using the empirical expression derived by Larson (1982,

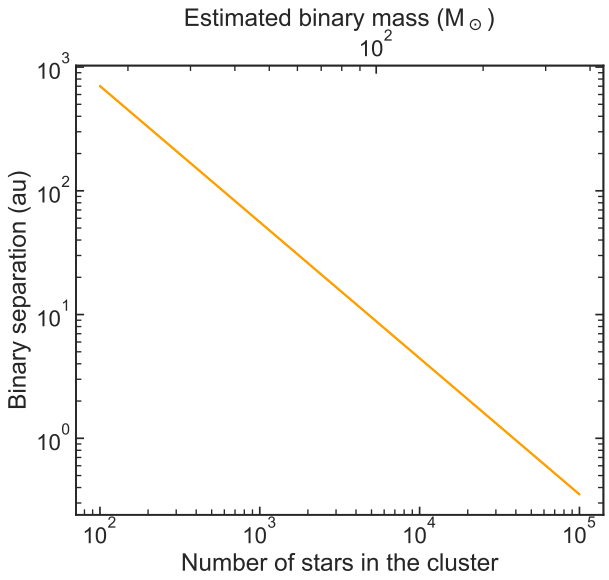

Figure 4.2: Minimum binary separation obtained through binary hardening as a function of cluster size, using an expected mass function to estimate the binary mass. $R_{\rm clust} = 0.5$ pc and $M_{\rm clust} = N_\star \times 1$ M$_\odot$.

2003b):

$$M_{\rm max} \sim 1.2 M_{\rm clust}^{0.45}, \tag{4.6}$$

and assuming the most-massive star in the cluster is the primary binary star (M_1), and the secondary star (M_2) is 0.75 times the mass of the primary. Using Equation 4.5 it is then possible to estimate the minimum separation of the binary given only the mass and size of its parent cluster. For a cluster of 1000 M$_\odot$ with a radius of 0.5 pc, stellar dynamics alone can form a high-mass binary system consisting of two stars of 27 and 20 M$_\odot$ with a minimum separation of 56 au. Given the number of stars in the cluster, $N_\star$, for a cluster with $R_{\rm clust} = 0.5$ pc and $M_{\rm clust} = N_\star \times 1$ M$_\odot$, Figure 4.2 shows the corresponding estimated binary mass ($M_{\rm bin} = M_{\rm bin1} + M_{\rm bin2}$) and the resulting minimum binary separation. Forming closer, or higher-mass binaries requires a different mechanism.

4.2.5 Accretion

Another consideration when attempting to form close high-mass binaries is the evidence indicating high-mass stars obtain most of their mass after formation (Bonnell et al., 1998). Taking the Trapezium cluster as an example, the Jeans mass in the protocluster cloud is estimated to have been as small as 0.3 M$_\odot$ (Zinnecker et al., 1993), but stars of much higher masses are observed in the cluster, such as the binary system θ^1 OriC, consisting of a primary star of

33 ± 5 $M_\odot$ and a secondary star of 11 ± 5 $M_\odot$ (Balega et al., 2014). Collisions were briefly mentioned earlier as a way to build up mass, another option, which is not dependent on stellar density, is accretion.

Assuming a wide low-mass binary system has already formed, accretion could turn it into a high-mass system. In a cluster formation process fragmentation of higher mass cores produces stars, and high-mass stars will then grow at the core of the cluster through accretion (Bonnell et al., 2004; Smith et al., 2009). In their simulations Smith et al. (2009) showed that low density gas spread throughout the cluster environment would funnel from large radii and accrete onto massive central stars. Observations of clusters suggest that most of its mass is actually held in gas, rather than stars, up to 90 % (Lada & Kylafis, 1991). This implies there is in fact material available for accretion to take place in a larger cluster formation process. Furthermore, in Chapter 3 I showed that, given material is available, accretion onto stars can continue for longer than previously assumed, even after photoionisation has been triggered.

So assuming accretion can take place it will inevitably lead to more massive binaries, however it might not be conducive to a close system. Using Kepler's 3rd law and the centre of mass condition the expression for the separation of a binary can be completely defined by its mass and angular momentum according to:

$$s = \frac{(1+q)^4}{q^2} \frac{L_{\rm bin}^2}{G M_{\rm bin}^3}. \tag{4.7}$$

$M_{\rm bin}$ is the total mass of the binary, $L_{\rm bin}$ is the angular momentum of the binary, and q is the mass ratio of the two stars. This equation shows that increasing the binary mass, keeping everything else the same, would bring the two stars closer together. Conversely, increasing angular momentum, keeping the mass constant, would force the two stars further apart. During accretion both the mass and angular momentum of the infalling material is added to the binary system, therefore achieving both a close and high-mass system is not guaranteed.

Bonnell & Bate (2005) suggested accretion of low-angular momentum material, which would ensure a high-mass close binary system, but this would be limited by the significant non-zero angular momentum in the infalling gas. I propose magnetic braking could be a solution to this problem; a magnetic field in the cloud transporting angular momentum along its field lines. This is the theory I will be testing in the remainder of this chapter. Magnetic braking has been explored in other contexts such as pre-cloud collapse (Mouschovias & Paleologou,

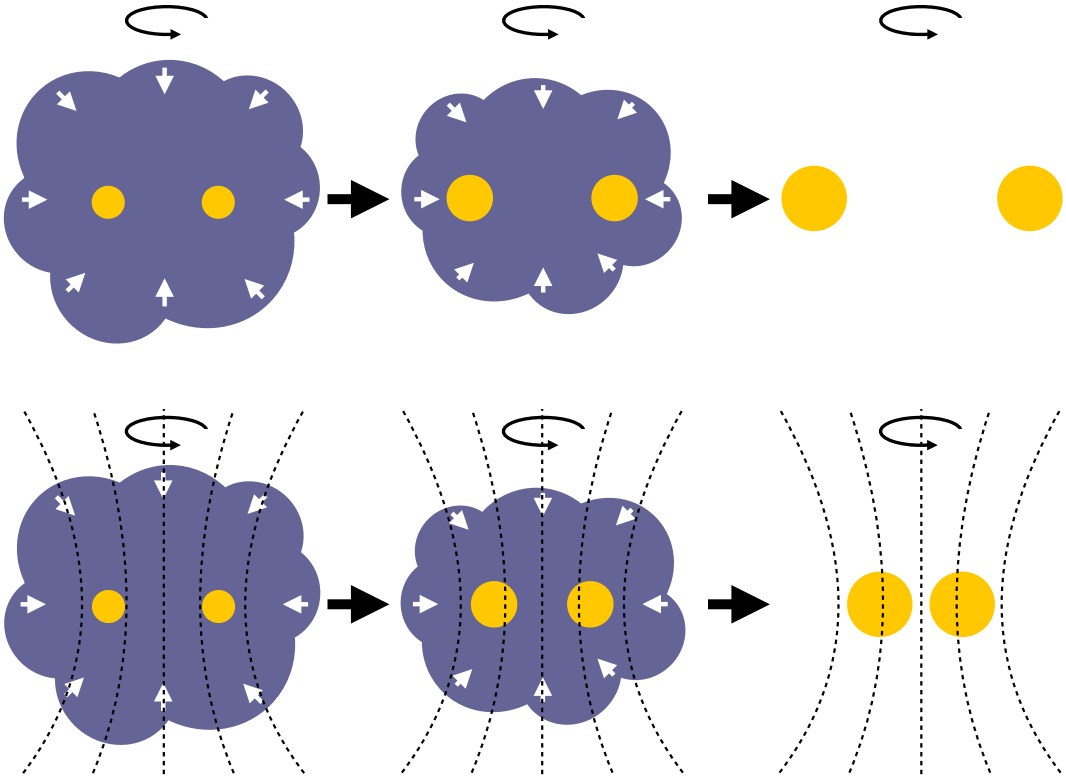

Figure 4.3: Accretion of material from a molecular cloud onto a wide low-mass binary without (*top*) and with (*bottom*) the presence of an interstellar magnetic field threading the cloud. The masses of the binary stars will increase in either case, but the final separation of the stars is more likely to decrease if a magnetic field has stripped the system of some of its angular momentum.

1979) and stellar winds (Mestel, 1984; Ud-Doula et al., 2009), but never in relation to the formation of binaries. As discussed in Section 1.1.1 magnetic fields are observed to be present in molecular clouds, with strengths that indicate they can be relevant in an accretion process (Crutcher, 1999; Bourke et al., 2001). Furthermore, if the material being accreted is low in density, as suggested by Smith et al. (2009), it is likely to remain coupled to an interstellar magnetic field. Thus a magnetic field could potentially transport angular momentum away from the molecular cloud surrounding the binary system and allow mass accretion from the cloud to occur with less angular momentum being added to the binary system. This process would drive the binary system to both higher masses and smaller separations. To visualise the idea see Figure 4.3.

4.3 Semi-analytic accretion model

In this section I will present a semi-analytic model describing the accretion of gas from a molecular cloud onto a wide low-mass binary. The model includes the effects of rotation and turbulence, as well as magnetic braking, which removes angular momentum from the infalling gas. The aim is to investigate what initial conditions are required to produce both massive and close binary systems through accretion. The main focus will be on the effect of a magnetic field threading the molecular cloud. The model is kept as simple as possible to make causality clear, aiding understanding of how each of the parameters impact the properties of the resulting binary.

4.3.1 The basics

The model starts off with a wide and low-mass binary star system; two 1 $M_\odot$ stars separated by 100 au. The mass and separation are the only two properties of the binary that I am ultimately interested in, these will change through the process of accretion. As I am more concerned with the quantity, and associated angular momentum, of any accreted material than its distribution across the two stars I do not need to resolve the stars individually to get the information I am interested in. Hence the two stars making up the binary system are approximated as a point mass of $M_{\rm bin} = 2$ $M_\odot$ with an angular momentum pointing along the rotation axis, z. To simplify the system further I assume a constant mass ratio of 1. In which case the binary separation defined earlier in Equation 4.7 can be written as:

$$s = \frac{16 L_{z\rm bin}^2}{G M_{\rm bin}^3}. \tag{4.8}$$

The binary system is placed at the centre of a spherical molecular cloud, its properties are completely independent of the chosen cloud, ignoring any potential dependence between the binary and its birthplace. The molecular cloud is given a solid body rotation around the same axis of rotation as the binary and two different density profiles are applied to the cloud; a uniform density, $\rho = \rho_0$, and a centrally condensed density, $\rho \propto R^{-2}$. The reality would probably be a cloud made up of a clumpy medium with an average density somewhere between the two profiles, however I will stick to a simple density distribution. The binary and the surrounding smooth cloud are the only two components considered, there will be no interactions between

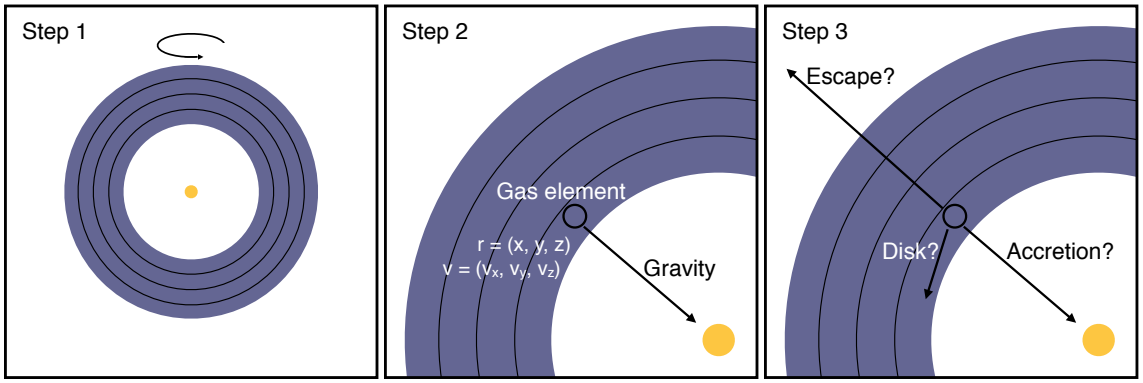

Figure 4.4: *Step 1*: Split the molecular cloud into concentric shells. *Step 2*: Pick a random gas element within the shell and assign it velocity and angular momentum based on its position. *Step 3*: Track the evolution of the gas element until it escapes the system, ends up in a disk surrounding the binary or is accreted. Steps 2 and 3 are repeated until all the gas throughout the cloud is accounted for.

this system and other stars, despite real binaries likely being located at the centre of stellar clusters.

The purpose of the model is to determine how much of the molecular cloud ends up being accreted, and update the binary system accordingly. If material from the molecular cloud moves within a so-called accretion radius $R_{\rm acc}$, defined as being equal to the binary separation ($R_{\rm acc} \equiv s$), it will fall onto the binary. The process, which is illustrated in Figure 4.4, can be split into these four steps:

1. Divide the molecular cloud into concentric shells.
2. Pick a random gas element within the innermost non-empty shell.
3. Track the path of the gas element to determine its fate.
   (a) Does it escape?
   (b) Does it settle in a disk?
   (c) Does it accrete?
4. Repeat steps 2 and 3 until all the gas in the molecular cloud is accounted for.

The collapse of the molecular cloud is modelled as an inside out process by considering successive shells of the cloud, cycling through them from the innermost to the outermost. For each shell a large number of gas elements are sampled, the more elements the more accurate

the model, however the computational time also increases. In total the code considers 10^6 elements spread across 10^4 shells. All the gas elements have the same mass, m_e, with their combined mass adding up to the total mass of the molecular cloud. Every gas element is assigned a random position (x, y, z) falling within the shell from which it is sampled, an initial velocity and an angular momentum. Due to the solid body rotation of the cloud (implying a constant angular velocity, Ω), the initial velocity of the gas element depends only on its radius, as follows:

$$\vec{v} = \vec{\Omega} \times \vec{R}. \tag{4.9}$$

This velocity potentially has an extra component added due to turbulence, see section 4.3.2. The angular momentum of the gas element depends on both its position and its velocity, and is given by:

$$\vec{L}_e = m_e(\vec{R} \times \vec{v}). \tag{4.10}$$

The fate of each element is determined by tracking their path through first order Euler integrations of their position and velocity. The resulting movement of the element depends on its initial position and velocity, as well as the gravitational attraction by the central binary system. No element is affected by another or by other external factors. The size of each time step used in the integration, Δt, decreases as the gas element moves closer to the binary and as the velocity increases, according to

$$\Delta t = |10^{-3}\frac{R}{v}|. \tag{4.11}$$

The time steps are scaled by 10^{-3}, a value chosen for numerical expediency. The integration stops after one of three possible events occur: the gas element escapes the system, settles in a disk or accretes. The element escapes, and is ignored by the code, if it leaves the cloud with a velocity exceeding the escape velocity of the system. Assuming the element does not escape, its angular momentum will determine whether it settles in a stable orbit surrounding the binary as part of a disk or accretes onto the binary. It all depends on whether it reaches the critical radius of a stable orbit or the accretion radius of the system first.

The critical radius, where a gas element would settle in a stable orbit, is defined as the

radius where the force from the rotational motion of the element,

$$\vec{F}_{\text{rot}} = \frac{m_e v_{\phi e}^2}{R}\hat{r}, \tag{4.12}$$

and the strength of gravity,

$$\vec{F}_G = -\frac{GM_{\text{inner}}m_e}{R^2}\hat{r} \tag{4.13}$$

are balanced:

$$R_{\text{crit}} = \frac{J_{ze}^2}{GM_{\text{inner}}}. \tag{4.14}$$

The M_{inner} term in the above equations represents all mass within the current radius of the gas element, i.e. the mass of the binary and potentially also disk mass. Note that for the purposes of Equation 4.13, M_{inner} is assumed to be a spherical attracting mass. The critical radius is only dependent on M_{inner} and the z component of the specific angular momentum of the gas element, $J_{ze} = L_{ze}/m_e$. If $R_{\text{crit}} > R_{\text{acc}}$, the element will reach the critical radius before the accretion radius. In this case the specific angular momentum of the gas element is stored and it is placed in a disk surrounding the binary stars. Material from the disk may at a future point end up accreting onto the binary, if the accretion radius of the system evolves past the critical radius of the gas element.

As soon as any element, sampled from the cloud or residing in the disk, passes the accretion radius it is accreted onto the binary. This happens whenever

$$R_{\text{crit}} \leq R_{\text{acc}}. \tag{4.15}$$

Equation 4.15 acts as an accretion criterion and, assuming $M_{\text{inner}} \approx M_{\text{bin}}$, it can be rewritten in terms of the specific angular momentum of the element and the binary as $|J_{ze}| \leq |4J_{zb}|$. Consequently the relative sizes of the specific angular momentum values is the only factor that determines whether or not the gas element is able to accrete onto the binary. The factor of 4 comes from the assumption that the two binary stars are always equal in mass, $q = 1$, in Equation 4.7.

If accretion occurs the mass of the element is added to the binary mass,

$$M_{\text{bin}_{\text{new}}} = M_{\text{bin}} + M_e, \tag{4.16}$$

and its angular momentum is added to the total angular momentum of the binary system,

$$\vec{L}_{\mathrm{bin}_{\mathrm{new}}} = \vec{L}_{\mathrm{bin}} + \vec{L}_{e}. \tag{4.17}$$

This ignores that some of the angular momentum could in theory go to the spin of the individual stars. Based on the new mass and angular momentum a new binary separation, and accretion radius, is calculated,

$$s_{\mathrm{new}} = R_{\mathrm{acc}_{\mathrm{new}}} = 16\frac{L^2_{z\mathrm{bin}_{\mathrm{new}}}}{GM^3_{\mathrm{bin}_{\mathrm{new}}}}. \tag{4.18}$$

The system shrinks when s_{new} is smaller than the original s value. This is the case when $|J_{ze}| < |1.5J_{z\mathrm{bin}}|$ is satisfied. Hence I define three regimes according to the specific angular momentum of the gas;

1. $|J_{ze}| > |4J_{z\mathrm{bin}}|$: no accretion.

2. $|J_{ze}| \leq |4J_{z\mathrm{bin}}|$: accretion.

3. $|J_{ze}| < |1.5J_{z\mathrm{bin}}|$: accretion and decreased separation.

Once every gas element in the innermost shell has escaped the system or accreted onto the binary or the surrounding disk the same process is repeated for the next shell. This continues until all the gas in the entire molecular cloud has been processed.

Feedback from the central binaries in the form of ionisation, stellar winds and radiation pressure will occur simultaneously to the accretion process described here, as they grow into high-mass stars. These effects are not included in my model, but none of them should prevent the physics I have described from happening. Simulations of feedback show that it tends to escape the cloud through weak points of low column density in the envelope (Krumholz et al., 2005; Dale et al., 2005, 2014). On smaller scales, accretion has been shown to occur through a disk even in the presence of feedback (Kuiper et al., 2010, 2015; Kuiper & Hosokawa, 2018).

4.3.2 Turbulence

Turbulence is introduced to the model by randomising the Cartesian velocity components of the gas elements according to:

$$\begin{aligned} v_x &= \overline{v}_x + \sigma\xi, \\ v_y &= \overline{v}_y + \sigma\xi, \\ v_z &= \overline{v}_z + \sigma\xi. \end{aligned} \tag{4.19}$$

Each ξ represents a different random number sampled from a Gaussian distribution that ensures the resulting velocities follow a Gaussian distribution with a mean $\overline{v}$ and standard deviation σ. The mean velocities in the x, y and z directions ($\overline{v}_x$, $\overline{v}_y$, $\overline{v}_z$) correspond to the overall solid body rotation of the cloud (Equation 4.9), and the standard deviation σ is given by the following relation (Larson, 1981; Heyer & Brunt, 2004),

$$\sigma = 0.8 \text{ km s}^{-1} \sqrt{\frac{\text{R}}{1 \text{ pc}}}. \tag{4.20}$$

In the case of a cloud rotating with $\Omega = 3 \times 10^{-14}$ rad s^{-1}, a gas element at a radius of 1 pc is given a rotational velocity of $\Omega R \approx 0.9$ km s^{-1}. How this velocity splits into $\overline{v}_x$, $\overline{v}_y$ and $\overline{v}_z$ depends on the position of the gas element and thus changes in time. The standard deviation introduced by turbulence at this particular radius is 0.8 km s^{-1}. As the standard deviation is of the same order of magnitude as the rotational velocity, turbulence causes significant deviations from pure solid body rotation on this length scale.

The overall velocity contribution from turbulent motion alone (v_{turb}) can be calculated by subtracting the velocity corresponding to solid body rotation from the total velocity:

$$v_{\text{turb}} = v - \Omega R. \tag{4.21}$$

4.3.3 Magnetic fields

As discussed in Section 1.1.1, magnetic fields are observed within dense star-forming cores of magnetic clouds, hence the final component of the model places the turbulent molecular

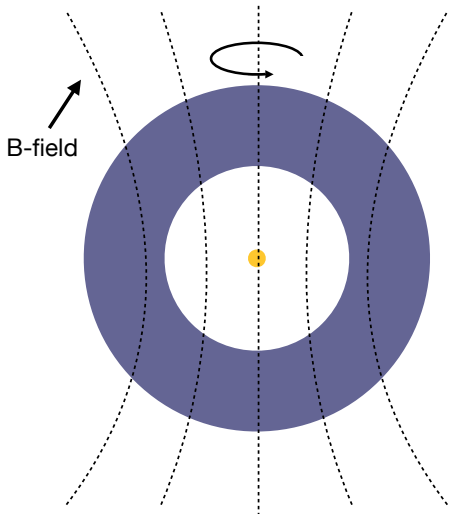

Figure 4.5: A magnetic field is introduced to the accretion model, threading the molecular cloud along the direction of its rotation axis. The rotation of the cloud causes the field lines to be dragged azimuthally.

cloud inside a magnetic field. For the sake of simplicity, the only orientation I will consider is the model cloud being threaded by an initially uniform magnetic field along the direction of the rotation axis; $B_z = B_0$. A different alignment of the field would result in weaker magnetic braking (Joos et al., 2012; Li et al., 2013).

As the magnetic field is added to a rotating cloud, the rotation bends and twists the field lines (Stahler & Palla, 2004), see Figure 4.5. This means a toroidal magnetic field component, B_ϕ, is induced. This component is estimated by comparing the rotational velocity of the cloud, v_ϕ, to the Alfvén velocity acting along the magntic field lines, v_A (Equation 1.2). The resulting azimuthal magnetic field component is:

$$B_\phi = B_0 \frac{v_\phi}{v_A}. \tag{4.22}$$

I impose an upper limit on this azimuthal field strength of $B_\phi = B_0$, corresponding to $v_\phi = v_A$. This is considered to be the maximal twisting that can be supported against magnetic instabilities, as found for accretion disks (Armitage, 2010). After first running the accretion model with the variable B_ϕ described by Equation 4.22, and then trying again keeping the field fixed at its upper limit, I find there is only a slight difference in the results between the two. Hence, for ease and simplicity, $B_\phi = B_0$ is used for all simulations presented in this chapter.

The B_0 value is kept constant, which assumes any growth of the field strength would be

offset by dissipative non-ideal processes. As the cloud collapses the magnetic field strength would increase towards the centre of the system, but at the same time ambipolar diffusion would weaken the field. The ratio of the ambipolar diffusion time (Equation 1.11) to the free-fall time (Equation 1.14), given some ionisation fraction (Equation 1.15), can be written in terms of the cloud mass, cloud radius and magnetic field alone:

$$\frac{t_{\rm AD}}{t_{\rm ff}} = 0.0067\left(\frac{M_{\rm cloud}}{1\ {\rm M}_\odot}\right)^2\left(\frac{B_0}{1\ \mu{\rm G}}\right)^{-2}\left(\frac{R_{\rm cloud}}{1\ {\rm pc}}\right)^{-4}. \tag{4.23}$$

Hence a cloud of 500 $M_\odot$ with a radius of 0.2 pc placed in a 100 μG field gives $t_{\rm AD}/t_{\rm ff} \approx 105$, and would collapse long before any significant field dissipation. The same cloud, but with a radius of 1 pc however gives $t_{\rm AD}/t_{\rm ff} \approx 0.17$ and would spend most of its lifetime as essentially a non-magnetised cloud. By applying a magnetic field all the way throughout the molecular cloud collapse I am implicitly assuming the ambipolar diffusion time exceeds the time it takes for the collapse to occur.

Having established the orientation and strength of my magnetic field, what remains is determining what effect its presence has on the accretion process. As the magnetic field only impacts charged ions (Stahler & Palla, 2004), the overall effect of the magnetic field on the cloud material will be approximated by having the field act on all the gas elements, but multiplying by an estimate of what fraction of the gas is ionised, I_f (Equation 1.15). This ionisation fraction effectively acts as a coupling coefficient between the gas and the magnetic field. Because the magnetic field lines are bent, there exists a tension attempting to straighten them, this results in a magnetic torque (Masson et al., 2016). For this scenario the magnetic torque is given by (Armitage, 2010):

$$\tau_o = \frac{B_z B_\phi R}{2\pi} A, \tag{4.24}$$

where A is the area the torque is acting on. The presence of a torque means there is a rate of change of angular momentum,

$$\vec{\tau_o} = \frac{d\vec{L}}{dt}. \tag{4.25}$$

The angular momentum of the cloud propagates away from the centre of the cloud along the magnetic field lines by Alfvén waves and, in time, is removed from the system (Masson et al., 2016). How much angular momentum is removed from each gas element depends both on the strength of the torque and the time over which that torque acts. Hence Angular momentum is stripped away after each step of the integration scheme used to track the path of the gas

$M_{\rm bin}$ ($M_\odot$)	s (au)	Ω (rad s^{-1})	$M_{\rm cloud}$ ($M_\odot$)	$R_{\rm cloud}$ (pc)
2	100	3×10^{-14}	500	0.5

Table 4.1: Initial parameter values for the accretion model. Columns show, respectively, binary mass, binary separation, angular velocity, molecular cloud mass and molecular cloud radius.

elements according to

$$L_{ze,\rm new} = L_{ze} - I_f \tau_o(R) \Delta t, \tag{4.26}$$

where I_f is the ionisation fraction, $\tau_o(R)$ is the strength of the torque at a given radius and Δt is the size of the timestep. It is assumed that only the z-component of the angular momentum is being reduced by the torque, as a consequence the x- and y-velocity components of the gas element needs to be updated accordingly before the next integration step.

4.4 Results and discussion

4.4.1 Setup

For the following results the two binary stars are placed in a molecular cloud with a mass of 500 $M_\odot$, a radius of 0.5 pc and an angular velocity of 3×10^{-14} rad s^{-1}. These parameter values are chosen as an example of typical properties of clumps where high-mass star formation occurs (Goodman et al., 1993; Urquhart et al., 2014). A summary of the parameters is listed in Table 4.1.

I want the chosen parameters to result in a system where the cloud would in fact collapse, and not be supported by forces such as rotation or turbulence. This can be tested by comparing energies. The gravitational binding energy of the cloud,

$$E_G = \frac{3GM_{\rm cloud}^2}{5R_{\rm cloud}}, \tag{4.27}$$

is compared with the rotational energy,

$$E_{\rm rot} = \frac{1}{2} I_m \Omega_{\rm cloud}^2, \tag{4.28}$$

where I_m is the moment of inertia. The result is an estimate of their relative dynamical importance in this particular scenario:

$$\frac{E_{\text{rot}}}{E_G} = \frac{5R_{\text{cloud}}I_m\Omega_{\text{cloud}}^2}{6GM_{\text{cloud}}^2}. \tag{4.29}$$

For the purpose of this calculation the molecular cloud is treated as a uniformly dense sphere, thereby neglecting the empty central region within the accretion radius. This does not change the resulting energy substantially as the central hole only corresponds to $\sim 0.1\%$ of the total radius. Assuming this uniform spherical distribution the moment of inertia can be written as

$$I_m = \frac{2}{5}M_{\text{cloud}}R_{\text{cloud}}^2, \tag{4.30}$$

which simplifies the energy ratio to

$$\frac{E_{\text{rot}}}{E_G} = \frac{R_{\text{cloud}}^3\Omega_{\text{cloud}}^2}{3GM_{\text{cloud}}}. \tag{4.31}$$

As for turbulence, the associated kinetic energy is estimated by summing the kinetic energy corresponding to the turbulent motion of every element in the cloud:

$$E_{\text{turb}} = \frac{1}{2}M_e\Sigma v_{\text{turb}}^2. \tag{4.32}$$

Again, the impact of turbulence is evaluated by comparing it to the gravitational binding energy:

$$\frac{E_{\text{turb}}}{E_G} = \frac{5R_{\text{cloud}}M_e\Sigma v_{\text{turb}}^2}{6GM_{\text{cloud}}^2}. \tag{4.33}$$

For the chosen parameters, this results in $E_{\text{rot}}/E_G \approx 0.02$ and $E_{\text{turb}}/E_G \approx 0.06$, that means gravity is dominating both rotation and turbulence. Consequently I expect the cloud would collapse.

4.4.2 Testing the model

The effect of adding different levels of physics to the accretion model is studied in Figure 4.6. Starting with a rotating cloud, I add turbulence and lastly a magnetic field. For each added feature the evolution of the central binary system changes. The plots show the change in binary mass and separation during the cloud collapse, with arrows indicating the direction

of evolution in time. The horizontal dashed line marks a separation of 1 au, below which I consider the separation to be close. In the top and bottom plots the binary is placed in respectively a uniform ($\rho = \rho_0$) or centrally dense ($\rho \propto R^{-2}$) molecular cloud. The initial binary and cloud properties are the ones listed in Table 4.1.

As discussed in Section 4.3.1, the only factor of the model determining whether or not gas is able to accrete, is its specific angular momentum. Furthermore, if accretion takes place, the specific angular momentum also controls the change in binary separation. It is possible for the two stars to gain mass, but move further apart as a consequence (Bate & Bonnell, 1997). The only version of the model where this is seen in Figure 4.6 is in the case of rotation alone. In the uniformly dense cloud $|1.5J_{zb}| < |J_{ze}| \leq |4J_{zb}|$ is satisfied throughout the entire collapse, whereas in the centrally condensed cloud this is the case only in the latter part of the collapse.

With added turbulence, the gas element velocities span a larger range, and there is more material in the clouds at small specific angular momenta. As a result, in the case of turbulent clouds both plots show binary separation decreasing with increasing mass, that means $|J_{ze}| < |1.5J_{zb}|$. Note the slope of the lines where binary separation decreases is the same for all versions of the model ($s \propto M_{\rm bin}^{-3}$) and suggests the accreted material in all these cases adds a negligible amount of angular momentum to the binaries (equivalent to a constant $L_{z\rm bin}$ in Equation 4.8). As successive cloud shells collapse, the gas elements originate from larger radii, their specific angular momentum increases, which eventually halts the accretion once $|J_{ze}| > |4J_{zb}|$. At this point the only way for the stars to grow even bigger is by introducing magnetic fields which act to reduce the specific angular momentum of the infalling gas, ensuring more material meets the criteria for accretion. Both plots show the full model, which includes 100 μG magnetic fields, results in the closest binaries. In the case of the uniform molecular cloud, the magnetic field is required in order to reach a close system.

The full accretion model is run both starting with the standard solar mass stars, as well as a binary of 10 $M_\odot$, shown as the darkest line on the plots. Increasing the initial mass means the starting point of the system is shifted along the x-axis, the binary evolution however goes on to run in parallel to the lower-mass full model line, only stopping at a lower separation.

The main difference between the uniform and non-uniform density clouds results from the centrally condensed cloud having more mass at low specific angular momenta. This generally leads to more gas being accreted under the condition which brings the binary stars closer

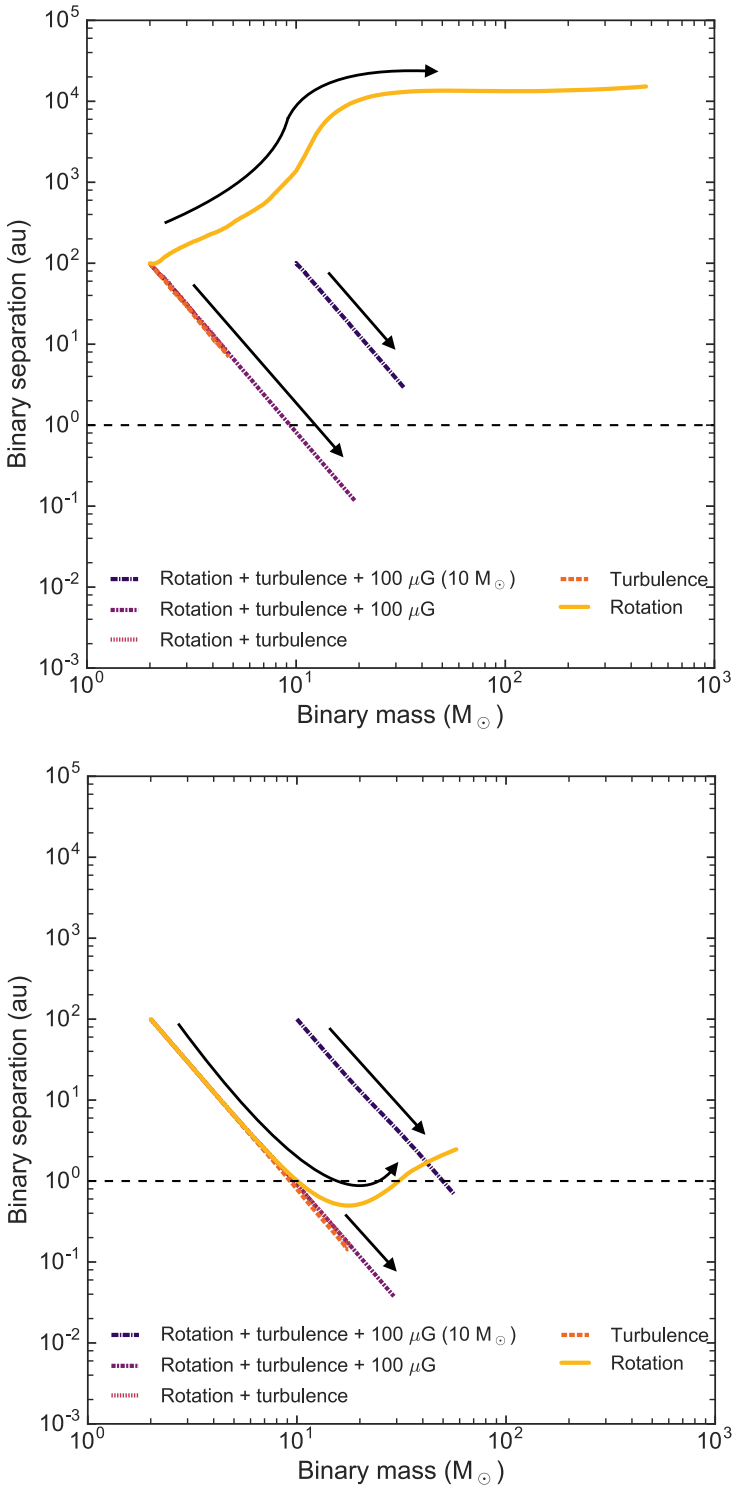

Figure 4.6: Change in binary mass and separation during accretion from a molecular cloud. *Top*: The molecular cloud is uniformly dense ($\rho = \rho_0$). *Bottom*: The molecular cloud is centrally dense ($\rho \propto R^{-2}$). The different coloured lines correspond to models with different cloud features. Note that three of the lines overlap (rotation + turbulence + 100 μG, rotation + turbulence and turbulence).

The horizontal dashed line marks a separation of 1 au, below which binary stars are likely to merge and the arrows indicate the direction of evolution in time. For the darkest line the initial mass of the binary is 10 $M_\odot$, in every other scenario it is 2 $M_\odot$. $M_{\rm cloud} = 500$ $M_\odot$, $R_{\rm cloud} = 0.5$ pc, $\Omega_{\rm cloud} = 3 \times 10^{-14}$ rad s^{-1} and $B_0 = 100$ μG.

together, hence smaller separations are reached for every version of the model. Apart from that, the general trends are the same across both plots, hence I choose to use only uniformly dense clouds for the remainder of this chapter.

4.4.3 Varying the magnetic field strength

Having established that magnetic fields help binary stars move closer together, the natural next step is considering the effect of different magnetic field strengths. Figure 4.7 shows how the binary mass (*left*), separation (*middle*) and angular momentum (*right*) evolve for a range of different magnetic field strengths, as successive shells of the cloud collapse. Since the cloud collapses from the inside out, the shell radius along the x-axis acts as a proxy for time. The different field strengths, indicated by different colours on the plots, are essentially equivalent to considering different levels of magnetic coupling by varying the ionisation fraction (Equation 1.15). The field strength determines the amount of angular momentum that is stripped from the infalling gas, which impacts the amount of material that is accreted and the separation of the final binary.

The initial binary and cloud parameters used are again the ones listed in Table 4.1; $M_{\rm bin} = 2$ $\mathrm{M}_\odot$, $s = 100$ au, $\Omega = 3\times10^{-14}$ rad s^{-1}, $M_{\rm cloud} = 500$ $\mathrm{M}_\odot$ and $R_{\rm cloud} = 0.5$ pc. For this particular system, the central binary stars increase in mass and decrease their separation even in the case where no magnetic field is present. However, the combined mass does not even reach 5 $\mathrm{M}_\odot$ and the binary separation is almost 10 au. In other words, this is not a close high-mass system. In contrast, a magnetic field of 100 μG or more results in a binary mass exceeding 19 $\mathrm{M}_\odot$ with a separation of less than 0.12 au. The effect of the magnetic field increases with increasing field strength. In the case of the strongest field strength, 500 μG, most of the gas accreted from the cloud is stripped entirely of angular momentum. This is illustrated in the right panel of Figure 4.7 showing, in the case of the 500 μG field, practically no angular momentum is being added to the binary during accretion of material starting at radii larger than ~ 0.2 pc.

The assumption being made that each of these magnetic fields would be present throughout the entire cloud collapse is tested in Figure 4.8. The ambipolar diffusion time exceeds the free fall time of this particular cloud ($t_{\rm AD} > t_{\rm ff}$) only for field strengths up to ~ 160 μG. Hence, it is not the case that, when searching for high-mass close binaries, the stronger the field the better. As shown in Figure 4.8, a strong field may dissipate before the cloud has finished collapsing, or alternatively it might become a hindrance to the cloud collapse.

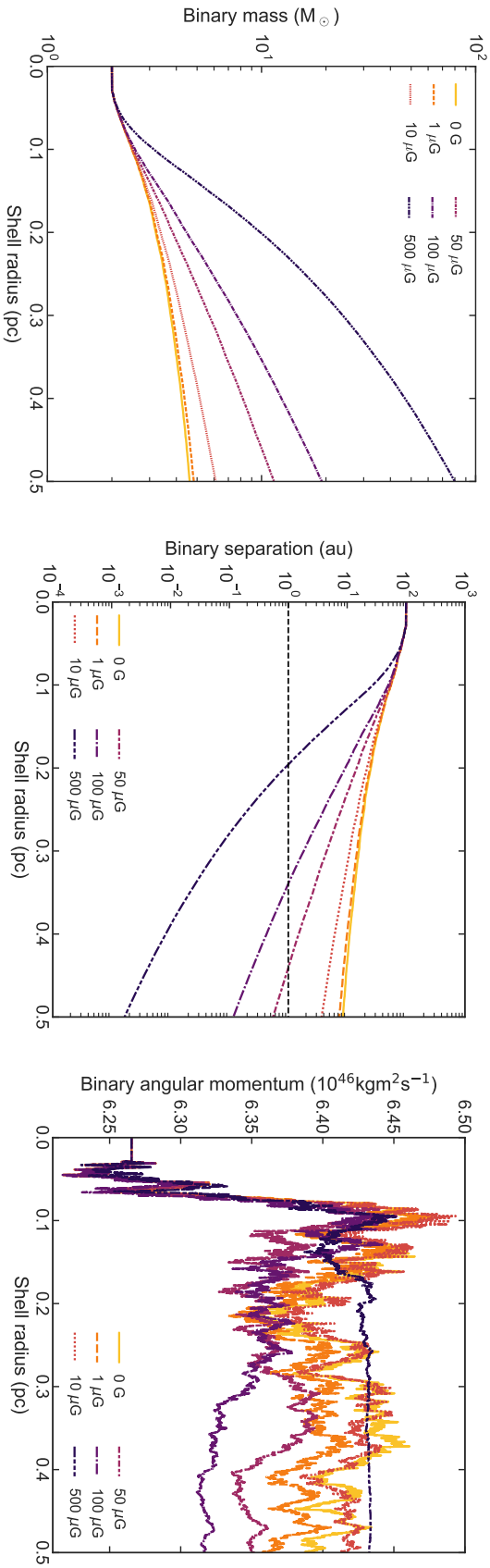

Figure 4.7: Change in binary mass (*left*), separation (*middle*) and angular momentum (*right*) as consecutive shells of a uniformly dense and turbulent molecular cloud collapses. The different coloured lines correspond to placing the clouds in magnetic fields of different strengths. The horizontal dashed line in the middle plot marks a separation of 1 au, below which binary stars are likely to merge. $M_{\rm cloud} = 500\,{\rm M}_{\odot}$, $R_{\rm cloud} = 0.5$ pc and $\Omega_{\rm cloud} = 3 \times 10^{-14}$ rad s^{-1}.

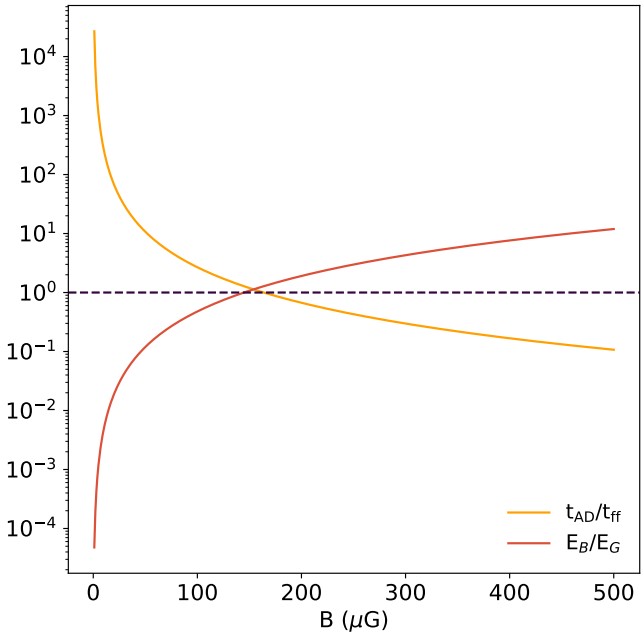

Figure 4.8: For a cloud placed in magnetic fields of different strengths, the yellow line shows the ratio of ambipolar diffusion time to free fall time (Equation 4.23) and the red line shows the ratio of magnetic energy to gravitational binding energy (Equation 4.35). The cloud considered has properties $M_{\text{cloud}} = 500$ M$_\odot$, $R_{\text{cloud}} = 0.5$ pc and $\Omega_{\text{cloud}} = 3 \times 10^{-14}$ rad s^{-1}. The purple dotted line marks where the ratios equal 1. If $t_{\text{AD}}/t_{\text{ff}} < 1$ the magnetic field will dissipate before the cloud collapses. If $E_B/E_G > 1$ the cloud is prevented from collapsing by magnetic support.

Stronger magnetic fields provide the cloud with greater magnetic support. At some point the support becomes large enough to prevent the cloud from collapsing. Similarly to how I considered the importance of the rotational and turbulent energies, the ratio of magnetic energy (Hartmann, 1998),

$$E_B = \frac{4\pi}{3\mu_0} R_{\rm cloud}^3 B_0^2, \tag{4.34}$$

to the gravitational binding energy (Equation 4.27) can be written as:

$$\frac{E_B}{E_G} = \frac{20\pi R_{\rm cloud}^4 B_0^2}{9\mu_0 G M_{\rm cloud}^2}. \tag{4.35}$$

This ratio is plotted as a function of field strength in Figure 4.8, it shows fields above ~ 225 μG will support the cloud against collapse. For the scenarios considered in Figure 4.7 with $B_0 = 1$, 10, 50, 100, 500 μG, the corresponding ratios are $E_B/E_G \approx 4.7\times10^{-5}$, 4.7×10^{-3}, 0.12, 0.47, 11.86. Gravity dominates in every case except for the 500 μG field. A more common way of estimating the level of magnetic support however is through the mass-to-flux ratio, M/ϕ_B. In units of the critical value (Equation 1.6), it relates to the above energy ratio as follows:

$$\frac{M}{\phi_B} = \frac{1}{c_1}\sqrt{\frac{E_G}{E_B}}, \tag{4.36}$$

where $c_1 \sim 0.53$ (Mouschovias & Spitzer, 1976). Hence for my range of magnetic field strengths the mass-to-flux ratios are $M/\phi_B \approx 275$, 28, 5.4, 2.8, 0.5. The system is critical ($M/\phi_B = 1$) when $E_B/E_G \approx 3.56$, corresponding to $B_0 \approx 273$ μG.

A different way of evaluating the magnetic field strength is by calculating the Alfvén Mach number, M_A, the ratio of the local flow velocity to the local Alfvén speed:

$$M_A = \frac{\Omega R}{v_A}. \tag{4.37}$$

This value changes at different points of the cloud depending on radius. Figure 4.9 shows the radial dependence for the different magnetic field strengths. The three strongest fields stay sub-Alfvénic throughout the cloud, with maximum values of ~ 0.8, 0.4 and 0.08 respectively.

In conclusion, the ideal magnetic field has to be strong enough to strip the cloud of a significant amount of angular momentum, thereby facilitating the formation of close high-mass binaries. But it also has to be weak enough that it does not prevent cloud collapse or

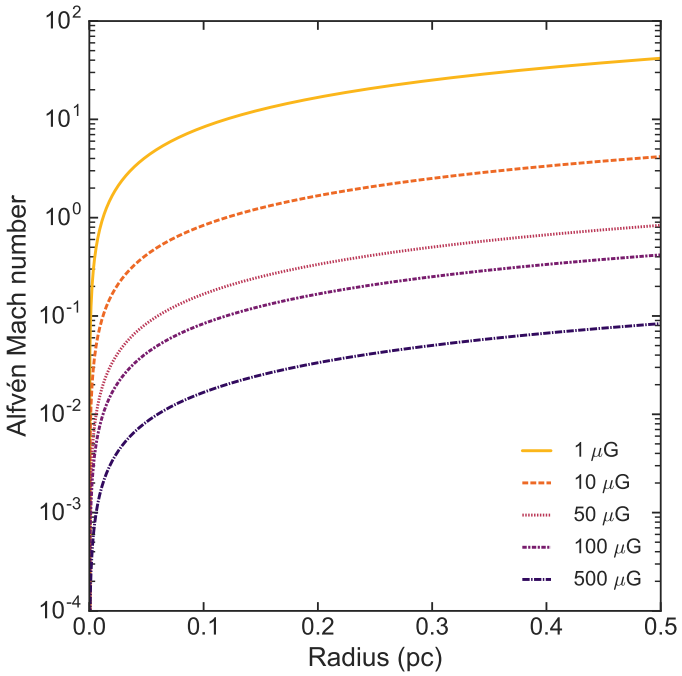

Figure 4.9: Alfvén Mach number as a function of molecular cloud radius. The different coloured lines correspond to placing the clouds in magnetic fields of different strengths. $M_{\rm cloud} = 500$ M$_\odot$, $R_{\rm cloud} = 0.5$ pc and $\Omega_{\rm cloud} = 3 \times 10^{-14}$ rad s^{-1}.

dissipate before the collapse has completed.

4.4.4 Exploring the parameter space

Up to this point I have been placing the same binary system in the same molecular cloud (properties given in Table 4.1), and changing the physics of the model or the magnetic fields strengths. In this section I will consider what happens during accretion if I place the same initial binary in molecular clouds with a variety of different combinations of masses and radii.

The y- and x- axes of the plots in figure 4.10 show cloud masses and radii respectively. I consider 20 different cloud masses ranging from 100 to 10000 $M_\odot$ and 20 different cloud radii ranging from 0.01 to 10 pc, totalling 400 simulations. The black boxes outline the approximate combinations of masses and radii of observed molecular cloud clumps associated with high-mass star formation (Urquhart et al., 2014). The colours of the images plotted correspond to the final binary mass divided by the final separation, $M_{\rm bin}/s$, resulting from placing the binary system in a molecular cloud with the properties given by the axes. Any system with $M_{\rm bin}/s$ in excess of 20 (colours ranging from light green to pink) is considered a close high-mass binary. This value corresponds to two 10 $M_\odot$ stars orbiting at 1 au.

In order to limit the total run time of the simulations, as well as avoiding unphysical systems, I set restrictions on the final binary mass and separation. If the binary system grows to a mass of 100 $M_\odot$ or the separation decreases to 0.01 au the simulation will stop regardless of how much of the cloud has yet to collapse. The most massive binary system observed is approximately 250 $M_\odot$ (Tehrani et al., 2019), so I cap the total binary mass at 100 $M_\odot$ as an order of magnitude estimate. The binary separation limit of 0.01 au corresponds to ~ 2 $R_\odot$, which means at this distance the two stars would be likely to merge even if they do not grow beyond the initial solar masses. Running the simulations with these two limits in place results in a maximum $M_{\rm bin}/s$ value of ~ 4300, corresponding to two 50 $M_\odot$ stars at a separation of ~ 5 $R_\odot$ (0.023 au).

The two plots of Figure 4.10 compare results when the binary is placed in non-magnetized molecular clouds (top plot) and clouds with a magnetic field of 100 μG (bottom plot). The smallest clouds, below 0.07 pc in radius, have small angular momenta and thus are all able to form high-mass close binaries. This is the case regardless of whether or not a magnetic field is present, in fact, in this region the two plots are identical, and the magnetic field has no effect.

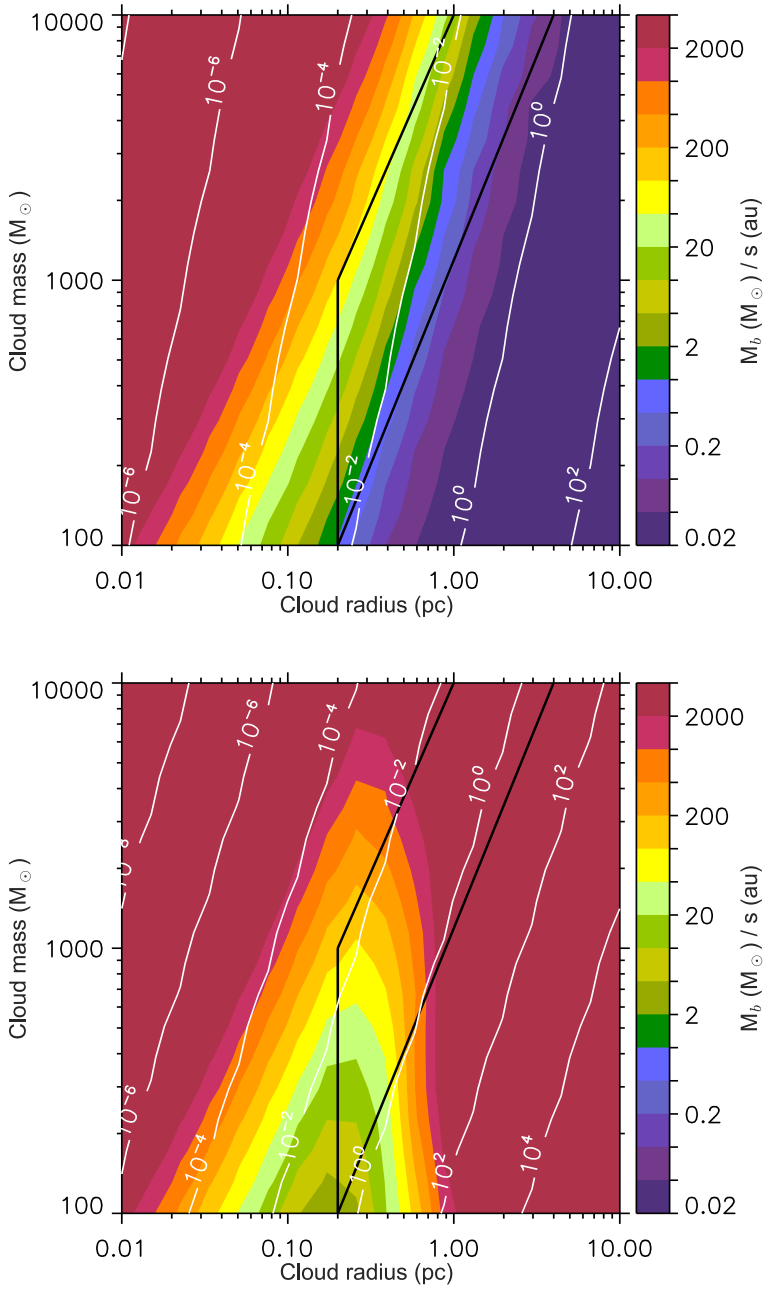

Figure 4.10: The final binary mass divided by the binary separation for uniformly dense, turbulent clouds with a range of different masses and radii. The two plots consider a non-magnetic cloud (*top*) and a cloud with a constant magnetic field of 100 μG (*bottom*). The binary mass, $M_{\rm bin}$, is restricted to be less than 100 $M_\odot$ and the binary separation, s, to be greater than 0.01 au. I consider a close high-mass binary to be one with $M_{\rm bin}/s$ in excess of 20, corresponding to two 10 $M_\odot$ stars orbiting at 1 au. The maximum value of $M_{\rm bin}/s \approx 4300$ corresponds to two 50 $M_\odot$ stars at a separation of approximately 5 $R_\odot$ (0.023 au). The black boxes outline the likely mass-radius relationship of clumps where high-mass star formation occurs (Urquhart et al., 2014). The white contour lines show $E_{\rm rot}/E_G$ (Equation 4.31) and E_B/E_G (Equation 4.35) in the top and bottom plots respectively. $\Omega_{\rm cloud} = 3 \times 10^{-14}$ rad s^{-1}.

When moving to larger clouds however the impact of the magnetic field becomes significant. In the non-magnetic case, the larger the radii, the larger the mass required to form high-mass close binaries. For a 1145 $M_\odot$ cloud with a radius of 0.26 pc, the resultant binary has a mass of 14.8 $M_\odot$ and a separation of $\sim$ 0.3 au. Beyond $\sim$ 0.9 pc the non-magnetic clouds only result in low-mass wide binaries. For instance, a 1.31 pc cloud of 1145 $M_\odot$ forms a 2.9 $M_\odot$ binary with a separation of $\sim$ 35.8 au. In contrast, the same cloud with a 100 μG field, results in a binary system of 43.1 $M_\odot$ and a separation of 0.01 au. See Table 4.5 for more example cases. With magnetic fields, it is increasingly easy to form very close, very high-mass binaries with increasing cloud radius. The size of the cloud is very important as it relates both to the free fall time (Equation 1.14), and the resultant torque strength (Equation 4.24). Larger clouds have both a larger lever-arm, and a longer time over which the torque can act.

The black boxes, which contain clouds of particular interest for high-mass star formation, fall within the parameter space where there is a big difference between the magnetic and non-magnetic case. Without a magnetic field this particular region is very limited in its ability to form moderately high-mass or close binaries; no clouds with a radii above $\sim$ 0.7 pc or a mass below $\sim$ 500 $M_\odot$ achieves this. With magnetic fields however, the vast majority of the box contains high-mass close binaries. Table 4.5 provides the final masses and separations of binaries placed in magnetic and non-magnetic clouds with masses (100–10000 $M_\odot$) and radii (0.17–2.96 pc) covering this region.

The white contour lines in Figure 4.10 show estimates of the cloud support due to either rotation or magnetic fields. The lines on the top plot represent the ratio of rotational energy to gravitational energy, gravity dominates over rotation for most of the parameter space and the entire region of interest. The lines on the bottom plot represent the ratio of the magnetic energy to gravitational energy. These could be relabelled in terms of M/ϕ_B according to Equation 4.36, for instance the two contour lines that are approximately bounding the region of interest, E_B/E_G=1, 0.01, correspond to $M/\phi_B \approx$2, 20. In general for a magnetic field of 100 μG the mass-to-flux ratio can be written as:

$$\frac{M}{\phi_B} = 0.136\left(\frac{M_{\rm cloud}}{100\ {\rm M}_\odot}\right)\left(\frac{R_{\rm cloud}}{1\ {\rm pc}}\right)^{-2}, \tag{4.38}$$

in units of the critical value. The clouds within the region of interest have mass-to-flux ratios that range from 34, at the corner with 1000 $M_\odot$ and 0.2 pc, down to 0.85 in the top right

corner. See Table 4.5 for values corresponding to specific clouds in this region. The numbers suggest there is a small section of the black box where the magnetic field would be able to support the clouds. Observations of real magnetic clouds have inferred that typical mass-to-flux ratios are supercritical with M/ϕ_B of approximately 2-3 (Crutcher, 1999; Bourke et al., 2001).

Figure 4.11 shows the ratio of the ambipolar diffusion time to free fall time (Equation 4.23) for the same clouds as presented in Figure 4.10. From left to right the three plots consider these clouds placed in magnetic fields of 1, 100 and 500 μG. A purple colour means the magnetic field would be present throughout the cloud collapse, whereas the orange corresponds to a dissipated magnetic field. In the 100 μG case there are clouds towards higher radii and lower masses where the magnetic field would likely have dissipated before the collapse had finished. This suggests the accretion model overestimates the impact of the magnetic field for these same clouds shown in the bottom plot of Figure 4.10. The clouds within the region of interest outlined in Figure 4.10 however seem to all maintain their magnetic fields, see Table 4.5 for examples of specific clouds.

4.5 Conclusions

The formation of high-mass close binary systems is problematic in any formation model of high-mass stars. Close systems cannot form from a direct fragmentation process due to their overlapping Jeans radii. Dynamical hardening of binaries is limited by the binding energy of the cluster in which the binary is formed and so is also unable to explain the origin of high-mass close binary systems. A straight accretion process is problematic due to the angular momentum likely contained within the accreted gas. As a solution I propose that magnetic braking of the accretion flow within a cluster environment can result in the formation of high-mass close binary systems.

I have developed a semi-analytic model to investigate how accretion onto a central low-mass wide binary stellar system can result in a close high-mass binary system. The model places the binary in a molecular cloud which is rotating, turbulent, and threaded by a magnetic field. The molecular cloud is made to collapse spherically with material either accreting onto the central stars, settling in a disk or escaping. My main finding was that the addition of a magnetic field parallel to the rotation axis can have a significant effect on the accretion process.

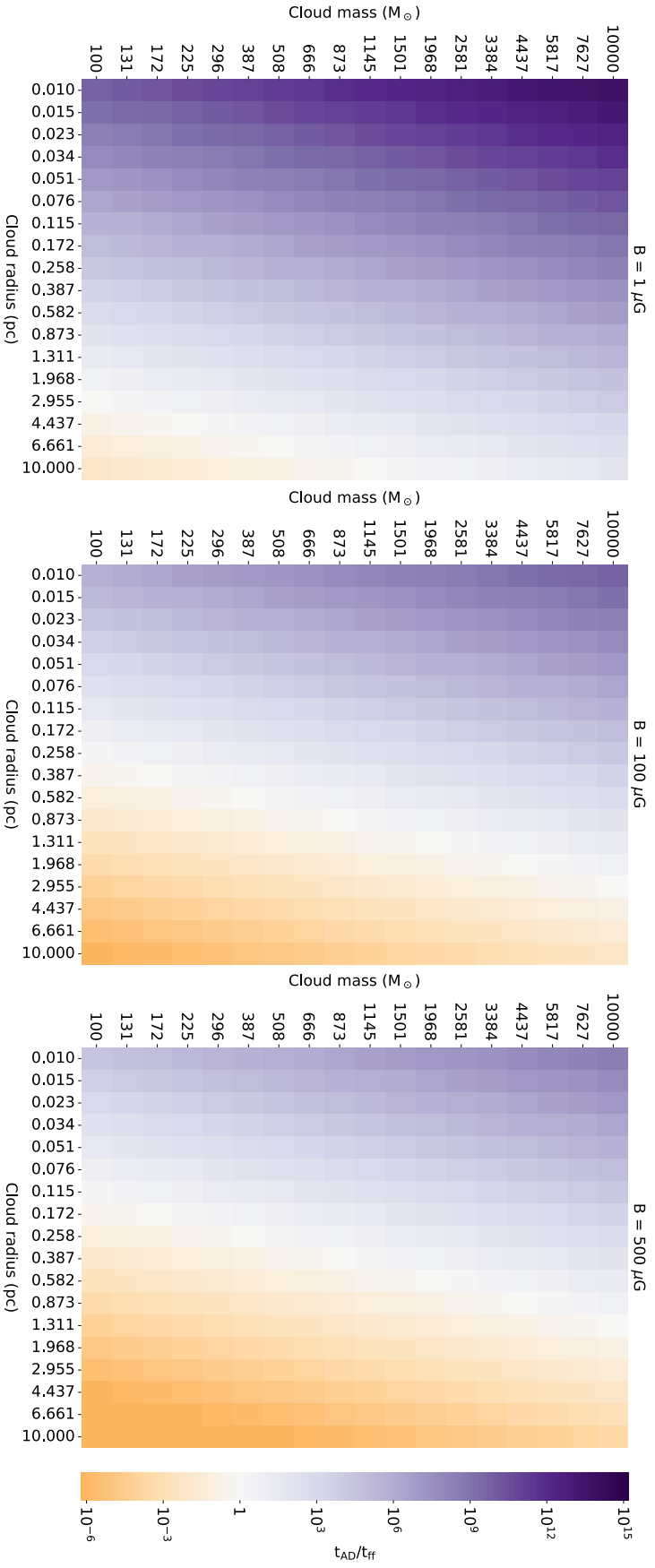

Figure 4.11: Ratio of ambipolar diffusion time to free fall time (Equation 4.23) for clouds with a range of different masses and radii placed in magnetic fields of three different strengths. The purple regions represent cases where the cloud collapses before the magnetic field dissipates.

Through magnetic braking it allows for the accretion of mass while limiting the gain in angular momentum, hence easing the formation of high-mass close binaries. Typical molecular clouds with 1145 $M_\odot$, a radius of 0.58 pc and a magnetic field of 100 μG results in the formation of a high-mass binary system with a separation as close as 10 solar radii. This corresponds to a mass-to-flux ratio of 4.6 times the critical value, which is greater than the typical values of $\sim$ 2-3. This suggests the magnetic field strength in this particular cloud could reasonably be doubled, which would lead to even higher binary masses and even smaller separations.

My model is admittedly simple, with a number of limitations and assumptions, but the physical processes highlighted should still occur and should aid in the formation of close high-mass binary stars. Hence I conclude that through my simulations I have achieved a proof of concept; magnetic braking is at the very least a feasible way of forming the most massive close binary systems. In the future, detailed numerical simulations of the formation of a stellar cluster including non-ideal magnetic fields, ambipolar diffusion, turbulence and stellar feedback are needed to verify my conclusion.

4.A Data

Table 4.2: A comparison of the final masses and separations of binaries after accretion in magnetic and non-magnetic clouds with a range of different masses and radii. The range of masses and radii presented here are chosen based on typical values for clouds where high-mass star formation occurs (Urquhart et al., 2014). The columns show cloud mass, cloud radius, binary mass and separation (non-magnetic and magnetic case), the mass-to-flux ratio and the ratio of the ambipolar diffusion time to free fall time of the magnetic clouds.

Cloud properties		Results using non-magnetic clouds		Results using magnetic clouds (100 μG)			
$M_{\rm cloud}$ ($M_\odot$)	$R_{\rm cloud}$ (pc)	$M_{\rm bin}$ ($M_\odot$)	s (au)	$M_{\rm bin}$ ($M_\odot$)	s (au)	M/ϕ_B	t_{AD}/t_{ff}
100	0.17	5.9	4.536	6.8	2.713	4.71	7.67E+00
100	0.26	4.1	11.964	7.4	2.062	2.01	1.51E+00
100	0.39	3.0	31.842	11.3	0.596	0.89	2.97E-01
100	0.58	2.4	55.494	17.7	0.143	0.40	5.85E-02
100	0.87	2.2	75.910	31.9	0.025	0.18	1.15E-02
100	1.31	2.1	88.911	43.1	0.010	0.08	2.27E-03
100	1.97	2.0	95.943	43.1	0.010	0.04	4.46E-04
100	2.96	2.0	97.825	43.1	0.010	0.02	8.78E-05
131	0.17	6.7	3.074	7.6	2.004	6.16	1.32E+01
131	0.26	4.7	8.806	8.0	1.511	2.64	2.60E+00
131	0.39	3.3	22.429	11.7	0.560	1.17	5.11E-01
131	0.58	2.6	48.019	19.4	0.111	0.53	1.01E-01
131	0.87	2.2	72.280	34.4	0.020	0.24	1.98E-02
131	1.31	2.1	85.851	43.1	0.010	0.10	3.90E-03
131	1.97	2.0	96.837	43.1	0.010	0.05	7.67E-04

Table 4.5 - *continued*

$M_{\rm cloud}$ ($M_\odot$)	$R_{\rm cloud}$ (pc)	$M_{\rm bin}$ ($M_\odot$)	s (au)	$M_{\rm bin}$ ($M_\odot$)	s (au)	M/ϕ_B	$t_{\rm AD}/t_{\rm ff}$
131	2.96	2.0	97.687	43.1	0.010	0.02	1.51E-04
171	0.17	8.0	1.990	8.6	1.460	8.05	2.27E+01
171	0.26	5.2	5.371	8.6	1.292	3.44	4.46E+00
171	0.39	3.6	17.586	12.0	0.479	1.53	8.78E-01
171	0.58	2.8	39.102	21.4	0.084	0.69	1.73E-01
171	0.87	2.3	64.400	37.1	0.016	0.31	3.40E-02
171	1.31	2.1	84.479	43.1	0.010	0.14	6.70E-03
171	1.97	2.0	94.365	43.1	0.010	0.06	1.32E-03
171	2.96	2.0	96.167	43.1	0.010	0.03	2.60E-04
225	0.17	9.0	1.323	9.6	1.034	10.59	3.90E+01
225	0.26	6.1	3.845	9.4	0.975	4.53	7.67E+00
225	0.39	4.1	12.554	12.4	0.432	2.01	1.51E+00
225	0.58	2.9	32.285	23.3	0.062	0.91	2.97E-01
225	0.87	2.4	56.618	39.8	0.013	0.40	5.85E-02
225	1.31	2.2	80.242	43.1	0.010	0.18	1.15E-02
225	1.97	2.1	90.510	43.1	0.010	0.08	2.27E-03
225	2.96	2.0	95.782	43.1	0.010	0.03	4.46E-04
295	0.17	10.3	0.892	10.8	0.730	13.88	6.70E+01
295	0.26	7.0	2.395	10.3	0.724	5.93	1.32E+01
295	0.39	4.7	8.105	13.0	0.352	2.64	2.60E+00
295	0.58	3.2	23.117	24.1	0.057	1.19	5.11E-01
295	0.87	2.5	50.395	43.2	0.010	0.53	1.01E-01
295	1.31	2.2	71.260	43.0	0.010	0.23	1.98E-02
295	1.97	2.1	87.660	43.1	0.010	0.10	3.90E-03
295	2.96	2.0	92.714	43.1	0.010	0.05	7.67E-04
387	0.17	11.7	0.558	12.6	0.547	18.21	1.15E+02
387	0.26	8.1	1.603	11.6	0.566	7.79	2.27E+01
387	0.39	5.4	5.545	13.9	0.318	3.46	4.46E+00
387	0.58	3.5	16.749	24.3	0.055	1.56	8.78E-01
387	0.87	2.7	40.946	43.4	0.010	0.70	1.73E-01
387	1.31	2.3	65.431	43.2	0.010	0.31	3.40E-02
387	1.97	2.1	85.799	43.1	0.010	0.14	6.70E-03
387	2.96	2.0	94.450	43.1	0.010	0.06	1.32E-03
508	0.17	13.6	0.385	14.1	0.364	23.91	1.98E+02
508	0.26	9.3	1.046	12.8	0.418	10.22	3.90E+01
508	0.39	6.1	3.783	14.8	0.246	4.54	7.67E+00
508	0.58	4.0	12.296	24.2	0.055	2.05	1.51E+00
508	0.87	2.9	34.033	43.8	0.010	0.91	2.97E-01
508	1.31	2.4	55.722	43.1	0.010	0.40	5.85E-02
508	1.97	2.2	79.339	43.1	0.010	0.18	1.15E-02
508	2.96	2.1	90.504	43.1	0.010	0.08	2.27E-03
666	0.17	15.3	0.255	15.9	0.250	31.34	3.40E+02
666	0.26	10.9	0.679	14.0	0.283	13.40	6.70E+01
666	0.39	7.2	2.410	16.2	0.186	5.96	1.32E+01
666	0.58	4.6	9.205	24.3	0.060	2.69	2.60E+00
666	0.87	3.2	26.329	43.5	0.010	1.20	5.11E-01
666	1.31	2.5	52.910	43.2	0.010	0.53	1.01E-01
666	1.97	2.2	73.549	43.2	0.010	0.23	1.98E-02
666	2.96	2.1	89.430	43.1	0.010	0.10	3.90E-03
873	0.17	17.9	0.171	18.1	0.163	41.08	5.85E+02
873	0.26	12.3	0.448	15.9	0.237	17.56	1.15E+02
873	0.39	8.2	1.478	17.9	0.151	7.81	2.27E+01

Table 4.5 - *continued*

$M_{\rm cloud}$ ($M_\odot$)	$R_{\rm cloud}$ (pc)	$M_{\rm bin}$ ($M_\odot$)	s (au)	$M_{\rm bin}$ ($M_\odot$)	s (au)	M/ϕ_B	$t_{\rm AD}/t_{\rm ff}$
873	0.58	5.2	6.452	25.2	0.051	3.53	4.46E+00
873	0.87	3.5	18.465	43.2	0.010	1.57	8.78E-01
873	1.31	2.7	42.567	43.4	0.010	0.69	1.73E-01
873	1.97	2.3	68.581	43.1	0.010	0.31	3.40E-02
873	2.96	2.1	86.393	43.1	0.010	0.14	6.70E-03
1145	0.17	20.9	0.114	20.7	0.111	53.88	1.01E+03
1145	0.26	14.8	0.297	17.8	0.174	23.04	1.98E+02
1145	0.39	9.5	0.999	20.0	0.117	10.24	3.90E+01
1145	0.58	5.9	3.842	26.5	0.046	4.63	7.67E+00
1145	0.87	3.9	13.220	43.1	0.010	2.06	1.51E+00
1145	1.31	2.9	35.801	43.1	0.010	0.91	2.97E-01
1145	1.97	2.4	59.899	43.1	0.010	0.40	5.85E-02
1145	2.96	2.1	82.678	43.2	0.010	0.18	1.15E-02
1501	0.17	24.2	0.076	23.5	0.073	70.64	1.73E+03
1501	0.26	16.9	0.189	19.6	0.124	30.20	3.40E+02
1501	0.39	11.1	0.647	22.0	0.089	13.42	6.70E+01
1501	0.58	7.0	2.593	28.3	0.035	6.07	1.32E+01
1501	0.87	4.4	9.816	44.1	0.010	2.70	2.60E+00
1501	1.31	3.1	27.775	43.5	0.010	1.19	5.11E-01
1501	1.97	2.5	55.977	43.4	0.010	0.53	1.01E-01
1501	2.96	2.2	77.021	43.2	0.010	0.23	1.98E-02
1968	0.17	27.1	0.049	27.3	0.051	92.61	2.97E+03
1968	0.26	19.2	0.129	21.6	0.086	39.59	5.85E+02
1968	0.39	12.8	0.417	23.8	0.065	17.60	1.15E+02
1968	0.58	8.1	1.628	31.0	0.028	7.96	2.27E+01
1968	0.87	5.0	6.584	42.6	0.010	3.54	4.46E+00
1968	1.31	3.3	21.737	42.8	0.010	1.56	8.78E-01
1968	1.97	2.6	47.504	43.4	0.010	0.69	1.73E-01
1968	2.96	2.2	71.746	43.2	0.010	0.31	3.40E-02
2580	0.17	31.9	0.037	29.7	0.034	121.41	5.11E+03
2580	0.26	21.6	0.095	24.6	0.064	51.91	1.01E+03
2580	0.39	14.6	0.288	25.9	0.044	23.07	1.98E+02
2580	0.58	8.5	1.191	33.9	0.022	10.43	3.90E+01
2580	0.87	5.3	5.811	42.2	0.010	4.64	7.67E+00
2580	1.31	3.6	18.469	43.3	0.010	2.04	1.51E+00
2580	1.97	2.6	42.746	43.2	0.010	0.90	2.97E-01
2580	2.96	2.3	70.531	43.2	0.010	0.40	5.85E-02
3383	0.17	37.3	0.024	32.7	0.021	159.20	8.78E+03
3383	0.26	25.6	0.061	27.6	0.049	68.06	1.73E+03
3383	0.39	17.1	0.186	28.9	0.034	30.25	3.40E+02
3383	0.58	10.6	0.694	37.0	0.018	13.68	6.70E+01
3383	0.87	6.0	3.527	42.5	0.010	6.08	1.32E+01
3383	1.31	4.0	12.397	42.1	0.010	2.68	2.60E+00
3383	1.97	3.0	30.322	43.3	0.010	1.19	5.11E-01
3383	2.96	2.4	65.065	43.5	0.010	0.53	1.01E-01
4436	0.17	44.5	0.017	39.7	0.015	208.75	1.51E+04
4436	0.26	29.4	0.039	30.5	0.030	89.24	2.97E+03
4436	0.39	19.0	0.107	31.1	0.031	39.66	5.85E+02
4436	0.58	13.7	0.469	41.0	0.012	17.93	1.15E+02
4436	0.87	7.1	2.099	42.7	0.010	7.97	2.27E+01
4436	1.31	4.6	8.925	43.9	0.010	3.52	4.46E+00
4436	1.97	3.1	28.671	43.0	0.010	1.55	8.78E-01

Table 4.5 - *continued*

$M_{\rm cloud}$ ($M_\odot$)	$R_{\rm cloud}$ (pc)	$M_{\rm bin}$ ($M_\odot$)	s (au)	$M_{\rm bin}$ ($M_\odot$)	s (au)	M/ϕ_B	t_{AD}/t_{ff}
4436	2.96	2.4	62.446	43.2	0.010	0.69	1.73E-01
5817	0.17	47.0	0.010	49.4	0.010	273.74	2.60E+04
5817	0.26	34.7	0.026	36.3	0.025	117.03	5.11E+03
5817	0.39	24.0	0.075	33.7	0.018	52.01	1.01E+03
5817	0.58	14.4	0.316	43.4	0.010	23.52	1.98E+02
5817	0.87	8.3	1.128	42.5	0.010	10.45	3.90E+01
5817	1.31	5.5	6.133	43.4	0.010	4.61	7.67E+00
5817	1.97	3.5	21.598	42.7	0.010	2.04	1.51E+00
5817	2.96	2.7	41.738	43.2	0.010	0.90	2.97E-01
7626	0.17	42.5	0.010	48.7	0.010	358.87	4.46E+04
7626	0.26	39.4	0.017	38.8	0.015	153.42	8.78E+03
7626	0.39	28.0	0.047	38.2	0.015	68.19	1.73E+03
7626	0.58	17.6	0.190	45.0	0.010	30.83	3.40E+02
7626	0.87	10.4	0.798	46.4	0.010	13.70	6.70E+01
7626	1.31	5.8	3.615	44.3	0.010	6.04	1.32E+01
7626	1.97	3.9	12.354	43.1	0.010	2.67	2.60E+00
7626	2.96	2.7	37.635	43.5	0.010	1.18	5.11E-01
10000	0.17	45.4	0.010	52.4	0.010	470.59	7.67E+04
10000	0.26	41.2	0.010	46.5	0.011	201.18	1.51E+04
10000	0.39	30.1	0.028	42.2	0.012	89.41	2.97E+03
10000	0.58	19.6	0.112	42.8	0.010	40.43	5.85E+02
10000	0.87	12.7	0.508	38.3	0.010	17.97	1.15E+02
10000	1.31	7.0	2.315	44.5	0.010	7.92	2.27E+01
10000	1.97	4.6	9.877	43.8	0.010	3.50	4.46E+00
10000	2.96	3.0	28.118	43.4	0.010	1.55	8.78E-01

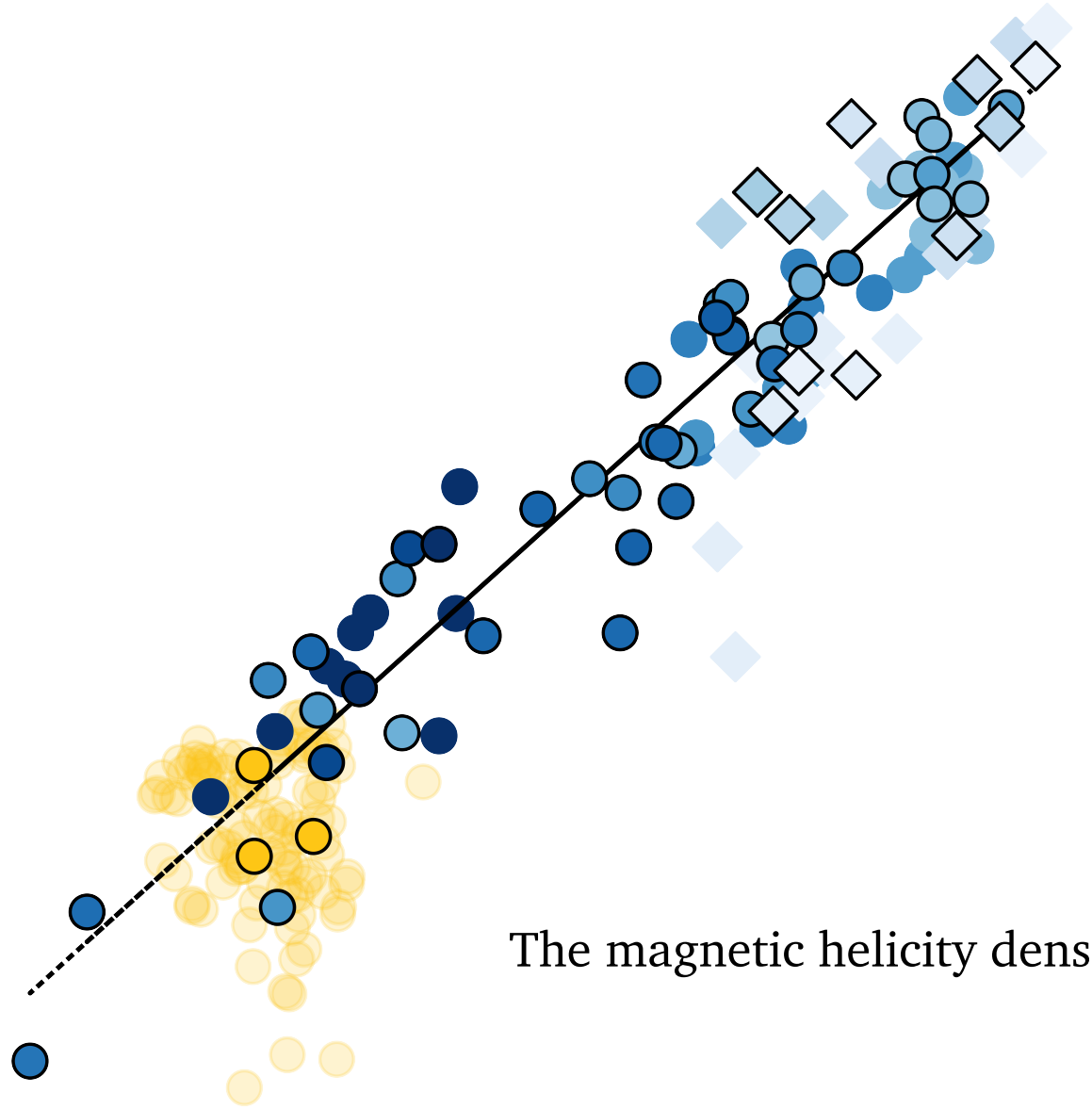

5

The magnetic helicity density of stars

This chapter is based on Lund et al. (2020). Prior to this work, studies of the helicity of stellar magnetic fields were focused on one star - the sun. In this chapter I provide an expression for calculating the large-scale magnetic helicity density across the surface of any star, using only observable quantities. For a sample of 51 stars, I present the first estimates of stellar magnetic helicity density and show how it relates to a number of other stellar properties. Furthermore, I explore how the stellar values compare to the large-scale helicity density of the Sun across a solar cycle.

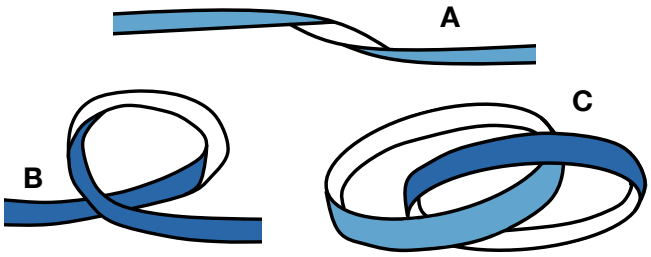

Figure 5.1: Illustration showing twist (A), writhe (B) and linkage (C). By imagining the ends of B are pulled further apart, or the ends of A are pushed closer together, it becomes clear that twist and writhe are essentially the same property.

5.1 Introduction

The helicity of a magnetic field (H) relates to its structural properties and can be described as a measure of the twist, writhe and linkage (illustrated in Figure 5.1) of the magnetic field lines within some volume, V (Berger & Field, 1984). Helicity is conserved fully in ideal MHD (Woltjer, 1958), as well as to an excellent degree in non-ideal MHD (Taylor, 1974; Berger & Field, 1984). This makes it one of the most powerful measures of a magnetic field, and fundamental to our understanding of magnetic field generation and evolution (Brandenburg & Subramanian, 2005; Chatterjee et al., 2011). For a good primer on helicity, see Blackman (2015).

Mathematically, helicity can be defined in terms of the vector potential, $\boldsymbol{A}$, and the corresponding magnetic field ($\boldsymbol{B} = \boldsymbol{\nabla} \times \boldsymbol{A}$) as (Woltjer, 1958):

$$H = \int \boldsymbol{A} \cdot \boldsymbol{B} \mathrm{dV}. \tag{5.1}$$

This reveals one of the inherent challenges in determining helicity; depending on the circumstances, the answer may not be unique. Gauge transformations of the vector potential results in the same magnetic field, but not necessarily the same helicity. Given $A \rightarrow A + \nabla\psi$, the corresponding change in helicity is $\Delta H = \int \nabla\psi \cdot \boldsymbol{B} \mathrm{dV} = \oint_S \psi \boldsymbol{B} \cdot \hat{\boldsymbol{n}} \mathrm{dS}$. For a volume bounded by a closed magnetic surface this problem is resolved as $\boldsymbol{B} \cdot \hat{\boldsymbol{n}}|_S = 0$, ensuring a gauge-invariant helicity. However, if field lines cross the boundary, helicity must be measured relative to some reference field. This is normally chosen to be the potential field with the same boundary flux as the magnetic field of interest (Berger & Field, 1984).

To date helicity has been measured for the Sun, but not other stars. There are many areas of current solar research where helicity plays a significant role, but I limit my discussion here to helicity in relation to solar activity. For a more detailed, yet concise, review of this subject see Nindos (2013). Considering magnetic helicity is well preserved, the amount of helicity in an active region will depend on how much helicity is injected into the region and how much is carried away. Helicity is injected by magnetic field lines emerging from the convection zone and by motions parallel to the surface. Studies of differential rotation (Démoulin et al., 2002; Green et al., 2002) and shearing motions (Nindos & Zhang, 2002) in active regions suggest neither is the dominant source of helicity, leaving magnetic flux emergence as the top contender. Accumulated helicity can be expelled from the solar active regions into the ISM via ejecta (Berger & Ruzmaikin, 2000; Zhang & Low, 2005; Zhang, 2013). In fact, Rust (1994) proposed CMEs are a direct result of the conservation of helicity, necessary in order to remove excess helicity from the Sun. Subsequently helicity has been studied extensively as a diagnostic of solar eruptivity.

Theoretical studies have been done on how much magnetic helicity can be stored in various field configurations, it is suggested that if helicity accumulates in the corona beyond a certain limit it initiates a non-equilibrium situation, prompting a CME (Zhang et al., 2006; Zhang & Flyer, 2008; Zhang et al., 2012; Nindos, 2013). A number of authors have argued against this, presenting models which indicate either that helicity might be necessary for an eruption to take place, but not sufficient (Amari et al., 2003), or that eruptions are triggered completely independently of helicity (Phillips et al., 2005). Somewhere in between lies Pariat et al. (2017). In an attempt to improve space weather predictions, they ran a series of eruptive and non-eruptive simulations and tested various quantities as diagnostics of solar eruptivity. They find the total helicity is a poor proxy for eruptivity, however the ratio of current carrying magnetic helicity to total helicity is very effective at predicting eruptions. Zuccarello et al. (2018) takes this idea one step further by suggesting this ratio has a threshold value.

Despite there not being a consensus on which role helicity plays in triggering solar eruptions, if any, studies such as the ones just mentioned have motivated numerous authors to attempt measurements of magnetic helicity in the solar atmosphere - see reviews by Démoulin (2007) and Démoulin & Pariat (2009). Calculations of the helicity of solar active regions based on magnetograms reveal statistically higher values for eruptive active regions (Nindos & Andrews, 2004; Tziotziou et al., 2012). On a larger scale, calculations of helicity flux across the

northern and southern solar hemisphere, using data sets spanning 60 years, suggest it is a property that can be used to predict the amount of solar activity up to five years in advance (Hawkes & Berger, 2018).

Magnetic helicity in stellar research is not as well studied as the solar case, and no measurements have been made based on observations. Most recently, Warnecke & Peter (2019) used 3D MHD simulations to model the corona of solar-like stars. By injecting different amounts of magnetic helicity into the model and calculating the X-ray emission flux of each simulation they find the rise in X-ray emission with increasing rotation rate can only be explained through the variation in the helicity.

My work in this chapter extends the study of magnetic helicity from the Sun to a large sample of stars using observations of magnetic fields at stellar surfaces. The fields are split into poloidal and toroidal field components ($\boldsymbol{B} = \boldsymbol{B}_{\rm pol} + \boldsymbol{B}_{\rm tor}$), as Berger (1985) and Berger & Hornig (2018) describe in detail how this decomposition allows for a simple expression of helicity as the net linking of toroidal and poloidal fields. This particular field decomposition has the added advantage of avoiding the need for a reference field; since the corresponding potential field with the same boundary flux is purely poloidal, it has zero helicity.

The poloidal and toroidal field components for my stellar sample come from stellar magnetic maps obtained using the ZDI technique described in Section 1.3.1. Since ZDI only provides *surface* magnetic fields, as illustrated in in Figure 5.2, there is not enough information available to calculate magnetic helicity; a quantity defined within a *volume*. Consequently, I consider magnetic helicity density evaluated at the stellar surfaces instead. Furthermore, because ZDI only observes large-scale magnetic field topology, I am limited to exploring the large-scale helicity density of stars.

By also applying the technique to observed and simulated solar magnetograms, which combined almost span both solar cycle 23 and 24, the Sun can be be used to help interpret the stellar observations. Despite a large range of length scales being available for the solar data, I reduce its resolution to mimic lack of sensitivity to small-scale fields. This makes it easier to compare the Sun to the rest of the stars.

Interestingly, Pipin et al. (2019) recently also used poloidal and toroidal field components to calculate the evolution of the magnetic helicity density of the Sun across solar cycle 24. But whereas my focus is on the large-scale helicity density of a sample of stars, the sun being

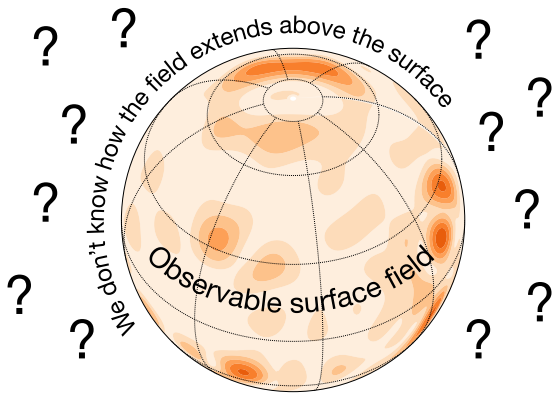

Figure 5.2: The magnetic field of a star can be measured at the surface of the star, however the radial extension of the field is unknown.

merely one of them, their work is solely on the Sun. They explore in depth the relationship between the small-scale and large-scale solar helicity density over time. According to their results, the two start off with opposite signs at the beginning of the solar cycle and evolve to show the same sign in the declining phase. Furthermore they measure the large-scale helicity density to be an order of magnitude smaller than the small-scale helicity density.

In this chapter I present a simple equation for helicity density, given the poloidal and toroidal decomposition of any stellar magnetic field and the corresponding stellar radius. I use this expression to study the large-scale helicity density of the Sun and 51 additional stars. The stellar sample consists of F, G, K and M stars, with masses spanning 0.1–1.34 $M_\odot$. My aim is to discover how the stellar helicity density of these stars relates to other stellar properties, and to interpret the results in the context of the evolution of solar helicity density throughout the solar cycle.

5.2 Calculating magnetic helicity density

The magnetic helicity density is given by the integrand of Equation 5.1:

$$h = \boldsymbol{A} \cdot \boldsymbol{B}. \tag{5.2}$$

The magnetic field and vector potential field are expanded into their poloidal and toroidal components as follows:

$$h = (\boldsymbol{A}_{\rm pol} + \boldsymbol{A}_{\rm tor}) \cdot (\boldsymbol{B}_{\rm tor} + \boldsymbol{B}_{\rm pol}). \tag{5.3}$$

An expression for the magnetic field is derived in Section 5.2.1, a corresponding vector potential is calculated in Section 5.2.2, and I combine them to obtain an expression for the helicity density in Section 5.2.3.

5.2.1 Magnetic field components

The stellar magnetic field is decomposed in terms of a poloidal and toroidal component following Appendix III of Chandrasekhar (1961):

$$\boldsymbol{B}_{\rm pol} = \boldsymbol{\nabla} \times [\boldsymbol{\nabla} \times [\Phi \hat{\boldsymbol{r}}]], \tag{5.4}$$

$$\boldsymbol{B}_{\rm tor} = \boldsymbol{\nabla} \times [\Psi \hat{\boldsymbol{r}}]. \tag{5.5}$$

In a spherical coordinate system[1] the scalars Φ and Ψ can be written in terms of spherical harmonics as:

$$\Phi = S(r) c_{lm} P_{lm} e^{im\phi}, \tag{5.6}$$

$$\Psi = T(r) c_{lm} P_{lm} e^{im\phi}. \tag{5.7}$$

$S(r)$ and $T(r)$ are functions describing the radial behaviour of the field, P_{lm} is short for the Legendre Polynomial $P_{lm}(\cos\theta)$ of mode l and order m, and c_{lm} is the associated normalisation constant:

$$c_{lm} = \sqrt{\frac{2l+1}{4\pi}\frac{(l-m)!}{(l+m)!}}. \tag{5.8}$$

Expanding the poloidal and toroidal field components gives the following expressions:

$$\begin{aligned} \boldsymbol{B}_{\rm pol}(r,\theta,\phi) = &\sum_{lm} \frac{l(l+1)}{r^2} S(r) c_{lm} P_{lm} e^{im\phi} \hat{\boldsymbol{r}} \\ &+ \sum_{lm} \frac{1}{r}\frac{\mathrm{d}S(r)}{\mathrm{d}r} c_{lm} \frac{\mathrm{d}P_{lm}}{\mathrm{d}\theta} e^{im\phi} \hat{\boldsymbol{\theta}} \\ &+ \sum_{lm} \frac{im}{r\sin\theta}\frac{\mathrm{d}S(r)}{\mathrm{d}r} c_{lm} P_{lm} e^{im\phi} \hat{\boldsymbol{\phi}}, \end{aligned} \tag{5.9}$$

[1] I am using a right-handed spherical coordinate system where a positive radial field component points out of the star, the meridional (θ) component is positive pointing from North to South and the azimuthal (ϕ) component is positive in the clockwise direction as viewed from the South pole

$$\begin{aligned}\boldsymbol{B}_{\text{tor}}(r,\theta,\phi) = &\sum_{lm} \frac{T(r) im}{r\sin\theta} c_{lm} P_{lm} e^{im\phi}\,\hat{\boldsymbol{\theta}} \\ &-\sum_{lm} \frac{T(r)}{r} c_{lm} \frac{\mathrm{d}P_{lm}}{\mathrm{d}\theta} e^{im\phi}\,\hat{\boldsymbol{\phi}}.\end{aligned} \tag{5.10}$$

The sums $\sum_{lm}$ run from mode $l = 1$ to $l = l_{\text{max}}$, and from order $m = -l$ to $m = l$, where the maximum mode depends on the resolution of the data available.

5.2.2 Vector potential fields

Having determined a general magnetic field expression, the next step is deducing a corresponding vector potential field $\boldsymbol{A}$:

$$\boldsymbol{B} = \nabla \times \boldsymbol{A}. \tag{5.11}$$

Given Equations 5.4 and 5.5, it follows that the poloidal and toroidal components of the vector potential field are:

$$\boldsymbol{A}_{\text{pol}} = \boldsymbol{\nabla} \times [\Phi \hat{\boldsymbol{r}}], \tag{5.12}$$

$$\boldsymbol{A}_{\text{tor}} = \Psi \hat{\boldsymbol{r}}. \tag{5.13}$$

Substituting Equations 5.6 and 5.7 for Φ and Ψ results in:

$$\begin{aligned}\boldsymbol{A}_{\text{pol}} = &\sum_{lm} \frac{im}{r\sin\theta} S(r) c_{lm} P_{lm} e^{im\phi}\,\hat{\boldsymbol{\theta}} \\ &-\sum_{lm} \frac{1}{r} S(r) c_{lm} \frac{\mathrm{d}P_{lm}}{\mathrm{d}\theta} e^{im\phi}\,\hat{\boldsymbol{\phi}},\end{aligned} \tag{5.14}$$

$$\boldsymbol{A}_{\text{tor}} = \sum_{lm} T(r) c_{lm} P_{lm} e^{im\phi}\,\hat{\boldsymbol{r}}. \tag{5.15}$$

5.2.3 Helicity density

When expanding Equation 5.3 it follows from the properties of curl that both $\boldsymbol{A}_{\text{pol}} \cdot \boldsymbol{B}_{\text{pol}}$ and $\boldsymbol{A}_{\text{tor}} \cdot \boldsymbol{B}_{\text{tor}}$ are zero. Consequently the helicity density equation simplifies to:

$$h = \boldsymbol{A}_{\text{pol}} \cdot \boldsymbol{B}_{\text{tor}} + \boldsymbol{A}_{\text{tor}} \cdot \boldsymbol{B}_{\text{pol}}. \tag{5.16}$$

By inserting the magnetic field from Section 5.2.1 (Equations 5.9 and 5.10) and the vector potential from Section 5.2.2 (Equations 5.14 and 5.15), the real part of the magnetic helicity

density is given by:

$$h(r,\theta,\phi) = \mathrm{Re}\Bigg(\sum_{lm}\sum_{l'm'} \frac{1}{r^2} S(r)T(r) c_{lm} c_{l'm'} e^{i\phi(m+m')} \\ \left(P_{lm} P_{l'm'} \left(l(l+1) - \frac{mm'}{\sin^2\theta} \right) + \frac{\mathrm{d}P_{lm}}{\mathrm{d}\theta} \frac{\mathrm{d}P_{l'm'}}{\mathrm{d}\theta} \right) \Bigg). \tag{5.17}$$

As the helicity density is calculated by taking the dot product of sums running between the same limits, the toroidal components have been denoted with a prime in order to distinguish the different sums.

The radial functions $S(r)$ and $T(r)$ are the only terms in Equation 5.17 that require information about the specific star considered. Using the ZDI technique (Semel, 1989), large scale magnetic fields can be determined at stellar surfaces ($\mathrm{r} = R_\star$), which provides values for $S(R_\star)$ and $T(R_\star)$. Unfortunately it is unknown how the stellar magnetic field extends beyond this, hence the magnetic helicity density can only be evaluated at the stellar surface.

The observed magnetic surface fields are decomposed into poloidal and toroidal components (e.g. Donati et al., 2006; Vidotto, 2016):

$$\begin{aligned} \boldsymbol{B}_{\mathrm{pol}}(\theta,\phi) = & \sum_{lm} \alpha_{lm} c_{lm} P_{lm} e^{im\phi} \hat{\boldsymbol{r}} \\ & + \sum_{lm} \frac{\beta_{lm}}{(l+1)} c_{lm} \frac{\mathrm{d}P_{lm}}{\mathrm{d}\theta} e^{im\phi} \hat{\boldsymbol{\theta}} \\ & + \sum_{lm} \frac{\beta_{lm} im}{(l+1)\sin\theta} c_{lm} P_{lm} e^{im\phi} \hat{\boldsymbol{\phi}}, \end{aligned} \tag{5.18}$$

$$\begin{aligned} \boldsymbol{B}_{\mathrm{tor}}(\theta,\phi) = & \sum_{lm} \frac{\gamma_{lm} im}{(l+1)\sin\theta} c_{lm} P_{lm} e^{im\phi} \hat{\boldsymbol{\theta}} \\ & - \sum_{lm} \frac{\gamma_{lm}}{(l+1)} c_{lm} \frac{\mathrm{d}P_{lm}}{\mathrm{d}\theta} e^{im\phi} \hat{\boldsymbol{\phi}}, \end{aligned} \tag{5.19}$$

which are characterised by α_{lm}, β_{lm}, and γ_{lm} coefficients[2]. A detailed description of how these coefficients are determined given observational data in the form of radial, meridional and azimuthal magnetic field components can be found in Vidotto (2016). Equating this surface field with the full magnetic field (Equations 5.9 and 5.10) evaluated at $r = R_\star$; $\boldsymbol{B}(\theta,\phi) =$

[2]The data I use throughout this chapter, describing magnetic maps of my stellar sample (see Table 5.2) and the Sun, is in the form of α_{lm}, β_{lm}, and γ_{lm} coefficients.

$\boldsymbol{B}(R_\star, \theta, \phi)$, gives:

$$S(R_\star) = \frac{\alpha_{lm} R_\star^2}{l(l+1)}, \tag{5.20}$$

$$T(R_\star) = \frac{\gamma_{lm} R_\star}{(l+1)}. \tag{5.21}$$

Having established expressions for $S(R_\star)$ and $T(R_\star)$, Equation 5.17 can be evaluated at $r = R_\star$, which gives the magnetic helicity density at any point (θ, ϕ) on the stellar surface:

$$\begin{aligned} h(R_\star, \theta, \phi) = \mathrm{Re}\Bigg(\sum_{lm} \sum_{l'm'} & \frac{\alpha_{lm}\gamma_{l'm'} R_\star}{(l'+1)l(l+1)} c_{lm} c_{l'm'} e^{i\phi(m+m')} \\ & \left(P_{lm} P_{l'm'} \left(l(l+1) - \frac{mm'}{\sin^2\theta} \right) + \frac{\mathrm{d}P_{lm}}{\mathrm{d}\theta} \frac{\mathrm{d}P_{l'm'}}{\mathrm{d}\theta} \right) \Bigg). \end{aligned} \tag{5.22}$$

This expression for helicity density can be applied to any star given only its stellar radius and the α_{lm} and γ_{lm} coefficients characterising its poloidal and toroidal magnetic field components.

Note that the β_{lm} coefficient does not appear in the helicity density equation. This is due to helicity being the linking of toroidal and poloidal fields. The toroidal field lines lie on spherical surfaces, and the poloidal field lines pass through these surfaces. However, only the radial component of the poloidal field links through the toroidal field, the θ and ϕ components lie on the same spherical surfaces as the toroidal field and so provide no "linkage". Since the radial part of the poloidal field depends only on α_{lm}, and the toroidal field depends only on γ_{lm}, β_{lm} is not needed.

When comparing the helicity density of different stars, or at different times, rather than considering the helicity density at specific points (θ, ϕ) on the stellar surface, it is more convenient to calculate an average helicity density value across some surface area A:

$$\langle h \rangle = \frac{\int h(R_\star, \theta, \phi)\, \mathrm{d}A}{A}. \tag{5.23}$$

5.2.4 Coordinate systems

The given expression for magnetic helicity density is derived using a right-handed coordinate system. It is important to be aware of which coordinate system the expression is in, and which coordinate system the magnetic map described by the input coefficients was in; a mismatch

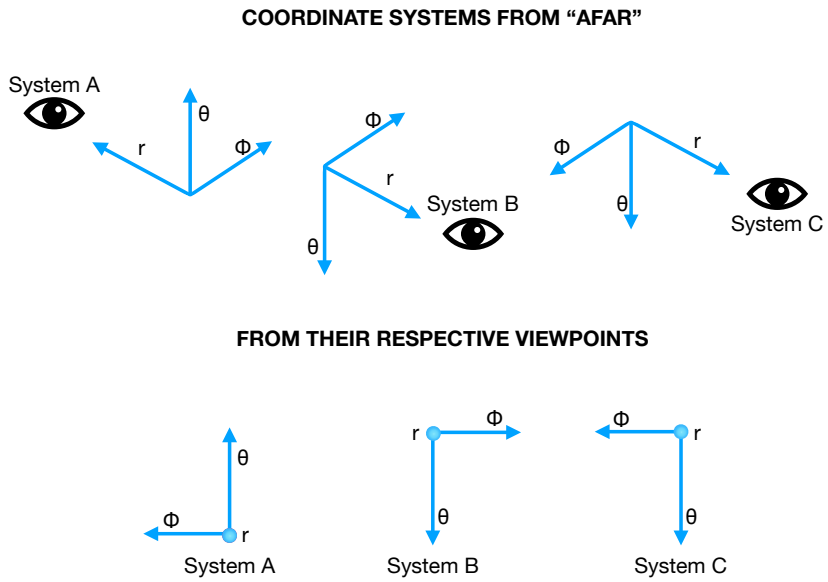

Figure 5.3: Comparing spherical coordinate systems. The top panel shows the systems with observers (represented by the eyes) from a distance, and the bottom panel shows the systems from the perspective of the observers. Note that in the bottom panel the radial vectors are all pointing out of the page.

could result in helicity values being mapped to incorrect positions on the star, having the wrong sign, or both.

As an example, in Figure 5.3 I compare the three different coordinate systems Donati et al. (2006) (System A), Chandrasekhar (1961) (System B) and Vidotto (2016) (System C) use when describing their poloidal and toroidal magnetic field components. All three observers, represented by the eyes in the top panel, would describe a magnetic field differently. In each case the radial component points towards the observer, whereas the azimuthal and meridional components differ. Table 5.1 shows how the different coordinate systems translate to different signs of the radial, meridional and azimuthal parts of the poloidal and toroidal magnetic field components. Furthermore, different directions being positive or negative in the different coordinate systems means there is disagreement on the positions of the (θ, ϕ) points on a sphere; if considering a sphere in equirectangular projection, (0,0) would be placed at the bottom right, top left and top right for the A, B and C coordinate systems respectively.

Coordinate system	$B_{\rm r}^{\rm pol}$	$B_{\theta}^{\rm pol}$	$B_{\phi}^{\rm pol}$	$B_{\theta}^{\rm tor}$	$B_{\phi}^{\rm tor}$
A	-	-	-	-	+
B	+	+	+	+	-
C	+	+	-	+	+

Table 5.1: Signs of the radial (r), meridional (θ) and azimuthal (ϕ) parts of the poloidal and toroidal magnetic field components when placed in the different coordinate systems shown in Figure 5.3.

In order to use the helicity density expression from the previous section as written (corresponding to coordinate system B), the input coefficients might have to go through a coordinate transformation depending on their system of origin:

$$\alpha_{lm}, \beta_{lm}, \gamma_{lm} = \begin{cases} -\alpha_{lm}(-1)^{l+m}, -\beta_{lm}(-1)^{l+m}, \gamma_{lm}(-1)^{l+m} & \text{coordinate system A,} \\ \alpha_{lm}, \beta_{lm}, \gamma_{lm} & \text{coordinate system B,} \\ \alpha_{lm} e^{2{\rm im}(\pi-\phi)}, \beta_{lm} e^{2{\rm im}(\pi-\phi)}, \gamma_{lm} e^{2{\rm im}(\pi-\phi)} & \text{coordinate system C,} \end{cases} \tag{5.24}$$

5.3 Observational and simulated data

Using the magnetic helicity expression from the previous section I calculate the large-scale helicity density of the Sun, as well as 51 additional stars listed in Table 5.2. The magnetic maps (all obtained using the ZDI technique) used for each star are referenced in the last column of the table. From left to right the remaining columns show the name of the star, stellar mass, stellar radius, rotation period, Rossby number, age, absolute helicity density ($l \leq 4$) averaged across the visible stellar hemisphere, the maximum l-mode and the number of magnetic maps used. For references to the stellar parameters listed, as well as a more detailed table with further information on these stars see Vidotto et al. (2014).

The stellar sample consists of stars with spectral types F, G, K and M, with masses ranging from 0.1-1.34 $M_{\odot}$. The stellar masses are plotted against rotation periods in Figure 5.4. The stars in the sample roughly follow the trend of an increasing rotation period with increasing stellar mass. There is one notable example of a higher-mass star which is rotating fairly fast, namely AB Dor ($M_{\star} = 0.76\ M_{\odot}$, $P_{\rm rot} = 0.5$ days). However, the plot shows generally there is a lack of higher-mass rapid rotators and lower-mass slow rotators. The challenge in filling the gap of higher-mass stars is that they mostly have to be caught at a very young age in order to be

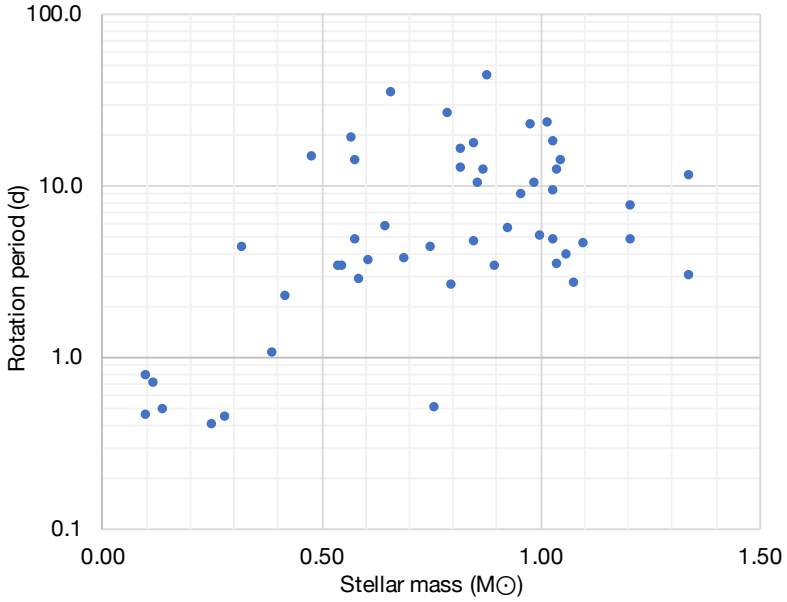

Figure 5.4: Rotation period versus mass for the stellar sample described in Table 5.2

rotating rapidly. Whereas the problem with lower-mass slow rotators is poor signal-to-noise. The lower-mass stars are faint and when they rotate slowly their spectral lines are thin, this makes it hard to pick out any features.

The Sun is included in this study to place it in a wider context. Moreover the wealth of solar data may provide additional insights into the stellar results. The solar magnetic maps I use come from observations taken by the Helioseismic and Magnetic Imager (HMI) on-board the Solar Dynamics Observatory (SDO) (Scherrer et al., 2012; Pesnell et al., 2012). I also use surface magnetograms taken from the 3D non-potential magnetic field simulation presented in Yeates & Mackay (2012). Together the data spans almost two whole solar cycles; the observed solar data covers most of solar cycle 24, and the simulation follows solar cycle 23. There is a slight overlap in time between the two data sets, which proves useful when checking for consistency between the simulated and observed data.

When comparing stars an important consideration is resolution. The true magnetic fields of distant stars will not necessarily be recovered to the same level of detail, and they will look decidedly worse than the solar magnetic field. The way magnetic fields are decomposed, in terms of spherical harmonics, their resolution correlates to the number of l-modes used to express them. Consider a 3D non-potential magnetic field simulation where the true field is known exactly. By decomposing it into spherical harmonics the effect of different numbers of

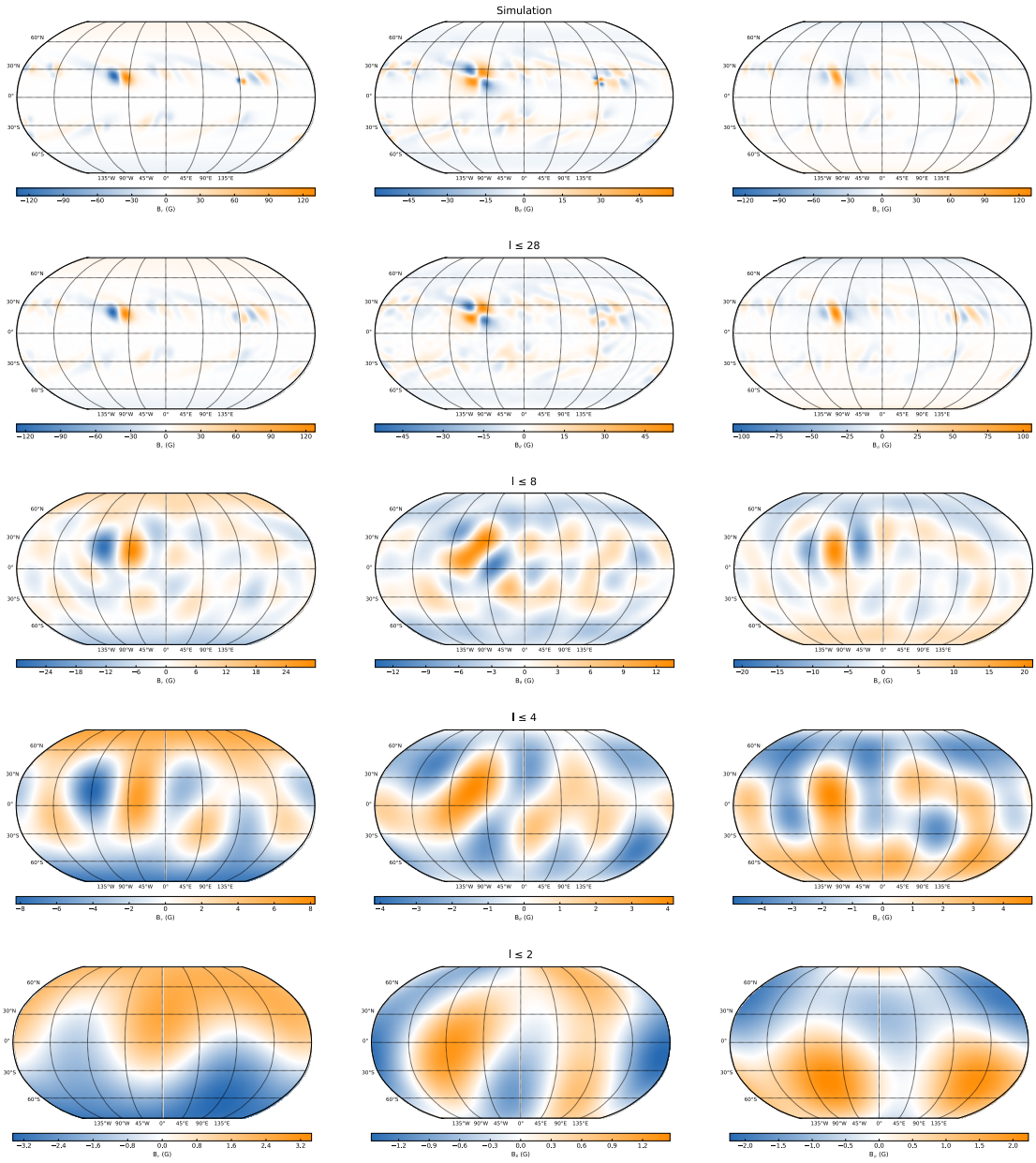

Figure 5.5: The top panel shows magnetic field components from a simulation. The remaining panels show the extent to which this field is recovered when it is decomposed in terms of spherical harmonics with decreasing numbers of l-modes allowed.

l-modes can be visualised, see Figure 5.5. Going to higher modes results in a higher resolution, meaning smaller scale magnetic fields are detected.

The resolutions of the magnetic maps of the stellar sample range from $l_{\max} = 4$ to 25. For the sake of consistency, I use the same number of l-modes when comparing the stellar and solar data. This limits the investigation to large-scale helicity density. Even when considering the Sun alone, its resolution is capped in order to mimic what it would look like if viewed

from a distance, like the other stars. Hence, when the solar helicity density is presented in Section 5.4.1 it is calculated up to $l = 8$ only, as this is a reasonable resolution for most of the stars in the sample. When considering stellar helicity densities, in Section 5.4.2, both limits of $l \leq 8$ and $l \leq 4$ are used. As seen in Table 5.2, the majority of the M-dwarfs and hot Jupiter hosts have resolutions below $l_{\max} = 8$, as such they are omitted from any analysis where $l \leq 8$. Therefore, for the latter part of the study the number of modes is sacrificed in order to include a greater range of stars. $l \leq 4$ is chosen as $l = 4$ is the highest common mode of the stellar sample.

5.4 Results and discussion

Using the helicity density equation presented in Section 5.2 I calculate values for the sample of stars described in Section 5.3, including the Sun. First I consider how the solar helicity density changes over time, then I explore how the stellar helicity densities compare to other known stellar properties; mass, Rossby number, magnetic energy and age. These first ever estimates of stellar helicity density presents exciting possibilities of new insight into the nature of stellar magnetic fields.

5.4.1 Large-scale solar helicity densities

Helicity density averaged across longitudes

In Figure 5.6 I present longitudinally averaged helicity densities for every simulated (*left*) and observed (*right*) solar magnetic map as a function of time. The average helicity densities are calculated across thin latitude bands with widths of 3°, this resolution seems sufficient, as 1° latitude bands resulted in visually indistinguishable plots. The images are saturated in order to reveal more structure towards the equator; the helicity density values are limited to $\pm 2 \times 10^{12}$ Mx^2 cm^{-3} (*left*) and $\pm 2 \times 10^{11}$ Mx^2 cm^{-3} (*right*). I use Gaussian smoothing, with a sigma of 2 pixels in latitude (6°) and 5 pixels in time (observed sun: $\sim$ 0.3 years, simulated sun: $\sim$ 0.5 years) to remove small variations and highlight the overall trends. The original data are plotted in the top panel and the processed data in the bottom panel.

The helicity density at the poles of the simulated Sun is approximately a full order of magnitude stronger than that of the observed Sun. The reason for this is unclear, but perhaps it could be related to our limited view of the solar poles from Earth, a factor which would not

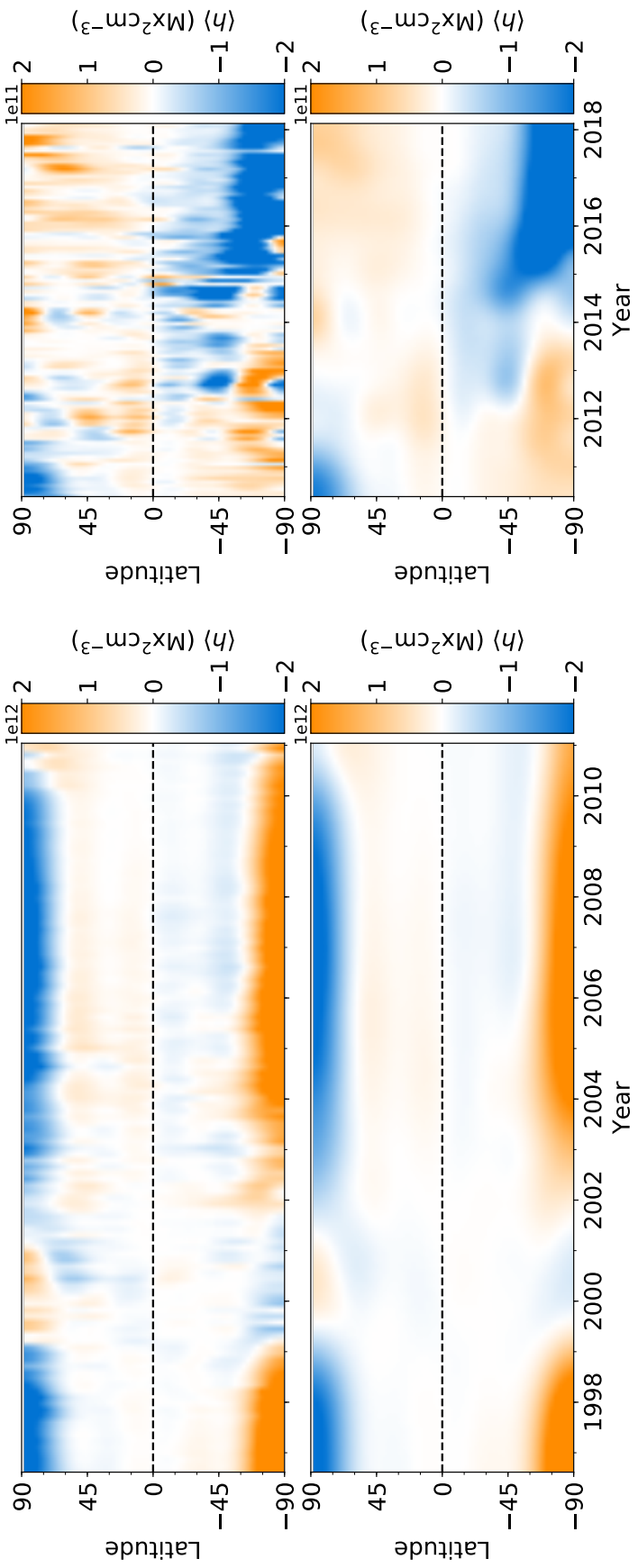

Figure 5.6: The evolution in time of the average solar helicity density for $l \leq 8$ at each latitude, using simulated data (*left*) and observational data (*right*). Gaussian smoothing has been applied to remove small variations and highlight overall trends. The colour tables saturate at $\pm 2 \times 10^{12}$ $\mathrm{Mx}^2\ \mathrm{cm}^{-3}$ (*left*) and $\pm 2 \times 10^{11}$ $\mathrm{Mx}^2\ \mathrm{cm}^{-3}$ (*right*).

be an issue in simulations. Apart from the discrepancy in magnitude, the two plots show consistent results and match up nicely in the overlapping year ($\sim$ 2010-2011) showing a positive south pole and a negative north pole. In both cases, the strong signal at the poles overshadows most structure around the equator and the sign of the helicity density flips across the equator. The helicity is predominantly negative in the northern hemisphere and positive in the southern hemisphere until $\sim$ 2014, when it reverses. A much shorter sign reversal can also be seen around 2000. It is perhaps worthwhile to note that 2000 and 2014 are the years with the highest solar Sunspot activity during solar cycles 23 and 24 respectively[3]. I cannot confidently state whether this is coincidence or consequence.

Pipin et al. (2019) also plotted the evolution of large-scale helicity density with time and latitude in their paper exploring the solar magnetic helicity density throughout solar cycle 24. My result is consistent with their Figure 5a; our plots have matching patterns, but opposite polarities. The change in sign however is expected since we are using different coordinate systems.

Helicity density averaged across hemispheres

Calculating the average helicity density across both hemispheres allows a more quantitative comparison of the two. The top panel of Figure 5.7 shows the helicity density over time averaged across the southern (orange) and northern (yellow) hemispheres respectively. The triangles correspond to the simulated Sun, and the circles correspond to the HMI observations. Despite having already established that the helicity density flips signs across the equator, this plot reveals more clearly that the overall helicity density of the Sun is never exactly zero. In the case of the simulated Sun, there are period where the helicity density is approximately mirrored across the equator, and over time it will average to more or less zero. For the observed Sun on the other hand the helicity density in the southern hemisphere dominates throughout the second half of the time period. This could be due to computational errors, or there could be a real imbalance. Yang & Zhang (2012) showed an asymmetry between the large-scale magnetic helicity fluxes in the northern and southern hemispheres across solar cycle 23, which would lead to different amounts of helicity accumulating in each hemisphere.

The bottom panel of Fig. 5.7 shows how the solar magnetic energy behaves throughout the same time period over which the helicity density is presented in the top panel. The mean

[3]Sunspot data from http://www.sidc.be/silso/ (SILSO, World Data Center, accessed Nov 2019)

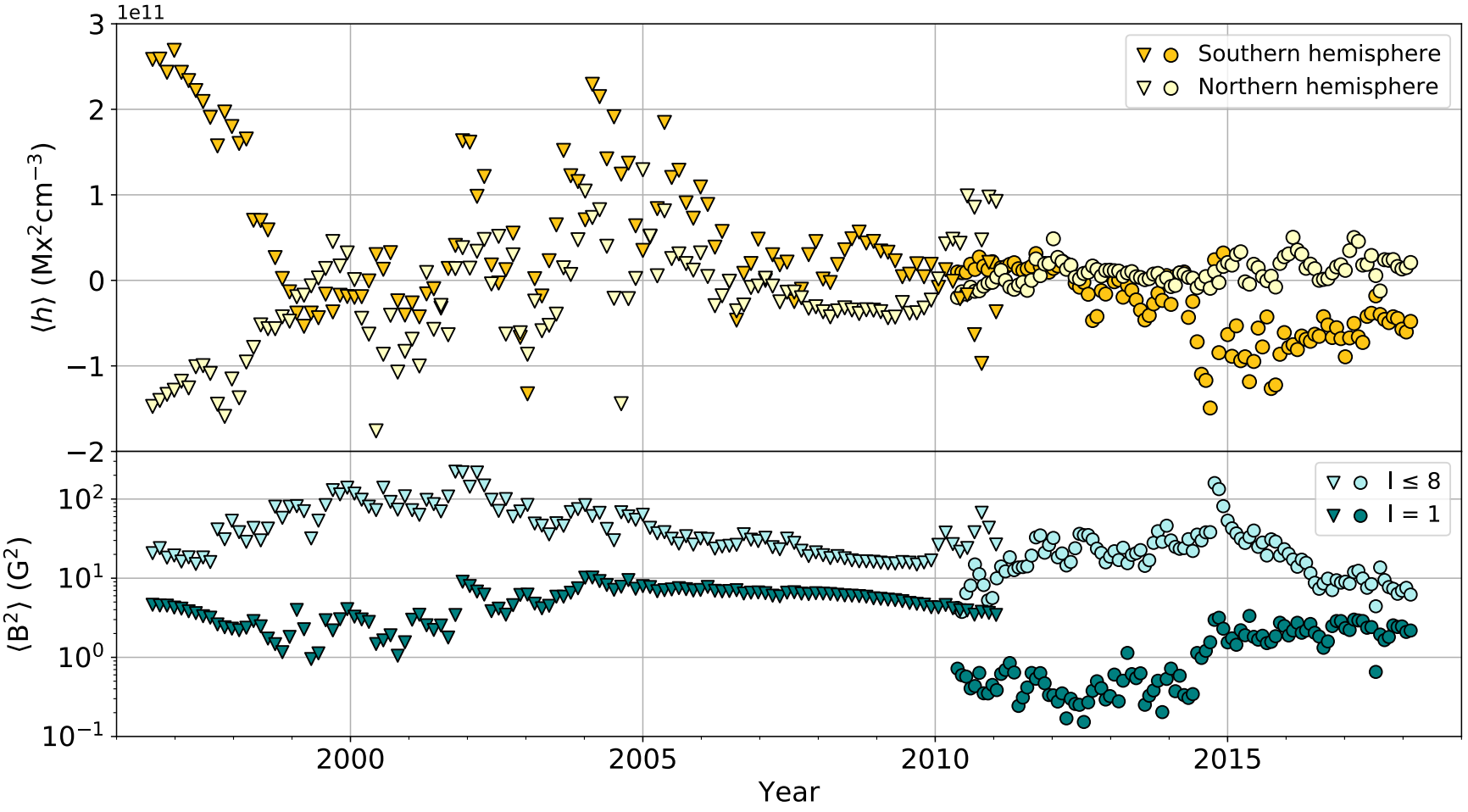

Figure 5.7: *Top*: The evolution in time of the average solar helicity density for $l \leq 8$ across the southern (orange) and northern (yellow) hemispheres *Bottom*: The mean squared magnetic flux density for $l \leq 8$ (light teal) and $l = 1$ (dark teal) across the same time period. The triangles and circles correspond to results based on simulated and observational data respectively.

squared magnetic flux density across the Sun $\left(\langle B^2 \rangle\right)$ represents a proxy for magnetic energy. The symbols have the same meaning as before and the light and dark teal colours correspond to the energy proxies being calculated for $l = 1$ (a dipole) and $l \leq 8$ respectively. The results for both the simulation and the real Sun follow a similar pattern, except with the latter being shifted to lower values, a jump of approximately one order of magnitude. The maxima of the total energy ($l \leq 8$) roughly coincide with the minima of the dipole energy. During the climb of the total energy towards cycle maximum, the dipole energy decreases. During the slow decline of the total energy, the dipole energy first grows then falls at a similar rate to that of the total energy. The helicity density also appears to follow a cyclic pattern, however it is harder to spot due to the combination of a drop in magnitude once the observational values are reached and the linear axis. There might be a relation between the helicity density and the magnetic energy cycle, some phase shift potentially, but it is not obvious from this plot.

5.4.2 Large-scale stellar helicity densities

Based on the exploration of solar helicity density in the previous section I choose to compare the helicity densities of my stellar sample in terms of their averages across a single hemisphere. I propose, due to the observed sign change across the equator, the helicity density averaged across a single hemisphere provides a more meaningful result than an average across the entire sphere, which represents a residual value. I use the hemisphere pointing towards the observer, noting that the other is partially obscured, and even partially invisible. When the Sun is plotted for comparison throughout this section, I am using the $\sim$ 2010–2018 observations of the solar southern hemisphere. Because the sign of the helicity density can change across hemispheres or over time, once I have calculated the average across a hemisphere I take its absolute value. For the sake of simplicity, from this point onward, whenever I mention helicity density I am referring to the absolute value of the average across a hemisphere.

The impact of resolution on helicity density

To explore the importance of the chosen resolution, I plot the helicity density calculated up to three different l-mode limits as a function of stellar mass in Figure 5.8. The different colours correspond to $l = 1$ (dipole), $l \leq 2$ (quadrupole) and $l \leq 8$. Consequently the stars in Table 5.2 with $l_{\max} < 8$, are excluded from this plot. The points without black outlines show multiple values for the same star, and the points with black outlines represent average values. An

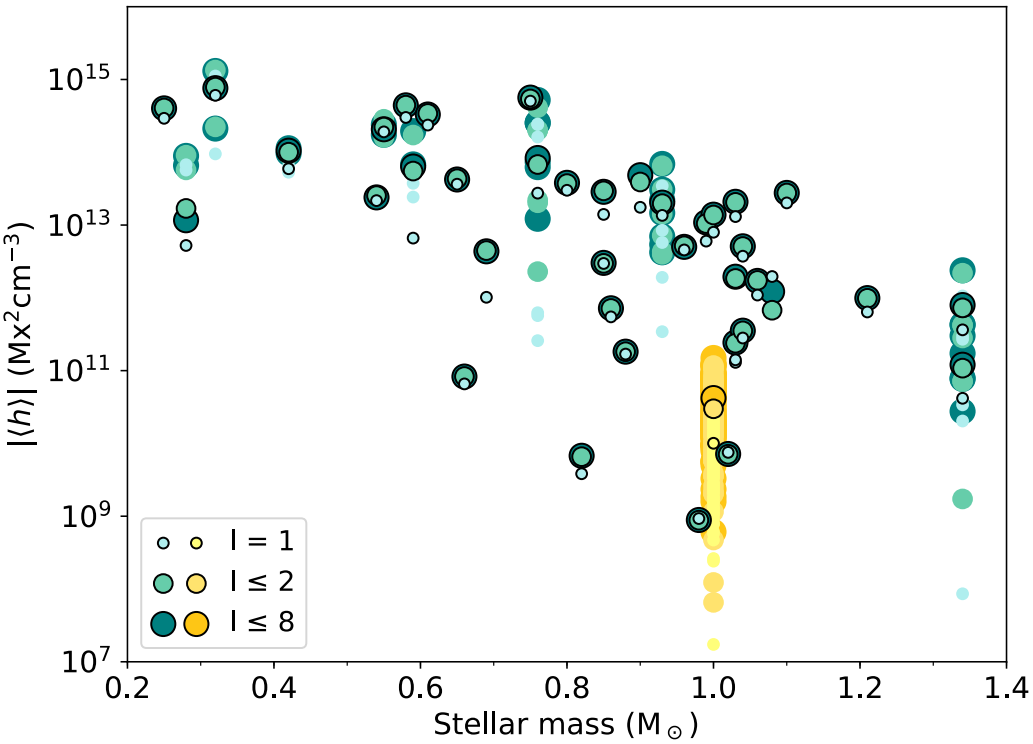

Figure 5.8: The absolute value of the helicity density averaged across a single hemisphere as a function of stellar mass. The orange shades show the southern hemisphere of the Sun between ∼ 2010–2018, and the teal shades show the stars in the stellar sample. The helicity densities are calculated up to different modes, which are represented by different sizes and colours. $l_{\rm max}$ increases from small and light to large and dark. Symbols without an outline represent multiple measurements for the same stars, and the symbols with black edges are average values.

example of this is the Sun, shown in orange shades, where the points with outlines are the average values across ∼ 2010–2018. The plot suggests the helicity densities recovered using dipole or quadrupole fields alone result in good representations of the $l \leq 8$ helicity density. Including higher-order modes changes the magnitude of the helicity density slightly, on average the $l = 1$ and $l \leq 2$ points deviate by ∼ 40 and 13 % from the $l \leq 8$ points, but the general trend across stellar masses remains the same. Hence, for the remainder of this chapter I limit the number of included modes to $l \leq 4$ in order to increase the number of eligible stars and particularly capture the hot Jupiter hosts and M dwarfs better.

Helicity density versus stellar mass

Figure 5.8 shows the helicity density increases with decreasing stellar mass, potentially reaching a plateau. The high helicities of the lower-mass stars is not surprising considering their

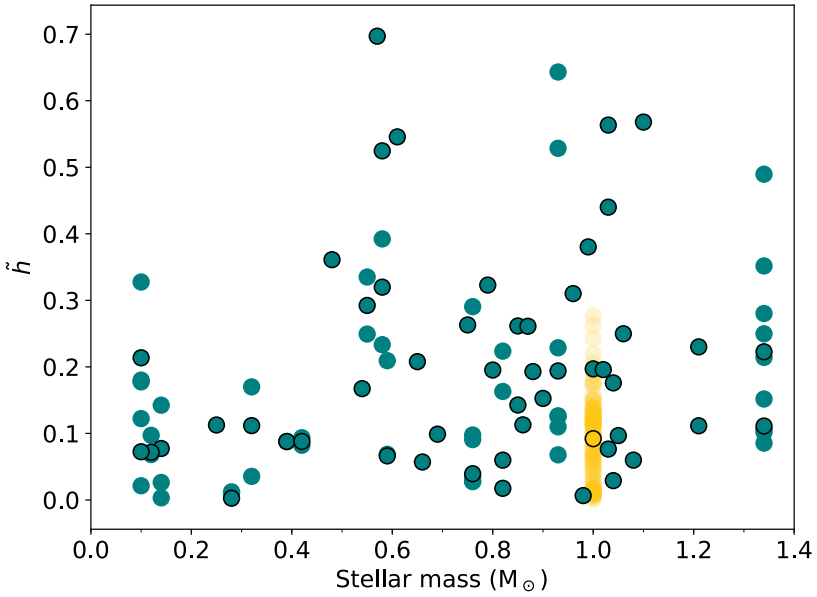

Figure 5.9: The helicity energy fraction ($l \leq 4$) versus stellar mass. The orange circles represent solar values between $\sim$ 2010–2018. Symbols without an outline represent multiple measurements for the same stars, and the symbols with black edges are average values.

generally high magnetic field strengths (Donati et al., 2008a; Morin et al., 2008b, 2010; See et al., 2015). Figure 5.9 explores this further by showing stellar mass plotted against a parameter I will refer to as the helicity energy fraction; $\tilde{h} = |\langle h \rangle| / \langle R_\star B^2 \rangle$. The helicity density is divided by the mean squared magnetic flux density across the entire surface of a star, $\langle B^2 \rangle$, which acts as a proxy for magnetic energy, as well as stellar radius in order to reach a dimensionless quantity. Again, the points without black outlines show multiple values for the same star, and the points with black outlines represent average values. The orange points represent the Sun between $\sim$ 2010–2018. There is an even spread of low helicity energy fractions across all stellar masses, however only stars with $M_\star \gtrsim 0.5$ $M_\odot$ exceed a fraction of 0.5. This means that even though the lower-mass stars are shown in Figure 5.8 to be among the stars with the highest helicity density, relative to their total energy budget they are producing less helicity than the more massive stars.

The change in the behaviour of helicity around 0.5 $M_\odot$, makes it the newest addition to a collection of magnetic properties which have been discovered to differ across this boundary. Below 0.5 $M_\odot$ the stellar magnetic field is largely axisymmetric and poloidal, whereas above 0.5 $M_\odot$ non-axisymmetric fields dominate, there is a larger fraction of toroidal fields, and the toroidal field energies have a steeper power law dependence on poloidal field energies (Donati

et al., 2008a; Morin et al., 2008b, 2010; Gregory et al., 2012; See et al., 2015). Donati et al. (2008a) suggest the sudden change in properties is related to the onset of the sharp transition in internal stellar structure from partially convective stars with inner radiative interiors out to $\sim 0.5\ R_\star$ (at 0.5 $M_\odot$) to fully convective stars (at 0.35 $M_\odot$). Motivated by this, I divide the stellar sample at 0.5 $M_\odot$; in upcoming plots stars below or above this mass are represented by different symbols.

Helicity density versus Rossby number

As previously noted by See et al. (2015), the correlation between stellar mass and rotation period for the ZDI sample (see Figure 5.4) makes it hard to say whether the helicity trends in Figures 5.8 and 5.9 are a result of mass or rotation. To sidestep this issue, I instead consider the Rossby number, R_o; a parameter which contains information about both mass and rotation period (see Equation 1.31). In Figure 5.10 I plot the helicity density versus the Rossby numbers listed in Table 5.2, originally calculated and published in Vidotto et al. (2014) and Folsom et al. (2016). Stellar mass is denoted by the colour of the symbols, circles represent stars with masses higher than 0.5 $M_\odot$, and diamonds represent stars with lower masses. The points without black outlines show multiple values for the same star, and the points with black outlines represent average values. The orange circles show the range of solar values between $\sim$ 2010–2018, assuming a solar Rossby number of 1.96 (Cranmer & Saar, 2011).

Whereas the Sun appears in Figures 5.8 and 5.9 to have a relatively low helicity density for its mass, when plotting against Rossby number instead it falls entirely within the scatter of the other stars and looks completely normal. Hence the Sun is not discrepant, it is simply a slower rotator than many other stars in the stellar sample of similar mass. In fact, the Sun has one of the highest Rossby numbers in the stellar sample, moving towards lower Rossby numbers the helicity density increases steadily until a maximum, or possibly a saturation point, is reached at $R_o \sim 0.1$. The largely-convective stars with masses below 0.5 $M_\odot$ are all grouped together beyond this point, alongside two higher mass stars (AB Dor at $R_o = 0.026$ and GJ 182 at $R_o = 0.054$).

Similar behaviour around the $R_{o\sim0.1}$ point has been reported for several other activity indicators. X-ray emission increases with decreasing Rossby number and saturates at the empirical threshold $R_{o\sim0.13}$ (Wright et al., 2011), additionally supersaturation has been observed in G and K dwarfs (e.g. Jeffries et al., 2006), but not yet confirmed in M dwarfs (James et al., 2000;

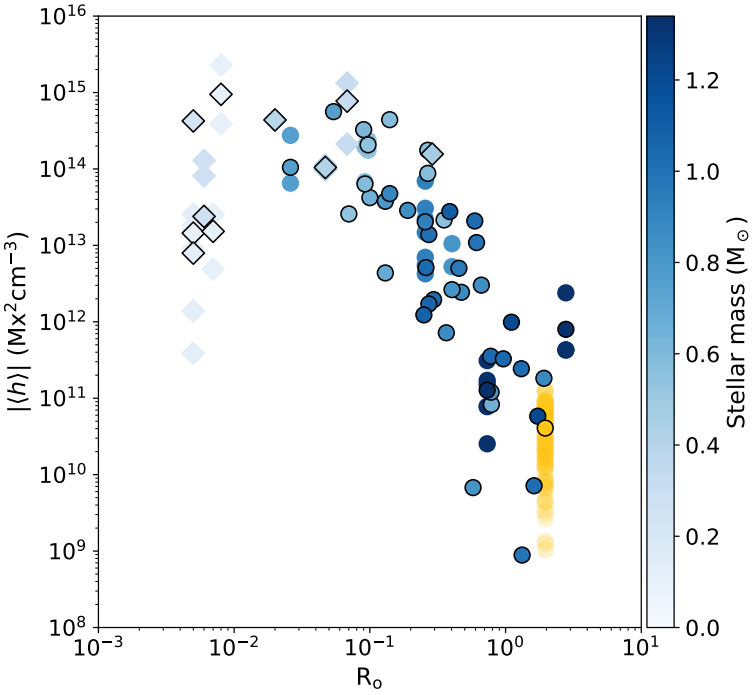

Figure 5.10: The absolute value of the helicity density averaged across a single hemisphere ($l \leq 4$) versus Rossby number. The shade of blue corresponds to stellar mass, and the diamonds represent stars with $M_\star < 0.5$ M$_\odot$. The orange circles show the range of solar values between $\sim$ 2010–2018.Symbols without an outline represent multiple measurements for the same stars, and the symbols with black edges are average values.

Jeffries et al., 2011; Wright et al., 2011). Likewise, both toroidal and poloidal magnetic energy densities increase with decreasing Rossby number and saturate at $R_{o\sim0.1}$ (See et al., 2015). Mondrik et al. (2019) suggests a peak, not a saturation, in the rate of large M-dwarf flares at $R_{o\approx}$ 0.1, which is also the point where See et al. (2017) find maximum mass and angular momentum loss rates.

As mentioned earlier, it is hard to tell whether $R_{o\sim0.1}$ represents a maximum or a saturation point. Most of the helicity densities recorded at lower Rossby numbers ($R_o < 0.1$) stay at a constant level, within a spread of approximately one magnitude, except four points which are grouped together at significantly lower values. This could signal the onset of a decrease in helicity density or it is possible that this is a manifestation of bi-stability; stars with similar parameters exhibiting either strong, simple fields, or weaker, more complex ones (Morin et al., 2011b; Schrinner et al., 2012; Gastine et al., 2013), see Section 1.3.2 for an introduction to this phenomenon. Further observations are required to confirm whether this is a plausible explanation for the range of helicity densities at low Rossby numbers.

Helicity density versus magnetic energy

In Figure 5.11 I consider how helicity density varies with magnetic energy. Again the mean squared magnetic flux density across the star ($\langle B^2 \rangle$) acts as a proxy for magnetic energy. The shades of blue correspond to stellar mass, and the diamonds indicate stars with $M_\star < 0.5$ $M_\odot$. The symbols without an outline represent multiple measurements of the same star, and the symbols with a black outline are average values. Values for the Sun spanning $\sim$ 2010–2018 are shown in orange, with the circles labelled 1, 2 and 3 being mean values for the periods $\sim$ 2010–2012, 2013–2015 and 2015–2018. These points show broadly how the position of the Sun on the plot evolves in time. It is notable that the solar cyclic variation is within the scatter in values for other stars.

Generally speaking, helicity density increases with increasing magnetic energy. The dashed lines show the best fit of $|\langle h \rangle| \propto \langle B^2 \rangle^\alpha$ calculated using the average values only. Applying this relation to all the stars would produce a value of $\alpha = 0.87 \pm 0.05$, but every star with $M_\star < 0.5$ $M_\odot$ would fall below the line and the overall fit would not be tight. Consequently best fit lines of stars with $M_\star > 0.5$ $M_\odot$ and $M_\star < 0.5$ $M_\odot$ are shown separately, resulting in $\alpha = 1.04 \pm 0.05$ and $\alpha = 0.78 \pm 0.18$ respectively.

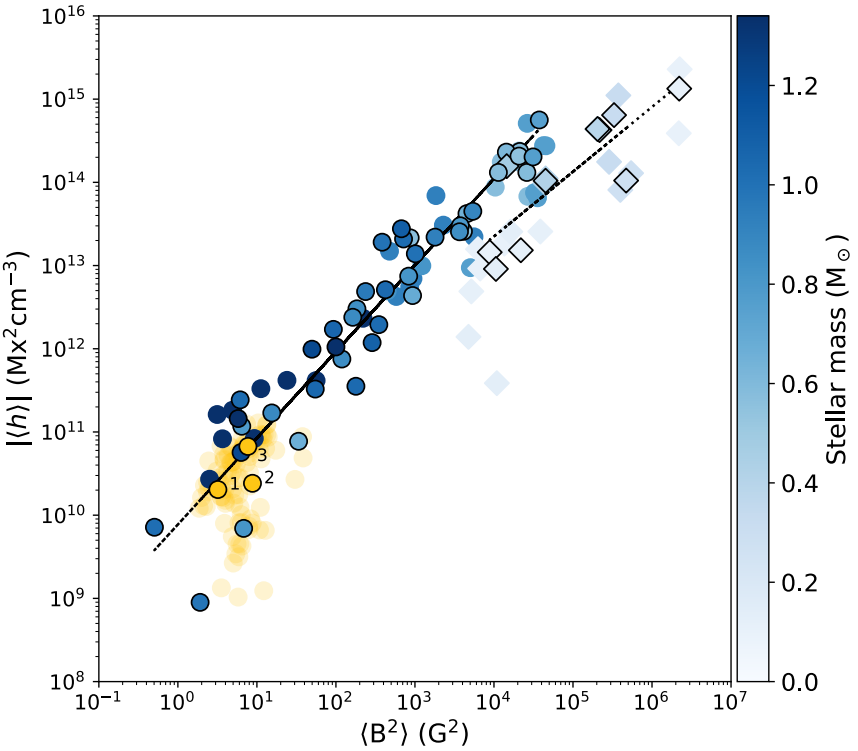

Figure 5.11: The absolute value of the helicity density averaged across a single hemisphere versus the mean squared magnetic flux density ($l \leq 4$). The symbols are the same as in Figure 5.10. Mean values of the solar data are given for the periods $\sim$ 2010–2012, 2012–2015 and 2015–2018, labelled 1, 2 and 3 respectively. The dashed lines show the best fit of $|\langle h \rangle| \propto \langle B^2 \rangle^{\alpha}$ calculated using the average values only. For $M_\star > 0.5$ M$_\odot$ and $M_\star < 0.5$ M$_\odot$, $\alpha = 1.04 \pm 0.05$ and 0.78 ± 0.18 respectively.

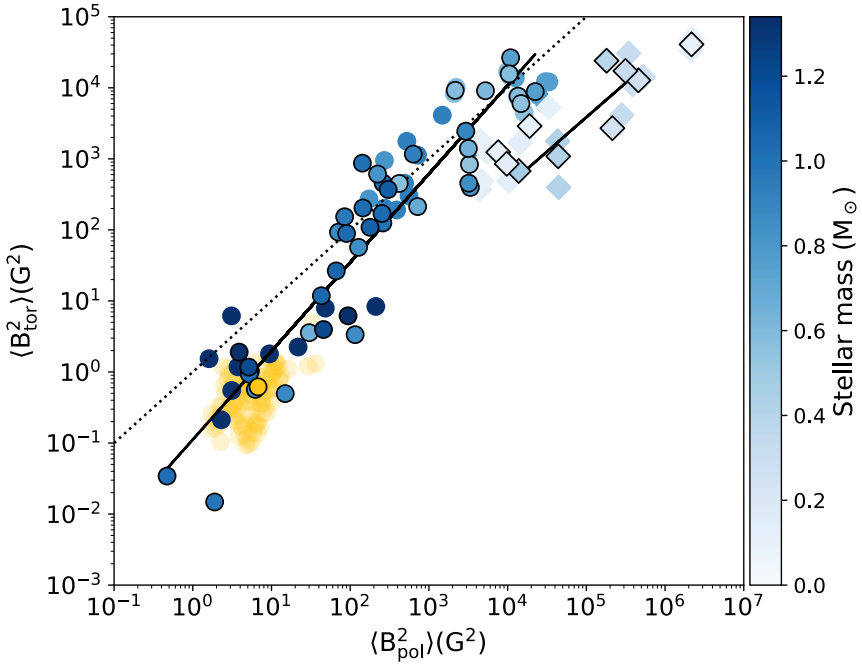

Figure 5.12: The mean squared toroidal magnetic flux density vs the mean squared poloidal magnetic flux density ($l \leq 4$). The symbols are the same as in Figure 5.10. The dotted line is the line of equality. The solid lines show best fit of $\langle B^2_{tor}\rangle \propto \langle B^2_{pol}\rangle^{\alpha}$ for $M_\star > 0.5$ $M_\odot$ and $M_\star < 0.5$ $M_\odot$, with $\alpha = 1.24 \pm 0.08$ and 0.97 ± 0.30 respectively.

Interestingly, when See et al. (2015) plotted toroidal magnetic energy against poloidal magnetic energy it resulted in a very similar plot to Figure 5.11; with different slopes for the same sub-samples of stellar mass. I have recreated their plot in Figure 5.12 using my stellar sample. The dotted line is the line of equality, and the solid lines show the best fit of $\langle B^2_{tor}\rangle \propto \langle B^2_{pol}\rangle^{\alpha}$ for $M_\star > 0.5$ $M_\odot$ and $M_\star < 0.5$ $M_\odot$, with $\alpha = 1.24 \pm 0.08$ and 0.97 ± 0.30 respectively. Note that my slopes are slightly different from those quoted in See et al. (2015). This is not surprising as they are calculating their energy components using however many l-modes are available for each star, whereas I am imposing a limit of $l \leq 4$ on every star. Based on this plot alone it is impossible to determine whether the $M_\star < 0.5$ $M_\odot$ stars have an "excess" of poloidal field or a "deficit" of toroidal field compared to the more massive stars, but it is clear there is some difference in their magnetic field composition. In light of this, it might be more informative to plot the helicity density against toroidal and poloidal magnetic energy separately, rather than the combined energy.

Figure 5.13 is essentially presenting the same plot as in Figure 5.11, but replacing the magnetic energy by its poloidal (*top*) and toroidal (*bottom*) components. When helicity density is plotted against the poloidal magnetic energy, it very much resembles the original plot against

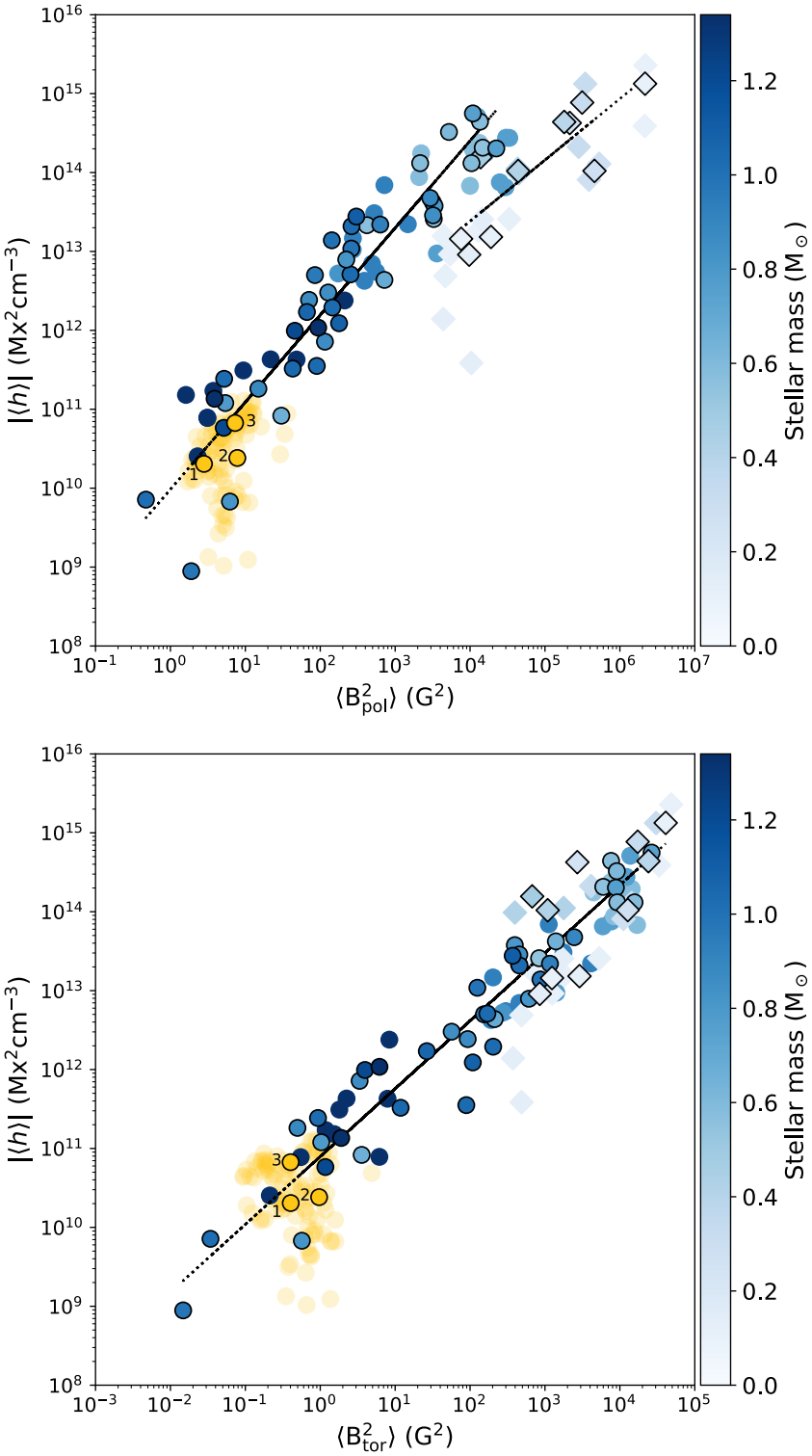

Figure 5.13: The absolute value of the helicity density averaged across a single hemisphere versus the mean squared poloidal (*top*) and toroidal (*bottom*) magnetic flux density ($l \leq 4$). The symbols are the same as in Figure 5.10. Mean values of the solar data are given for the periods $\sim$ 2010–2012, 2012–2015 and 2015–2018, labelled 1, 2 and 3 respectively. The dashed lines show the best fit of $|\langle h \rangle| \propto \langle B^2 \rangle^\alpha$ calculated using the average values only. In the poloidal case $M_\star > 0.5$ M$_\odot$ and $M_\star < 0.5$ M$_\odot$ are fitted separately, resulting in $\alpha = 1.10 \pm 0.07$ and 0.78 ± 0.18 respectively. In the toroidal case however, one fit is given for all the stars, which results in $\alpha = 0.86 \pm 0.04$.

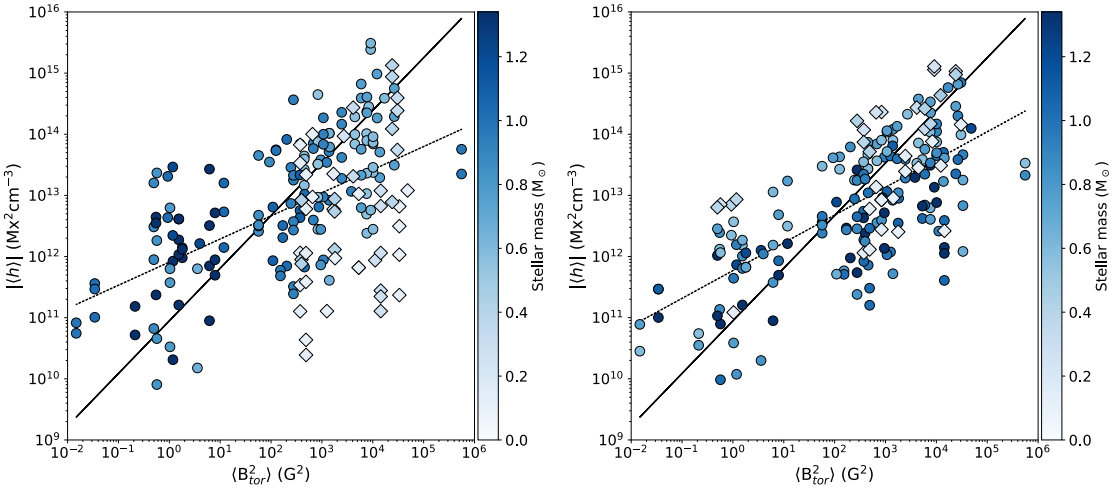

Figure 5.14: The absolute value of the helicity density averaged across a single hemisphere versus the mean squared toroidal magnetic flux density of stars with "fake" magnetic fields ($l \leq 4$). The toroidal and poloidal magnetic field components from stars in the stellar sample are randomly matched to create new fields. With the stellar mass and radii either adopted from the star corresponding to the toroidal (*left*) or poloidal (*right*) field component. The symbols are the same as in Figure 5.10. The dashed lines show the best fit of $|\langle h \rangle| \propto \langle B^2_{\rm tor} \rangle^{\alpha}$, with $\alpha = 0.36 \pm 0.04$ and 0.45 ± 0.03 in the left and right plots respectively. The solid lines show the best fit line from the equivalent plot in Figure 5.13.

total magnetic energy. When fitting $|\langle h \rangle| \propto \langle B^2_{\rm pol} \rangle^{\alpha}$, the two stellar sub-samples (split at 0.5 $M_\odot$) appear to follow different power laws. $\alpha = 1.10 \pm 0.07$ for the more massive stars with a significant radiative interior and $\alpha = 0.78 \pm 0.18$ for the largely-convective lower-mass stars. In contrast, when helicity density is plotted against the toroidal magnetic energy there is much less scatter and all stars follow the relation $|\langle h \rangle| \propto \langle B^2_{\rm tor} \rangle^{0.86 \pm 0.04}$, regardless of their interior structure.

In order to make sure the tight relationship between the toroidal magnetic energy and helicity density is not a mathematical artefact of the helicity calculation, I consider "fake" magnetic fields as a sanity check. Figure 5.14 shows the helicity density versus toroidal magnetic energy for 200 magnetic fields created by randomly matching toroidal and poloidal magnetic field components from stars in the stellar sample. The stellar radii and masses are either adopted from the star corresponding to the toroidal (*left*) or poloidal (*right*) field component. In both cases the best fit lines (dashed) do not match the fit shown for real stars in Figure 5.13 (solid), and there is significantly more scatter. This suggests $|\langle h \rangle| \propto \langle B^2_{\rm tor} \rangle^{0.86 \pm 0.04}$ is a real property of stellar magnetic fields.

Due to the tight correlation between helicity density and toroidal energy density, and dif-

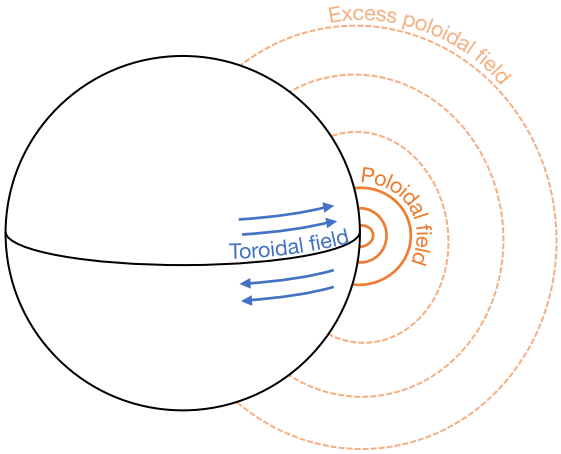

Figure 5.15: Could poloidal magnetic field lines which do not "link" with the toroidal field explain the existence of stars with an apparent "excess" of poloidal magnetic field? The illustration shows a star with a toroidal field (blue arrows) concentrated close to the equator, and a poloidal field (orange lines) extending almost pole to pole. The solid lines indicate the part of the poloidal field that links to the toroidal and the dotted lines represent the "excess" field.

ferent trends for stellar sub-samples in the poloidal case, largely-convective lower-mass stars ($M_\star < 0.5\mathrm{M}_\odot$) appear to have excess poloidal energy density. This sheds light on the change in behaviour for these stars observed in previous plots. For instance, it suggests their position relative to other stars in the plot of toroidal versus poloidal energy in Figure 5.12 is a shift towards larger poloidal energies, not lower toroidal energies. Moreover, it implies their low helicity energy fractions in Figure 5.9 is due to their relatively strong poloidal fields.

This excess poloidal energy prompts interesting questions. Is it perhaps possible that the stars in question have a poloidal field where only a fraction of it overlaps and links with the toroidal field at the stellar surface? This theory is visualised in Figure 5.15. Alternatively, as the differential rotation rate is very low for these stars they might be covered with randomly oriented small scale fields that are not organised at large-scales. The systematically oriented small-scale fields observed on the Sun causes the polar field strength to drop, triggering periodic polarity flips. These random fields however would not have this effect, which might explain the excess of poloidal field. See Figure 5.16 for an illustration of these two different types of small-scale fields. To explore this further it would be useful to map the helicity density along with the toroidal and poloidal magnetic fields on the surfaces of the lowest mass stars, to show where they are all concentrated relative to each other. Tracking this over a longer time period would also be very interesting, but requires additional observations of these stars.

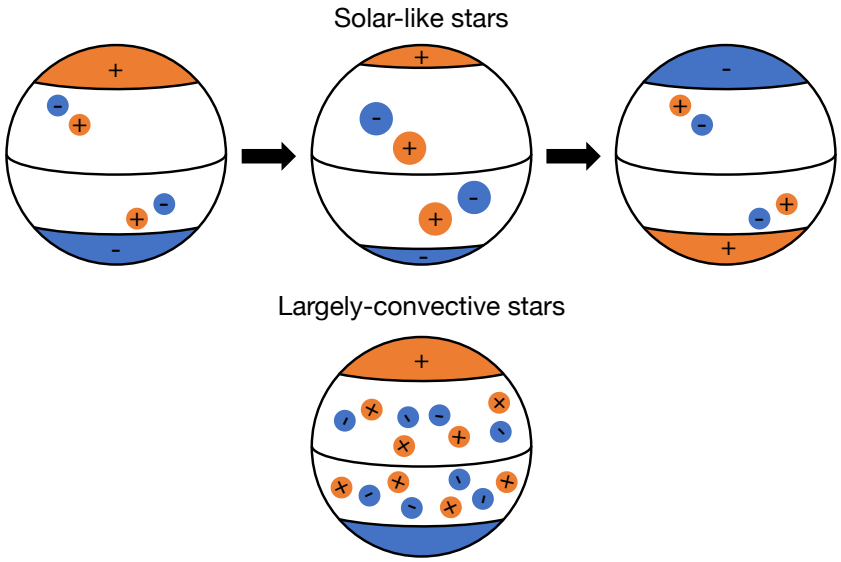

Figure 5.16: *Top*: The differential rotation of the Sun causes a systematic orientation of small scale fields over time. These fields erode the polar field until the polarity eventually flips. *Bottom*: Could low differential rotation in largely-convective stars result in randomly oriented small-scale fields which are not organised at large-scales and do not erode the polar field?

Rewinding to Figure 5.13, I want to consider the position of the Sun. It appears its evolution in time relative to the best-fit line is different depending on whether the helicity density is plotted against the poloidal or toroidal energy. In the toroidal case the solar values seem to move from one side of the line to the other, whereas in the poloidal case it mainly stays to the right. To explore this further I plot the poloidal (dark grey) and toroidal (light grey) solar magnetic flux density against time in Figure 5.17. The two energy components have a similar shape, but seem to be peaking at different times. As the solar data is not covering an entire cycle, and the poloidal and toroidal components are out of phase of each other this could explain the difference. Perhaps more interestingly, both the toroidal and poloidal plots in Figure 5.13 reveal the variation in solar values is in line with the general scatter of the stellar values, as has generally been the case in all the plots showing the Sun alongside the stars. This could indicate the stellar scatter is a sign of the stars undergoing cycles similar to the Sun. However, it is important to note there could easily be other explanations for the scatter, such as different stellar inclination angles (Lehmann et al., 2019).

Helicity density versus stellar age

As stellar age is known to affect the magnetic properties of stars, the helicity density is plotted against age in Figure 5.18. The ages used are listed in Table 5.2 and more information and

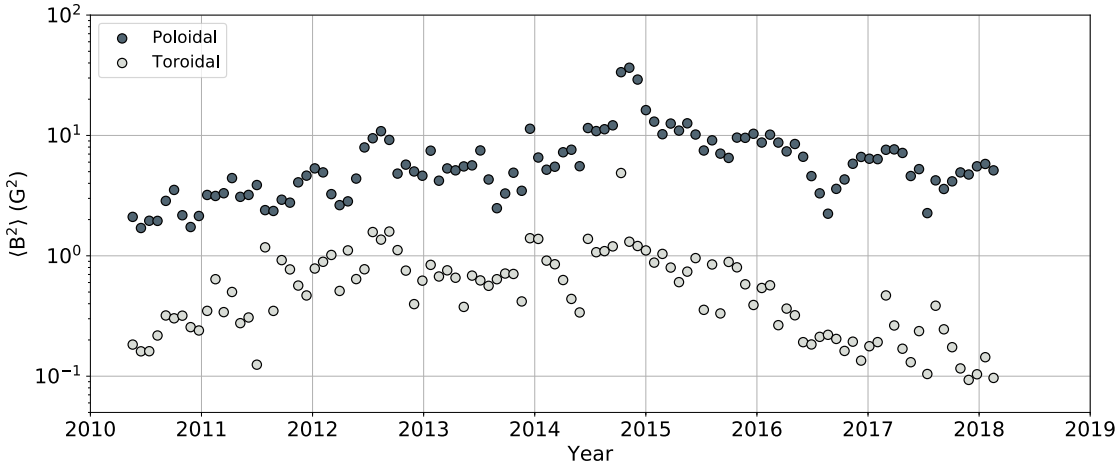

Figure 5.17: The mean squared magnetic flux density of the poloidal (dark grey) and toroidal (light grey) magnetic field components ($l \leq 4$) of the Sun plotted as a function of time. The results are based on observational solar data.

references for these can be found in Vidotto et al. (2014). Unfortunately ages are lacking for most of the M dwarfs in the sample, including all but one of the stars below 0.5 $M_\odot$, hence these are omitted from the plot. Due to the decreased mass range the plot is not able to explore any differences between stars with masses below and above 0.5 $M_\odot$. Instead, what the figure does show is a clear decline in helicity density with age, despite a large spread of values. Given the correlation outlined earlier between helicity density and magnetic field strength this result can be interpreted as a reflection of the decline of field strength with age. Additionally, given the current investigation into helicity as a diagnostic of solar activity/eruptivity, this trend might suggest a decline in stellar active phenomena with age.

5.5 Conclusions

In this chapter I have derived a general expression for calculating the large-scale magnetic helicity density of any star given its poloidal and toroidal magnetic field components and radius. Subsequently, I presented solar helicity densities along with the first measured helicity densities at the surfaces of 51 stars other than the Sun. The results are as follows, and all refer to the absolute value of the average helicity density across the visible hemisphere only:

- The helicity density rises and reaches a plateau with decreasing stellar mass. The saturation occurs at ~ 0.5 $M_\odot$.
- The helicity density rises with decreasing Rossby number R_o up until $R_o \sim 0.1$. Beyond

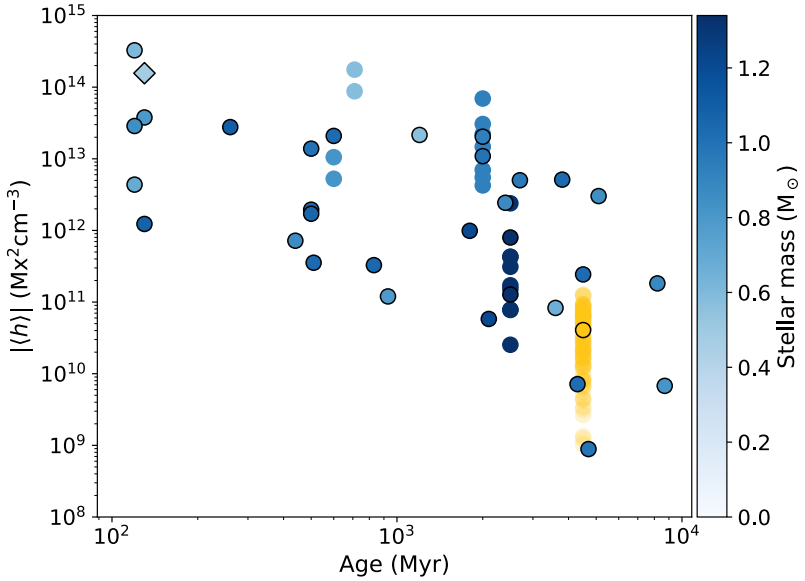

Figure 5.18: The absolute value of the helicity density averaged across a single hemisphere ($l \leq 4$) versus stellar age. Symbols are the same as in Figure 5.10.

this point it is unclear whether the helicity density begins to drop again, or saturates at two different levels as a result of bi-stability.

- The helicity density of all stars in my sample, spanning 0.1–1.34 $M_\odot$, relates to the magnetic toroidal energy density according to: $|\langle h \rangle| \propto \langle B^2_{\rm tor} \rangle^{0.86\pm0.04}$.

- The helicity density, when plotted against total magnetic energy density or poloidal energy density, separates the stellar sample into two groups; stars with $M_\star > 0.5$ $M_\odot$, and largely-convective stars with $M_\star < 0.5$ $M_\odot$. The two families are offset from each other and indicated on the plots by different slopes.

- The helicity density of $M_\star > 0.5$ $M_\odot$ stars decays with age.

- In terms of helicity density, the Sun is a normal example of a star of its mass and rotation period.

- The variation of the solar helicity density across its cycle is consistent with the scatter in the stellar helicity densities.

In conclusion the helicity density of stars plotted against stellar mass, Rossby number, total magnetic energy or poloidal magnetic energy are different for stellar masses lower or higher than 0.5 $M_\odot$. Whether this is an effect of the bias in the stellar sample (increasing rotation

period with increasing stellar mass) will remain unclear until more magnetic maps of rapidly rotating higher-mass stars or slowly rotating lower-mass stars become available. Nevertheless, the fact that the helicity density of a star of any mass can be determined by the strength of its toroidal magnetic field strongly implies the differences in behaviour is due to the lower-mass stars having relatively strong poloidal fields.

Having the Sun as part of this study allows an interpretation of the stellar results in the context of the variations in helicity density through the solar cycle. Considering the helicity density of the Sun stretches across approximately two orders of magnitude the spread in stellar helicity density is perhaps not so surprising. It may be due to other stars undergoing cycles similar to the Sun, with their helicity density similarly varying in time.

In the future, given magnetic maps of the same star over a longer time period, it would be interesting to investigate how stellar helicity density evolves in time, compared to the solar case. This would confirm or disprove whether the scatter in stellar helicity density can, at least in part, be attributed to stellar cycles.

5.A Data

Table 5.2: My stellar sample. From left to right the columns show: star name, mass, radius, rotation period, Rossby number, absolute helicity density calculated up to $l \leq 4$ averaged across the visible hemisphere (a mean value if more than one magnetic map is available), $l_{\max}$, number of magnetic maps used and references to those magnetic maps. A more comprehensive table can be found in Vidotto et al. (2014).

Star ID	$M_\star$ ($M_\odot$)	$R_\star$ ($R_\odot$)	$P_{\rm rot}$ (d)	R_o	Age (Myr)	$\lvert\langle h\rangle\rvert_{l\leq4}$ (Mx^2 cm^{-3})	$l_{\max}$	No. of maps	Ref.
Solar-like stars									
HD 3651	0.88	0.88	43.4	1.916	8200	1.823e+11	10	1	1
HD 9986	1.02	1.04	23.0	1.621	4300	7.158e+09	10	1	1
HD 10476	0.82	0.82	16.0	0.576	8700	6.769e+09	10	1	1
HD 20630	1.03	0.95	9.30	0.593	600	2.086e+13	10	1	2
HD 22049	0.86	0.77	10.3	0.366	440	7.187e+11	10	1	3
HD 39587	1.03	1.05	4.83	0.295	500	1.949e+12	10	1	1
HD 56124	1.03	1.01	18.0	1.307	4500	2.433e+11	10	1	1
HD 72905	1	1	5.00	0.272	500	1.386e+13	10	1	1
HD 73350	1.04	0.98	12.3	0.777	510	3.542e+11	10	1	1
HD 75332	1.21	1.24	4.80	>1.105	1800	9.878e+11	15	1	1
HD 78366	1.34	1.03	11.4	>2.781	2500	1.083e+12	10	3	4
HD 101501	0.85	0.9	17.6	0.663	5100	3.019e+12	10	1	1
HD 131156A	0.93	0.84	5.56	0.256	2000	2.193e+13	10	7	5, 6
HD 131156B	0.99	1.07	10.3	0.611	2000	1.088e+13	10	1	1

Table 5.2 - *continued*

Star ID	$M_\star$ ($M_\odot$)	$R_\star$ ($R_\odot$)	$P_{\rm rot}$ (d)	R_o	Age (Myr)	$\|\langle h \rangle\|_{l\leq4}$ (Mx^2 cm^{-3})	$l_{\rm max}$	No. of maps	Ref.
HD 146233	0.98	1.02	22.7	1.324	4700	8.872e+08	10	1	7
HD 166435	1.04	0.99	3.43	0.259	3800	5.122e+12	10	1	1
HD 175726	1.06	1.06	3.92	0.272	500	1.710e+12	10	1	1
HD 190771	0.96	0.98	8.80	0.453	2700	5.019e+12	10	1	7
HD 201091A	0.66	0.62	34.2	0.786	3600	8.290e+10	10	1	8
HD 206860	1.10	1.04	4.55	0.388	260	2.769e+13	10	1	9
Young Suns									
AB Dor	0.76	0.96	0.5	0.026	120	2.021e+14	25	6	10
BD-16351	0.9	0.83	3.39	$0.14^{+0.01}_{-0.02}$	30	4.756e+13	15	1	11
HII 296	0.8	0.74	2.61	$0.13^{+0.01}_{-0.01}$	130	3.774e+13	15	1	11
HII 739	1.08	1.03	2.7	$0.25^{+0.01}_{-0.08}$	130	1.231e+12	15	1	11
HIP 12545	0.58	0.57	4.83	$0.14^{+0.02}_{-0.02}$	21	4.410e+14	15	1	11
HIP 76768	0.61	0.6	3.64	$0.09^{+0.03}_{-0.02}$	120	3.268e+14	15	1	11
TYC 0486-4943-1	0.69	0.68	3.75	$0.13^{+0.03}_{-0.03}$	120	4.360e+12	15	1	11
TYC 5164-567-1	0.85	0.79	4.71	$0.19^{+0.04}_{-0.05}$	120	2.869e+13	15	1	11
TYC 6349-0200-1	0.54	0.54	3.39	$0.07^{+0.01}_{-0.02}$	21	2.579e+13	15	1	11
TYC 6878-0195-1	0.65	0.64	5.72	$0.10^{+0.04}_{-0.03}$	21	4.213e+13	15	1	11
Hot Jupiter Hosts									
τ Boo	1.34	1.42	3	>0.732	2500	1.359e+11	8,5	6	12, 13, 14, 15
HD 73256	1.05	0.89	14	0.962	830	3.278e+11	4	1	15
HD 102195	0.87	0.82	12.3	0.473	2400	2.433e+12	4	1	15
HD 130322	0.79	0.83	26.1	0.782	930	1.199e+11	4	1	15
HD 179949	1.21	1.19	7.6	>1.726	2100	5.815e+10	6	1	16
HD 189733	0.82	0.76	12.5	0.403	600	7.896e+12	5	2	17
M dwarf Stars									
GJ 569A	0.48	0.43	14.7	<0.288	130	1.565e+14	5	1	18
GJ 410	0.58	0.52	14	<0.267	710	1.316e+14	5	2	18
GJ 182	0.75	0.82	4.35	0.054	21	5.619e+14	8	1	18
GJ 49	0.57	0.51	18.6	<0.352	1200	2.152e+13	5	1	18
GJ 494A	0.59	0.53	2.85	0.092	-	1.315e+14	8	2	18
GJ 388	0.42	0.38	2.24	0.047	-	1.045e+14	8	2	19
EQ Peg A	0.39	0.35	1.06	0.02	-	4.376e+14	4	1	19
EQ Peg B	0.25	0.25	0.4	0.005	-	4.247e+14	8	1	19
GJ 873	0.32	0.3	4.37	0.068	-	7.712e+14	8	2	19
GJ 9520	0.55	0.49	3.4	0.097	-	2.067e+14	8	2	18
V374 Peg	0.28	0.28	0.45	0.006	-	1.050e+14	10	2	20
GJ 1111	0.1	0.11	0.46	0.0059	-	1.445e+13	6	3	21
GJ 1156	0.14	0.16	0.49	0.0081	-	9.107e+12	6	3	21
GJ 1245 B	0.12	0.14	0.71	0.011	-	1.527e+13	4	2	21
WX UMa	0.1	0.12	0.78	0.01	-	1.337e+15	4	2	21

1: Petit et al. (in prep); 2: do Nascimento et al. (2016); 3: Jeffers et al. (2014); 4: Morgenthaler et al. (2011); 5: Morgenthaler et al. (2012); 6: Jeffers et al. (in prep); 7: Petit et al. (2008); 8: Boro Saikia et al. (2016a); 9: Boro Saikia et al. (2015); 10: Donati et al. (2003); 11: Folsom et al. (2016); 12: Catala et al. (2007); 13: Donati et al. (2008c); 14: Fares et al. (2009); 15: Fares et al. (2013); 16: Fares et al. (2012); 17: Fares et al. (2010); 18: Donati et al. (2008a); 19: Morin et al. (2008b); 20: Morin et al. (2008a); 21: Morin et al. (2010)

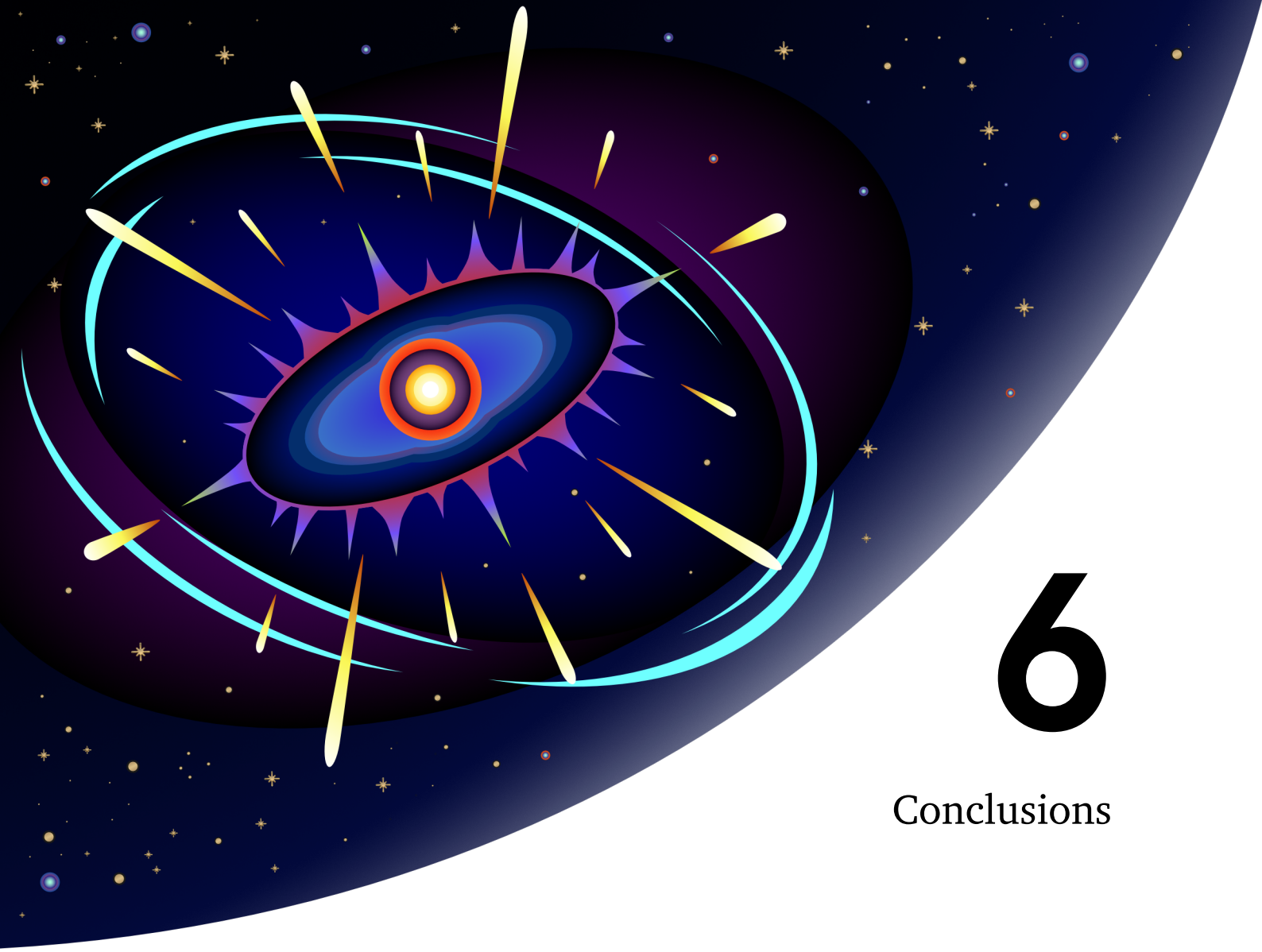

6

Conclusions

In this thesis I have studied the possibility of accretion as a means of forming high-mass stars. Specifically I have explored whether accretion can continue after the growing star begins to emit ionising radiation and whether accretion in the presence of a magnetic field can explain close high-mass binary star systems. In the latter part of the thesis I moved on to something completely different - investigating the helicity of stellar magnetic fields. In this chapter I will present my main results along with ideas for future work that could build on those results.

6.1 Ionised accretion flows

In the classic picture of HII region evolution the region grows by a pressure-driven expansion and the gravity of the central star is neglected (e.g. Spitzer, 1978). This would mean that accretion onto the star stops as soon as it begins emitting ionising radiation. However, Mestel (1954) and Keto (2002a,b, 2003) argue gravity dominates the gas dynamics for as long as the HII region is smaller than a critical radius of approximately the ionised sonic point, thus preventing a pressure-driven expansion. Whilst the HII region is trapped accretion continues through the ionisation front. The ionised region grows due to the increase in mass/luminosity until eventually its radius exceeds the critical value for gravitational trapping. Not until this point does accretion stop and the HII region begins a pressure-driven expansion.

Mestel (1954) and Keto (2002b, 2003) modelled the HII region evolution as a sequence of spherically symmetric steady state solutions with increasing ionising luminosity. In Chapter 3 (based on Lund et al. (2019)) I investigated this theoretical model by using a radiation hydrodynamics code to simulate spherically symmetric accretion onto an ionising star. The numerical simulations reproduced the main features of the analytic steady state analyses. Gravitationally trapped HII regions and ionised accretion flows were observed for as long as the ionisation fronts were within the critical radius. Beyond that point the HII regions began to expand and no more material passed through the ionisation fronts. In other words, the simulations support ionised accretion flows onto stars even after they begin to emit ionising radiation.

Contrary to the steady state analytic solutions, the numerical simulations of gravitationally trapped spherically symmetric HII regions were found to be unstable. The regions were still gravitationally trapped, but they oscillated. Any slight density perturbation initiated a runaway instability. The HII regions periodically collapsed, then reappeared at the same radius. This behaviour is specific to idealised spherically symmetric systems (Vandenbroucke et al., 2019).

In the future this work will be extended to less ideal 3D simulations. Rotation will be introduced, which should lead to accretion happening via a dense equatorial disk and most of the ionising radiation being directed along the rotation axis into the lower density regions (Keto, 2007). Additionally, once the simulations become more realistic the aim is to produce synthetic continuum and line intensity maps in order to compare with real observations.

6.2 Gravitational trapping of ultra-compact HII regions

Observations of UCHII regions suggest an average lifetime exceeding 10^5 years (Wood & Churchwell, 1989a). This is considerably longer than the time it would take to evolve from a UCHII region to a diffuse HII region via pressure-driven expansion (Wood & Churchwell, 1989b). This implies that some process must be slowing or halting the expansion. The answer could be the gravitational trapping explored in Chapter 3. During trapping the growth of the HII region depends on the accretion timescale and is relatively slow compared to pressure-driven expansion.

In Chapter 3 I presented a rough calculation of the typical duration of gravitational trapping. I first determined the required growth in luminosity and hence the additional mass needed for a given HII region to break free. Then I estimated the time it would take to accrete this amount based on the rate of flow of material. The result was a timescale of the order of 10^6 years, which does exceed the required minimum lifetime value of 10^5 years. This suggests gravitational trapping could explain the longevity of UCHII regions.

6.3 Magnetic braking of accretion flows

There is no consensus on what formation mechanism leads to high-mass stars (e.g. Zinnecker & Yorke, 2007). Any theory must be able to explain why these stars are usually discovered in close (stellar separation ≤ 0.1 au) multiple systems (Mason et al., 1998; García & Mermilliod, 2001; Zinnecker & Mathieu, 2001; Chini et al., 2012; Sana et al., 2014). Close high-mass binary stars must either have formed in situ or have evolved into this state. As discussed in Chapter 4 (based on Lund & Bonnell (2018)), both options have their difficulties. Assuming a wide low-mass binary system has already formed, accretion could drive it to smaller separations and higher masses, as long as the infalling material does not contain a significant amount of angular momentum (Bonnell & Bate, 2005).

In Chapter 4 I explored the possibility that magnetic braking of accretion flows can remove sufficient angular momentum to form close high-mass binaries. I developed a simple semi-analytic model that places a wide low-mass binary in a rotating and turbulent molecular cloud that is threaded by a magnetic field. Using this model I investigated which conditions lead to a simultaneous increase in binary mass and decrease in binary separation. I found the presence

of a magnetic field makes it substantially easier to form binary systems that are both close and high-mass. For instance, placing a 2 $M_\odot$ binary system separated by 1 au in a molecular cloud with 1145 $M_\odot$, a radius of 0.58 pc and a magnetic field of 100 μG resulted in a 26.5 $M_\odot$ binary system with a separation of $\sim$ 10 $R_\odot$.

Based on my model, magnetic braking of accretion flows seems to be a possible way of creating the most massive close binary systems. However, more advanced simulations are required to determine whether or not it is a likely formation mechanism. What follows are suggested features I would ideally like to see added in a future model of this scenario: a more complex density distribution, with denser clumps of material which would be less coupled to the magnetic field; a cluster environment, with gravitational pull from other stars; non-ideal magnetic effects such as ambipolar diffusion and magnetic reconnection; stellar feedback in the form of ionisation, stellar winds and radiation pressure. This physics could be captured using a radiation magnetohydrodynamics code.

6.4 A stellar magnetic helicity density expression

Helicity is a fundamental property of magnetic fields and its level of conservation makes it a powerful tool when studying topics such as field generation and evolution (e.g. Brandenburg & Subramanian, 2005; Chatterjee et al., 2011). There has been growing interest in magnetic helicity as an indicator of stellar activity (Nindos, 2013), but measurements have been limited to the Sun. In Chapter 5 (based on Lund et al. (2020)) the observational study of helicity was extended to other stars.

I provided a technique for mapping the large-scale magnetic helicity density across any stellar surface in terms of observable quantities: the poloidal and toroidal magnetic field components and the stellar radius. The aim is for this to be a simple expression that can allow anyone to calculate stellar helicity densities given the input data. Hopefully this is just the first step and more investigation into the helicity of stars will follow as a result.

6.5 The typical solar magnetic helicity density

In Chapter 5 I calculated the helicity density of a sample of 52 stars, including the Sun. Both simulated and observational solar data was used, however the resolution was reduced in order to mimic the Sun as a distant star. I found that the solar helicity density varies in magnitude and

sign across the solar cycle, and generally the sign is always flipped across the equator. I believe this informs how helicity density is best expressed when comparing values between stars. The fact that the helicity density in the two solar hemispheres approximately cancels suggests an average across a single hemisphere gives a more meaningful value than an average across the entire sphere. Furthermore, the absolute value of the average helicity density is taken because the sign can vary in time. For ease I refer to the absolute value of the average helicity density across the visible hemisphere simply as the helicity density from now on.

I compared the helicity density of the observed Sun with those of the other stars in my stellar sample. When sorting the values by stellar mass the Sun appeared to have a relatively low helicity density, however when plotting against Rossby number it looked normal. This suggests the Sun is not discrepant, it just has a lower rotation rate than many of the other stars in the stellar sample of similar mass. Solar values across a long time period were plotted, and despite being spread across approximately two orders of magnitude, it seemed to always fall within the scatter of the stellar values. In conclusion, I found the solar values to be consistent with the stellar data available.

The fact that the solar data fits so nicely within the stellar scatter could suggest the stars have similar cycles to the Sun, and are being imaged at different stages of their cycles. There could however be other explanations for the scatter, such as it being an effect of different stellar inclination angles (Lehmann et al., 2019). In the future it would be interesting to investigate variations in stellar helicity density over time. With magnetic maps of stars such as 61 Cyg A (Boro Saikia et al., 2016b) or τ Boo (Fares et al., 2009, 2013), which have been monitored over longer time periods, it would be possible to plot helicity density as a function of time and compare the results to the behaviour of the Sun.

6.6 Magnetic helicity density of fully and partially convective stars

Stellar magnetic fields have been shown to exhibit different properties depending on whether the mass of the host star is above or below 0.5 $M_\odot$ (Donati et al., 2008a; Morin et al., 2008b, 2010; Gregory et al., 2012; See et al., 2015). This is believed to be related to the sudden transition in stellar internal structure from partially convective stars with inner radiative interiors out to ~ 0.2 $R_\star$ (at 0.5 $M_\odot$) to fully convective stars (at 0.3 $M_\odot$) (Donati et al., 2008a). When exploring the behaviour of stellar magnetic helicity density in Chapter 5 I found that it too

changes at this boundary. It rises with decreasing stellar mass, potentially reaching a plateau around 0.5 $M_\odot$.

Moving on from masses to Rossby numbers, various indicators of magnetic activity have been reported to reach their highest levels at $R_o \sim 0.1$ (Wright et al., 2011; See et al., 2017; Mondrik et al., 2019). Similarly, I found that the magnetic helicity density rises with decreasing Rossby number, until $R_o \sim 0.1$. It is not clear whether the helicity density reaches a peak or a saturation at this point. The region beyond $R_o \sim 0.1$ is populated by the majority of the largely convective stars with masses below 0.5 $M_\odot$ along with a couple of rapidly rotating higher-mass stars. The observed spread in the helicity density values of these stars could either be a drop with decreasing Rossby number or saturation at two different levels, attributed to a bi-stable dynamo (Morin et al., 2011b; Schrinner et al., 2012; Gastine et al., 2013).

Currently it is not possible to say for certain whether the differences in behaviour across masses and Rossby numbers are a product of bias in the stellar sample. There is a lack of magnetic maps of rapidly rotating stars above $\sim$ 0.5 $M_\odot$ and slowly rotating stars below $\sim$ 0.5 $M_\odot$. Filling these gaps would strengthen observational studies of the properties of stellar magnetic fields across fully and partially convective stars. Additionally, observing a greater number of stars with low Rossby numbers could help confirm the potential existence of bi-stable magnetic dynamos.

Plotting helicity density against magnetic energy components revealed a potential cause of the difference in helicity density between largely convective ($M_\star < 0.5$ $M_\odot$) and partially convective ($M_\star > 0.5$ $M_\odot$) stars. The helicity density of these two groups of stars are offset from each other and have different slopes when plotted against the full stellar magnetic energy or the poloidal energy. However, when plotting against the toroidal energy all the stars in the stellar sample follow the same power law: $|\langle h \rangle| \propto \langle B_{tor}^2 \rangle^{0.86 \pm 0.04}$. Because the stellar helicity density was found to be so tightly correlated with the toroidal magnetic field, it implies the different trends reported for the partially convective and largely convective stars is due to the latter having relatively strong poloidal fields.

Future work should aim to explain the "excess" poloidal field discovered in the largely convective stars - answering questions such as where it comes from, and why it does not contribute to the magnetic helicity. A possible initial approach could be mapping poloidal and toroidal magnetic field components on a surface map and comparing them to the distribution

of the corresponding magnetic helicity. Perhaps a visual representation of how these properties relate on a number of fully and partially convective stars will shed some light on the differences between these two groups of stars.

Bibliography

Adelman, S. J. 2004, in IAU Symposium, Vol. 224, The A-Star Puzzle, ed. J. Zverko, J. Ziznovsky, S. J. Adelman, & W. W. Weiss, 1–11

Ahmed, O. W., Qahwaji, R., Colak, T., Higgins, P. A., Gallagher, P. T., & Bloomfield, D. S. 2013, Sol. Phys., 283, 157

Alves, J., Lombardi, M., & Lada, C. J. 2007, AA, 462, L17, astro-ph/0612126

Amari, T., Luciani, J. F., Aly, J. J., Mikic, Z., & Linker, J. 2003, ApJ, 595, 1231

Argiroffi, C. et al. 2019, Nature Astronomy, 3, 742, 1905.11325

Armitage, P. J. 2010, Astrophysics of Planet Formation

Babcock, H. W. 1947, ApJ, 105, 105

Balega, Y. Y., Chentsov, E. L., Leushin, V. V., Rzaev, A. K., & Weigelt, G. 2014, Astrophysical Bulletin, 69, 46

Baliunas, S. L. et al. 1995, ApJ, 438, 269

Ballesteros-Paredes, J., Klessen, R. S., Mac Low, M. M., & Vazquez-Semadeni, E. 2007, in Protostars and Planets V, ed. B. Reipurth, D. Jewitt, & K. Keil, 63, astro-ph/0603357

Baraffe, I., & Chabrier, G. 1996, ApJL, 461, L51

Baraffe, I., Chabrier, G., Allard, F., & Hauschildt, P. H. 2002, AA, 382, 563, astro-ph/0111385

Bate, M. R. 1998, ApJL, 508, L95, astro-ph/9810397

Bate, M. R., & Bonnell, I. A. 1997, MNRAS, 285, 33

Benz, A. O. 2008, Living Rev. Sol. Phys., 5, 1

Beresnyak, A. 2019, Living Reviews in Computational Astrophysics, 5, 2, 1910.03585

Berger, M. A. 1985, ApJS, 59, 433

Berger, M. A., & Field, G. B. 1984, J. Fluid Mech., 147, 133

Berger, M. A., & Hornig, G. 2018, J Phys Math Gen, 51, 495501

Berger, M. A., & Ruzmaikin, A. 2000, J. Geophys. Res., 105, 10481

Bisbas, T. G. et al. 2015, MNRAS, 453, 1324, 1507.05621

Blackman, E. G. 2015, Space Sci. Rev., 188, 59, 1402.0933

Bobra, M. G., & Ilonidis, S. 2016, ApJ, 821, 127, 1603.03775

Bodenheimer, P., & Ostriker, J. P. 1970, ApJ, 161, 1101

Bondi, H. 1952, MNRAS, 112, 195

Bondi, H., & Hoyle, F. 1944, MNRAS, 104, 273

Bonnell, I. A. 1994, MNRAS, 269, 837

Bonnell, I. A. 1999, in NATO Advanced Science Institutes (ASI) Series C, Vol. 540, NATO Advanced Science Institutes (ASI) Series C, ed. C. J. Lada & N. D. Kylafis, 479

Bonnell, I. A., & Bate, M. R. 1994, MNRAS, 271, astro-ph/9411081

——. 2002, MNRAS, 336, 659

——. 2005, MNRAS, 362, 915, astro-ph/0506689

——. 2006, MNRAS, 370, 488, astro-ph/0604615

Bonnell, I. A., Bate, M. R., Clarke, C. J., & Pringle, J. E. 1997, MNRAS, 285, 201

——. 2001a, MNRAS, 323, 785, astro-ph/0102074

Bonnell, I. A., Bate, M. R., & Zinnecker, H. 1998, MNRAS, 298, 93, astro-ph/9802332

Bonnell, I. A., Clarke, C. J., Bate, M. R., & Pringle, J. E. 2001b, MNRAS, 324, 573, astro-ph/0102121

Bonnell, I. A., Larson, R. B., & Zinnecker, H. 2007, in Protostars and Planets V, ed. B. Reipurth, D. Jewitt, & K. Keil, 149, astro-ph/0603447

Bonnell, I. A., Vine, S. G., & Bate, M. R. 2004, MNRAS, 349, 735, astro-ph/0401059

Boro Saikia, S. et al. 2016a, AA, 594, A29, 1606.01032

——. 2016b, AA, 594, A29, 1606.01032

Boro Saikia, S., Jeffers, S. V., Petit, P., Marsden, S., Morin, J., & Folsom, C. P. 2015, AA, 573, A17, 1410.8307

Bourke, T. L., Myers, P. C., Robinson, G., & Hyland, A. R. 2001, ApJ, 554, 916, astro-ph/0102469

Brandenburg, A., & Subramanian, K. 2005, Phys. Rep, 417, 1, astro-ph/0405052

Briquet, M. 2015, in European Physical Journal Web of Conferences, Vol. 101, European Physical Journal Web of Conferences, 05001, 1411.7549

Brown, S. F., Donati, J. F., Rees, D. E., & Semel, M. 1991, AA, 250, 463

Carrington, R. C. 1859, MNRAS, 20, 13

Catala, C., Donati, J.-F., Shkolnik, E., Bohlender, D., & Alecian, E. 2007, MNRAS, 374, L42, astro-ph/0610758

Cernicharo, J. 1991, in NATO Advanced Science Institutes (ASI) Series C, Vol. 342, NATO Advanced Science Institutes (ASI) Series C, ed. C. J. Lada & N. D. Kylafis, 287

Cesaroni, R., Galli, D., Lodato, G., Walmsley, C. M., & Zhang, Q. 2007, in Protostars and Planets V, ed. B. Reipurth, D. Jewitt, & K. Keil, 197, astro-ph/0603093

Chabrier, G. 2003, PASP, 115, 763, astro-ph/0304382

Chabrier, G., & Baraffe, I. 1997, AA, 327, 1039, astro-ph/9704118

Chabrier, G., & Hennebelle, P. 2010, ApJL, 725, L79, 1011.1185

Chandrasekhar, S. 1961, Hydrodynamic and Hydromagnetic Stability (Clarendon Press)

Charbonneau, P., & MacGregor, K. B. 1997, ApJ, 486, 502

Chatterjee, P., Guerrero, G., & Brandenburg, A. 2011, AA, 525, A5, 1005.5335

Chini, R., Hoffmeister, V. H., Nasseri, A., Stahl, O., & Zinnecker, H. 2012, MNRAS, 424, 1925, 1205.5238

Churchwell, E. 2002, ARAA, 40, 27

Cid, C., Palacios, J., Saiz, E., Guerrero, A., & Cerrato, Y. 2014, J. Space Weather. Space Clim., 4, A28

Clarke, C. J., & Bonnell, I. A. 2008, MNRAS, 388, 1171

Clarke, C. J., & Pringle, J. E. 1991, MNRAS, 249, 584

Cliver, E. W., Feynman, J., & Garrett, H. B. 1990, J. Geophys. Res., 95, 17103

Commerçon, B., Hennebelle, P., & Henning, T. 2011, ApJL, 742, L9, 1110.2955

Courant, R., Friedrichs, K., & Lewy, H. 1967, IBM J. Res. Dev, 11, 215

Cram, L. E., Kuhi, L. V., Jordan, S., Thomas, R., Goldberg, L., & Pecker, J.-C. 1989, FGK stars and T Tauri stars, Vol. 502

Cranmer, S. R., & Saar, S. H. 2011, ApJ, 741, 54, 1108.4369

Crowther, P. A. et al. 2016, MNRAS, 458, 624, http://oup.prod.sis.lan/mnras/article-pdf/458/1/624/8181162/stw273.pdf

Crowther, P. A., Schnurr, O., Hirschi, R., Yusof, N., Parker, R. J., Goodwin, S. P., & Kassim, H. A. 2010, MNRAS, 408, 731, 1007.3284

Crutcher, R. M. 1999, ApJ, 520, 706

Crutcher, R. M. 2012, ARAA, 50, 29, https://doi.org/10.1146/annurev-astro-081811-125514

Crutcher, R. M., Hakobian, N., & Troland, T. H. 2009, ApJ, 692, 844, 0807.2862

Cyganowski, C. J. et al. 2014, ApJL, 796, L2, 1410.2605

Dale, J. E., Bonnell, I. A., Clarke, C. J., & Bate, M. R. 2005, MNRAS, 358, 291, astro-ph/0501160

Dale, J. E., Ngoumou, J., Ercolano, B., & Bonnell, I. A. 2014, MNRAS, 442, 694, 1404.6102

Darwin, G. H. 1879, Philos. Trans. R. Soc. London, Ser. I, 170, 1

de la Fuente, E., Porras, A., Trinidad, M. A., Kurtz, S. E., Kemp, S. N., Tafoya, D., Franco, J., & Rodríguez-Rico, C. 2020, MNRAS, 492, 895, 1912.08958

De Pree, C. G., Wilner, D. J., Deblasio, J., Mercer, A. J., & Davis, L. E. 2005, ApJL, 624, L101, astro-ph/0504230

Démoulin, P. 2007, Adv. Space Res, 39, 1674

Démoulin, P., Mandrini, C. H., van Driel-Gesztelyi, L., Thompson, B. J., Plunkett, S., Kovári, Z., Aulanier, G., & Young, A. 2002, AA, 382, 650

Démoulin, P., & Pariat, E. 2009, Adv. Space Res, 43, 1013

do Nascimento, J. D., J. et al. 2016, ApJL, 820, L15, 1603.03937

Dobbs, C. L., Bonnell, I. A., & Clark, P. C. 2005, MNRAS, 360, 2, astro-ph/0502479

Donati, J. F. 2001, Imaging the Magnetic Topologies of Cool Active Stars, ed. H. M. J. Boffin, D. Steeghs, & J. Cuypers, Vol. 573, 207

Donati, J.-F. et al. 2003, MNRAS, 345, 1145

Donati, J.-F. et al. 2011, MNRAS, 417, 1747, http://oup.prod.sis.lan/mnras/article-pdf/417/3/1747/3797026/mnras0417-1747.pdf

Donati, J.-F. et al. 2006, MNRAS, 370, 629, astro-ph/0606156

Donati, J. F., & Landstreet, J. D. 2009, ARAA, 47, 333, 0904.1938

Donati, J.-F. et al. 2008a, MNRAS, 390, 545, 0809.0269

Donati, J. F. et al. 2008b, MNRAS, 390, 545, 0809.0269

Donati, J.-F. et al. 2008c, MNRAS, 385, 1179, 0802.1584

Draine, B. T., Roberge, W. G., & Dalgarno, A. 1983, ApJ, 264, 485

Drake, J. J., Peres, G., Orlando, S., Laming, J. M., & Maggio, A. 2000, ApJ, 545, 1074

Drissen, L., Moffat, A. F. J., Walborn, N. R., & Shara, M. M. 1995, AJ, 110, 2235

Duarte-Cabral, A., Bontemps, S., Motte, F., Gusdorf, A., Csengeri, T., Schneider, N., & Louvet, F. 2014, AA, 570, A1, 1407.6400

Durisen, R. H., Gingold, R. A., Tohline, J. E., & Boss, A. P. 1986, ApJ, 305, 281

Edgar, R., & Clarke, C. 2004, MNRAS, 349, 678, astro-ph/0312325

Elmegreen, B. G. 2000, ApJ, 539, 342, astro-ph/0005455

Ercolano, B., & Gritschneder, M. 2011, in IAU Symposium, Vol. 270, Computational Star Formation, ed. J. Alves, B. G. Elmegreen, J. M. Girart, & V. Trimble, 301–308, 1010.5374

Essinger, J. 2004, Jacquard's Web: How a Hand-loom Led to the Birth of the Information Age, Collection of Jamie and Michael Kassler (Oxford University Press)

Evans, Neal J., I. et al. 2009, ApJS, 181, 321, 0811.1059

Fabian, A. C., Pringle, J. E., & Rees, M. J. 1975, MNRAS, 172, 15

Falceta-Gonçalves, D., Bonnell, I., Kowal, G., Lépine, J. R. D., & Braga, C. A. S. 2015, MNRAS, 446, 973, 1410.2774

Falceta-Gonçalves, D., & Kowal, G. 2015, ApJ, 808, 65, 1506.06398

Fares, R. et al. 2009, MNRAS, 398, 1383, 0906.4515

——. 2012, MNRAS, 423, 1006, 1202.4472

——. 2010, MNRAS, 406, 409, 1003.6027

Fares, R., Moutou, C., Donati, J.-F., Catala, C., Shkolnik, E. L., Jardine, M. M., Cameron, A. C., & Deleuil, M. 2013, MNRAS, 435, 1451, 1307.6091

Federrath, C. 2016, in J. Phys. Conf. Ser, Vol. 719, J. Phys. Conf. Ser, 012002, 1606.03121

Ferrière, K. M. 2001, Rev. Mod. Phys, 73, 1031, astro-ph/0106359

Feynman, J., & Gabriel, S. B. 2000, J. Geophys. Res., 105, 10543

Folsom, C. P. et al. 2016, MNRAS, 457, 580, 1601.00684

Futaana, Y., Stenberg Wieser, G., Barabash, S., & Luhmann, J. G. 2017, Space Sci. Rev., 212, 1453

Garay, G., & Lizano, S. 1999, PASP, 111, 1049, astro-ph/9907293

García, B., & Mermilliod, J. C. 2001, AA, 368, 122

Gastine, T., Morin, J., Duarte, L., Reiners, A., Christensen, U. R., & Wicht, J. 2013, AA, 549, L5, 1212.0136

Geen, S., Pellegrini, E., Bieri, R., & Klessen, R. 2020, MNRAS, 492, 915, 1906.05649

Godunov, S. K. 1959, Mat. Sb. (N.S.), 47

Goodman, A. A., Benson, P. J., Fuller, G. A., & Myers, P. C. 1993, ApJ, 406, 528

Gravity Collaboration et al. 2018, AA, 620, A116, 1809.10376

Green, L. M., López fuentes, M. C., Mandrini, C. H., Démoulin, P., Van Driel-Gesztelyi, L., & Culhane, J. L. 2002, Sol. Phys., 208, 43

Gregory, S. G., Donati, J. F., Morin, J., Hussain, G. A. J., Mayne, N. J., Hillenbrand, L. A., & Jardine, M. 2012, ApJ, 755, 97, 1206.5238

Gritschneder, M., Naab, T., Walch, S., Burkert, A., & Heitsch, F. 2009, ApJL, 694, L26, 0901.2113

Grunhut, J. H. et al. 2017, MNRAS, 465, 2432, 1610.07895

Hale, G. E. 1908, ApJ, 28, 315

Hale, G. E., Ellerman, F., Nicholson, S. B., & Joy, A. H. 1919, ApJ, 49, 153

Hall, S. M., Clarke, C. J., & Pringle, J. E. 1996, MNRAS, 278, 303, astro-ph/9510153

Harries, T. 2014, TORUS: Radiation transport and hydrodynamics code, Astrophysics Source Code Library, 1404.006

Harries, T. J. 2000, MNRAS, 315, 722

——. 2015, MNRAS, 448, 3156, 1501.05754

Harries, T. J., Douglas, T. A., & Ali, A. 2017, MNRAS, 471, 4111, 1706.04017

Harten, A., D. Lax, P., & van Leer, B. 1983, SIAM Rev, 25, 35

Hartmann, L. 1998, Accretion Processes in Star Formation

Hawkes, G., & Berger, M. A. 2018, in IAU Symposium, Vol. 335, Space Weather of the Heliosphere: Processes and Forecasts, ed. C. Foullon & O. E. Malandraki, 20–22

Haworth, T. J., & Harries, T. J. 2012, MNRAS, 420, 562, 1110.5266

Haworth, T. J., Harries, T. J., Acreman, D. M., & Bisbas, T. G. 2015, MNRAS, 453, 2277, 1508.00900

He, Y.-X. et al. 2015, MNRAS, 450, 1926, 1504.00438

Heggie, D. C. 1975, MNRAS, 173, 729

Heitsch, F., Hartmann, L. W., & Burkert, A. 2008, ApJ, 683, 786, 0805.0801

Heyer, M. H., & Brunt, C. M. 2004, ApJL, 615, L45, astro-ph/0409420

Hillenbrand, L. A. 1997, AJ, 113, 1733

Hobsbawm, E. 2010, Age Of Revolution: 1789-1848 (Orion Publishing Group)

Hodgson, R. 1859, MNRAS, 20, 15

Hosokawa, T., & Inutsuka, S.-i. 2006, ApJ, 646, 240, astro-ph/0511165

Houdebine, E. R., Foing, B. H., & Rodono, M. 1990, AA, 238, 249

Hoyle, F. 1953, ApJ, 118, 513

Hummer, D. G., & Seaton, M. J. 1963, MNRAS, 125, 437

Hunter, C. 1962, ApJ, 136, 594

Jakosky, B. M. et al. 2018, Icarus, 315, 146

James, D. J., Jardine, M. M., Jeffries, R. D., Randich, S., Collier Cameron, A., & Ferreira, M. 2000, MNRAS, 318, 1217, astro-ph/0007159

Janiak, A., & Newton, I. 2004, Correspondence with Richard Bentley [1692–3], ed. A. Janiak, Cambridge Texts in the History of Philosophy (Cambridge University Press), 94–105

Jeans, J. H. 1902, Philos. Trans. R. Soc. London, Ser. A, 199, 1

——. 1919, Problems of cosmogony and stellar dynamics

Jeffers, S. V., Petit, P., Marsden, S. C., Morin, J., Donati, J.-F., & Folsom, C. P. 2014, AA, 569, A79

Jeffries, R. D., Evans, P. A., Pye, J. P., & Briggs, K. R. 2006, MNRAS, 367, 781, astro-ph/0512441

Jeffries, R. D., Jackson, R. J., Briggs, K. R., Evans, P. A., & Pye, J. P. 2011, MNRAS, 411, 2099, 1010.2152

Joos, M., Hennebelle, P., & Ciardi, A. 2012, AA, 543, A128, 1203.1193

Jørgensen, C. S., Karoff, C., Senthamizh Pavai, V., & Arlt, R. 2019, Sol. Phys., 294, 77, 1906.10884

Joung, M. K. R., & Mac Low, M.-M. 2006, ApJ, 653, 1266, astro-ph/0601005

Kahn, F. D. 1974, AA, 37, 149

Kawaler, S. D. 1988, ApJ, 333, 236

Kay, C., Opher, M., & Kornbleuth, M. 2016, ApJ, 826, 195, 1605.02683

Keto, E. 2002a, APJ, 568, 754

——. 2002b, ApJ, 580, 980

——. 2003, ApJ, 599, 1196, astro-ph/0309131

——. 2007, ApJ, 666, 976, astro-ph/0603856

Kim, K.-T., & Koo, B.-C. 2001, ApJ, 549, 979, astro-ph/0010535

Kiraga, M., & Stepien, K. 2007, Acta Astronaut., 57, 149, 0707.2577

Kitchatinov, L. L., Moss, D., & Sokoloff, D. 2014, MNRAS, 442, L1, 1401.1764

Klaassen, P. D. et al. 2018, AA, 611, A99

Klaassen, P. D., & Wilson, C. D. 2007, ApJ, 663, 1092, 0704.1245

Klassen, M., Kuiper, R., Pudritz, R. E., Peters, T., Banerjee, R., & Buntemeyer, L. 2014, ApJ, 797, 4, 1410.4259

Klessen, R. S., Heitsch, F., & Mac Low, M.-M. 2000, ApJ, 535, 887, astro-ph/9911068

Klessen, R. S., & Hennebelle, P. 2010, AA, 520, A17, 0912.0288

Kobulnicky, H. A., & Fryer, C. L. 2007, ApJ, 670, 747

Kochukhov, O., & Shulyak, D. 2019, ApJ, 873, 69, 1902.04157

Kong, S., Tan, J. C., Caselli, P., Fontani, F., Liu, M., & Butler, M. J. 2017, ApJ, 834, 193, 1609.06008

Kowal, G., Falceta-Gonçalves, D. A., & Lazarian, A. 2011, New J. Phys, 13, 053001, 1012.5125

Kowal, G., Falceta-Gonçalves, D. A., Lazarian, A., & Vishniac, E. T. 2017, ApJ, 838, 91, 1611.03914

Krieger, A. S., Vaiana, G. S., & van Speybroeck, L. P. 1971, in IAU Symposium, Vol. 43, Solar Magnetic Fields, ed. R. Howard, 397

Kroupa, P. 2001, MNRAS, 322, 231, astro-ph/0009005

Krumholz, M. R. 2014, Phys. Rep., 539, 49, 1402.0867

——. 2015, ASSL, Vol. 412, The Formation of Very Massive Stars, ed. J. S. Vink, 43

Krumholz, M. R., & Bonnell, I. A. 2009, Models for the formation of massive stars, ed. G. Chabrier, 288–320

Krumholz, M. R., & Burkhart, B. 2016, MNRAS, 458, 1671, https://academic.oup.com/mnras/article-pdf/458/2/1671/18242714/stw434.pdf

Krumholz, M. R., Klein, R. I., & McKee, C. F. 2007, ApJ, 656, 959, astro-ph/0609798

Krumholz, M. R., Klein, R. I., McKee, C. F., Offner, S. S. R., & Cunningham, A. J. 2009, Science, 323, 754, 0901.3157

Krumholz, M. R., McKee, C. F., & Klein, R. I. 2005, ApJL, 618, L33, astro-ph/0411526

Kudoh, T., & Basu, S. 2008, ApJL, 679, L97, 0804.4303

Kuiper, R., & Hosokawa, T. 2018, AA, 616, A101, 1804.10211

Kuiper, R., Klahr, H., Beuther, H., & Henning, T. 2010, ApJ, 722, 1556, 1008.4516

Kuiper, R., Yorke, H. W., & Turner, N. J. 2015, ApJ, 800, 86, 1412.6528

Kurtz, S., Churchwell, E., & Wood, D. O. S. 1994, ApJS, 91, 659

Lada, C. J., & Kylafis, N. D., eds. 1991, The physics of star formation and early stellar evolution, Vol. 342

Lakhina, G. S., & Tsurutani, B. T. 2016, Geosci. Lett., 3, 5

Lammer, H. et al. 2007, Astrobiology, 7, 185

Lammer, H., Stumptner, W., Molina-Cuberos, G. J., Bauer, S. J., & Owen, T. 2000, Planet. Space Sci., 48, 529

Larson, R. B. 1973, MNRAS, 161, 133

——. 1981, MNRAS, 194, 809

——. 1982, MNRAS, 200, 159

Larson, R. B. 1990, in ASSL, Vol. 162, Physical Processes in Fragmentation and Star Formation, ed. R. Capuzzo-Dolcetta, C. Chiosi, & A. di Fazio, 389–399

——. 2003a, Rep. Prog. Phys., 66, 1651, astro-ph/0306595

Larson, R. B. 2003b, in Astronomical Society of the Pacific Conference Series, Vol. 287, Galactic Star Formation Across the Stellar Mass Spectrum, ed. J. M. De Buizer & N. S. van der Bliek, 65–80, astro-ph/0205466

Lazarian, A., Vlahos, L., Kowal, G., Yan, H., Beresnyak, A., & de Gouveia Dal Pino, E. M. 2012, Space Sci. Rev., 173, 557, 1211.0008

Lehmann, L. T., Hussain, G. A. J., Jardine, M. M., Mackay, D. H., & Vidotto, A. A. 2019, MNRAS, 483, 5246, 1811.03703

Leighton, R. B. 1959, ApJ, 130, 366

Leitzinger, M. et al. 2020, MNRAS, 2002.04430

Li, Z.-Y., Krasnopolsky, R., & Shang, H. 2013, ApJ, 774, 82, 1301.6545

Liu, H., Liu, C., Wang, J. T. L., & Wang, H. 2020, ApJ, 890, 12, 2002.10953

Lucy, L. B. 1999, AA, 344, 282

Lund, K., & Bonnell, I. A. 2018, MNRAS, 1806.07394

Lund, K. et al. 2020, MNRAS, 493, 1003, https://academic.oup.com/mnras/article-pdf/493/1/1003/32532676/staa297.pdf

Lund, K., Wood, K., Falceta-Gonçalves, D., Vandenbroucke, B., Sartorio, N. S., Bonnell, I. A., Johnston, K. G., & Keto, E. 2019, MNRAS, 485, 3761, 1903.00486

Lunttila, T., Padoan, P., Juvela, M., & Nordlund, Å. 2008, ApJL, 686, L91, 0806.3854

——. 2009, ApJL, 702, L37, 0907.0587

Mac Low, M.-M., & Klessen, R. S. 2004, Rev. Mod. Phys, 76, 125, astro-ph/0301093

Mac Low, M.-M., Klessen, R. S., Burkert, A., & Smith, M. D. 1998, Phys. Rev. Lett., 80, 2754, astro-ph/9712013

Mac Low, M.-M., Toraskar, J., Oishi, J. S., & Abel, T. 2007, ApJ, 668, 980, astro-ph/0605501

Mac Low, M.-M., van Buren, D., Wood, D. O. S., & Churchwell, E. 1991, ApJ, 369, 395

Mackey, J., Langer, N., & Gvaramadze, V. V. 2013, MNRAS, 436, 859, 1308.5192

Maeder, A., & Meynet, G. 1987, AA, 182, 243

Mansbach, P. 1970, ApJ, 160, 135

Mason, B. D., Gies, D. R., Hartkopf, W. I., Bagnuolo, Jr., W. G., ten Brummelaar, T., & McAlister, H. A. 1998, AJ, 115, 821

Masson, J., Chabrier, G., Hennebelle, P., Vaytet, N., & Commerçon, B. 2016, AA, 587, A32, 1509.05630

Mathis, J. S., & Wood, K. 2005, MNRAs, 360, 227, astro-ph/0503577

McComas, D. J. et al. 2000, J. Geophys. Res., 105, 10419

McKee, C. F., & Ostriker, E. C. 2007, ARAA, 45, 565, 0707.3514

McKee, C. F., & Tan, J. C. 2003, ApJ, 585, 850, astro-ph/0206037

Mestel, L. 1954, MNRAS, 114, 437

Mestel, L. 1984, in Lect. Notes Phys, Berlin Springer Verlag, Vol. 193, Cool Stars, Stellar Systems, and the Sun, ed. S. L. Baliunas & L. Hartmann, 49

Mestel, L., & Spitzer, L., J. 1956, MNRAS, 116, 503

Michell, J. 1767, Philos. Trans. R. Soc. London, 57, 234, https://royalsocietypublishing.org/doi/pdf/10.1098/rstl.1767.0028

Miller, G. E., & Scalo, J. M. 1979, ApJS, 41, 513

Moeckel, N., & Bally, J. 2007a, ApJL, 661, L183, 0704.1162

——. 2007b, ApJ, 656, 275, astro-ph/0610633

Mondrik, N., Newton, E., Charbonneau, D., & Irwin, J. 2019, ApJ, 870, 10, 1809.09177

Montesinos, B., Thomas, J. H., Ventura, P., & Mazzitelli, I. 2001, MNRAS, 326, 877

Morgenthaler, A., Petit, P., Morin, J., Aurière, M., Dintrans, B., Konstantinova-Antova, R., & Marsden, S. 2011, Astron. Nachr., 332, 866, 1109.3982

Morgenthaler, A. et al. 2012, AA, 540, A138, 1109.5066

Moriña, D., Serra, I., Puig, P., & Corral, Á. 2019, Sci. Rep, 9, 2393

Morin, J., Delfosse, X., Donati, J. F., Dormy, E., Forveille, T., Jardine, M. M., Petit, P., & Schrinner, M. 2011a, in SF2A-2011: Proceedings of the Annual meeting of the French Society of Astronomy and Astrophysics, ed. G. Alecian, K. Belkacem, R. Samadi, & D. Valls-Gabaud, 503–508, 1208.3341

Morin, J. et al. 2008a, MNRAS, 384, 77, 0711.1418

——. 2008b, MNRAS, 390, 567, 0808.1423

Morin, J., Donati, J. F., Petit, P., Delfosse, X., Forveille, T., & Jardine, M. M. 2010, MNRAS, 407, 2269, 1005.5552

Morin, J., Dormy, E., Schrinner, M., & Donati, J. F. 2011b, MNRAS, 418, L133, 1106.4263

Morison, I. 2014, A Journey through the Universe

Motte, F., Andre, P., & Neri, R. 1998, AA, 336, 150

Motte, F. et al. 2018, Nature Astronomy, 2, 478, 1804.02392

Mouschovias, T. C. 1987, in NATO ASIC Proc. 210: Physical Processes in Interstellar Clouds, ed. G. E. Morfill & M. Scholer, 453–489

Mouschovias, T. C. 1991, ApJ, 373, 169

Mouschovias, T. C., & Paleologou, E. V. 1979, ApJ, 230, 204

Mouschovias, T. C., & Spitzer, Jr., L. 1976, ApJ, 210, 326

Muller, C. 2014, Origins of Life and Evolution of the Biosphere, 44, 185

Nakamura, F., & Li, Z.-Y. 2008, ApJ, 687, 354, 0804.4201

Nakano, T. 1973, PASJ, 25, 91

——. 1989, ApJ, 345, 464

Neugebauer, M., & Snyder, C. W. 1962, Science, 138, 1095

Nindos, A. 2013, in IAU Symposium, Vol. 294, Solar and Astrophysical Dynamos and Magnetic Activity, ed. A. G. Kosovichev, E. de Gouveia Dal Pino, & Y. Yan, 519–530

Nindos, A., & Andrews, M. D. 2004, ApJL, 616, L175

Nindos, A., & Zhang, H. 2002, ApJL, 573, L133

Nony, T. et al. 2018, AA, 618, L5, 1810.01404

Norman, M. L., Wilson, J. R., & Barton, R. T. 1980, ApJ, 239, 968

Noyes, R. W., Hartmann, L. W., Baliunas, S. L., Duncan, D. K., & Vaughan, A. H. 1984, ApJ, 279, 763

Ogino, S., Tomisaka, K., & Nakamura, F. 1999, PASJ, 51, 637

Osterbrock, D. E., & Ferland, G. J. 2006, Astrophysics of gaseous nebulae and active galactic nuclei

Padoan, P., Federrath, C., Chabrier, G., Evans, N. J., I., Johnstone, D., Jørgensen, J. K., McKee, C. F., & Nordlund, Å. 2014, in Protostars and Planets VI, ed. H. Beuther, R. S. Klessen, C. P. Dullemond, & T. Henning, 77, 1312.5365

Padoan, P., & Nordlund, Å. 2011, ApJ, 730, 40, 0907.0248

Palla, F., & Stahler, S. W. 1993, ApJ, 418, 414

Pallavicini, R., Golub, L., Rosner, R., Vaiana, G. S., Ayres, T., & Linsky, J. L. 1981, ApJ, 248, 279

Pariat, E., Leake, J. E., Valori, G., Linton, M. G., Zuccarello, F. P., & Dalmasse, K. 2017, AA, 601, A125, 1703.10562

Parker, E. N. 1955, ApJ, 122, 293

——. 1962, Space Sci. Rev., 1, 62

Pesnell, W. D., Thompson, B. J., & Chamberlin, P. C. 2012, Sol. Phys., 275, 3

Peters, T., Mac Low, M.-M., Banerjee, R., Klessen, R. S., & Dullemond, C. P. 2010, ApJ, 719, 831, 1003.4998

Petit, P. et al. 2008, MNRAS, 388, 80, 0804.1290

Phillips, A. D., MacNeice, P. J., & Antiochos, S. K. 2005, ApJL, 624, L129

Pipin, V. V., Pevtsov, A. A., Liu, Y., & Kosovichev, A. G. 2019, ApJ, 877, L36, 1905.00772

Pizzolato, N., Maggio, A., Micela, G., Sciortino, S., & Ventura, P. 2003, AA, 397, 147

Press, W. H., & Teukolsky, S. A. 1977, ApJ, 213, 183

Price, D. J., & Bate, M. R. 2008, MNRAS, 385, 1820, 0801.3293

Reiners, A., & Basri, G. 2009, AA, 496, 787, 0901.1659

Reiners, A., Schüssler, M., & Passegger, V. M. 2014, ApJ, 794, 144, 1408.6175

Richardson, J. D., & Stone, E. C. 2009, Space Sci. Rev., 143, 7

Riley, P., & Love, J. J. 2017, Space Weather, 15, 53

Roberts, P. H. 2007, Alfvén's Theorem and the Frozen Flux Approximation, ed. D. Gubbins & E. Herrero-Bervera (Dordrecht: Springer Netherlands), 7–11

Robinson, R. D., Worden, S. P., & Harvey, J. W. 1980, ApJL, 236, L155

Rodríguez-Mozos, J. M., & Moya, A. 2019, AA, 630, A52, 1908.06695

Roger, R. E. 1987, Los Alamos Science, 15, 131

Roth, N., & Kasen, D. 2015, ApJS, 217, 9, 1404.4652

Roxburgh, I. W. 1966, ApJ, 143, 111

Rust, D. M. 1994, Geophys. Res. Lett., 21, 241

Sadavoy, S. I., & Stahler, S. W. 2017, MNRAS, 469, 3881, http://oup.prod.sis.lan/mnras/article-pdf/469/4/3881/17700538/stx1061.pdf

Salpeter, E. E. 1955, ApJ, 121, 161

Salz, M., Banerjee, R., Mignone, A., Schneider, P. C., Czesla, S., & Schmitt, J. H. M. M. 2015, AA, 576, A21, 1502.06517

Sana, H. et al. 2014, ApJS, 215, 15, 1409.6304

Santos-Lima, R., de Gouveia Dal Pino, E. M., Falceta-Gonçalves, D. A., Nakwacki, M. S., & Kowal, G. 2017, MNRAS, 465, 4866, 1611.10183

Scherrer, P. H. et al. 2012, Sol. Phys., 275, 207

Schöller, M. et al. 2017, AA, 599, A66, 1611.04502

Schrijver, C. J., Cote, J., Zwaan, C., & Saar, S. H. 1989, ApJ, 337, 964

Schrinner, M., Petitdemange, L., & Dormy, E. 2012, ApJ, 752, 121, 1202.4666

See, V. et al. 2017, MNRAS, 466, 1542, 1705.01835

——. 2015, MNRAS, 453, 4301, 1508.01403

See, V., Jardine, M., Vidotto, A. A., Petit, P., Marsden, S. C., Jeffers, S. V., & do Nascimento, J. D. 2014, AA, 570, A99, 1409.1237

See, V. et al. 2019, ApJ, 876, 118, 1903.05595

Segura, A., Walkowicz, L. M., Meadows, V., Kasting, J., & Hawley, S. 2010, Astrobiology, 10, 751, 1006.0022

Semel, M. 1989, AA, 225, 456

Shaltout, A. M. K., Amin, E. A., Beheary, M. M., & Hamid, R. H. 2019, Adv. Space Res, 63, 2300

Shepherd, D. S., & Churchwell, E. 1996, ApJ, 472, 225

Shepherd, D. S., Claussen, M. J., & Kurtz, S. E. 2001, Science, 292, 1513

Shu, F. H., Adams, F. C., & Lizano, S. 1987, ARAA, 25, 23

Silaj, J., Jones, C. E., Sigut, T. A. A., & Tycner, C. 2014, ApJ, 795, 82

SILSO, World Data Center. accessed Nov 2019, Sunspot Number and Long-term Solar Observations, Royal Observatory of Belgium, on-line Sunspot Number catalogue: http://www.sidc.be/silso/,1998-2018

Smith, R. J., Longmore, S., & Bonnell, I. 2009, MNRAS, 400, 1775, 0908.3910

Sollins, P. K., & Ho, P. T. P. 2005, ApJ, 630, 987, astro-ph/0506057

Sollins, P. K., Zhang, Q., Keto, E., & Ho, P. T. P. 2005, ApJ, 631, 399, astro-ph/0506059

Solomon, P. M., Rivolo, A. R., Barrett, J., & Yahil, A. 1987, ApJ, 319, 730

Spiegel, E. A., & Zahn, J. P. 1992, AA, 265, 106

Spitzer, L. 1978, Physical processes in the interstellar medium

Stahler, S. W., & Palla, F. 2004, The formation of stars

Stone, J. M., Ostriker, E. C., & Gammie, C. F. 1998, ApJL, 508, L99, astro-ph/9809357

Strömgren, B. 1939, ApJ, 89, 526

Sweby, P. K. 2001, in Godunov Methods, ed. T. E. F. (Boston: Springer), 879–898

Szebehely, V. 1967, PNAS, 58, 60

Taylor, J. B. 1974, Phys. Rev. Lett., 33, 1139

Tehrani, K. A., Crowther, P. A., Bestenlehner, J. M., Littlefair, S. P., Pollock, A. M. T., Parker, R. J., & Schnurr, O. 2019, MNRAS, 484, 2692, 1901.04769

Thies, I., & Kroupa, P. 2007, ApJ, 671, 767, 0708.1764

Tigé, J. et al. 2017, AA, 602, A77, 1703.09839

Tziotziou, K., Georgoulis, M. K., & Raouafi, N.-E. 2012, ApJL, 759, L4, 1209.5612

Ud-Doula, A., Owocki, S. P., & Townsend, R. H. D. 2009, MNRAS, 392, 1022, 0810.4247

Urquhart, J. S. et al. 2014, MNRAS, 443, 1555, 1406.5078

Vacca, W. D., Garmany, C. D., & Shull, J. M. 1996, ApJ, 460, 914

van Buren, D., Mac Low, M.-M., Wood, D. O. S., & Churchwell, E. 1990, ApJ, 353, 570

van der Tak, F. F. S., & Menten, K. M. 2005, AA, 437, 947, astro-ph/0504026

Vandenbroucke, B. et al. 2019, MNRAS, 1903.00479

Vandenbroucke, B., & Wood, K. 2018a, CMacIonize: Monte Carlo photoionisation and moving-mesh radiation hydrodynamics, Astrophysics Source Code Library, 1802.003

——. 2018b, Astron. Comput., 23, 40

Venot, O., Rocchetto, M., Carl, S., Roshni Hashim, A., & Decin, L. 2016, ApJ, 830, 77, 1607.08147

Vida, K., Kővári, Z., Pál, A., Oláh, K., & Kriskovics, L. 2017, ApJ, 841, 124, 1703.10130

Vida, K., Leitzinger, M., Kriskovics, L., Seli, B., Odert, P., Kovács, O. E., Korhonen, H., & van Driel-Gesztelyi, L. 2019, AA, 623, A49, 1901.04229

Vidotto, A. A. 2016, MNRAS, 459, 1533, 1603.09226

Vidotto, A. A. et al. 2014, MNRAS, 441, 2361, 1404.2733

Vidotto, A. A., Jardine, M., Morin, J., Donati, J. F., Lang, P., & Russell, A. J. B. 2013, AA, 557, A67, 1306.4789

Vidotto, A. A., Jardine, M., Opher, M., Donati, J. F., & Gombosi, T. I. 2011, MNRAS, 412, 351, 1010.4762

Viljanen, A., Myllys, M., & Nevanlinna, H. 2014, J. Space Weather. Space Clim., 4, A11

Walmsley, M. 1995, in Revista Mexicana de Astronomia y Astrofisica Conference Series, ed. S. Lizano & J. M. Torrelles, Vol. 1, 137

Walter, F. M., & Bowyer, S. 1981, ApJ, 245, 671

Wang, K. et al. 2014, MNRAS, 439, 3275, 1401.4157

Warnecke, J., & Peter, H. 2019, arXiv e-prints, arXiv:1910.06896, 1910.06896

Webb, D. F., & Howard, T. A. 2012, Living Rev. Sol. Phys., 9, 3

Weber, E. J., & Davis, Leverett, J. 1967, ApJ, 148, 217

Weidner, C., & Kroupa, P. 2006, MNRAS, 365, 1333, astro-ph/0511331

Weidner, C., Kroupa, P., & Bonnell, I. A. D. 2010, MNRAS, 401, 275, 0909.1555

Weidner, C., & Vink, J. S. 2010, AA, 524, A98, 1010.2204

Williams, H. A., & Tohline, J. E. 1988, ApJ, 334, 449

Williams, J. P., Bergin, E. A., Caselli, P., Myers, P. C., & Plume, R. 1998, ApJ, 503, 689

Williams, J. P., Blitz, L., & McKee, C. F. 2000, in Protostars and Planets IV, ed. V. Mannings, A. P. Boss, & S. S. Russell, 97, astro-ph/9902246

Williams, R. J. R., Bisbas, T. G., Haworth, T. J., & Mackey, J. 2018, MNRAS, 479, 2016, 1805.09273

Wilson, O. C. 1978, ApJ, 226, 379

Wolfire, M. G., & Cassinelli, J. P. 1987, ApJ, 319, 850

Woltjer, L. 1958, PNAS, 44, 489

Wood, B. E. 2004, Living Rev. Sol. Phys., 1, 2

Wood, B. E., Müller, H.-R., Zank, G. P., & Linsky, J. L. 2002, ApJ, 574, 412, astro-ph/0203437

Wood, D. O. S., & Churchwell, E. 1989a, ApJ, 340, 265

Wood, D. O. S., & Churchwell, E. 1989b, ApJS, 69, 831

Wood, K., & Loeb, A. 2000, ApJ, 545, 86, astro-ph/9911316

Wood, K., Mathis, J. S., & Ercolano, B. 2004, MNRAS, 348, 1337, astro-ph/0311584

Wood, K., & Reynolds, R. J. 1999, ApJ, 525, 799, astro-ph/9905289

Wright, N. J., & Drake, J. J. 2016, Nature, 535, 526, 1607.07870

Wright, N. J., Drake, J. J., Mamajek, E. E., & Henry, G. W. 2011, ApJ, 743, 48, 1109.4634

Wright, N. J., Newton, E. R., Williams, P. K. G., Drake, J. J., & Yadav, R. K. 2018, MNRAS, 479, 2351, 1807.03304

Yang, S., & Zhang, H. 2012, ApJ, 758, 61

Yeates, A. R., & Mackay, D. H. 2012, ApJ, 753, L34, 1206.2327

Yorke, H. W., & Bodenheimer, P. 1999, ApJ, 525, 330

Yorke, H. W., & Kruegel, E. 1977, AA, 54, 183

Yorke, H. W., & Sonnhalter, C. 2002, ApJ, 569, 846, astro-ph/0201041

Zendejas, J., Segura, A., & Raga, A. C. 2010, Icarus, 210, 539, 1006.0021

Zhang, M. 2013, in IAU Symposium, Vol. 294, Solar and Astrophysical Dynamos and Magnetic Activity, ed. A. G. Kosovichev, E. de Gouveia Dal Pino, & Y. Yan, 505–518, 1211.3190

Zhang, M., & Flyer, N. 2008, ApJ, 683, 1160, 0805.1783

Zhang, M., Flyer, N., & Chye Low, B. 2012, ApJ, 755, 78, 1206.2411

Zhang, M., Flyer, N., & Low, B. C. 2006, ApJ, 644, 575, astro-ph/0603011

Zhang, M., & Low, B. C. 2005, ARAA, 43, 103

Zinnecker, H. 1982, Ann. N. Y. Acad. Sci, 395, 226

Zinnecker, H., & Mathieu, R., eds. 2001, IAU Symposium, Vol. 200, The Formation of Binary Stars

Zinnecker, H., McCaughrean, M. J., & Wilking, B. A. 1993, in Protostars and Planets III, ed. E. H. Levy & J. I. Lunine, 429

Zinnecker, H., & Yorke, H. W. 2007, ARAA, 45, 481, 0707.1279

Zuccarello, F. P., Pariat, E., Valori, G., & Linan, L. 2018, ApJ, 863, 41, 1807.00532